GREENER SYNTHESIS OF NANOSTRUCTURED CERIA BASED MATERIALS FOR POLLUTANT REMOVAL AND OPTICAL SENSING APPLICATIONS

Thesis submitted to the
University of Calicut in partial fulfillment of
the requirements for the degree of

DOCTOR OF PHILOSOPHY IN CHEMISTRY
In the Faculty of Science

By

REMANI K. C.

Research and Post Graduate Department of Chemistry
Sree Neelakanta Government Sanskrit College
Pattambi
(Affiliated to University of Calicut, Kerala, India)

October 2020

SreeNeelakanta Govt. Sanskrit College
Pattambi, Palakkad Dt, Kerala - 679 306
(Accredited by NAAC with A Grade)
Ph: 0466-2212223 e-mail: sngscollege@gmail.com
Website: www.sngscollege.org

CERTIFICATE

This is to certify that the thesis entitled "**GREENER SYNTHESIS OF NANOSTRUCTURED CERIA BASED MATERIALS FOR POLLUTANT REMOVAL AND OPTICAL SENSING APPLICATIONS**", bound herewith is a bonafide work done by Mrs. Remani K. C. under my supervision in the Research and Post Graduate Department of Chemistry, SNGS College, Pattambi. I also certify that the corrections/suggestions from the adjudicators have been incorporated in the revised thesis.

Place: Pattambi
Date: 24-06-2021

Dr. Binitha N. N.
(Supervising Guide)
Research and Post Graduate
Department of Chemistry
S.N.G.S. College, Pattambi

SreeNeelakanta Govt. Sanskrit College
Pattambi, Palakkad Dt, Kerala - 679 306
(Accredited by NAAC with A Grade)
Ph: 0466-2212223 e-mail: sngscollege@gmail.com
Website: www.sngscollege.org

CERTIFICATE

Certified that the thesis entitled "**GREENER SYNTHESIS OF NANOSTRUCTURED CERIA BASED MATERIALS FOR POLLUTANT REMOVAL AND OPTICAL SENSING APPLICATIONS**", submitted by Mrs. Remani K. C. is an authentic record of research work carried out by she under my supervision at the Research and Post Graduate Department of Chemistry, SNGS College, Pattambi in partial fulfillment of the requirements for the award of degree of Doctor of Philosophy in Chemistry of the University of Calicut, and has not been included in any other thesis submitted previously for the award of any other degree.

Place: Pattambi
Date: 27-10-2020

Dr. Binitha N. N.
(Supervising Guide)
Research and Post Graduate
Department of Chemistry
S.N.G.S. College, Pattambi

DECLARATION

I hereby declare that the present work entitled "**GREENER SYNTHESIS OF NANOSTRUCTURED CERIA BASED MATERIALS FOR POLLUTANT REMOVAL AND OPTICAL SENSING APPLICATIONS**" is an authentic record of the original work done by me under the guidance of Dr. Binitha N. N., Assistant Professor, Research and Post Graduate Department of Chemistry, SNGS College, Pattambi in partial fulfillment of the requirement for the award of degree of Doctor of Philosophy in Chemistry of the University of Calicut, and has not been included in any other thesis submitted previously for the award of any other degree.

Place: Pattambi **Remani K. C.**

Date: 27-10-2020

DEDICATED
To
All, who helped to accomplish this venture,

ACKNOWLEDGEMENTS

There have been many people who have walked along with me during this period of research. They have supported me, cited opportunities in front of me, and showed me the doors that might be useful to go through. I use this opportunity to express my sincere gratitude to all of them, who gave coherent support during my Ph.D. tenure.

First and foremost, I would like to eloquent my indebtedness and amiable gratefulness towards my supervising guide Dr. Binitha N. N, Assistant Professor, Research and Postgraduate Department of Chemistry, SNGS College Pattambi. I extend my deepest thanks for her patience, help, motivation, enthusiasm, and immense knowledge that she has showered on me for the successful completion of the present thesis. Dear teacher, please accept my intense protestations of gratitude.

I express my heartfelt gratitude to the University Grant Commission, New Delhi, India for providing the financial supports for the successful completion of the minor project entitled "Ceria Zirconia solid solution based three way catalyst: Application in diesel engine exhaust gas treatment" which I worked that has been extended as a part of my Ph.D. work.

I greatly acknowledge SNGS College Pattambi, the wonderful place where I seeded to bloom. I am grateful to this institution for providing the infrastructure facilities for carrying out my research work.

I wish to express my immense gratitude towards the Head of Research and Postgraduate Department of Chemistry, Dr. P Venugopalan and all other faculties Resmi teacher, Manoj sir,

Anjaly teacher, Roy sir, Usha, and Ramlath teacher for their constant encouragement and valuable advice on time. On this occasion, I am grateful to the former HODs of the Chemistry department, Dr. M. Ravindran, and Dr. P. Narayanan (Late) for their unflagging encouragement and constant support. I also extend my warm gratitude to my former colleagues Femina teacher, Vinod sir, Jincy, and Suchitra for their continuous encouragement.

I extend my gratitude to the non-teaching staff Surettan, Ushachechi, Vijayechi, Pramodettan, Mohanettan, and Habeebikka for their unconditional love, help, and support.

I am thankful to Smt. Prasanna P. K., Principal, SNGS College Pattambi, and also the former Principals Dr. Jothiraj M, Dr. Sheela S, Prof. Anithakumari P.N, Dr. Suma K K., Prof. P. M. Raghavan, Dr. K. Premalatha, and Dr. Vilasini. My acknowledgment will never be completed without memorizing the former principal Prof. M. P. Raveendrakumar (Late) and former Vice-Principal Prof. Muralidharan R, who helped a lot in the initial stages of the project work.

I thank administrative faculties in the SNGS College for clearing official procedures as early as possible.

I am grateful to Dr. S. K. Ghosh, Scientist (Rtd), MMD Ceramics, NIIST, Tvm; who had opened me the door to the world of research for the first time during my research as a project assistant at NIIST. I can never forget his valuable scientific discussions, creative ideas, and constant encouragement. I am also thankful to Dr. K. G. K. Warrier, former head of the MMD division for his valuable advice during that time.

My sincere thanks to the University of Calicut for upgrading SNGS College as a research center and providing me a golden opportunity to do Ph.D. here.

I express my genuine thanks to Dr. N. K. Renuka, Dr. P. Raveendran, Dr. Anilkumar, Dr. M Sathian Dr. H. K. Santhosh, and Dr. Resmi M. R, the doctoral committee members.

I am thankful to SAIF-STIC, Cochin, CSIF, University of Calicut, IIT Kanpur, PSG Institute of Advanced Studies, Coimbatore for various sample analysis.

I wish to express my heartfelt gratitude to my colleagues, Dr. Vinu V. V. and Dr. Silija P. who helped a lot during the working of the minor research project on three way catalysis. I also that my colleagues Dr. Divya, Dr. Sudha, Dr. Soumya, Vijayasree, Shameena, Suvarna,. Dr. Rajeena, Dr. Deepthi, Dr. Shaniba, and Sreeja for their supports.

I would like to acknowledge all my friends for their moral support and motivation, which has always driven me to give my best. My special thanks to all my students in the college especially to those in the Chemistry department for their affection, supports, and help they have given throughout these years.

I owe my deepest gratitude to all my teachers who had uplifted me to the world of knowledge. I am forever indebted to my loving teachers at SSMUP School, Naranipuzha, and Govt. HSS, Mookkuthala, they showed me by example and stressed the importance of diligence and determination. I also wish to express my deep sense of gratitude to all my teachers at L. F. College, Guruvayur, and Govt. Victoria College Palakkad for their excellent guidance, encouragement, and motivation.

Finally, I would like to acknowledge my beloved parents, Achan and Amma, the main driving force for all my achievements. No words to express my gratefulness to my Uniettan, Rithukkuttan and Richuttan for being my strength and untiring support. Thanks to my brothers and sisters for their endless love and care.

Remani K. C.

PREFACE

The considerable deterioration in the quality of soil, air and water due to the increased amount of pollution in these segments; which aroused due to the fast development of industries and economic growth has become one of the great concerns in the present scenario. The incomplete combustion of fossil fuels in thermal power plants, incinerators and vehicles generates a huge amount of gaseous pollutants such as CO and unburnt hydrocarbons in the atmosphere which causes detrimental effects on atmosphere such as formation of photochemical smog, acid rain, global warming etc. in addition to the harmful health effects on the creatures on earth. Also, the large consumption of chemical products by the increased population around the world leads to the establishment of more number of chemical industries which introduce various chemical pollutants in the water bodies. Some of the important classes of pollutants detected in waterbodies are antibiotics, dyes and nitro aromatic compounds. Presence of antibiotic norfloxacine, which is a fluoroquinolone antibiotic in water leads to the spread of antibiotic resistant bacteria and also harmful to the aquatic organisms. Presence of azodyes such as Congo red poses long term health hazards to human beings as they are toxic, carcinogenic and mutagenic in nature. Thus it is of great significant to eliminate these gaseous as well as water pollutants by some effective methods.

Selective and sensitive detection of polynitroaromatics such as picric acid in the environment is crucial since even trace amount of its

presence causes several health issues such as headache, dizziness, nausea, vomiting, irritation to eyes/skin and also effect organs in the respiratory systems and liver. Similarly, an accurate and rapid determination of H_2O_2 in biological systems is of great relevance since H_2O_2 is an important reactive intermediate formed in human being as a byproduct of metabolic reactions.

Green synthesis of metal oxide nanoparticles using biological media have been developed recently to avoid the toxicological effect of synthesis and to produce biocompatible nanoparticles. Plant extracts have been proved to be a major source of various bioactive organic compounds which act as reducing, chelating and stabilizing agents in the preparation of nanoparticles with reduced size and agglomeration.

The present work deals with the synthesis of CeO_2 nanoparticles by green methods and the characterization of the synthesized materials using different analytical techniques. Here we have synthesized CeO_2 nanoparticles by sol-gel method using various phytochemicals present in garlic and fenugreek extracts as the chelating agents and stabilizing agents. The material synthesized using garlic extract are used as effective adsorbents as well as photo Fenton catalysts for the removal of Congo red dye; whereas that synthesized from fenugreek extract was applied in the fluorescence sensing of picric acid. CeO_2 nanoparticles in ultra small dimension could be prepared using 2 M ammonia as the precipitating agent which have been utilized as an effective photocatalyst in the degradation of antibiotic norfloxacin. Impregnation of cobalt into ultrasmall CeO_2 nanoparticles synthesized by ammonia precipitation method lead to the

formation of cobalt doped CeO_2 catalysts that are effectively used for the simultaneous removal of CO and model hydrocarbon pollutant propane. The same series of catalysts have also been used as a peroxidase-like catalyst in the colorimetric detection of H_2O_2.

This thesis is structured into 7 chapters. Chapter 1 gives an introduction into ceria nanostructures and its important properties, applications and synthesis strategies. Chapter 2 explains the materials and methods employed for the sample preparation, material charactrization and their applications. In the chapter 3, preparation of ultrasmall CeO_2 nanoparticles by precipitation method using ammonia of different concentration as the precipitating agents and their applicability in the photocatalytic degradation of antibiotic norfloxacin has been investigated. Chapter 4 describes the development of mesoporous CeO_2 nanoparticles using garlic extract for the removal of Congo red dye via adsorption as well as photo Fenton degradation. Chapter 5 discusses about the synthesis of CeO_2 nanostructures by sol-gel method in presence of fenugreek extract for the selective sensing of picric acid via fluorescence quenching method. In chapter 6, the preparation of cobalt doped CeO_2 samples and its application for the simultaneous removal of CO and propane; and also its applicability in the colorimetric sensing of H_2O_2 is narrated. Thesis is concluded with chapter 7 that summarizes the present work, which deals about the use of CeO_2 based materials for the removal of above mentioned pollutants from air and water; and also for the optical sensing of picric acid and H_2O_2.

CONTENTS

Chapter 1

Ceria:Brief Introduction and Literature Review

1.0 Cerium

Cerium is one of the rare earth elements with the symbol Ce and atomic number 58. It is a silvery-white colored, ductile,soft metal that can be cut even with a knife. This element belongs to the lanthanide series (second element) and is the 26^{th} most abundant element on the earth's crust. Cerium was discovered in Sweden by Jöns Jakob Berzelius and Wilhelm Hisinger in 1803, and independently by Martin Heinrich Klaproth in Germany,~~in~~ the same year. The name cerium was suggested by Berzelius, after the name of the dwarf planet Ceres, which was discovered two years earlier [1]. Its electronic configuration is $[Xe]4f^{1}5d^{1}6s^{2,}$ in which the energy of the 4f electrons is nearly the same as that of 5d and 6s electrons and gives rise to two oxidation states [2]. Thus cerium shows the formal oxidation state of +3, characteristics of lanthanides, and can be oxidized to its stable oxidation state of +4 [3]. At standard pressure, four allotropic forms are known to exist at different temperatures, which are δ-cerium (body-centered cubic crystal), γ-cerium (face-centered cubic crystal), β-cerium (double hexagonal close-packed), and α-cerium (face-centered cubic crystal) [4]. Four stable isotopes of cerium exist in naturally occurring cerium, in which ^{140}Ce is the most common isotope (88.4%). ^{136}Ce (0.19%), ^{138}Ce (0.25%), and ^{142}Ce (11.1%) are the other three isotopes, which undergo double beta decay and alpha decay to the isotope of barium [5]. There is an abundance of ^{140}Ce,as it has a closed neutron shell of 82 neutrons and a very low cross-section towards further neutron capture [6]. Bastnasite (a rare earth fluorcarbonate mineral), Monazite (a rare-earth phosphate), and

Loparite are the principal ores of cerium. The deposits of these ores occur in California, Nebraska, United States, Australia, Mongolia, and China. Solvent extraction, selective precipitation, and ion-exchange methods are used for the commercial production of cerium [7]. The purified cerium should be stored under an inert atmosphere to avoid oxidation. Cerium metal is a pyrophoric substance and readily burns at 150 °C to form cerium(IV)oxide, which can reduce to cerium(III) oxidewith hydrogen gas [8]. Cerium, the electropositive metal, forms cerium hydroxides and halides in reaction with water and halogens [9]. The standard electrode potential of the $Ce^{4+/}Ce^{3+}$ couple depends on the presence of surrounding anions. The representative value is +1.72 V, and that for Ce^{3+}/Ce is -2.34 V [10]. Cerium metal is primarily used in the preparation of ferrocerium-fired steel metal alloy, which applies in lighter flints. It is also added in small quantities to alloys as an oxygen scavenger to impart oxidative resistance. Compounds of cerium have a variety of uses: for example,cerium fluoride can use as an additive to lubricants, cerium carboxylates to improve the properties of silicone polymers, cerium(IV) sulfates as standard reagents for volumetric analysis in cerimetric titrations, andcerium nitrate for antimicrobial treatment for third-degree burns [11-14]. Among the compounds of cerium, cerium(IV) oxide, also known as ceria, is the most commonly used, in a wide variety of applications.

1.1 Cerium oxide (Ceria)

Cerium(IV) oxide is the important oxide of cerium,which is also known by different names such as ceric oxide, ceric dioxide, ceria,

cerium oxide,and cerium dioxide. It is a pale yellow-white powder with the chemical formula CeO_2. Ceria is formed mainly by the calcination of cerium oxalate or cerium hydroxide. It is an intermediate in the process of isolation of cerium metal from its ores. Ceria and ceria-based materials have been a subject of surplus research, both in the academy and in industries, due to some of their exceptional properties [15]. The distinctive property that makes it applicable for versatile applications is its ability to undergo reversible conversion to a non-stoichiometric oxide [16]. The important physical properties of ceria are given below intable 1.1 [3,13].

Table 1.1 Physical properties of ceria

Property	Value
Molecular weight	172.115 (g/mol)
Appearance	white or pale yellow solid
Density	7.215 (g/cm^3)
Melting point	2400 °C (4,350 °F; 2,670 K)
Boiling point	3500 °C (6,330 °F; 3,770 K)
Solubility	Insoluble
Odor	Odorless
Toxicity	No
Thermal conductivity	12 $Wm^{-1}K^{-1}$
Electrical conductivity	2.48 x 10^{-8} S/cm at room temperature
Magnetic susceptibility	+26.0x10^{-6} cm^3/mol
Crystal structure	cubic fluorite

1.1.1 Structure of CeO_2

Among the two oxidation states of cerium, the Ce^{4+} state is more stable due to its stable $[Xe]4f^0$ configuration,as compared to the Ce^{3+} state which has $[Xe]4f^1$ electronic state. Analysis of the thermodynamic parameters shows that cerium metal is unstable in the presence of oxygen, and intermediate oxides are formed whose stoichiometry depends on the temperature and oxygen pressure [17]. Among these, the formation of two extreme compositions i.e., Ce_2O_3(cerium sesquioxide) and $CeO_2$are spontaneous since the free energy of the formation of these oxides at 298 K is -1796 KJ/mol and -1089 KJ/mol respectively [18]. CeO_2 has a fluorite structure with a face-centered cubic (FCC) unit cell with space group Fm3m (a = 0.541134 nm, JCPDS 34-394).

In this structure, each Ce cation is surrounded by eight equivalent oxygen anions at the corners of a cube, and each anion is coordinated by four cations forming tetrahedra as shown in figure 1.1 [19]. The removal of O^{2-} anions from the ceria lattice results in the generation of anion vacant sites according to the following equation, thereby forming reduced ceria.

$$4Ce^{4+} + O^{2-} \rightarrow 4Ce^{4+} + 2e/\square + 0.5O_2 \rightarrow 2Ce^{4+} + 2Ce^{3+} + \square + 0.5O_2 \quad (1.1)$$

where □ represents an anion-vacant site (an empty position) originated from the removal of O^{2-} from the lattice.

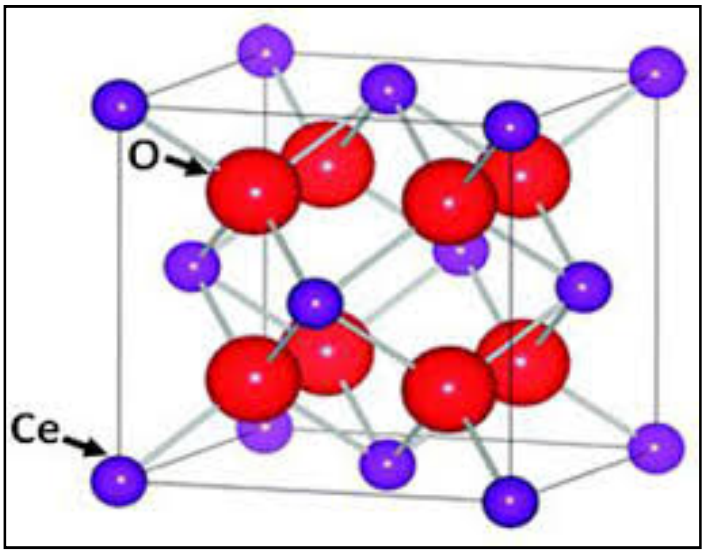

Fig 1.1 FCC structure of ceria [19]

The electrical neutrality is maintained by the conversion of two Ce^{4+} ions into Ce^{3+} state. At temperatures greater than 685 °C and at low oxygen pressures,non-stoichiometric oxygen-deficient oxides are formed with composition in the range $1.714<x<2$ for CeO_x, which are called α phase ceria [20]. This phase is stable at high temperatures and has a disordered non-stoichiometric fluorite-related structure. The lattice parameter (a) calculated from the high-temperature XRD pattern shows that the value increases as x decreases or with the increasing content of Ce^{3+} [21]. This is because the ionic radius of Ce^{3+} (1.14 Å) is larger than that of Ce^{4+} (0.97 Å) [22]. As the temperature is lowered, the α phase transformsinto a series of fluorite-related phases with the general formula Ce_nO_{2n-2m} [23]. Some of the important phases observed in between the composition CeO_2 to $CeO_{1.714}$ are Ce_6O_{11} (the

β phase, monoclinic), $Ce_{11}O_{20}$ (the δ phase, triclinic), Ce_7O_{12} (rhombohedral), and Ce_9O_{16} (γ phase, rhombohedral) [24-26].

1.1.2 Defects in Ceria

Dislocations of atoms or ions from the crystal lattice may break the symmetry of the perfect ceria crystal lattice. In ceria, both intrinsic and extrinsic defects can occur. Intrinsic defects may arise due to the disorder in the crystal and can be formed by the redox reaction of the solid with some gases in the surrounding atmosphere. Frenkel and Schottky defects are the main intrinsic defects in CeO_2. Extrinsic defects arise due to the incorporation of some impurities into the lattice. The Schottky type (eqn.1.2) and Frenkel type (equation (eqn)1.3 and 1.4) defects seen in ceria crystals are represented by Kroger and Vink defect notation;

$$Ce_{Ce} + 2O_O \leftrightarrow V''''_{Ce} + 2V_o + CeO_2 \qquad \Delta E = 3.53eV \quad \text{(eqn 1.2)}$$

$$Ce_{Ce} \leftrightarrow Ce_i^{\cdots} + V''''_{Ce} \qquad \Delta E = 11.11\ eV \quad \text{(eqn 1.3)}$$

$$O_O \leftrightarrow O_i'' + V_o \qquad \Delta E = 3.2\ eV \quad \text{(eqn 1.4)}$$

where O_O and Ce_{Ce} represent oxygen and cerium at their respective lattice sites, V_o and V''''_{Ce} respectively indicate oxygen and a cerium vacancy; $Ce_i^{\cdots}$ and O_i'' a cerium and oxygenion in interstitial position. A dot (•) is indicated for each positive charge and a prime (') for each negative charge. The predominant defect category in ceria is the anion Frenkel-type as evidenced by the energy value that leads to the formation of pairs of oxygen vacancies and oxygens in interstitial positions [27]. However, this does not affect the stoichiometry of ceria

as the concentrations of this type of defect are very low. When exposed to reducinggaseous atmospheres, the concentration of defects increases.In that state, ceria has a higher content of cerium compared to the anion, i.e., the cation/anion ratio becomes greater than 0.5. For each oxygen ion removed, two electrons are introduced into the crystal to maintain electrical neutrality. These electrons are associated with two cerium atoms that will change the oxidation state of cerium from +4 to +3. The process is represented as,

$$CeO_2 \leftrightarrow CeO_{2-x} + x/2O_2(g);\ x<0.5 \qquad \text{(eqn 1.5)}$$

It can also be represented by the following defect reaction

$$CeO_2 \leftrightarrow 2xCe_{Ce}^{'} + (1-2x)Ce_{Ce} + xV_o + (2-x)O_o + 0.5xO_2(g) \qquad \text{(eqn 1. 6)}$$

The reaction shows that as x moles of atomic oxygen are removed from the lattice, the corresponding quantity of O^{2-} sites are occupied by oxygen vacancies leaving 2-x moles of O^{2-} anions in their original positions. 2x moles of $Ce^{3+}$is formed (Ce'_{Ce}), leaving l-2x moles of Ce^{4+}.

1.1.3 Properties of Ceria

1.1.3.1 Oxygen Storage Capacity and Redox Properties

A wide range of applications of ceria and ceria-based materials in catalytic oxidation of exhaust gases, water gas shift reaction, hydrocarbon reforming,etc.are associated with the oxygen storage capacity (OSC) a fundamental property of ceria [28-30].Ceria can store oxygen under oxygen-rich conditions and release oxygen under

oxygen-deficient conditions. This property is termed the oxygen storage capacity (OSC) and it makes ceria excellent support of noble metals in the treatment of exhaust gases to operate in a wide range of air/fuel ratios (λ) under dynamic conditions [31-32]. The OSC of a solid is defined as the concentration (μmol $O \cdot g^{-1}$) of the most reactive and readily available (labile) oxygen atoms in the solid. The oxygen storage capacity complete (OSCC) of a solid is defined as the maximum concentration (μmol $O \cdot g^{-1}$) of oxygen species removed from the solid under the prevailing experimental conditions for the measurement (e.g., pulse size, T). OSC of ceria is attributed to the rapid conversion of cerium between +3 and +4 oxidation states after a change in exhaust-gas composition between fuel-lean and fuel-rich conditions. Under these conditions, ceria undergoes rapid oxidation and reduction, and the composition changes between CeO_2 and CeO_{2-x} according to equation (1.5) [33-34].The redox properties of ceria are investigated by OSC measurement. Total OSC can be obtained from temperature-programmed reduction (TPR) and reoxidation. The common reductants used are CO, H_2, and hydrocarbons (HCs), and oxidants are O_2 and NO [35-38]. The OSC values of ceria depend on several factors such as surface area, particle size, thermal or chemical treatment, synthetic procedures, etc. [39]. Incorporation of other metals such as Zr, Cu, Ni,etc., will improve the OSC of ceria through the formation of structural defects and local compound formation[40]. Supported metals like Ru, Ir, Pd, and Pt also increase the OSC by activating oxygen species of the support [41].

1.1.3.2 Electrical Properties: Ionic and Electrical Conductivity

Ceria is considered as a semiconductor with both electronic and ionic conduction and the application of ceria as a solid electrolyte is based on these properties [42]. The properties of electrical conduction and oxygen diffusion depend on the factors such as temperature, oxygen partial pressures, and the presence of dopants which in turn affect the concentration and mobility of lattice defects. The total conductivity in CeO_{2-x} is the sum of the contributions from electrons, holes, and oxygen vacancies, which are the primary charge carriers in ceria. The conductivity is given by the equation,

$$\sigma_t = [Ce_{Ce}^{'}]\, e\mu_e + [h^{\cdot}]\, e\mu_h + [V_o]\, 2e\mu_{Vo} \quad \text{(eqn 1.7)}$$

In the equation,in the RHS, the first term is the contribution of electrical conductivity, the second term is due to the presence of holes, the third is the ionic conductivity, and μ is the mobility of the carrier. The ionic transport results from the hopping of oxide ions to the vacant sites and the ionic conductivity increases with increasing oxide ion vacancy concentration which at 1000 °C is estimated to be ca. 7×10^{-2} Scm^{-1} for $CeO_{1.9}$ [43]. The n-type conductivity (electronic conductivity, σ_e) in ceria is due to small polaron transport [44-45]. A polaron is a defect formed when an electronic carrier is trapped at a given vacancydue to the displacement of adjacent atoms or ions in the crystal lattice. This defect (an electron or electron-hole) migrates by thermally activated hopping. $Ce_{Ce}^{'}$ is identified as the polaron in CeO_{2-x}. In the vicinity of stoichiometry (up to $x \approx 10^{-2}$), electronic conductivity

is proportional to x and saturation occurs at x ≈ 0.04, and σ_e has a broad maximum with a peak value at x ≈ 0.1.p-type conductivity (electron-hole) also has been observed in ceria in the temperature range of 600 °C –1100 °Cat oxygen pressure ≈ 1–400 atm [46]. Electron-hole mobility is estimated to be significantly lower than that of electrons at the same temperature [47].

1.1.3.3 Optical Properties

The bandgap of ceria nanoparticles can be calculated from the edge of the optical absorption band [48]. Making use of the dependence of the absorption coefficient α on the energy of a light quantum hν;

$$\alpha h\upsilon = C\,(h\upsilon - E_g)^n \qquad \text{(eqn 1.8)}$$

where n = 1/2 for direct transitions and n = 2 for indirect transitions. By plotting $(\alpha h\nu)^2$ against the photon energy, the intersection on the x-axis gives the value of direct bandgap energy E_g. In ceria, an important factor affecting the bandgap energy is the concentration of oxygen vacancies or conversion of Ce^{4+} into Ce^{3+} state. When all the cerium ions exist in a 4+ oxidation state or no oxygen vacancies are present, the bandgap is 4 eV for CeO_2. When Ce^{3+} ions are present in the lattice, it will generate a trap state at 3 eV above the CeO_2 valence band, which corresponds to the Ce5d - Ce4f transition [49].The bandgap of Ce_2O_3 is determined to be in between 3.04 eV – 3.7 eV and depends on the synthesis method and particle size [50]. If the bandgap

of ceria is close to 3 eV, then the crystal containsa higher concentration of Ce^{3+} and oxygen vacancies.

Though ceria is quite transparent to visible light, it strongly absorbs ultraviolet light on account of the charge-transfer transition from O(2p) to the Ce^{4+}(4f) orbital [51]. Ultrafine ceria crystals show a red shift in absorption, and an associated green-colored emission is shown that can attribute to the higher concentration of Ce^{3+} ions in the lattice [52**]**. The surface entropy of Ce^{3+} ions is higher than that of the bulk, so most of the surface ceria atoms exist in the Ce^{3+} state. With an increase in surface area (or decrease in particle size), the Ce^{3+} to Ce^{4+} ratio also increases. These Ce^{3+} ions will form an intermediate band in between the valence band and conduction band of ceria. Consequently, electron excitation takes place from the valence band to this newly formed intermediate band having lower energy that results in a redshift of absorption [53]. Ceria thin films are suitable for applications in optical, electro-optical, microelectronic, and optoelectronic devices because of their high refractive index (2.05) and dielectric constant. Also, ceria appears natural on the skin without imparting an excessive pale-white look. Thus ceria is used in personal care products as a UV blocking material. For such applications,the photocatalytic activity of ceria has to be suppressed as it generates reactive oxygen species.

1.1.4 Nanosize Effect

Nanoparticles exhibit distinctly different physicochemical properties compared to their bulk counterparts, and this is one of the

motivating forces for the fast development of nanoparticle synthesis [54]. On decreasing the particle size to the nanorange, the surface to volume ratio increases and enables ceria to react differently and exhibit unique properties. Ceria nanostructures show several size-induced property changes such as lattice expansion, the blueshift in ultraviolet absorption spectra, Raman-allowed mode shifting and broadeningas well as pressure-induced phase transformation. With a reduction in the particle size, cerium tends to exist as Ce^{3+} ions, resulting in more oxygen vacancies.Tsunekawa et al. studied the lattice expansions in monodisperse CeO_{2-x} nanoparticles using electron diffraction experiments [55]. X-ray photoelectron spectroscopy (XPS) results showed that the reduction of Ce^{4+} into Ce^{3+} ions decreases the electrostatic force of attraction among the lattice points ultimately leading to lattice expansion (lattice relaxation).The lattice expansion can be observed in ceria nanoparticles with an average size range of 4–60 nm, and Zhou et al. reported that in ultra-small ceria nanoparticles (1.1 nm), a major fraction of cerium atoms attain the fully reduced state, despite retaining the cubic lattice. The size and strain in nanoparticles resultedin the broadening of the diffraction line. In particles with a size less than 5nm, the size contributes to line broadening, whereas for larger crystals,the strain effect dominates. Zhang et al. studied the change in absorption wavelength with a change in particle size. For the particlesin the range of 4-7 nm, both the direct and indirect bandgap energies increase due to the quantum size effect, which is evident from the blue shift in the absorption band [56-

57]. But for nanocrystals with size < 5nm, the bandgap energy remains almost unchanged since the blue-shifting due to the quantum size effect counteracts the redshift due to the dielectric confinement effect [58]. Spanier et al. studied the Raman spectra of CeO_{2-y} nanoparticles and observed that the peak position of the triply degenerate Raman line at 464 $cm^{-1}$is shifted to lower energies, broadened, and becomes asymmetric on the low energy side [59]. This change occursdue to a combination of strain and phonon confinement effects. In most catalytic applications, the particle size determines the performance of ceria. Thus we can tune the reactivity of the ceria catalyst by controlling the size of the nanoparticles, which can be accomplished by adopting suitable synthesis strategies and synthetic conditions.

1.1.5 Synthesis Methods of Ceria

Some of the properties of ceria, such as its crystalline phase, particle size, surface area, catalytic activities, and OSC, etc., depend strongly on the synthesis methods. So many researchers have focused on the synthesis strategies with several modifications to develop ceria nanoparticles having excellent catalytic applications. Some common methods for the synthesis of ceria include solution precipitation, hydrothermal, solvothermal, ball milling, thermal decomposition, spray pyrolysis, thermal hydrolysis, and sol-gel [60]. Recently, bio-mediated synthesis is also investigated, which usesbiomolecules or natural products as stabilizing agents of CeO_2 nanoparticles.

1.1.5.1 Precipitation and Co-precipitation Method

Precipitation is a simple and easily operable method to prepare ceria nanomaterials and utilizes a chemical precipitating agent to precipitate cerium salt in a liquid medium. Usually, cerium is precipitated as hydroxide or oxalate by adding alkali solution or oxalic acid to an aqueous solution of a cerium salt. Heat treatment of the precipitate under suitable temperature gives ceria. Several factors such as the pH value and concentration of the aqueous solution, nature of the precipitating agent, reaction temperature, aging time, etc., affect the morphology and particle size of the material formed [61]. In some processes known as homogeneous precipitation, precipitants are generated simultaneously and uniformly throughout the solution using a controlled release of the participating species by some chemical reactions in the solution medium. For example, urea or hexamethylenetetramine on heating in an aqueous solution liberates ammonia to cause precipitation of cerium salt [62]. The co-precipitation method is the commonly used one for the preparation of mixed oxides, in which salts of several metals are dissolved in the same solvent and precipitated simultaneously. Chen et al. studied the effect of reaction temperature and oxygen content of the O_2/N_2 atmosphere in the precipitation method and found that the average particle size increased by either raising the reaction temperature or lowering the oxygen content [63]. Several other researchers also have reported the synthesis of ceria by using NH_4OH, NH_4CO_3, NaOH, etc., as the precipitating agents [64-65].

1.1.5.2 Hydrothermal/Solvothermal Treatment

The solvothermal process is carried out under controlled temperature and pressure in autoclaves in which the precursors and solvent are mixed. The reflux of solvent vapor can elevate the reaction temperature and reaches the pressure of vapor saturation while the temperature of the reaction and the amount of solution determine the internal pressure in the autoclave. Thus it is possible to control the morphology, size distribution and crystallinity of the nanocrystals formed [66]. The nature of solvents and reactants used, the solubility and ionic properties, and their changes at elevated temperatures play a prominent role in producing high-quality ceria nanocrystals [67]. Aqueous NaOH solution, $PO_4^{3-,}$ urea, NH_4OH, and H_2O_2 are the commonly used solutions in hydrothermal synthesis [68-72]. Single-crystalline nanopolyhedra exposed (111) and (100) crystal planes, nanorods exposed (110) and (100) crystal planes and nanocubes that exposed (100) planes are synthesized by using different concentrations of NaOH at 100-180 ℃ temperatures [73]. Mai et al. suggested the three main factors leading to the shape evolution: the development of hexagonal $Ce(OH)_3$ intermediate species, conversion of $Ce(OH)_3$ into CeO_2 at elevated temperature, and the base concentration [74]. Small organic acids such as C_2H_5COOH were also used as structure-directing agents in hydrothermal synthesis to synthesize mesoporous spheres with high surface-to-volume ratios having uniform size distributions [75]. CeO_2 nanoplates, nanotubes, and nanorods were successfully

synthesized hydrothermally by using hexadecyltrimethylammonium bromide (CTAB) as a structure-directing agent, in which the shape of the nanomaterial formed depended on the temperature, reaction time, and CTAB/Ce(III) ratio [76]. The presence of anions in the reaction medium also affects the morphology and properties of synthesized ceria, as they selectively interact with specific facets of the nanocrystals during the synthesis [77].

1.1.5.3 Thermal Decomposition (Thermolysis)

In this method, heat is continuously applied to the ceria precursor and is converted to ceria at its decomposition temperature. The process is endothermic, and heat energy is absorbed to break the chemical bonds. Monodisperse nanocrystals can be obtained by this method. Uniform CeO_2 nanoflowers have been reported by Zhou et al. by the rapid thermolysis of $(NH_4)_2Ce(NO_3)_6$ in mixed solvents containing oleic acid (OA) and oleylamine (OAm). CeO_2 nanoflowers with another cubic, four-petaled, and star-like shapes were also prepared by varying the reaction conditions such as solvent composition, precursor concentration, thermal decomposition temperature, and time [78]. Monodispersed CeO_2 nanopolyhedra were reported by Si et al. through thermal decomposition of its benzoylacetonate complex in OA/OAm mixed solvents, in which these molecules act as capping agents [79].

1.1.5.4 Sol-Gel Method

This method is particularly suitable for the preparation of ultrafine oxide materials at relatively low temperatures. In this process, metal alkoxides dissolved in alcohol or metal salts undergo hydrolysis and polymerization or peptization to form a sol. The removal of the solvent phase/charge leads to a continuous network of connected particles called a gel. The gel after drying and heat treatment at suitable temperatures give ceria having a large surface area, suitable for various applications. For the preparation of ceria-based oxides by the sol-gel method, cerium isopropoxide, cerium acetylacetonate, cerium nitrate, etc., are used as the precursors. Since the hydrolysis-condensation of molecular precursors is too rapid, to control the microstructure of the obtained product, chelating ligands such as organic additives are added in the process to modify the reactivity of the reagents [80]. Several research groups have reported the synthesis of well-crystallized CeO_2 microspheres by this method in solvents such as ethanol, diphenyl ether together with benzyl alcohol, OA/OAm as co-surfactants, etc. [81-83].

1.1.5.5 Flame Spray Pyrolysis (FSP)

In Flame spray pyrolysis, a metal-organic precursor dissolved in alcohol is sprayed into a combustion chamber along with an oxidizing gas. The spray undergoes combustion inside the chamber to decompose the precursors to produce metal oxide or metal. Both ceria and mixed oxides of ceria with high purity and crystallinity can be

obtained by this method, by using appropriate precursors and solvents under suitable operating conditions [84]. Pratsinis et al. have synthesized ceria from cerium acetate precursors in acetic acid solution with the addition of iso-octane/2-butanol mixture solution [85]. It is possible to control the size distribution, phase, morphology, specific surface area, and composition of the nanoparticles by controlling the oxygen dispersion and flow rates of the liquid precursor. Feng et al. synthesized ceria and ceria titania mixed oxide spherical morphology by FSP method by dissolving cerium and titanium mixture precursors in a flammable solvent [86].

1.1.5.6 Microemulsion Method

The microemulsion is an isotropic system containing two immiscible liquids such as oil and water in the presence of surfactants/co-surfactants, with a diameter varying from 1-100 nm. This method is based on the formation of micelles or reverses micelles. When the microemulsions containing the reactants are mixed, an interchange of the reactant molecules takes place due to the collision of nanodroplets, and the final size of the particles is controlled by the droplet size. After attaining the final size, the surfactant molecules prevent further growth of the particles and thus can control the particle size of the material. Micelles with different shapes such as ellipsoids, cylinders, and bilayers can be obtained depending on the molecular geometryof the surfactants and reaction conditions such as surfactant concentration, pH, temperature, and ionic strength of the solution [87].

Masui et al. have synthesized ultrafine ceria nanoparticles using microemulsions of cerium nitrate and ammonium hydroxide by reversed micelles method [88]. CeO_2 nanoparticles with size distribution in the range of 6–16 nm were prepared by Kaskel et al.using an inverse microemulsion technique. In this process, diluted ammonia was added to a ternary system containing n-heptane, surfactant, and cerium nitrate solution to produce nanosized $Ce(OH)_3$ particles inside the micelles. Cerium dioxide nanoparticles possessing good soot combustion activity were obtained after filtration and drying processes [89].

1.1.5.7 Green Synthesis Methods

To prepare biocompatible CeO_2 nanoparticles, several bio-directed methods have been studied, in which natural and organic matrices are used as the stabilizing agents. These green approaches involve plant-mediated, nutrient-mediated, and biopolymer-mediated syntheses. Photosynthesis of CeO_2 nanoparticles has been reported by several researchers using plant extracts, such as *Olea europaea*, *G. superb*, *Prosopis juliflora*, *aloe vera*, *Acalypha indica*, *Datura metal*, *Origanum majorana L.*, *Sida acuta*, *Azadirachta indica*, *Pisonia alba,* etc., in which the different organic moieties in the extract act as stabilizing and capping agents of CeO_2 nanoparticles [90-99]. Nutrients and natural materials, such as egg white (EW) protein, and honey were also used for the synthesis [100-101]. The two proteins of EW, ovalbumin, and lysozyme acted as green binders/stabilizing

agents. Biopolymers are also used as templates for the bio-directed synthesis of ceria nanoparticles. Here the hydroxyl groups get attached to the ceria nanoparticles, and the particle size can be controlled. Biopolymers such as starch, agarose, gum tragacanth, dextran, etc., have been used as stabilizing and coating agents by different groups [102-104].

1.1.5.8 Other Preparation Methods

In addition to the above-discussed methods, several other methods such as electrochemical deposition, microwave-assisted synthesis, ultrasonic irradiation (sonochemical synthesis), etc., have also been used for synthesizing ceria nanoparticles [105-107].

1.1.6 Structural Modifications of Ceria

When ceria is subjected to high temperature for a long time, the sintering of ceria particles occurs, which will decrease the OSC of ceria that affects the overall performance of catalytic systems in high-temperature applications. Doping of different metals into ceria is one method to stabilize ceria against sintering. Among the different cations, zirconium has proved to be an efficient dopant to inhibit sintering, especially by the formation of ceria-zirconia solid solution [108]. Incorporation of several transitions, noble and rare earth metals in ceria lattice produceda higher number of oxygen vacancies by a charge-compensating effect of foreign cations, which increases the OSC of the material. Since the concentration and structure of oxygen vacancies depend on the type of exposed facets of a ceria crystal, it is

possible to tune its redox and catalytic properties by the controlled synthesis of different nanostructures like rodes, cubes, polyhedral, etc [109]. In applications such as three-way catalysts (TWC), to increase the catalytic performance of noble metal nanoparticles, ceria is often used as support that provides a high surface area for the dispersion of nanoparticles and also due to the strong metal-support interactions at the interface. The exposed facets of ceria support have a strong influence on the TWC reactivity of metal nanoparticles.

1.1.7 Applications of Ceria

As mentioned earlier, ceria is a versatile material having distinctive properties, among which the unique feature is the OSC. The presence of mobile oxygen in ceria lattice results in oxygen buffering action, making it suitable in several applications involving catalysis, sensing, electrochemical and photochemical fields, etc. Some of the important applications of ceria are discussed in the following sections.

1.1.7.1 Three-Way Catalysts (TWCs)

The environmental pollution due to large quantities of automobile exhaust gases could reduce to a large extent by introducing TWCs in catalytic converters in internal combustion engines. The functions of TWCs involve the simultaneous oxidation of carbon monoxide (CO) and hydrocarbons (HC) as well asthe reduction of nitrogen oxides (NO_x). In catalytic converters, the catalyst is supported on cordierite monolith with a honeycomb structure. The catalytic

material contains thermally stable support usually made of doped Al_2O_3, catalytically active noble metals like Pd and/or Pt mainly for oxidation and Rh for NOx reduction as well as a ceria-based promoter (usually $Ce_xZr_{1-x}O_2$) [110]. The complete removal of all pollutants can happen only at a narrow window around the stoichiometric value of air/fuel ratio (A/F), which is about 14.6 [111]. It is not easy to attain this particular stoichiometry under all conditions, and the gas coming out from the engine always haseither lean (A/F >14.6) to rich conditions (A/F<14.6). The role of CeO_2 in TWC is to provide oxygen for the oxidation of CO and HC by its reductioninto CeO_{2-x}. On the other hand, the reduced ceria CeO_{2-x}can store oxygen and promote the reduction of NO_x under the lean-to-rich A/F ratio transients according to the following equations [112].

$$CeO_2 + xCO \rightarrow CeO_{2-x} + xCO_2 \quad \text{(eqn 1.9)}$$

$$CeO_2 + C_xH_y \rightarrow CeO_{2-(2x+0.5y)} + xCO_2 + 0.5yH_2O \quad \text{(eqn 1.10)}$$

$$CeO_2 + xH_2 \rightarrow CeO_{2-x} + xH_2O \quad \text{(eqn 1.11)}$$

$$CeO_{2-x} + xNO \rightarrow CeO_2 + x/2N_2 \quad \text{(eqn 1.12)}$$

$$CeO_{2-x} + xH_2O \rightarrow CeO_2 + xH_2 \quad \text{(eqn 1.13)}$$

$$CeO_{2-x} + x/2O_2 \rightarrow CeO_2 \quad \text{(eqn 1.14)}$$

One of the drawbacks of ceria in using TWC is that, when it is exposed to higher temperatures (around 1000 ℃) inside the engine,the sintering of particles occurs results in a reduction of surface area and

the loss of contact between ceria and the active noble metals [113]. This in turn affects the OSC and reduction properties of ceria and leads to diminishing the TWC property of ceria. The problem was solved using advanced TWC in which, CeO_2-ZrO_2 solid solution is used instead of pure CeO_2 [114]. ZrO_2 in the CeO_2-ZrO_2 mixed oxide modifies the oxygen sublattice, and introduced more Frenkel-type defects in the crystal, resulting in increased oxygen mobility and reducibility of the solid even at low temperatures, at the start of the engine [115-116]. Neutron activation studies show that the defects are annihilated in ceria on heat treatment above 800 °C, whereasthey are quite unaffected in CeO_2-ZrO_2even at high temperatures. Also, the sintering phenomenon is lower in CeO_2-ZrO_2, while compared to pure ceria, and so the negative effect of the high-temperature exposure can be ruled out [117].

1.1.7.2 Diesel Soot Oxidation

The main pollutants involved in the exhaust emission of diesel engines are CO, HC, nitrogen oxides, and carbon particulates (soot) which are proven to be harmful to human health [118]. The soot particles can be reduced using catalytic filters on which the soot particles will be accumulated and canthen be oxidized in the presence of a catalyst to regenerate the filter [119]. Ceria-based material has been one of the most successful candidates for this purpose as it can significantly decrease the combustion temperature and provide a less power-consuming filter generation method [120]. Because of the

oxygen storage/release property, ceria can prop up the production of "active oxygen species" that are the key ingredients in soot oxidation [121]. Two mechanisms accepted for the ceria-based soot combustion are given in figure1.2.

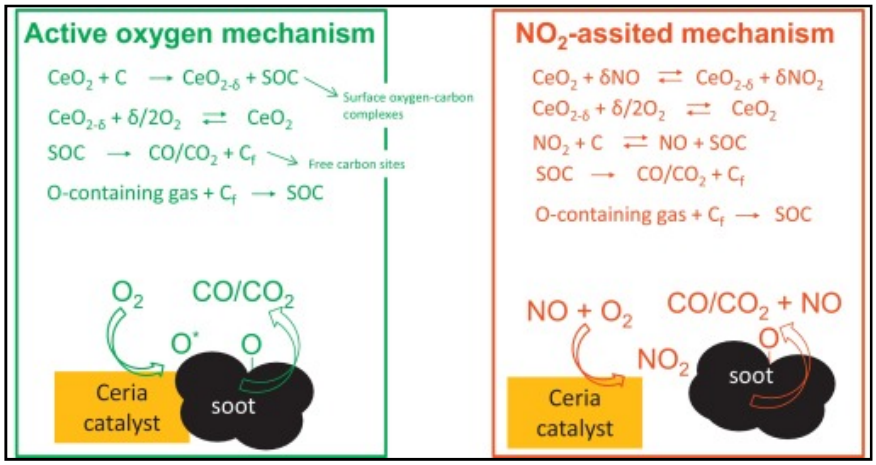

Fig. 1.2 Mechanism of Diesel Soot Oxidation by Ceria [122]

One is the active oxygen mechanism in which the active oxygen species such as superoxides (O_2^-) are formed by the interaction of gas-phase O_2 and surface oxygen vacancies of reduced ceria promoting carbon oxidation [122]. The other is a NO_2assisted mechanism based on the ability of ceria to oxidize NO. NOis a better oxidant than gas-phase O_2 and it oxidizes soot at a lower temperature [123]. Low-temperature oxidation and thermal stability in ceria can be achieved by modifying ceria with Zr and/or other rare earth metals as well as by modifying ceria and/or ceria-zirconia with transition metals or noble metals that act as active phases. For example,CeO_2 supported cobalt oxide prepared by ultrasonic-assisted incipient-wetness

impregnation displayed better soot oxidation activity than the corresponding CeO_2 catalyst [124]. Ceria modified with rare earth elements like La, Pr, Sm and Y showed improved soot oxidation performance because of the increase in meso/macropore volume [125]. Trovarelli et al. reported the incorporation of alkali metals in ceria that promoted soot oxidation, as it favors the chemisorption of molecular oxygen with the formation of carbon surface complexes, which eventually react with soot [126]. Soot oxidation is a surface-dependent reaction, and so the catalytic activity can be improved by exposing specific surfaces [127-128]. Modification of the crystal shape having more percentage of (100) and (110) surfaces than less active (111) surfaces increases the soot oxidation at lower temperatures. This is attributed to the higher reducibility of these surfaces, and the higher number of active oxygen species in the nanostructures. As a result, nanocubes, nanorods, and related nanostructures with (100) and (110) exposed surfaces show much better soot oxidation than nanopolyhedra having (111) exposed surfaces. Sudarsanam et al.reported that the deposition of Co_3O_4 onto the ceria cubes substantially increased the catalytic activity in the low-temperature soot oxidation [129].

1.1.7.3 Solid Oxide Fuel Cells

Researches in the area of solid oxide fuel cells (SOFCs) are celebrated recently, as fuel cells are eco-friendly and hence assure sustainable electrical energy.They are highly efficient in converting chemical energy to electrical energy, as it is not bound by the

thermodynamic limit of a Carnot cycle [130]. In a SOFC, a solid electrolyte capable of conductingoxide ions is sandwiched between the cathode and anode electrodes, both of which are porous. The electrolyte should possess high ionic conductivity and low electronic conductivity at the operating conditionsand must be stable in both oxidizing and reducing environments. Ceria can be applied in SOFC in three parts: (1) as an electrolyte, (2) as a barrier layer for cathodes to prevent reaction with the YSZ (yttria-stabilized zirconia) electrolyte, and (3) as a catalyst in both cathode and anode [131]. Gd, Sm, Y, and Ca doped ceria have been used as low-temperature electrolytes since they have significant electronic conductivity under reducing conditions [132]. Another advantage of ceria-based electrolytes is their higher resistance to carbon deposition, which helps the hydrocarbon fuels directly passedinto the anodes [133]. The catalyst morphology is another parameter that highly influences the SOFC performance. Pd@CeO_2 core-shell systems are reported to be effective anodic catalysts when H_2 and CH_4 are used because the anode is extra stabilized when it is covered by Pd@CeO_2 nanoparticles. Thus, activities are retained even at high temperatures during oxidizing and reducing atmospheres [134]. Sun et al. reported an anode based on Ru-CeO_2 catalyst having porous flower-like microsphere morphology with enhanced performance using isooctane as fuel [135]. Ni containing YSZ electrodes infiltered with ceria nanoparticles have considerably improved sulfur tolerance and they give a power density of 220−240 $mWcm^{-2}$ for 500 h with H_2 fuel contaminated with 45 ppm of H_2S.On

the other hand, when the electrode is used without ceria, the power density dropped to zero in 13 mins [136]. Much improvement in performance and durability was observed in Ni-samaria-doped ceria (Ni-SDC) instead of Ni yttriya stabilized zirconia (Ni-YSZ) as the anode. This is ascribed to the higher electronic conductivity of SDC due to the partial reduction of Ce^{4+} to Ce^{3+} under the reducingatmosphere and the higher catalytic activity of Ni-SDC [137]. Zhuet al. reporteda two-phase electrolyte in which doped ceria is combined with other salts due to the highly improved ionic conductivity arising from the binary conductive nature (O^{2-}/H^{+}) [138]. Among these,ceria combined with carbonates, oxides, hydroxides, sulfates, and halidesis becoming emerging electrolytes [139-143].

1.1.7.4 Water Gas Shift Reaction (WGSR) and Preferential Oxidation (PROX) of CO

Water-gas shift reaction (WGSR) is an extensively studied reaction because of the growing development of fuel cell technology [144].

$$CO + H_2O \leftrightarrow CO_2 + H_2 \quad \text{(eqn 1.15)}$$

This reaction reduces the CO content and adjusts the CO/H_2 ratio in the outlet gas of the reactor. The reduction of CO is necessary to avoid the poisoning of the catalyst in ammonia synthesis [145]. The processes such as FischerTropsch and methanol synthesis require specific concentrations of CO, CO_2, and H_2, which is obtained by

adjusting the H_2/CO ratio. This can be accomplished by a combination of the water-gas shift reaction (WGSR) and the preferential oxidation (PROX) of residual CO, in the presence of an excess of H_2, using O_2 [146]. Since WGSR is an exothermic reaction, to obtain a high CO removal,a low reaction temperature is required, where the reaction rate also will be lower. Thus WGSR takes place commercially in two successive steps; one at higher temperatures (300–450°C) (HT-WGSR) and the other at lower temperatures (200–310°C) (LT-WGSR). Several ceria-based materials have been used as catalysts in WGSR due to their oxygen mobility and redox properties, which can be improved by dopant incorporation. Among them, noble metals Pt and Au, as well as Cu in finely dispersed form supported on ceria and ceria-zirconia, are the mostly investigated ones [147]. Pt/CeO_2 is found to give a significant performance, but it undergoes carbonate deposition and subsequent deactivation [148]. This can be avoided by using $Ce_xZr_{1-x}O_2$ instead of CeO_2 in which the reaction proceeds by a redox route [149]. Pt supported on La-doped CeO_2 also catalyzes the reaction, and the highest activity was observed for $Ce_{0.8}La_{0.2}O_{2-\delta}$, which had the maximum OSC in the 250−550 °C temperature range [150]. Au nanoparticles of less than 5 nm in size supported on CeO_2 are the most promising catalysts for H_2 purification [151]. There are several reports on Au-based catalysts supported on different ceria systems such as, CeO_2-Al_2O_3, CeO_2-Fe_2O_3, CeO_2-MnO_2,CeO_2-SnO_2 and CeO_2-Ga_2O_3 [152-155]. Transition metals such as Ni, Cu, and Fe were also reported to show good activity if well dispersed on ceria

supports [156]. Literature studies report that WGSR and PROX take place through either formate route or redox route. In PROX of CO, Pt, Au, and Cu supported CeO_2-based oxides gave the best performance [157]. Gao et al. studied the effects of the morphology of CeO_2nanoparticles in the PROX of CO oxidation and found that the reactivity order is nanorod > cube> octahedral for the Pt/CeO_2 catalyst. This is according to the same order of reducibility and oxygen vacancies in the material [158]. In Au/CeO_2, both the particle size of CeO_2 and Au are significant in PROX reaction. The rate of CO oxidation using the catalyst, nanocrystalline CeO2 is two times higher than that using bulk CeO_2, which is attributed to the higher interaction between the two components; CO gets adsorbed on Au atoms, and additionally, the defective CeO_2can activate O_2 for oxidation {159}. In the case of Cu/CeO_2 catalyst, partial reduction of Cu(II) occurred at the interface of CeO_2-CuO, and CO molecules predominantly got adsorbed on Cu(I),also undergoing oxidation [160]. The morphology of the CeO_2 also influenced the reaction.The order of selectivity is nanocubes> rodes > spheres which is in the order of the number of exposed (100) faces that is attributed to the strong interaction between CuO and (100) face of ceria [161]. Bimetallic catalysts composed of metals like Pt, Au, and Cu supported ceria are also used in PROX of CO. Among these, Pt-Au/CeO_2, Pt-Cu/CeO_2, and Au-Cu/CeO_2 catalysts show better performance compared to the monometallic catalysts [162-164].

1.1.7.5 Oxidation of Volatile Organic Compounds (VOC)

The reducibility and OSC of ceria make it a useful catalyst for the oxidation of volatile organic compounds [165]. The reaction is considered to proceed via Mars-van Krevelen type mechanism, in which oxygen is supplied by ceria for the reaction, and it is reoxidized by the gas phase oxygen [166]. Several ceria-based catalysts in which noble metals (Pd, Pt, and Au) are dispersed on high surface area ceria support are reported in the literature as showing activity at low temperatures. Methane is one of the greenhouse gases, which causes ozone depletion and is difficult to get oxidized [167]. Since the catalytic presentation is ascribed to the ability to release oxygen, metal-doped ceria systems show lower conversion temperatures compared to pure ceria. Liottaet al. reported Co/CeO_2 catalyst as having good methane oxidation capacity due to the strong electronic interaction between Co_3O_4 and CeO_2 [168]. Yanget al. employed CuO/CeO_2 catalyst that has similar activity [169]. Flower-like mesoporous microspheres made of $La_xCe_{1-x}O_{x/2}^{2-}$ or $Pr_xCe_{1-x}O_{x/2}^{2-}$ synthesized by Liet al., showed increased activity in methane combustion, due to an increase in oxygen vacancies and oxygen mobility [170]. Noble metal-based catalysts such as Pd/CeO_2andPt/CeO_2show significantly higher performances in methane oxidation [171-172]. One of the major disadvantages of Pd catalysts is that it undergoes sulfur poisoning, and the catalyst gets deactivated,whereas the presence of Pt gives resistance to both water and SO_2 poisoning [173-174]. CeO_2-ZrO_2 catalysts have been widely

used forchlorinated VOCs, non-methane VOC (NMVOCs) in addition to methane combustion [175]. For example, $Ce_{1-x}Zr_xO_2$ (x =0−0.3) was studied as a catalyst for the catalytic combustion of benzene and toluene with the light off temperature corresponding to 50% conversion (T50%) reduced to 100 °C lower than that of pure ceria [176]. Delimariset al. reported a MnOx−CeO_2 mixed oxide suitable for the oxidation of ethanol, ethyl acetate, formaldehyde, and toluene [177]. Pure ceria and ceria-based materials have been used for the oxidation of many of the chlorinated hydrocarbons, such as trichloroethylene (TCE), 1,2-dichloroethane (DCE), and chlorobenzene (CB) [178]. Nanostructured ceria having flower-like microspheres obtained by the hydrothermalmethod shows a much increase in TCE oxidation, compared to ceria obtained by thermal decomposition [179]. Ceria, when added as an additive in other catalysts such as zeolites, V_2O_5,and noble metalscould improve the performance of these catalysts to a greater extent [180-182]. For example,the addition of CeO_2 in H-ZSM5 type zeolite increased its DCE oxidation activity with high HCl selectivity.

1.1.7.6 Biomedical Applications

Ceria nanoparticles have promising biomedical applications due to superoxide dismutase mimetic activity, catalase mimetic activity, hydroxyl radical scavenging,nitric oxide radical scavenging, peroxidase mimetic activity, oxidase mimetic activity, and phosphatase-mimetic activity. Ceria nanoparticles having a size over

20 nm possess antibacterial activity toward both gram-negative and gram-positive bacteria, due to the higher percentage of Ce^{3+} ions in ceria [183-184]. Since CeO_2 nanoparticles can removereactive oxygen species (ROS) or prevent their formation, it is being used for the treatment of neurodegenerative diseases like Parkinson's disease, trauma, ischemic stroke, Alzheimer's disease (AD), and aging, which arise due to the increased oxidative stress and production of free radicals [185]. Many reports are there on the neuroprotective effects of ceria nanoparticles. For example, Guo et al.reported that CeO_2nanoparticles (CNPs) modulate transforming growth factor-beta (TGF-β) signaling, and protect neurons against oxidative stress-induced injury [186]. Arya et al. reported PEG-coated 3 nm CeO_2-NPs promoted neurogenesis and decreased oxidative stress [187]. CeO_2 NPs can behave as artificial oxidase enzymes, and have catalasesuperoxide dismutase (SOD), and peroxidase-like activity. Bhushan and Gopinath synthesized biocompatible ceria-albumin nanoparticles (BCNP) with ROS scavenging activity that preserved the antioxidant defense system of the cells [188]. CeO_2 nanoparticles of size >5 nm undergo Ce^{3+} oxidation, and the SOD mimetic activity decreases. To improve the superoxide-scavenging activity of these NPs, Li et al. proposed a strategy to retain the SOD mimetic activity by incubation with native CuZn-SOD in phosphate-buffered saline [189]. Akhtar et al. reported that the catalase activity of CeO_2-NPs could increase the intracellular glutathione (GSH) in cells, the presence of which can regulate the cell growth and division, metabolism of

carcinogens, and protecting DNA from oxidative damage [190]. Peroxidase-like activities of CeO_2 NPs have been used for the detection of breast cancer cells using nanostructure-based enzyme-linked immunosorbent assay (ELISA) [191].

1.2 Environmental Pollutant Degradation

The development of human society and the improved standard of living can be mainly attributed to the chemical-based industries. The fast-growing population around the world leads to a larger consumption of chemical products,which necessitates extensive production of various chemicals in industries.This scenario introduced large quantities of chemicals in the environment, which can cause potential harm to human health and many ecosystems [192]. The industrial contaminants in wastewater effluents include complex organic dyes, antibiotics, phenols, pesticides, chlorinated compounds, heavy metals, and radioactive nuclides [193-194]. These contaminants might be present in surface water and groundwater due to improper wastewater treatment, the random release of residual pesticides and fertilizers, agricultural runoff, contaminated soil, and leakage of hazardous compound storage [195]. Most of these compounds are toxic, endocrine-disrupting, mutagenic, and carcinogenic.Their degradation-resistant property results in the accumulationof these toxins in aquatic organisms, which in turn affects the human body, causing serious health issues even at very low concentrations [196]. As a result, the need for the efficient removal of these contaminants from

the environment is very crucial, and several techniques are in use nowadays to decontaminate polluted water. Some of the conventional methods currently available include biological treatment, ozonation, air stripping, coagulation/flocculation, reverse osmosis, ultrafiltration, chlorination, etc., which are less effective in the elimination of all types of organic contaminants, and most of them produce secondary pollutants [197]. Advanced oxidation processes (AOPs) have attracted significant attention as it is the most promising technology for the removal of biologically recalcitrant, persistent organic pollutants present in wastewater [198].

AOPs are based on the formation of highly reactive species like hydroxyl radical ($^{\cdot}OH$) having the highest oxidation potential of 2.33 V, compared to other conventional oxidizing agents such as O_3, H_2O_2, or $KMnO_4$. They attack the organic pollutants by hydrogen abstraction, electron transfer, and formation of a double bond, also decomposing them into smaller non-polluting molecules [199]. Various AOPs used for wastewater treatment are given in figure 1.3.

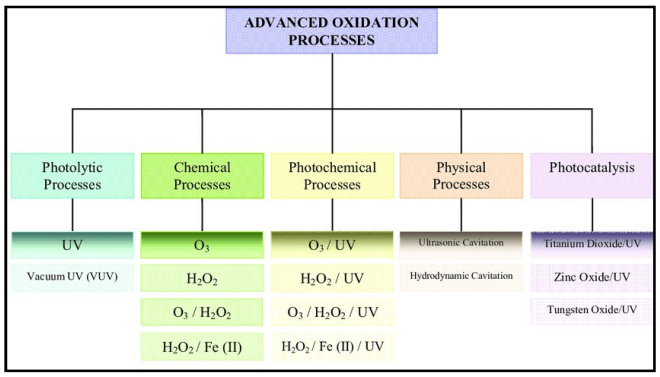

Fig.1.3 Various processes in advanced oxidation processes. [200]

1.3 Photocatalytic Degradation of Pollutants

Heterogeneous photocatalysis is an extensively studied technology since 1972 when Fujishima and Honda reported the photocatalytic splitting of water on TiO_2 electrodes [201]. Among the several AOPs, the photocatalytic technique has been widely used for wastewater treatment as it removes a broad range of organic pollutants at ambient temperature and pressure [202]. The process has several advantages such as complete mineralization, low cost, no waste disposal problem, high efficiency, green nature,etc., and therefore effectively used in water and air remediation [203]. The process involves a semiconductor photocatalyst, which on the absorption of radiation generates highly reactive oxidant species ($^{\cdot}OH$, $HO_2^{\cdot}$, and $O_2^{\cdot -}$) and oxidizes organic and inorganic pollutants into smaller molecules [204].

In heterogeneous photocatalytic systems, the degradation reactions take place by these reactive species on the surface of the catalyst. An efficient photocatalyst should have the properties such as visible and/or near UV light absorption, biological and chemical inertness, photostability, low-cost, and nontoxic nature [205].

1.3.1 Mechanism of Photocatalytic Degradation

A semiconductor (SC) photocatalyst possesses a valence band and a conduction band separated by an energy gap (E_g). Under the irradiation of light of energy equal to or greater than the bandgap, oxidants are formed on the surface of the semiconductor. On

absorption of energy, electrons (e^-) are excited from the valence band to the conduction band, leaving holes (h^+) in the valence band.

The photoinduced electron-hole pairs can undergo different reactions such as recombination with heat production, trapping in bulk or surface states, and migration to the surface giving rise to oxidation and reduction reactions if suitable acceptor (A) and Donor (D) are present. The mechanism of photocatalysis is represented in figure 1.4.

The various reactions taking place on the surface of the photocatalyst are given by the following reactions:

$$SC \rightarrow SC\,(e^-_{(CB)} + h^+_{(VB)}) \qquad \text{(eqn 1.16)}$$

$$h^+_{(VB)} + D \rightarrow D^{\cdot +} \qquad \text{(eqn 1.17)}$$

$$e^-_{(CB)} + A \rightarrow A^{\cdot -} \qquad \text{(eqn 1.18)}$$

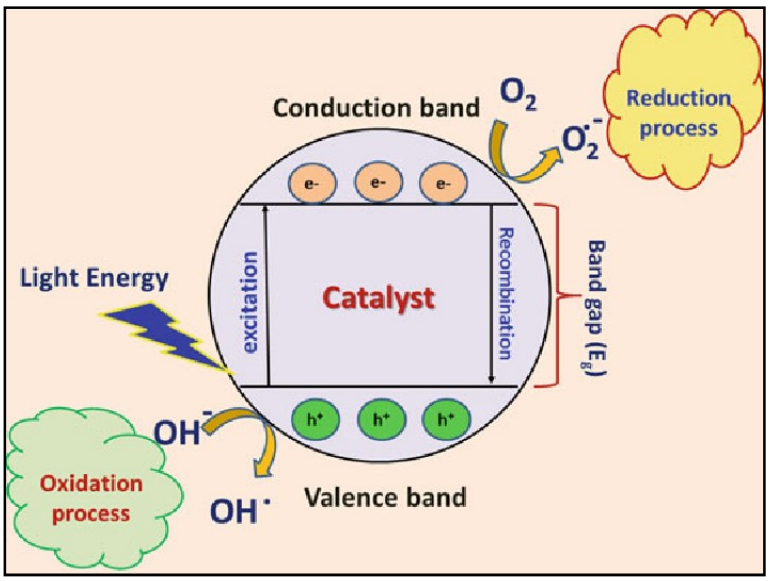

Fig. 1.4 Mechanism of photocatalytic degradation [206]

A or D could be protons, water, or any other adsorbed molecules. In the presence of H_2O and O_2, the following reactions can occur [207-208].

$$OH^- + h^+_{(VB)} \rightarrow {}^{\cdot}OH \quad \text{(eqn 1.19)}$$

$$H_2O + h^+_{(VB)} \rightarrow {}^{\cdot}OH + H^+ \quad \text{(eqn 1.20)}$$

$$O_2 + e^-_{(CB)} \rightarrow O_2^{\cdot -} \quad \text{(eqn 1.21)}$$

$$O_2^{\cdot -} + H^+ \rightarrow HO^{\cdot}_2 \quad \text{(eqn 1.22)}$$

$$2HO^{\cdot}_2 \rightarrow O_2 + H_2O_2 \quad \text{(eqn 1.23)}$$

$$H_2O_2 + O_2^{\cdot -} \rightarrow {}^{-}OH + {}^{\cdot}OH + O_2 \quad \text{(eqn 1.24)}$$

$${}^{\cdot}OH + \text{Organic compound} \rightarrow CO_2 + H_2O + \text{intermediates} \quad \text{(eqn 1.25)}$$

The ${}^{\cdot}OH$, $HO^{\cdot}_2$and $O_2^{\cdot -}$ (super oxide radical anion) are the reactive oxygen species (ROS) that degrade the organic pollutants in water.

1.3.2 Metal Oxides Photocatalysts

For a semiconductor to be photochemically active, the redox potential of the photogenerated hole must be sufficiently positive to generate ${}^{\cdot}OH$ radical, and that of the photogenerated electron must be sufficiently negative to produce superoxide radical from the adsorbed O_2 [205]. When we use a metal oxide nanoparticle as a photocatalyst, both electrons and holes are available on the surface for the reaction.In bulk materials, there is only one type of species available for the reaction, due to band bending [209]. Among the various metal oxide

photocatalysts, TiO_2 is the most widely studied and used catalyst, which is commercially available as Degussa P25. It can mineralize a wide range of organic pollutants like aliphatics, aromatics, detergents, dyes, pesticides, and herbicides. ZnO is another excellent photocatalyst under UV illumination even though its stability is less than that of titania [210]. Both TiO_2 and ZnO absorb in the UV light, but the visible light activity can be imparted by the process of metal doping or defect engineering. For example, black TiO_2 obtained by hydrogen doping or defects formation through the incorporation of nitrogen will enhance the photocatalytic activity under solar radiation [211-212]. Doping of ZnO with transition metals such as Mn and Co results in the absorption of visible light [213-214]. Other photocatalytic metal oxides include binary as well as ternary oxides of Fe, W, V, Mo, bismuth oxides, copper oxides (cuprous or cupric), CeO_2, zinc germanium oxide, $SrTiO_3$,etc [215]. Many nanocomposites and systems containing heterojunctions, such as, Au/TiO_2, TiO_2/graphene, TiO_2/SiO_2, CdS quantum dots/porous TiO_2 nanotubes, nanotube/WO_3 nanoparticle,etc., have increased charge separation and improved photocatalytic efficiency, also has been used for photocatalytic water treatment applications.

1.3.3 Ceria as a Photocatalyst

Recently, ceria and ceria-based materials have been attracted much attention for the treatment of contaminated water and air. Ceria is a wide bandgap semiconductor (3.0 – 3.4 eV); depending on the

morphology, it absorbs energy in the UV region and generates charge carriers having a comparatively larger lifetime than TiO_2 [15]. The main characteristics that make ceria ~~a~~n attractive photocatalyst are the high stability in the reaction medium, the electronic and optical properties due to the occurrence of 4f electrons, the ability to form nonstoichiometric oxygen-deficient CeO_{2-x} oxides, the considerable oxygen mobility, and the likelihood of giving rise to the reversible transformation, i.e., Ce^{4+}/Ce^{3+} [216]. To increase the visible light activity of ceria, several modifications are adopted, such as, doping of other metals, combination with other oxides, and incorporation of defects [217-219]. The lower part of the conduction band of CeO_2 (CB, Ce 4f) is around -0.4 eV vs. normal hydrogen electrode (NHE), and the top of the valence band (VB, O 2p) is ca. 2.5eV vs. NHE [220]. When ceria is irradiated with light of energy higher than the bandgap energy, electrons are excited to the conduction band within femtoseconds, leaving the same number of holes in the valence band. The electrons and holes then migrate to the surface of the ceria and undergo some redox reactions, generating ROS with a strong oxidative property that might oxidize the pollutant molecules as follows.

$$CeO_2 \rightarrow CeO_2\,(e^- + h^+) \quad \text{(eqn 1.26)}$$

$$O_2 + e^-_{(CB)} \rightarrow O_2^{\cdot -} \quad \text{(eqn 1.27)}$$

$$O_2^{\cdot -} + H^+ \rightarrow HOO^{\cdot} \quad \text{(eqn 1.28)}$$

$$2HOO^{\cdot} \rightarrow O_2 + H_2O_2 \quad \text{(eqn 1.29)}$$

$$H_2O_2 + e^- \rightarrow OH^- + {}^{\cdot}OH \quad \text{(eqn 1.30)}$$

$$OH^- + h^+_{(VB)} \rightarrow {}^{\cdot}OH \quad \text{(eqn 1.31)}$$

$$\text{ROS} + \text{Organic compound} \rightarrow CO_2 + H_2O + \text{intermediates} \quad \text{(eqn 1.32)}$$

The photocatalytic performance of ceria depends on several factors such as particle size, surface structure, oxygen mobility, and surface morphology. The presence of surface defects such as oxygen vacancies work as electron traps and decrease the electron-hole recombination. They also act as strong binding and dissociating sites for organic adsorbate molecules, thus increasing the photocatalytic performance of ceria [221]. Ce^{3+} ions are more efficient in activity over a wide range of pH compared to Ce^{4+} as they can produce a large number of ${}^{\cdot}OH$ radicals [222]. It is reported by Aneggiet al. that the (100) facet of ceria is showing higher activity than the corresponding (110) and (111) facets because of higher concentration of oxygen vacancies and chemical reactivity [223]. To improve the visible light activity of ceria the following modifications can be accomplished: 1) metal or nonmetal doping, 2) deposition of noble metals on CeO_2, 3) construction of CeO_2-based solid-solution, and 4) coupling of CeO_2 with other nanomaterials to form binary hybrid heterostructures and ternary nanocomposites [224]. Doping of ceria with 3d transition metals may increase the oxygen vacancies and increase the mobility of excitons to the catalyst surface, thus decreasing the electron-hole recombination [225]. The doped metal ions create an impurity level near CB and VB of ceria, and the split 3dstate can be mixed with the

CB or VB, and a new bandwidth can thus be inserted into the original band. As a result, the bandgap of CeO_2 is decreased, and the absorption edge of sunlight is broadened. Also, the dopant metal ion will capture the photoinduced electrons and holes and transfer them to the surface to react with the adsorbed molecules [226]. Yue et al. studied the photocatalytic activity of ceria doped with transition metals (Co, Ti, Fe, and Mn) and observed a redshift of adsorption edge to visible light as the bandgap of the doped catalysts decreased to lower energy [227]. Channei et al. synthesized Fe-doped CeO_2 nanoparticles and Fe-doped CeO_2 film having 3.8 times activity in methyl orange degradation compared to bare ceria [228]. Doping of non-metals like N, C, F, S, etc., changes the density of states near the VB edge of ceria. By density functional theory (DFT) calculation, Mao et al. found that both the VB and CB of N doped CeO_2 shifted to lower energies, thereby shifting the absorption to the visible region [229]. Also, S-doped ceria and F-doped ceria showed much better solar energy absorption and catalytic ability toward dye degradation compared to pure ceria [230-231]. The localized surface plasmon resonance (LSPR) of noble metal nanoparticles (Au, Ag,etc.) on ceria results in extended light response and enhanced photoactivity [232]. Au/CeO_2, 3D yolk-shell- Au@CeO_2 spheres, Ag NPs@CeO_2 (Ag@CeO_2), and Ag nanowires@CeO_2 (Ag NWs@CeO_2) core-shell structure are some noble metal/ceria based visible light active photocatalysts [233-234]. Many ceria-based solid solutions are reported to havewell visible-light photoactivity. Liyanage et al. synthesized Y doped ceria nanorods, with decreased bandgap and

higher amount of oxygen vacancies, by a hydrothermal method that showed higher catalytic performance for Rhodamine B (RhB) degradation [235]. ZrO_2-CeO_2 composites reported by Zhang et al., in which the oxo-bridged bimetallic linkage Zr^{IV}-O-Ce^{III} acted as a visible-light-driven redox center could improve the photocatalytic activities on RhB and 2,4-dichlorophenol degradation [236]. Recently, more effective photocatalysts were realized with heterostructures by incorporating CeO_2 with two or more nanomaterials. A p-n heterojunction system of CuO/CeO_2 composite was synthesized by Wang et al. for the decomposition of RhB,where the higher catalytic performance is due to the visible-light-driven CuO, the intrinsically strong photocatalytic redox capability of CeO_2, and the charge transfer channel between CuO and CeO_2 [237]. Binary heterosystems such as ring-shaped Bi_2WO_6@CeO_2, BiOBr/CeO_2 nanocomposites, Ag_3PO_4/CeO_2, CeO_2/TiO_2 nanobelt heterostructure, and ternary nanocomposites such as Bi_2O_3-CeO_2-ZnO, ternary Ag_2CO_3/CeO_2/AgBr hybrids, Ag/AgCl-CeO_2 composites, ZrO_2-CeO_2-TiO_2, CeO_2-Al_2O_3@graphene oxide (GO), CuO-CeO_2/GO,etc. exhibited superior visible light response as well as efficient transfer and separation of charge carriers which offered an enhanced photodegradation activity[238-247].

1.4 Photo Fenton Degradation

Fenton and Fenton-based reactions are important processes among AOPs, in which active oxygen species are formed by the

reaction of hydrogen peroxide on iron/iron-like ions to oxidize organic compounds. The reaction was first used by H.J.H Fenton in 1984 for the oxidation of tartaric acid [248]. Nowadays, Fenton reactions play a significant role in the removal of many hazardous pollutants in wastewater. The core of the Fenton chemistry is the oxidation of ferrous ions to ferric ions to decompose H_2O_2 into hydroxyl radicals and is referred to as the Fenton reaction. It is represented as:

$$Fe^{2+} + H_2O_2 \rightarrow Fe^{3+} + OH^- + {}^{\cdot}OH \quad \text{(eqn 1.33)}$$

The attractive features of Fenton reactions are that the reagents used for Fenton reactions are readily available. The reaction does not cause any damage to the environment, and it can be carried out at room temperature and atmospheric pressure [249]. However, due to the radical scavenging effect of H_2O_2, wastage of oxidant occurs, and also, the formation of iron sludge causes continuous loss of iron [250-251]. Several modifications on classical Fenton reaction are investigated to improve the oxidation efficiency; and are termed Fenton-like reactions. These are energy-consuming Fenton-based reactions such as the photo Fenton (PF) process, sono-photo Fenton process, sono-electro Fenton process, and photo-electro Fenton process [252]. In photo Fenton processes, more hydroxyl radicals are formed compared to conventional Fenton reaction and photolysis by a combination of H_2O_2 and UV radiation along with Fe^{2+} or Fe^{3+} oxalate ions, thus resulting in a higher rate of degradation of organic pollutants [253]. Photo Fenton processes are more efficient than the Fenton process, and the

cost of the process can be reduced by using sunlight instead of UV light [254].

1.4.1 Mechanism of Photo Fenton Degradation

The mechanism of Fenton's process can be summarized by the following steps [255].

Hydroxyl radicals are generated initially from a mixture of H_2O_2 and ferrous iron in an acidic solution, which in turn attack the organic pollutants present in the solution.

$$Fe^{2+} + H_2O_2 \rightarrow Fe^{3+} + OH^- + {}^{\cdot}OH \quad \text{(eqn 1.34)}$$

Regeneration of the catalyst ion Fe^{2+} occurs by the following reactions.

$$Fe^{3+} + H_2O_2 \leftrightarrow Fe\text{-}OOH^{2+} + H^+ \quad \text{(eqn 1.35)}$$

$$Fe\text{-}OOH^{2+} \rightarrow Fe^{2+} + HO_2^{\cdot} \quad \text{(eqn 1.36)}$$

In photo Fenton reaction, the photolysis of Fe^{3+} cations yields Fe^{2+} cations, and the newly generated Fe^{2+} ions again react with H_2O_2 to produce Fe^{3+} and hydroxyl radicals; this cycle continues.

$$Fe(OH)^{3+} + h\upsilon \rightarrow Fe^{2+} + {}^{\cdot}OH \quad \text{(eqn 1.37)}$$

$$Fe^{2+} + H_2O_2 \rightarrow Fe^{3+} + 2{}^{\cdot}OH \quad \text{(eqn 1.38)}$$

The effectiveness of the photo Fenton process is attributed to the photoreduction of Fe^{3+} ions into Fe^{2+} by which additional ${}^{\cdot}OH$ radicals are formed in comparison to the Fenton process. Direct

photolysis of H_2O_2 also produces $^{\cdot}OH$ radicals which can also cause oxidation of molecules. But in the presence of iron complexes that absorb radiation strongly, this reaction contributes only to a lesser extent to the pollutant degradation [256].

$$H_2O_2 + h\upsilon \rightarrow 2^{\cdot}OH \quad \text{(eqn 1.39)}$$

1.4.2 Heterogeneous Catalysts for Photo Fenton Degradation

Since iron-based Fenton reactions have several practical disadvantages, many researchers have worked on other metal-based systems for the generation of $^{\cdot}OH$ radicals from H_2O_2. An effective Fenton catalyst should possess an active metal with multiple oxidation states for efficient electron transfer to H_2O_2 and decompose H_2O_2 even at neutral pH under homogeneous and heterogeneous reaction conditions. Some non-ferrous metal species that can act as Fenton-like reagents are Al, Ce, Co, Cr, Cu, Mn, Ru,etc.[252]. The use of zero-valent aluminium (ZVAl) has a stronger thermodynamic driving force for the electron transfer to H_2O_2 compared to FeO or Fe^{2+}. The use of ZVAl in AOPs has several advantages, like high natural abundance and low weight [257]. Chromium in both +3 and +6 oxidation states react strongly with $H_2O_2$to produce a hydroxyl radical. Cr(VI) reacts with H_2O_2 with the replacement of oxo ligands by peroxo groups, and the metal center undergoes one-electron reduction to form Cr(V) complex, whereas H_2O_2subsequently decomposes to hydroxyl radical [258]. Heterogeneous Co^{2+} based Fenton-like catalysts like Co^{2+}/Al_2O_3, Co^{2+}/MCM-41, Co^{2+}/carbon aerogel,etc., are reported for

the oxidation of organic pollutants in the presence of H_2O_2 [259-261]. Cu^{2+}/H_2O_2 Fenton-like systems efficiently generate hydroxyl radicalsfor the oxidation of organic pollutants over a wide range of pH. Also, Cu^{2+} complexes with degradation intermediates are easily decomposed by $^{\cdot}OH$ radicals resulting in complete mineralization of pollutants [262]. Mn/H_2O_2 Fenton-like activity is enabled by theconversion of Mn^{2+} to Mn^{4+} via the intermediate Mn^{3+}, and the activity remained in the pH range of 3.5-7 [263]. Ruthenium (Ru) is the only platinum group metal having Fenton-like activity and Hu et al. could oxidize bisphenol A by using the redox couple Ru^{3+}/Ru^{2+} using Ru^{2+}-polypyridyl complex immobilized on cation exchange resin [264]. Ru catalysts are highly stable, and the metal leaching is minimum, and thus multiple catalytic cycles are possible using this catalyst.

1.4.3 Cerium Oxide as a Photo Fenton Catalyst

The report of the first application of cerium-based Fenton system in the production of reactive species was published in 2008, and since then several studies regarding the degradation of organic contaminants in wastewaterhave been reported [265]. The role of ceria is associated with the oxygen vacancies in the structure that can be increased by the presence of Ce^{3+} ions and produce active oxygen for the oxidation of pollutant molecules.

A mechanism for the ceria-based catalyst in Fenton reaction developed by Hamound et al. is given in figure 1.5, in which the

reaction initiates with the complexation of H_2O_2 with Ce^{3+} sites [266]. The presence of Ce^{3+} and the formation of associated oxygen vacancies trigger the reactivity with H_2O_2 forming peroxide-like species. Hamound et al. have synthesized CeO_2 nanocatalyst with a high specific surface area for the removal of binary mixtures of dyes by the heterogeneous Fenton reaction [266]. Dyes with opposite charges undergo paired adsorption and coagulation processes and are ultimately removed through oxidation by reactive species generated in the Fenton reaction [264].

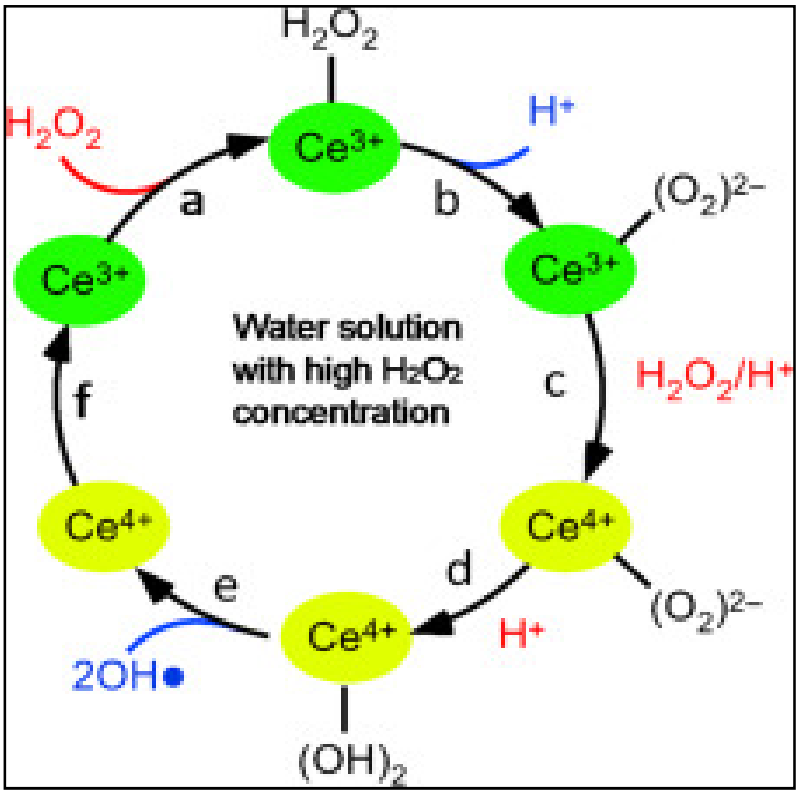

Fig. 1.5 Mechanism of H_2O_2 activation by ceria [266]

Wang et al. reported a 3D hierarchical H_2-reduced, Mn-doped CeO_2 microflowers (re-Mn-CeO_2 NMs) as an efficient Fenton-like photocatalyst for peroxymonosulfate (PMS) activation.The system had been used in the fast removal of tetracycline antibiotics in water, and a synergistic effect of the Fenton-like process and the photocatalysis occurred in the coupling system [267]. An efficient Fenton-like catalyst CuO/CeO_2 with increased oxygen vacancies was synthesized by Zhu et al. using ultrasonic impregnation to remove diclofenac from water and found that the (200) exposed surface of ceria are beneficial for the catalytic activity [268].

1.5 Adsorption of Pollutants

Among the various wastewater treatment technologies investigated so far, adsorption is one of the most preferred because of its simplicity in design, flexibility, low cost, insensitivity to toxic pollutants, and operational simplicity [269]. Adsorption is the process in which the molecules of materials are concentrated, on the surface of a solid, from its gaseous or liquid surroundings. The phenomenon was observed by Scheele in 1773 when carbon is exposed to gases, followed by a similar phenomenon of removing color-producing compounds by wood charcoal, vegetable, and animal charcoal. The term adsorption was first introduced by Kayser in 1881, to denote surface accumulation, and since then adsorption has been applied for removing both gaseous and liquid pollutants [270]. During the past few decades,the adsorption process has been used for the decolorization of

dye solutions, and the removal of toxic heavy metals as well as other organic compounds from water. If the attractive forces between solid and adsorbed molecules are only weak Van der Waals forces, the adsorption is termed physisorption, on the other hand, if chemical bonds are formed with the adsorbate on the solid surface, it is called chemisorption. An adsorbent is characterized by the quantity of adsorbate it can take up, which can be calculated from the adsorption isotherm according to the general equation;

$$q_t = (C_o - C_t)\, V/m \quad \text{(eqn 1.40)}$$

where q_t (mg/g) is the amount of adsorbateadsorbed per unit mass of the adsorbent at a time t, C_o and C_t are the concentration of the adsorbate at the initial time, and at time t respectively, V is the volume of the solution (L) and m is the mass (in g) of the adsorbent [271]. An ideal adsorbent should be porous with a high surface area, and it should reach the adsorption equilibrium in a short period; so the pollutant materials can be removed immediately.

1.5.1 Different Types of Adsorbents

Some of the adsorbents popularly used for dye removal from wastewater are alumina, silica gel, zeolite, and activated carbon [272]. The most popular and oldest adsorbent is the activated carbon, which is prepared from coal, coconut shell, lignite, wood,etc. Its structural characteristics such as porous texture and large surface area make it an efficient adsorbent for the removal of several pollutants such as metal

ions, phenols, pesticides, detergents, fumic substances, and organic compounds [273]. However, it is expensive, nonselective, and ineffective for dispersing and vat dyes.The expensive regeneration of saturated adsorbent makes it unjustified in several pollution treatment options [274]. Several researchers have investigatedlow-cost adsorbents produced from certain waste productsthat are potentially economical sorbents. Natural materials and wastes or byproducts from agriculture, industries,etc., can be used as adsorbents either as such, or after some minor treatment and are called low-cost adsorbents (LCAs). Some natural materials investigated as adsorbents are wood, coal, peat, chitin chitosan, biomass, cotton, and clays. Among the natural adsorbents, clays such as ball clay, bentonite, common clay, fire clay, Fullers earth, kaolin,etc., have a significant role because of the low cost, abundant availability, and good sorption capacity [272]. Many reports are there on the production of a variety of carbons from agricultural and food wastes such as bagasse, coir pith, banana pith, date pits, silk cotton hull, corn cob, maize cob, rice husk, rice hulls, fruit stones, nutshells, sawdust,etc [274]. The adsorption capacities of the prepared carbon structures depend on the source of raw materials, pyrolysis temperature, and activation time. Besides the wastes from agriculture, several byproducts/wastes from many industries such as power plants, steel, metal, sugar, and fertilizer industries,etc., have also been used as low-cost adsorbents. Fly ash, which is a waste material obtained in large quantities from coal-based thermal power plants, is used as a low-cost adsorbent for the removal of a wide variety of dyes

either alone or in combination with other materials such as coal mixtures [275]. Similarly, bagasse pith from the sugarcane industry, rice husk ash from rice mills, palm oil ash, red mud from the aluminium processing industry, blast furnace dust, and slag from steel plants, also have been used as sorbents for dyes. Biosorption has become a potential alternative to other sorbents for the removal/recovery of toxic metals from wastewater. Lignocellulosic biosorbentsmodified by some heat treatment or chemical modification such as delignification, esterification, methylation,etc., to increase their sorption capacities, have been used for the removal of metal contaminants like Cu, Hg. Cd, Ni, Pb, and Cr [276]. The potential of nanomaterials as nanosorbents has been discussed by Kyzas et al. Graphene oxide, multi-walled carbon nanotubes, hexagonal mesoporous carbon, hexagonal mesoporous silica, graphite oxide/chitosan nanocomposite,etc., has been reported as good adsorbents for the elimination of organic pollutants from wastewater. Also, Fe-La composite oxide, single-phase Fe/Mn oxy-hydroxide, Mg-doped α-Fe_2O_3, mercapto functionalized nano-Fe_3O_4 magnetic polymers, F-Ti bimetallic coated magnetic Fe_3O_4, carboxymethyl–β-cyclodextrin modified Fe_2O_3 nanoparticles,etc., reported by several research groups have also be been used for the effective removal of toxic metals from water [277].

1.5.2 Ceria as an Adsorbent

Recently, ceria has got enough attention in water treatment technologies as a promising adsorbent of several synthetic dyes and

toxic heavy metals due to its cyclic usability, biological and chemical inertness, and absolute stability against chemical corrosion. Ceria nanostructures of different morphologies having large surface areaswere synthesized by several research groups, and the materials showed excellent adsorption capability. Porous CeO_2 nanofibers of diameter 100-140 nm were prepared by Zhang et al., and they studied the adsorption of methyl orange, where the activity is mainly attributed to the large surface area and pore size of the prepared samples [278]. To overcome the recycling difficulties, Kong et al. synthesized CeO_2 nanoparticles immobilized on 40-60 mesh sand (ICe). The adsorbent showed excellent adsorption of dye AB10 with good recyclability and reusability [279]. Zheng et al. studied the shape-dependent behavior of CeO_2 by investigating the adsorption properties of Congored dye. Among the synthesized spindle ceria samples, octahedral and spherical ceria showed superior adsorption compared with others, which also showed good stability and reusability [280]. Yang et al. has reported a facile, economic route for the large-scale synthesis of mesoporous CeO_2 hollow spheres with an excellent adsorption capacity for the organic pollutant (Congo red) from wastewater [281]. Ceria hollow spheres (CHS) derived from a sol-gel reaction has been reported by Hu et al. with considerable adsorption capacity, 5 times higher than powdered activated carbon and ceria nanoparticles synthesized by solution combustion method. The higher performance is due to the porous structure and strong electrostatic interaction between the dye molecule and CHP [282]. Wu et al. have prepared uniform hierarchical

porous CeO_2 nanotubes with exposed (111) planes for effectively removing Congored dye with the adsorption capacity equilibrium of 362.32 mg/g [283]. Humic acid (HA)-supported CeO_2 nanosheet composites of 100–500 nm size were synthesized through the solvothermal method by Ling et al. The presence of CeO_2 nanosheets plays a crucial role in enhancing the surface area and overall mesoporous nature of the composite, resulting in enhanced adsorption capacity in the removal of Congored dye [284].

1.6 Gaseous Pollutant Degradation/Removal

With the rapid development of industry and economic growth, air pollution has become one of the major crises faced by worldwide countries. The main sources of air pollution are the fuel combustion processes in thermal power plants, vehicles, incinerators,etc. CO, NO_x, SO_x, unburnt hydrocarbons (HCs), and particulate matter (PM) are the primary pollutants of exhaust emissions [285]. These gases are harmful to human health and to the environment, causing acid rain, photochemical smog, ozone depletion, and global warming. Several technologies are there for the abatement of NO_x, which involve direct decomposition (on noble metals, metal oxides, perovskite-type catalysts, and zeolites), and selective catalytic reduction (SCR) (using many reductants, such as ammonia, urea, and HCs) overzeolite-type catalysts, supported noble metals,etc. NO_x traps, which are incorporated into the catalyst washcoat constitute an interesting NO_x control technology for gasoline and Diesel engines. NO_x traps are

multifunctional catalysts having adsorbent, oxidation, and reduction functionalities chemically bind with the NO_x species and convert them into solid species (metal bonded nitrates). Simultaneous removal of NO_x and soot are accomplished by using La-K-Cu-V-based perovskite catalysts [286]. Low-temperature catalytic oxidation has been widely used in the removal of volatile organic compounds (VOC). Noble metals like Pt, Pd, Ru, Rh, Ag, and Au are commonly used for the low-temperature oxidation of VOC. Metal oxide derivatives of group III B and II B are (eg., Ti, Cu, Mn, Al, Ce, Co, Fe, etc.) applied as catalysts in VOC oxidation reactions. Most of the metal oxide/sulfide semiconductor photocatalysts such as TiO_2, WO_3, ZnO, CdS, etc., are also reported to decompose VOCs in presence of either UV or visible light. Some of the technologies used for the VOCs treatment are regenerative catalytic oxidation (RCO), recuperative catalytic oxidation, hybrid treatment with catalysts, ozonation-catalytic oxidation, and non-thermal plasma-catalytic oxidation, etc. [287]. The most popular method used for the removal of SO_x from the pollutant gas stream is by reaction with lime/limestone, and the process is called desulfurization process that can effectively remove low concentrations of SO_x. Some of the advanced methods for removing NO_x and SO_x in high concentration levels are wet scrubbing, adsorption, electron beam treatment, discharge methods, etc. [288]. Three-way catalysis methods have been widely used for the simultaneous removal of CO, HC, and NO_x in the exhaust gas and are described in section 1.1.6.1, in the applications of ceria.

1.6.1 Carbon Monoxide (CO) Oxidation over Ceria based Catalysts

Carbon monoxide is a toxic gas emitted into the atmosphere due to the incomplete combustion of fuels.The primary sources of CO are exhausts from vehicles and non-road engines. Since CO is detrimental to the vegetation and all forms of life that respire, it is significant to control the quantity of CO to maintain air quality. The simplest way of removing CO is the catalytic oxidation into harmless CO_2, the essential gas for vegetation [289]. Some of the catalysts commonly used for the oxidation of CO are hopcalite (a mixed oxide of Mn, Co, Cu, and Ag), perovskites (with the general formula ABO_3 in which A are rare earth or alkaline earth metals and B, are transition metals), andsupported noble metal catalysts (Pt, Pd, Rh, Au,etc., on ceria, zirconia, titania, and alumina) [290-293]. Base metal catalysts such as copper-based catalysts and a combination of a copper catalyst with other oxides like ZnO, Cr_2O_3, Fe_2O_3, CoO, etc., also showed good catalytic activity towards CO oxidation [294].

Due to the unique redox properties and oxygen storage capacity,ceria and ceria-based materials have been used as catalysts for CO oxidation reactions. CO oxidation over the ceria surface has been reported to take place through a Mars-van Krevelen (MvK)-type mechanism, whereby CO molecule first reacts with surface ceria oxygen, leaving an oxygen vacancy, which is filled by the gas phase oxygen [295]. The interaction of CO with ceria surface is strongly

related to the structure. It is observed that ceria nanostructures like nanorods and nanocubes, possessing a higher abundance of (100) and (110) exposed facets, have higher catalytic performance compared to ceria particles with more number of (111) facets [296]. Piumettiet al. studied the structural dependency of CeO_2 on CO oxidation reaction by analyzing the CO oxidation activity of ceria nanocubes, nanorods, and mesoporous ceria as well as ceria synthesized by solution-combustion method. The ceria nanocubes performed maximum in low-temperature CO oxidation. The highest activity of nanocubes is a contribution of highly reactive (100) and (110) facets [297]. Among the ceria-based solid solutions, $Ce_xM_{1-x}O_2$(where M= Zr, Hf, L, and Pr) ceria-hafnia solid solution showed excellent CO oxidation activity as a result of its best oxygen storage capacity [298]. Noble metal and transition metal nanoparticles dispersed on the surface of ceria support are other ceria-based catalysts used in CO oxidation. Supported gold and silver catalysts over ceria are highly effective in low-temperature CO oxidation [299-302]. Lohrenscheit et al. has proved the role of oxygen vacancies in the room temperature oxidation of CO over ceria-supported gold by using Operando Raman Spectroscopy, supporting the Mars-van Krevelen (MvK)-type mechanism [303]. Au/CeO_2 catalysts can be promoted by the incorporation of other metals such as Cu and Co. The bimetallic catalysts such as $Au\text{-}Cu/CeO_2$ or $Au\text{-}Co/CeO_2$ catalysts can adsorb more CO, as the latter can get adsorbed on both the metal surfaces. This feature along with more oxygen vacancies enabled the catalyst to easily release the lattice oxygen,

resulting in higher oxidation [304]. Oxygen exchange capacities of ceria have been improved by the incorporation of transition metals by several research groups to enhance CO oxidation. Doping of transition metal ions such as Fe, Zn, Cu, Ni, Cr, Co,etc., into ceria enhanced the CO oxidation activity due to the improvement in OSC [305-308].

1.6.2 Hydrocarbon (HC) Oxidation

Unburnt hydrocarbons introduced into the atmosphere mainly by incomplete fuel combustion may cause several health issues to all forms of life and also generate secondary pollutants such as smog. Several methods are there for the significant removal of hydrocarbons. This process can be carried out in two directions: (1) heterogeneous/homogeneous oxidation by molecular oxygen in the gas or liquid phase, and (2) radiation-induced oxidation by molecular oxygen, oxidation under electric discharge, electrochemical oxidation in solutions,etc [309]. Metals, metal oxides, semiconductors, and complex semiconductors are the most widely used catalysts for the oxidation of hydrocarbons. Perovskite-type oxides containing transition metals such as Co, Mn, Fe,etc., have been used for the total oxidation of hydrocarbons [310]. Noble metal catalysts have been widely used for the oxidation of light alkanes, alkenes, and aromatics. Among these, Pt is the most suitable catalyst for hydrocarbons except methane, for which Pd is the best [311]. Diehl et al. used Pt/Al_2O_3 catalyst for the oxidation of heavy hydrocarbons and observed a correlation between oxidisability and volatility of hydrocarbons [312].

CeO_2 has been used for several years for the oxidation of hydrocarbons, and the main oxidation products are CO_2, and H_2O, where a trace of partial oxidation products are also obtained. Several studies have been reported for the oxidation of methane using pure ceria and ceria-based catalysts, such as doped ceria, ceria-supported noble metal catalysts,etc. [313]. Li et al. demonstrated that two dioxygen species, superoxide (O_2^-) and peroxide (O_2^{2-}) ions are present on the ceria surface. Isotope experiments proved that only one species (O_2^{2-}) are involved in hydrocarbon oxidation from room temperature to 400 °C,whereas the other is relatively inactive [314]. Investigations on the addition of noble metals in ceria (Pt, Pd, and Rh) could increase the reactivity of low-temperature oxygen species formed on ceria resulting in a higher oxidation performance under lower temperatures [315]. The same result was also obtained on the addition of transition metal oxide (CuO) since it favors the formation of highly reducible oxygen species [316]. The presence of dopants like Sr, La, Sc,etc., is found to enhance methane activation and is more sensitive than CO oxidation. Catalysts of ceria solid solution with AgO or V_2O_5 enhanced the oxidation of toluene to benzaldehyde and benzoic acid; the selectivity is also higher compared to pure ceria where the higher reactivity is attributed to the availability of even less reactive lattice oxygen in ceria solid solutions [317]. Bkour et al. developed a Ni-Mo bimetallic catalyst supported on ceria-zirconia (CZ) having an excellent partial oxidation activity on isooctane at high space velocities. The interaction between Ni and support is strengthened by the presence of Mo that also increased the

stability and overall performance of the catalyst [318]. The catalyst $TiO_2/Ce_xZr_{1-x}O_2$ synthesized by Zhong et al. showed better photocatalytic oxidation of gaseous benzene compared to pure TiO_2 due to the increase in active oxygen species and better absorption of radiation [319].

1.7 Optical Sensing Applications of Ceria

Sensing applications of ceria nanoparticles are related to both Ce^{3+} and Ce^{4+} on the ceria surface, and the ability to switch between these two oxidation states. Several investigations are there for the sensing of reactive oxygen species like H_2O_2 in living systems. On exposure to H_2O_2, the peroxide species are coordinated reversibly on the ceria surface resulting in a redshift of adsorption, and an increase in the coordination number. It is followed by a redox process between ROS and ceria, in which more Ce^{3+} are formed by the reduction of Ce^{4+}. Then the number of ROS adsorbed decreases, and also the coordination number of ceria gets decreased. This process can use for the sensing of H_2O_2 or ROS based on spectral or conductivity changes in the structure of these particles [320]. Ceria nanoparticles are excellent co-immobilization materials for many enzymes like cholesterol oxidase, glucose oxidase, horseradish peroxidase,etc., and their catalytic activity can use for the development of biosensors [321]. The OSC of ceria can be explored in the detection of small organic chemicals, metal ions, and biomarkers through colorimetric, electrochemical, fluorescent,and chemiluminescent methods.

1.7.1 Colorimetric Sensing using Ceria

Colorimetric sensing is a process based on absorption spectroscopy. A colorimetric sensor detects the presence of a particular analyte from an observable color change. An ideal sensor should possess some of the characteristics such as selectivity, sensitivity, robustness, accuracy, precision, minimal error, reproducibility, linearity, etc. Colorimetric sensors are chemical sensors or biosensors depending on the type of interacting molecules. Sensors that sense biomolecules such as antigen or antibody, protein, DNA,etc., are called biosensorswhereas, chemical sensors detect different chemical compounds such as volatile organic compounds, gas molecules, toxic organic molecules, and heavy metals. Many metal nanoparticles such as Au, Ag, Cu,etc., and nanocomposites are used for colorimetric sensing that is based on the phenomenon of surface plasmon resonance.

Ceria nanoparticles can be used both as colorimetric indicators, and colorimetric sensors since they function as chromogenic indicators in colorimetric probes in the presence of some analytes. Colorimetric sensors are the least expensive and are user-friendly compared to conventional analytical techniques for several medical diagnoses, environmental pollutant monitoring, and food quality analysis [322]. Ornatskaet al. have developed a ceria-based colorimetric sensor for the detection of food antioxidants by immobilized ceria nanoparticles (CNPs) on a filter paper [323]. When the filter paper is exposed to a

sample containing antioxidants, it will develop some color depending on the nature and concentration of the antioxidant. It does not require any other reagents and is highly stable for years compared to other biosensors. CNPs can also be used for the colorimetric detection of dopamine, a neurotransmitter [324]. On exposure to dopamine, CNPs undergo a color change from colorless to dark brown due to the reduction of Ce^{4+} to Ce^{3+} of CNPs. Enzymatic production of H_2O_2 can be detected by using a filter paper on which CNPs are immobilized with glucose oxidase by the silanization method.

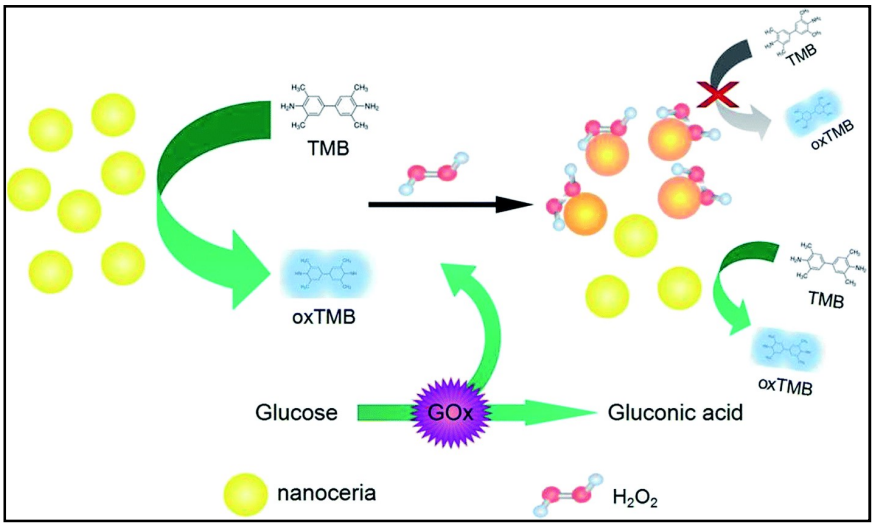

Fig. 1.6 Mechanism of Colorimetric Sensing of H_2O_2 and Glucose [325]

The assay (the mechanism is shown in figure 1.6) is concentration-dependent and can be reused for several measurements without loss of activity. [325].

A similar method is reported in the estimation of glucose, where a filter paper immobilized with CNPs and glucose oxidase exposed to glucose generatedH_2O_2, undergo oxidation and the peroxide bound on the surface of CNPs forms peroxide-Ce complexes. This results in a color change from yellowish-white to orange,depending on the concentration of H_2O_2 produced enzymatically, thus on the concentration of the enzyme and the substrate glucose [326].

Similarly, the peroxidase-like activity of CNPs catalyzes the oxidation of a peroxidase substrate 3,3′,5,5′-tetramethylbenzidine (TMB) in the presence of H_2O_2 to produce a blue color has been utilized for the colorimetric assay of H_2O_2 [327]. Here, H_2O_2 acted as a promoter in millimolar concentrations and an inhibitor at micromolar concentrations. Based onthese observations, a colorimetric method was developed for the detection of glucose having a LOD of 2 μM and a linear range between 4 to 40 μM since H_2O_2 is a product of glucose oxidation [328]. Liu et al. developed a 5,10,15,20-tetrakis(4-carboxyphenyl)-porphyrin (por) modified CeO_2 nanoparticles exhibiting peroxidase-like activity and used as a colorimetric probe for the detection of H_2O_2 using TMB. The catalyst showed a higher catalytic performance compared to pure ceria resulting from the synergetic effect of porphyrin and ceria. Thus, this catalyst has been used as a simple, sensitive, and cheap colorimetric sensor of H_2O_2 as well as glucose [329-330]. Cheng et al. modulated the oxidase-like catalytic activity of CeO_2 nanoparticles in situ via proton

producing/consuming enzyme-catalyzed bioreactions, and based on it they developed a colorimetric bioassay for determining nerve agents, drugs, and bioactive ions [331]. Peng et al. developed a magnetic colorimetric immunoassay strategy using ceria spheres showing excellent oxidase activity for the sensitive detection of human interleukin-6 (IL-6) [332]. CNPs can catalyze the oxidation of the substrate o-phenylenediamine (OPD) to a stable yellow-colored product 2,3-diamiopheazine (oxOPD), the absorbance of which reflects the concentration of IL-6. A CeO_2-montmorillonite (MMT) nanocomposite has been successfully synthesized by Sun et al. and used asa colorimetric biosensor for the detection of H_2O_2 using TMB as the substrate. The catalyst showed better peroxidase performance compared to other CeO_2 nanoparticles, and the sensor was successfully applied for H_2O_2 detection in milk samples [333].

1.7.2 Fluorescence Sensing using Ceria

In fluorescence sensing, the concentration of a fluorescent species is measured from the fluorescence intensity and has been used in the past decade in biochemical, chemical, environmental, and forensic analysis. Any mechanism that changes the fluorescent intensity, wavelength, or lifetime can be used for sensing. Among these, the most direct method is the measurement of change in fluorescence intensity of the probe in response to the analyte.

The redox property of ceria, i.e., by the ability to exist in two different oxidation states, Ce^{3+}, and Ce^{4+} ions on the surface, resulted

in its fluorescence property. Ceria nanoparticle is considered as a fluorescent material emitting green light (~530 nm) under UV excitation. The oxygen vacancies formed in ceria crystals to compensate for the charge of Ce^{3+} ions act as probes to scavenge some charged objects like radicals, metallic ions, and dissolved oxygen [334]. This adsorption of charged species on the oxygen vacancies leads to a decrease in fluorescence intensity, which is useful for a fluorescence sensor via the fluorescence quenching technique. The sensitivity of colorimetric sensors is limited in the absence of enzymes because it then depends mainly on the CNPs, and a high concentration of H_2O_2 is required for the color change. In some cases, selectivity issues also occur when other redox systems are present in the analyte, such as ascorbate, dopamine,etc.Fluorescent sensors were developed to overcome these limitations. Several research groups have reported the use of ceria nanoparticles for the sensing of dissolved oxygen (DO), tiny metal particles such as iron and lead, radicals,etc. [335-339]. Doped ceria nanoparticles with Al, Nd and La have also been reported as potential molecular probes for the sensing of DO and peroxides via fluorescence-quenching [340-343]. Shehata et. al. introduced gold nanoparticles to ceria, which could enhance both fluorescence intensity and lifetime for the effective sensing of metal particles. The increased intensity and lifetime are due to the possible coupling between the plasmonic resonance of gold nanoparticles and the fluorescence emission of ceria [344-345]. Negiet al. reported flake-like mesoporous ceria nanoparticles applicable both as a photocatalyst in picric acid

degradation and also for its sensing [346]. Some researchers have developed ceria nanoparticles with surface modification to improve the fluorescence emission properties and are used for versatile sensing applications. Krishnan et al. have synthesized ultrafine ceria nanoparticles with bilayer coating with oleic acid and used them as a fluorescence sensor for ascorbic acid at a concentration as low as 6 μM [347]. The green-colored fluorescence of the nanoparticles has been used as a sensor by modulating its Ce^{3+} concentration in the crystals. Tian et al. report that a fluorescence resonance energy transfer (FRET) between nanoceria and graphene quantum dots (GQDs) could occur effectively by the electrostatic interaction. They developed a fluorescence aptasensor for the determination of ochratoxin A (OTA), which is a mycotoxin produced as a secondary metabolite from various Aspergillus and Penicillium strains [348]. Liu et al. reported a glucose fluorescence sensor using CNPs adsorbed with fluorescent-labeled DNA on the surface by the phosphate ligand-binding ability of CNPs [349]. On adsorbing DNA, CNPs fluorescence gets completely quenched, whereas on adding H_2O_2 it got enhanced. The method could be used for the detection of H_2O_2 and glucose in blood serum. Eu and Gd doped CNPs are reported as capable of reaction with analytes, and by studying the change in fluorescence of CNPs, the imaging of analyte binding is possible [350]. By changing the pH of the solution, the oxidase activity can be tuned, and the oxidation of a substrate having fluorescence can thus be controlled. For example, at neutral pH, ceria is only mild oxidizing, and so CNPs oxidize amplify to a

fluorescent product, resorufin, and prevent further oxidation to non-fluorescent resazurin.These observations can be used for the identification of cancer biomarkers. Antibodies immobilized on the surface of CNPs were conjugated with protein G to identify the expression of epithelial cell adhesion molecule (EpCAM) in breast carcinoma patients and folate receptor in lung carcinoma patients. The detection can be completed in 3 hours, whereas the conventional enzyme-linked immunosorbent assay (ELISA) requires about 15 hours. Thus a sensitive cell-based ELISA can be developed using CNPs based ampliflu oxidation [351-352].

1.8 Scope of the Study

Cerium oxide is a rare earth metal oxide exhibiting unique properties, such as oxygen storage capacity (OSC). Cerium ions in ceria can exist in two different oxidation states +3 and +4, resulting in the formation of oxygen vacancies and are responsible for the OSC of ceria. This particular redox property makes ceria and ceria-based nanomaterials suitable for versatile applications such as three-way catalysis, water gas shift reactions, oxidation of volatile organic compounds, photocatalysis, sensing, etc. Even though ceria can be synthesized by several physical and chemical methods, preparation via green methodshas a great significance in the present era. In this work, the different organic compounds present in the garlic and fenugreek extracts have been used as stabilizing and chelating agents for preparing less agglomerated ceria nanoparticles through simple sol-gel

processes. Also, ultra-small ceria nanoparticles have been synthesized by using a 2 M ammonia solution for precipitation, and its cobalt-modified material was attained through wet impregnation of ceria nanoparticles.

The environmental pollution due to the presence of antibiotics and dyes in soil and water is of great concern in maintaining the quality of water and soil. Similar is the situation of air due to the extensive exhaust emissions containing CO and unburnt hydrocarbons from vehicles and power plants. The removal of various pollutants from water and air via simple methods using cost-effective materials is of great relevance in pollutant treatment systems. The optical sensing of the pollutants such as picric acid in water is of related importance since its presence even in trace amounts causes several health issues in human beings. The ceria nanomaterials synthesized in this work have been used in the removal of antibiotics and dyes efficiently through photocatalysis, adsorption, and photo Fenton degradation. Selective sensing of picric acid in different water samples is achieved here by the fluorescence quenching method using the ceria nanoparticles synthesized by the sol-gel method. The cobalt-doped ceria materials have been effectively utilized in the gaseous pollutant treatment (CO and the model pollutant propane), and also for the colorimetric sensing of H_2O_2, which is a main reactive oxygen species produced in many biological systems.

1.9 Objectives of the Present Work

The major objectives of the present study include;

- Green synthesis of CeO_2 nanoparticles by precipitation method using ammonia and sol-gel methods using garlic and fenugreek extracts.
- Synthesis of cobalt-doped ceria catalysts by wet impregnation of ceria prepared by ammonia precipitation.
- Characterization of the prepared systems using various analytical techniques to study the structure, morphology, and relevant properties (electronic, optical, and redox properties).
- Photocatalytic degradation of antibiotic norfloxacin on ceria nanoparticles prepared by ammonia precipitation.
- Adsorption and photo Fenton degradation of Congored dye by ceria nanoparticles synthesized by the sol-gel method using garlic extract.
- Investigation of cobalt-doped ceria catalysts in the simultaneous removal of carbon monoxide and hydrocarbons; and its Peroxidase like performance for colorimetric detection of H_2O_2
- Fluorescence sensing of 2,4,6-trinitrophenol (picric acid) by ceria nanoparticles prepared using fenugreek extract as the precipitating agent.

References

1. J. Emsley, *Nature's Building Blocks: An A-Z Guide to the Elements*, Oxford University Press, New York, 2011.
2. J. Börje, L. Wei, L. Sa, Ahuja and Rajeev *Sci. Rep.*, 2014, **4**, 6398.
3. A. F. Holleman, N. Wiberg and E. Wiberg, *Inorganic Chemistry*, San Diego: Academic Press, Berlin, 2001.
4. D. C. Koskimaki, K. A. Gschneidner and N. T. Panousis, *J. Cryst. Growth,* 1974, **22**, 225.
5. G. Audi, F. G. Kondev, M. Wang, W. J. Huang and S. Naimi, *Chin. Phys. C*, 2017, **41**, 030001.
6. A. G. W. Cameron, *Space Sci. Rev.*, 1973, **15**, 121.
7. A. Trovarelli, *Catalysis by Ceria and related materials*, Imperial College Press, London, 2001.
8. N. N. Greenwood and A. Earnshaw, *Chemistry of the elements*, Elsevier Limited, Oxford, New York, 1997.
9. Chemical reactions of Cerium, https://www.webelements.com/cerium/chemistry.html (accessed August 2020).
10. V. Valérie, P. Olivier, P. Mathieu, B. N. Lal, R. Florent and M. Rémi, *Dalton Trans.*, 2017, **46**, 13553.
11. J. M. Dumdum, H. E. Aldorf and E. C. Barnum, *Nat. Lubric. Grease Inst*.1984, **48**, 111.
12. Heidingsfeldova, *Kautsch. Gummi Kunstst*, 1984, **37**, 694.

13. K. A. Gschneidner, *Handbook on the Physics and Chemistry of Rare Earths*, Elsevier, North Holland, 2006.
14. F. M. A. Sroor and F. T. Edelmann, *Lanthanides: Tetravalent Inorganic". Encyclopedia of Inorganic and Bioinorganic Chemistry*, Wiley Online Library, 2012.
15. J. Paier, C. Penschke and J. Sauer, *Chem. Rev*. 2013, **113**, 3949.
16. K. Reinhardt and H. Winkler, *Ullmann's Encyclopedia of Industrial Chemistry*, John Wiley & Sons, New York, 2000.
17. L. R. Morss, *Handbook on the Physics and Chemistry of Rare Earths,* Elsevier Science, New York, 1994, **18**.
18. T. Montini, M. Melchionna, M. Monai and P. Fornasiero, *Chem. Rev.* 2016, **116**, 5987.
19. L. Malavasi, C. A. J. Fisher and M. S. Islam, *Chem. Soc. Rev*., 2010, **39**, 4370.
20. M. Yashima, D. Ishimura, Y. Yamaguchi, K. Ohoyama, and K. Kawachi, *Chem. Phys. Lett*., 2003, **372**, 784.
21. G. Brauer, K. A. Gingerich and V. J. Über Die Oxyde Des cers, *Inorg. Nucl. Chem*., 1960, **16**, 87.
22. R. D. Shannon, C. Prewitt, Acta Crystallogr. Sect. B: Struct. Crystallogr. Cryst. Chem., 1969, **25**, 925.
23. M. Zinkevich, D. Djurovic and F. Aldinger, *Solid State Ion.,* 2006, **177**, 989.
24. O. T. Sørensen, *J. Solid State Chem*. 1976, **18**, 217.
25. E. Kümmerle and G. Heger, *J. Solid State Chem.* 1999, **147**, 485.

26. S. P. Ray, D. E. Cox, *J. Solid State Chem*. 1975, **15**, 344.
27. L. Minervini, M. O. Zacate and R. W. Grimes, *Solid State Ion.*, 1999, **116**, 339.
28. J. Kašpar, P. Fornasiero, M. Graziani, *Catal. Today*, 1999, **50**, 285.
29. T. Bunluesin, R. J. Gorte, G. W. Graham, *Appl. Catal. B*, 1998, **15**, 107.
30. X. Wang and R. J. Gorte, *Catal. Lett*., 2001, **73**, 15.
31. Y. S. Otsuka, H. Morikawa, N. Izu and K. Okuda, *Japan. Inst. Metals*, 1995, **59**, 1237.
32. Y. M. S. Otsuka, T. Omata, N. Izu and H. Kishimoto, *J. Solid State Chem*., 1998, 138, 47.
33. M. Yoshimura, E. Tani and S. Somiya, *Solid State Ion.*, 1981, **3**, 477481.
34. E. Tani, M. Yoshimura and S. Somiya, *J. Am. Ceram. Soc.*, 1983, **77**, 506.
35. Y. Madier, C. Descorme, A. M. Le Govic and D. Duprez, *Oxygen J. Phys. Chem. B,* 1999, **103**, 10999.
36. T. Miki, T. Ogawa, M. Haneda, N. Kakuta, A. Ueno, S. Tateishi, S. Matsuura, M. Sato, *J. Phys. Chem.,* 1990, **94**, 6464.
37. T. Maillet, Y. Madier, R. Taha, J. Barbier, D. Duprez, *Stud. Surf. Sci. Catal*., 1997, **112**, 267.
38. B. Cho, *J. Catal*., 1991, **131**, 74.
39. H. Yao, Y. Y. Yao, *J. Catal*., 1984, **86**, 254.

40. A. Trovarelli, F. Zamar, J. Llorca, C. Leitenburg, G. Dolcetti and J. T. Kiss, *J. Cata.,* 1997, **169**, 490.
41. C. Descorme, R. Taha, N. Mouaddib-Moral and D. Duprez, *Appl. Catal. A,* 2002, **223**, 287.
42. J. C. Boivin and G. Mairesse, *Chem. Mater*., 1998, **10**, 2870.
43. M. Mogensen, T. Lindegaard, U. R. Hansen, G. Mogensen, *J. Electrochem. Soc*., 1994, **141**, 2122.
44. M. Kakihana, *J. Sol-Gel Sci. Technol.*, 1996, **6**, 7.
45. S. Bernal, G. Blanco, M. A. Cauqui, P. Corchado, J. M. Pintodo and J. M. Rodoriguez-Izuqierdo, *Chem. Comm*., 1997, **53**, 1545.
46. G. N. Vayssilov, A. Migani and K. Neyman, *J. Phys. Chem. C,* 2011, **115**, 16081.
47. V. I. Parvulescu, C. Tiseanu, *Catal. Today,* 2015, **253**, 33.
48. Z. Wang, Z. Quan and J. Lin, *Inorg. Chem*., 2007, **46**, 5237.
49. P. Patsalas, S. Logothetidis, L. Sygellou and S. Kennou, *Phys. Rev. B*, 2003, **68**, 035104.
50. L. Yin, Y. Wang, G. Pang, Y. Koltypin and A. Gedanken, *J. Coll. Int. Sci*., 2002, **246**,78.
51. A. Corma, P. Atienzar, H. Garcia and J. Y. Chane-Ching, *Nat. Mater*., 2004, **3**, 394.
52. A. Krishnan, T. S. Sreeremya, E. Murray and S. Ghosh, *J. Colloid Interf. Sci*., 2013, **389**, 16.
53. A. Krishnan, T. S. Sreeremya and S. Ghosh, *RSC Adv*., 2016, **6**, 53550.

54. R. J. White, R. Luque, V. L. Budarin, J. H. Clark and D. J. Macquarrie, *Chem. Soc. Rev*., 2009, **38**, 481.
55. S. Tsunekawa, K. Ishikawa, Z. Q. Li, Y. Kawazoe and A. Kasuya, *Phys. Rev. Lett.,* 2000, **85**, 3440.
56. X. D. Zhou and W. Huebner, *Appl. Phys. Lett*., 2001, **79**, 3512.
57. S. Tsunekawa, R. Sivamohan and T. Ohsuna, *Mater. Sci. Forum*, 1999, **315**, 439.
58. Y. W. Zhang, R. Si, C. S. Liao, *J. Phys. Chem. B*, 2003, **107**, 10159.
59. J. E. Spanier, R. D. Robinson, F. Zhang, S. W. Chan and I.P. Herman, *Phys. Rev. B*, 2001, **64**, 245407.
60. A. Dhall and W. Self, *Antioxidants*, 2018, **7**, 97.
61. D. Zhang, X. Du, L. Shia and R. Gao, *Dalton Trans*., 2012, **41**, 14455.
62. E. Matijevic and W. P. Hsu, *J. Colloid Interface Sci*., 1987, **118**, 506.
63. H. I. Chen and H. Y. Chang, *Ceram. Int*., 2005, **31**, 795.
64. M. C. Cabús-Llauradó, Y. Cesteros, F. Medina, P. Salagre and J. E. Sueiras, *Microporous Mesoporous Mater*., 2007, **100**, 167.
65. M. Yamashita, K. Kameyama, S. Yabe, S. Yoshida, Y. Fujishiro, T. Kawai and T. Sato, *J. Mater. Sci*., 2002, **37**, 683.
66. K. Wu, L. D. Sun and C. H. Yan, *Adv. Energy Mater*., 2016, **6**, 1600501.
67. C. Burda, X. Chen, R. Narayanan and M. A. El-Sayed, *Chem. Rev*., 2005, **105**, 1025.

68. H. X. Mai, L. D. Sun, Y. W. Zhang, R. Si, W. Feng, H. P. Zhang, H. C. Liu and C. H. Yan, *J. Phys. Chem. B*, 2005, **109**, 24380.
69. G. Li, K. Chao, H. Peng, K. Chen and Z. Zhang, *J. Phys. Chem. C*, 2008, **112**, 16452.
70. Z. R. Tang, Y. Zhang and Y. J. Xu, *RSC Adv*., 2011, **1**, 1772.
71. W. Q. Han, L. Wu and Y. Zhu, *J. Am. Chem. Soc*., 2005, **127**, 12814.
72. Y. J. Zhang, T. Cheng, Q. X. Hu, Z.Y. Fang and K. D. Han, *J. Mater. Res*., 2007, **22**, 1472.
73. H. X. Mai, L. D. Sun, Y. W. Zhang, R. Si, W. Feng, H. P. Zhang, H. C. Liu and C. H. Yan, *J. Phys. Chem. B,* 2005, **109**, 24380.
74. H. X. Mai, L. D. Sun, Y. W. Zhang, R. Si, W. Feng, H. P. Zhang, H. C. Liu and C. H. Yan, *J. Phys. Chem. B*, 2005, **109**, 24380.
75. X. Liang, J. Xiao, B. Chen, Y. Li, *Inorg. Chem*., 2010, **49**, 8188.
76. C. Pan, D. Zhang, L. Shi, *J. Solid State Chem*., 2008, **181**, 1298.
77. X. Liu, K. Zhou, L. Wang, B. Wang and Y. Li, *J. Am. Chem. Soc*., 2009, **131**, 3140.
78. H. P. Zhou, Y. W. Zhang, H. X. Mai, X. Sun, Q. Liu, W. G. Song and C. H. Yan*, Chem. Eur. J*., 2008, **14**, 3380.

79. R. Si, Y. W. Zhang, L. P. You, C. H. Yan, *Angew. Chem. Int. Ed*., 2005, **44**, 3256.
80. A. Vioux, *Chem. Mater*., 1997, **9**, 2292.
81. C. Laberty-Robert, J. W. Long, E. M. Lucas, K. A. Pettigrew, R. M. Stroud, M. S. Doescher and D. R. Rolison, *Chem. Mater*., 2006, **18**, 50.
82. T. Yu, J. Joo, Y. I. Park and T. Hyeon, *Angew. Chem. Int. Ed*., 2005, **117**, 7577.
83. H. Xiao, Z. Ai and L. Zhang, *J. Phys. Chem. C,* 2009, **113**, 16625.
84. B. Thiébaut, *Platinum Met. Rev*., 2011, **55**, 149.
85. L. Mädler, W. Stark and S. Pratsinis, *J. Mater. Res*., 2002, **17**, 1356.
86. X. Feng, D. C. Sayle, Z. L. Wang, M. S. Paras, B. Santora, A. C. Sutorik, T. X. Sayle, Y. Yang, Y. Ding and X. Wang, *Science,* 2006, **312**, 1504.
87. X. Chen and S. S. Mao, *Chem. Rev*., 2007, **107**, 2891.
88. T. Masui, K. Fujiwara, K. I. Machida, G. Y. Adachi, T. Sakata, H. Mori, *Chem. Mater*., 1997, **9**, 2197.
89. E. Kockrick, C. Schrage, A. Grigas, D. Geiger and S. Kaskel, *J. Solid State Chem*., 2008, **181**, 1614.
90. T. Arunachalam, M. Karpagasundaram and N. Rajarathinam, *Mater Sci-Poland*, 2017, **35**, 791.

91. Q. Maqbool, M. Nazar, S. Naz, T. Hussain, N. Jabeen, R. Kausar, S. Anwaar, F. Abbas and T. Jan, *Int J Nanomedicine*, 2016, **11**, 5015.
92. A. Arumugam, C. Karthikeyan, A.S.H. Hameed, K. Gopinath, S. Gowri and V. Karthika, *Mater. Sci. Eng. C,* 2015, **49**, 408.
93. D. Dutta, R. Mukherjee, M. Patra, M. Banik, R. Dasgupta, M. Mukherjee and T. Basu, *Colloid surf. B,* 2016*,* **147**, 45.
94. G.S. Priya, A. Kanneganti, K.A. Kumar, K.V. Rao and S. Bykkam, *Int. J. Sci. Res*., 2014, **4**, 2250.
95. S.K. Kannan and M. Sundrarajan, Int. J. Nanosci., 2014, 13, 1450018.
96. S. A. Nezhad, A. Es-haghi and M. H. Tabrizi, *Appl Organometal Chem*., 2020, **34**, 5314.
97. R.P. Senthilkumar, V. Bhuvaneshwari, R. Ranjithkumar, S. Sathiyavimal, V. Malayaman and B. Chandarshekar, *Int. J. Biol. Macromol*., 2017, **104**, 1746.
98. J.K. Sharma, P. Srivastava, S. Ameen, M.S. Akhtar, S.K. Sengupta and G. Singh, *Mater. Res. Bull.,* 2017, **91**, 98.
99. G. Sharmila, C. Muthukumaran, H. Saraswathi, E. Sangeetha, S. Soundarya and N.M. Kumar, Ceram. Inter., 2019, 45, 12382.
100. H. Kargar, H. Ghazavi and M. Darroudi M, *Ceramics Int*., 2015, **41**, 4123.
101. M. Darroudi M, S. J. Hoseini, R. K. Oskuee, H. A. Hosseini, L. Gholami and S. Gerayli, *Ceramics Int*., 2014, **40**, 7425.

102. M. Darroudi, M. Sarani, R. K. Oskuee, A. K. Zak, H. A. Hosseini and L. Gholami, *Ceramics Int*., 2014, **40**, 2041.
103. H. Kargar,F. Ghasemi and M. Darroudi, *Ceramics Int*., 2015, **41**, 1589.
104. E. Alpaslan, H. Yazici, N. H. Golshan, K. S. Ziemer and T. J. Webster, *ACS Biomater Sci Eng*., 2015, **1**, 1096.
105. X. Lu, T. Zhai, H. Cui, J. Shi, S. Xie, Y. Huang, C. Liang and Y. Tong, *J. Mater. Chem.,* 2011, **21**, 5569.
106. Y. Li, Q. Sun, M. Kong, W. Shi, J. Huang, J. Tang and X. Zhao, *J. Phys. Chem. C*, 2011, **115**, 14050
107. L. Yin, Y. Wang, G. Pang, Y. Koltypin and A. Gedanken, *J. Colloid Interface Sci.,* 2002, **246**, 78.
108. Ray, S. P.; Nowick, A. S. and Cox, D. E. *J. Solid State Chem.,* 1975, **15**, 344.
109. C. Sun, H. Li and L. Chen, *Energ. Environ. Sci*., 2012, **5**, 8475.
110. J. Kašpar, P. Fornasiero and N. Hickey, *Catal. Today,* 2003, **77**, 419.
111. M. Shelef, R. McCabe, *Catal. Today,* 2000, **62**, 35.
112. G. Adachi and N. Imanaka, *Chem. Rev*., 1998, **98**, 1479.
113. R. K. Usmen, R. W. McCabe, G. W. Graham, W. H. Weber, C. R. Peters, H. S. Gandhi, SAE International, 1992, 92233610.4271/922336.
114. J. Kašpar, P. Fornasiero, M. Graziani, *Catal. Today,* 1999, **50**, 285.

115. G. Balducci, M.S. Islam, J. Kaspar, P. Fornasiero and M. Graziani, *Chem. Mater*., 2000, **12**, 677.

116. G. Balducci, J. Kaspar, P. Fornasiero, M. Graziani and M.S. Islam, *J. Phys. Chem. B*, 1998, **102**, 557.

117. J. Kaspar, P. Fornasiero, G. Balducci, R. Di Monte, N. Hickey and V. Sergo, *Inorg. Chim. Acta,* 2003, **349**, 217.

118. B.A.A.L. van Setten and M. Makkee, *J.A. Catal. Rev*., 2001, **43**, 489.

119. M.V. Twigg, *Catal. Today*, 2011, **163**, 33.

120. A. Bueno-Lopez, Appl. Catal. B Environ., 2014, 146, 1.

121. T. Montini, M. Melchionna, M. Monai and P. Fornasiero, *Chem. Rev*., 2016. **116**, 5987

122. M. Machida, Y. Murata, K. Kishikawa, D.J. Zhang and K. Ikeue, *Chem. Mater*., 2008, **20**, 4489.

123. E. Aneggi, V. Rico-Perez, C. de Leitenburg, S. Maschio, L. Soler, J. Llorca and A. Trovarelli, *Angew. Chem. Int. Ed*., 2015, **54**, 14040.

124. V. Rico-Perez, E. Aneggi, A. Bueno-Lopez and A. Trovarelli, *Appl. Catal. B, Environ*. 2016, **197**, 95.

125. K. Krishna, A. Bueno-López, M. Makkee and J. A. Moulijn, *Appl. Catal. B,* 2007, **75**, 189.

126. E. Aneggi, C. de Leitenburg, G. Dolcetti and A. Trovarelli, *Catal. Today* ,2008, **136**, 3.

127. E. Aneggi, D. Wiater, C. de Leitenburg, J. Llorca and A. Trovarelli, *ACS Catal*., 2014, **4**, 172.

128. E. Aneggi, C. de Leitenburg, J. Llorca and A. Trovarelli, *Catal. Today*, 2012, **197**, 119.

129. P. Sudarsanam, B. Hillary, D. K. Deepa, M. H. Amin, B. Mallesham, B. M. Reddy and S. K. Bhargava, *Catal. Sci. Technol*., 2015, **5**, 3496.

130. S. C. Singhal and K. Kendall, Elsevier Advanced Technology, Oxford, (2003).

131. M. Mogensen, *J. Electrochem. Soc.,* 1994, **141**, 2122.

132. O. A. Marina, C. Bagger, S. Primdahl and M. A. Mogensen, *Solid State Ion.,* 1999, **123**, 199.

133. R. J. Gorte and J. M. Vohs, Curr. Opin. *Colloid Interface Sci.,* 2009, **14**, 236.

134. L. Adijanto, A. Sampath, A. S. Yu, M. Cargnello, P. Fornasiero, R. J. Gorte and J. M. Vohs, *ACS Catal*., 2013, **3**, 1801.

135. Z. Zhan and S. A. Barnett, *Science*, 2005, **308**, 844.

136. H. Kurokawa, T. Z. Sholklapper, C. P. Jacobson, L. C. De Jonghe and S. J. Visco, *Solid-State Lett*., 2007, **10**, B135.

137. Y. H. Lee, H. Sumi, H. Muroyama, T. Matsui and K. Eguchi, *J. Electrochem. Soc*., 2013, **160**, F579.

138. B. Zhu and M. D. Mat, *Int. J. Electrochem. Sci*., 2006, **1**, 383.

139. X. Wang, Y. Ma, R. Raza, M. Muhammed and B. Zhu, *Electrochem. Commun*., 2008, **10**, 1617.

140. R. Raza, G. Abbas, S. K. Imran, I. Patel and B. Zhu, *J. Fuel Cell Sci. Technol.,* 2011, **8**, 041012.

141. J. Hu, S. Tosto, Z. Guo and Y. Wang, *J. Power Sources*, 2006, **154**, 106.

142. X.R. Liu, B. Zhu, J. R. Xu, J. C. Sun and Z. Q. Mao, *Key Eng. Mater.,* 2005, **280**, 425.

143. B. Zhu, X. Liu, P. Zhou, Z. Zhu, W. Zhu and S. Zhou, *J. Mater. Sci. Lett.,* 2001, **20**, 591.

144. R.J. Gorte and S. Zhao, *Catal. Today*, 2005, **104**, 18.

145. D.B. Pal, R. Chand, S.N. Upadhyay and P.K. Mishra, *Renew. Sust. Energ. Rev*., 2018, **93**, 549.

146. D. L. Trimm, *Appl. Catal. A,* 2005, **296**, 1.

147. K. Polychronopoulou, C.M. Kalamaras and A.M. Efstathiou, *Recent Pat. Mater., Sci*.2011, **4**, 122.

148. X. Liu, W. Ruettinger, X. Xu and R. Farrauto, *Appl. Catal. B,* 2005, **56**, 69.

149. W. Ruettinger, X. Liu and R. J. Farrauto, *Appl. Catal. B,* 2006, **65**, 135.

150. K. C. Petallidou and A. M. Efstathiou, *Appl. Catal. B,* 2013, **140**, 333.

151. N. Hickey, P. Arneodo Larochette, C. Gentilini, L. Sordelli, L. Olivi, S. Polizzi, T. Montini, P. Fornasiero, L. Pasquato and M. Graziani, *Chem. Mater*., 2007, **19**, 650.

152. D. Andreeva, I. Ivanov, L. Ilieva, J. W. Sobczak, G. Avdeev and T. Tabakova, *Appl. Catal. A,* 2007, **333**, 153.

153. T. Tabakova, M. Manzoli, D. Paneva, F. Boccuzzi, V. Idakiev and I. Mitov, *Appl. Catal. B,* 2011, **101**, 266.

154. T. Tabakova, L. Ilieva, I. Ivanov, R. Zanella, J. W. Sobczak, W. Lisowski, Z. Kaszkur and D. Andreeva, *Appl. Catal. B,* 2013, **136**, 70.

155. J. Vecchietti, S. Collins, J. J. Delgado, M. Małecka, E. del Rio, X. Chen, S. Bernal and A. Bonivardi, *Top. Catal.,* 2011, **54**, 201.

156. D.B. Pal, R. Chand, S.N. Upadhyay and P.K. Mishra, *Renew. Sust. Energ. Rev*., 2018, **93**, 549.

157. N. Bion, F. Epron, M. Moreno, F. Mariño and D. Duprez, *Top. Catal*., 2008, **51**, 76.

158. Y. Gao, W. Wang, S. Chang and W. Huang, *Chem. Cat. Chem.,* 2013, **5**, 3610.

159. S. Carrettin, P. Concepción, A. Corma, J. M. López Nieto and V. F. Puntes, *Angew. Chem., Int. Ed.,* 2004, **43**, 2538.

160. D. Gamarra, G. Munuera, A. B. Hungria, M. Fernandez-Garcia, J. C. Conesa, P. A. Midgley, X. Q. Wang, J. C. Hanson, J. A. Rodriguez and A. Martinez-Arias, *J. Phys. Chem. C,* 2007, **111**, 11026.

161. T. Tabakova, G. Avgouropoulos, J. Papavasiliou, M. Manzoli, F. Boccuzzi, K. Tenchev, F. Vindigni and T. Ioannides, *Appl. Catal. B,* 2011, **101**, 256.

162. Y. Liu, B. Liu, Y. Liu, Q. Wang, W. Hu, P. Jing, L. Liu, S. Yu and J. Zhang, *Appl. Catal. B,* 2013, **142**, 615.

163. J. Kugai, T. Moriya, S. Seino, T. Nakagawa, Y. Ohkubo, H. Nitani and T. A. Yamamoto, *Catal. Lett.,* 2013, **143**, 1182.

164. X. Liao, W. Chu, X. Dai and V. Pitchon, *Appl. Catal. B,* 2013, **142**, 25.

165. S. M. Saqer, D. I. Kondarides and X. E. Verykios, *Top. Catal*., 2009, **52**, 517.

166. X. Tang, Y. Li, X. Huang, Y. Xu, H. Zhu, J. Wang and W. Shen, *Appl. Catal. B,* 2006, **62**, 265.

167. M. S. Kamal, S. A. Razzak and M. M. Hossain, *Atmos. Environ.,* 2016, **140**, 117.

168. L. F. Liotta, G. Di Carlo, G. Pantaleo, A. M. Venezia and G. Deganello, *Appl. Catal. B,* 2006, **66,** 217.

169. W. Yang, D. Li, D. Xu and X. Wang, *J. Nat. Gas Chem.,* 2009, **18**, 458.

170. H. Li, G. Lu, Y. Wang, Y. Guo and Y. Guo, *Catal. Commun*., 2010, **11**, 946.

171. P. Gélin, and M. Primet, *Appl. Catal. B,* 2002, **39**, 1.

172. G. N. Vayssilov, Y. Lykhach, A. Migani, T. Staudt, G. P. Petrova, N. Tsud, T. Skála, A. Bruix, F. llas, K. C. Prince, V. Matolín, K. M. Neyman and J. Libuda, *Nat. Mater.,* 2011, **10**, 310.

173. P. Hurtado, S. Ordonez, H. Sastre and F. V. Diez, *Appl. Catal. B,* 2004, **47**, 85.

174. K. Narui, H. Yata, K. Furuta, A. Nishida, Y. Kohtoku and T. Matsuzaki, *Appl. Catal. A,* 1999, **179**, 165.

175. J. I. Gutiérrez-Ortiz, B. de Rivas, R. López-Fonseca and J. R. González-Velasco, *Catal. Today,* 2005, **107**, 933.

176. M. Alifanti, M. Florea and V. I. Pârvulescu, *Appl. Catal. B,* 2007, **70**, 400.

177. D. Delimaris and T. Ioannides, *Appl. Catal. B,* 2008, **84**, 303.

178. Q. Dai, X. Wang and G. Lu, *Appl. Catal. B,* 2008, **81**, 192.

179. J. I. Gutiérrez-Ortiz, B. de Rivas, R. López-Fonseca and J. R. González-Velasco, *Appl. Catal. A,* 2004, **269**, 147.

180. Q. Huang, Z. Meng and R. Zhou, *Appl. Catal. B,* 2012, **115**, 179.

181. C. Gannoun, R. Delaigle, D. P. Debecker, P. Eloy, A. Ghorbel and E. M. Gaigneaux, *Appl. Catal. A,* 2012, **447**,1.

182. S. Pitkäaho, L. Matejova, S. Ojala, J. Gaalova and R. L. Keiski, *Appl. Catal. B,* 2012, **113**, 150.

183. S. Munusamy K. Bhakyaraj, L. Vijayalakshmi, A. Stephen and V. Narayanan, *Int J Innovative Res Sci Eng*., 2014, **2**, 318.

184. G. Pulido-Reyes, I. Rodea-Palomares and S. Das, *Sci Rep*., 2015, **5**, 15613.

185. B. Uttara, A. V. Singh, P. Zamboni and R. T. Mahajan, *Curr. Neuropharmacol*., 2009, **7**, 65.

186. C. Guo, R. Smith, T. W. Gant and M. O. Leonard, *Toxicol Res*., 2015, **4**, 464.

187. A. Arya, A. Gangwar and S. K. Singh, *Int. J. Nanomedicine*, 2016, **11**, 1159.

188. B. Bhushan and P. Gopinath, *J. Mater. Chem. B.* 2015, **3**, 4843.

189. Y. Li, X. He and J. J. Yin, *Angew. Chem. Int. Ed. Engl.,* 2015, **54**, 1832.

190. M. J. Akhtar, M. Ahamed, H. A. Alhadlaq, M. A. Khan and S. A. Alrokayan*, J. Colloid Interface Sci*., 2015, **453**, 21.

191. Z. Tian, J. Li, Z. Zhang, W. Gao, X. Zhou X and Y. Qu, *Biomaterials*, 2015, **59**, 116.

192. R. Ameta, S. Benjamin, A. Ameta and S. C. Ameta, *Mater. Sci. Forum*, 2013, **734**, 247.

193. P. Gu, S. Zhang, X. Li, X. Wang, T. Wen, R. Jehan, A. Alsaedi, T. Hayat and X. Wang, *Environ. Pollut*., 2018, **240**, 493.

194. P. Gu, J. Xing, T. Wen, R. Zhang, J. Wang, G. Zhao, T. Hayat, Y. Ai, Z. Lin and X. Wang, *Environ. Sci. Nano.,* 2018, **5**, 946.

195. N. Bolong, A. F. Ismail, M. R. Salim and T. Matsuura, *Desalination*, 2009, **239**, 229.

196. Y.L. Pang, A.Z. Abdullah and S. Bhatia, *Desalination*, 2011, **277**, 1.

197. C. Belvar, R. Bellod, A. Fuerte and M. F. Garcia, *Appl. Catal. B: Environ.,* 2006, **65**, 301.

198. D. B. Luiz, A. K. Genena, H. J. José, R. F. Moreira and H. F. Schröder, *Water Sci. Technol.*, 2009, **60**, 1869.

199. P. R. Gogate and A. B. Pandit, *Chemosphere*, 2004, **73**, 848.

200. J. O. Tijani, O. O. Fatoba, G. Madzivire and L. F. Petrik, *Water Air Soil pollut.*, 2014, **225**, 2102.

201. A. Fujishima and K. Honda, *Nature*, 1972, **238**, 37.

202. N. Daneshvar, S. Aber, M. S. Seyed Dorraji, A. R. Khataee and M. H. Rsaoulifard, *Sep. Purify. Technol.*, 2007, **58**. 91.

203. A. Mills, R. H. Davies and D. Worsley, *Chem. Soc. Revs.,* 1993, **22**, 417.

204. U. I. Gaya and A. H. Abdullah, *J. Photochem. Photobiol. C. Photochem. Rev*., 2008, **9**, 1.

205. D. S Bhatkhande, V. G Pangarkar and A. ACM Beenackers, *J. Chem. Technol. Biotechnol.,* 2002, **77**, 102.

206. R. Saravanan, F. J. Gracia and A. Stephen, Chapter 2 *Basic Principles, Mechanism , and Challenges of Photocatalysis*, Materials Science. 2017.

207. M. Schiavello , *Heterogeneous Photocatalysis*, John Wiley & Sons, New York, 1995.

208. N. Serpone and E. Pelizzetti, *Photocatalysis*, *Fundamentals and Applications*, Wiley, New York, 1989.

209. S. Baruah and J. Dutta, Environ. Chem. Lett., 2009, **7**, 191.

210. M. Y. Guo, M. K. Fung, F. Fang, X. Y. Chen, A. M. C. Ng, A. B. Djurisic, and W. K. Chan, *J. Alloys. Compd*, 2011, **509**, 1328.

211. Z Wang, C. Yang, T. Lin, H. Yin, P. Chen, D. Wan, F. Xu, F. Huang, J. Lin, X. Xie and M. Jiang, Adv. Funct. Mater., 2013, **23**, 5444.

212. T. Sano, N. Negishi, K. Koike, K. Takeuchi and S. Matsuzawa, J. Mater. Chem., 2004, **14**, 380.

213. R. Ullah and J. Dutta, J. Hazard. Mater., 2008, **156**, 194.

214. S. Colis, H. Bieber, S. Be ´gin-Colin, G. Schmerber, C. Leuvrey and A. Dinia, Chem. Phys. Lett., 2006, **422**, 529.

215. A. B. Djurisic, Y. H. Leung, A. M. Ching Ng, Mater. Horiz., 2014, **1**,400.

216. S. Xie, Z. Wang, F. Cheng, P. Zhang, W. Mai and Y. Tong, *Nano. Energy,* 2017, **34**, 313.

217. W. Zoua, Y. Shao, Y. Pu, Y. Luo, J. Sun, K. Ma, C. Tang, F. Gao and L. Dong, *Appl. Catal. B,* 2017, **218**, 51.

218. Q. Leng, D. Yang, Q. Yang, C. Hu, Y. Kang, M. Wang and M. Hashim, *Mater. Res. Bull*., 2015, **65**, 266.

219. M. Aslam, M.T. Qamar, M.T. Soomro, I.M.I. Ismail, N. Salah, T. Almeelbi, M.A. Gondal and A. Hameed, *Appl. Catal. B,* 2016, **180**, 391.

220. Z. Fan, F. Meng, J. Gong, H. Li, Y. Hu and D. Liu, *Mater. Lett*., 2016, **175**, 36.

221. A. D. Liyanage, S. D. Perera, K. Tan, Y. Chabal and K. J. Balkus, *ACS Catal.,* 2014, **4**, 577.

222. V.K. Klochkov, Y.V. Malyukin, G.V. Grygorova, O.O. Sedyh, N.S. Kavok, V.V. Seminko and V.P. Semynozhenko, *J. Photochem. Photobiol. A,* 2018, **364**, 282.

223. E. Aneggi, D. Wiater, C. de Leitenburg, J. Llorca and A. Trovarelli, *ACS Catal*., 2014, **4**, 172.

224. R. Ma, S. Zhang, T. Wen, P. Gu, L. Li, G. Zhao, F. Niu, Q. Huang, Z. Tang and X. Wang, *Catal. Today,* 2019, **335**, 20.

225. J. Yu, Q. Xiang and M. Zhou, *Appl. Catal. B,* 2009, **90**, 595.

226. M. Ni, M.K.H. Leung, D.Y.C. Leung and K. Sumathy, *Renew. Sustain. Energy Rev*., 2007, **11**, 401.

227. L. Yue and X. M. Zhang, *J. Alloys. Compd.,* 2009, **475**, 702.

228. D. Channei, B. Inceesungvorn, N. Wetchakun, S. Ukritnukun, A. Nattestad, J. Chen and S. Phanichphant, *Sci. Rep.,* 2014, **4**, 5757.

229. C. Mao, Y. Zhao, X. Qiu, J. Zhu and C. Burda, Phys. Chem. Chem. Phys., 2008, **10**, 5633.

230. H. Shi, T. Hussain, R. Ahuja, T.W. Kang and W. Luo, *Sci. Rep*., 2016, **6**, 31345.

231. H. Miao, G. F. Huang, J. H. Liu, B. X. Zhou, A. Pan, W. Q. Huang and G. F. Huang, Appl. Surf. Sci., 2016, **370**, 427.

232. L. Wu, F. Li, Y. Xu, J.W. Zhang, D. Zhang, G. Li and H. Li, *Appl. Catal. B,* 2015, **164**, 217.

233. J. Zhou, L. Xu, J. Sun, D. He and H. Jiao, *Surf. Coat. Tech*., 2015, **271**, 119.

234. L. Wu, S. Fang, L. Ge, C. Han, P. Qiu and Y. Xin, *J. Hazard. Mater*., 2015, **300**, 93.

235. A.D. Liyanage, S.D. Perera, K. Tan, Y. Chabal and K.J. Balkus, *ACS Catal*., 2014, **4**, 577.

236. C. Zhang and J. Lin, *Phys. Chem. Chem. Phys*., 2011, **13**, 3896.

237. N. Wang, Y. Pan, T. Lu, X. Li, S. Wu and J. Wu, *Appl. Surf. Sci*., 2017, **403**, 699.

238. H. Guo, Y. Guo, L. Liu, T. Li, W. Wang and W. Chen, *J. Chen. Green Chem*., 2014, **16**, 2539.

239. X. J. Wen, C. Zhang, C. G. Niu, L. Zhang, G. M. Zeng and X. G. Zhang, *Catal. Commun*., 2017, **90**, 51.

240. W. Lin, S. Zhang, D. Wang, C. Zhang and D. Sun, *Ceram. Int*., 2015, **41**, 8956.

241. J. Tian, Y. Sang, Z. Zhao, W. Zhou, D. Wang, X. Kang, H. Liu, J. Wang, S. Chen, H. Cai and H. Huang, *Small,* 2013, **9**, 3864.

242. A. Hezam, K. Namratha, Q.A. Drmosh, Z.H. Yamani and K. Byrappa, *Ceram. Int*., 2017, **43**, 5292.

243. X. J. Wen, C. G. Niu, H. Guo, L. Zhang, C. Liang and G. M. Zeng, *J. Catal*., 2018, **358**, 211.

244. X. J. Wen, C. G. Niu, D. W. Huang, L. Zhang, C. Liang and G. M. Zeng, *J. Catal.,* 2017, **355**, 73.

245. M. Li, S. Zhang, L. Lv, M. Wang, W. Zhang and B. Pan, *Chem. Eng. J*., 2013, **229**, 118.

246. S. K. Ponnaiah, P. Periakaruppan, B. Vellaichamy and B. Nagulan, *J. Colloid Interf. Sci*., 2018, **512**, 219.

247. T. Huang, J. Wu, Z. Zhao, T. Zeng, J. Zhang, A. Xu, X. Zhou, Y. Qi, J. Ren, R. Zhou and H. Tian, *Mater. Lett.,* 2016, **185**, 503.

248. H. J. H Fenton, *J. Chem. Soc. Trans.,* 1894, **65**, 899.

249. J. J. Pignatello, E. Oliveros and A. Mackay, *Crit. Rev. Environ Sci. Tech*., 2006, **36**, 1.

250. J. Levec and A. Pintar, *Catal Today*, 2007, **124**, 172.

251. J. Yoon, Y. Lee and S. Kim, Wat. *Sci. Technol*., 2001, **4**, 15.

252. S. M. Aramyan and M. Moussavi, *Int. J. Environ. Sci. Nat. Res*., 2017, **2**, 555594.

253. A. Zapata, I. Oller, L. Rizzo, S. Hilgert and M. I. Maldonado, *Appl. Catal. B: Environ.,* 2010, **97**, 292.

254. M. C. Ortega- Lie Bana, E. Sanchez-Lopez, J. Hidalgo-Carrillo, A. Marinas and J. M. Marinas, *Appl. Catal. B: Environ.*, 2012, **127**, 316.

255. J. Herney-Ramirez, M. A. Vicente and L. M. Madeira, *Applied Catalysis B: Environ.,* 2010, **98**, 10.

256. A. S. Amiri, J. R. Bolton and S. R. Cater, *Water Res.,* 1997, **31**, 787.

257. A. Bokare and W. Choi, *J. Hazard. Mater*., 2014, **275**, 121.

258. R. Codd, C. T. Dillon, A. Levina, P. A. Lay, *Coord. Chem. Rev*., 2001, **216**, 537.

259. I. A. Salem and M. S. El-Maazawi, *Chemosphere*, 2000, **41**, 1173.

260. S. Chaliha, K. G. Bhattacharrya, *J. Hazard. Mater.,* 2008, **150**, 728.

261. F. Duarte, F. J. Maldonado –Hodar, A. F. Perez-Cadenas and L. M. Madeira, *Appl. Catal. B Environ.,* 2009, **85**, 139.

262. J. I. Nieto Juarez, K. Pierzchla, A. Sienkiewicz, T. Kohn, *Environ. Sci. Technol*., 2010, **44**, 3351.

263. Y. F. Han, F. Chen, Z. Zhong, K. Ramesh and L. Chen, *Chem. Eng. J*., 2007, **134**, 276.

264. Z. Hu, C. F. Leung, Y. K. Tsang, H. Du and H. Liang, *New. J. Chem*., 2011, **35**, 149.

265. E.G. Heckert, S. Seal and W.T. Self, *Environ. Sci. Technol*., 2008, **42**, 5014.

266. H.I. Hamoud, B. Azambre and G. Finqueneisel, *J. Chem. Technol. Biotechnol*., 2016, **91**, 2462.

267. A. Wang, Z. Zheng, H. Wang, Y. Chen, C. Luo, D. Liang, B. Hu, R. Qiu and K. Yan, *Appl. Catal. B: Environ.*, 2020, **277**, 119171.

268. J. Zhu, G. Zhang, G. Xian, N. Zhang and J. Li, *Front. Chem*., 2019, **7**, 796.

269. I. Anastopoulos, A. Bhatnagar, B. H. Hameed, Y. S. Ok and M. Omirou, *J. Mol. Liq.,* 2017, **240**, 179.

270. A. Bhatnagar and A. K. Minocha, *Indian J. Chem. Technol.,* 2006, **13**, 203.

271. S. De Gisi, G. Lofrano, M. Grassi and M. Notarnicola, *SM&T.,* 2016, **9**, 10.

272. V. K. Gupta and Suhas, *J. Environ. Manage.,* 2009, **90**, 2313.

273. P. J. M. Carrot, M. M. L. R. Carrot and R. A. Robert, *Colloids Surf.,* 1991, **58**, 385.

274. G. Crini, *Bioresour. Technol.,* 2006, **97**, 1061.

275. Wang S and Wu H, *J. Hazard. Mater*., 2006, **136**, 482.

276. A. Demirbas, *J. Hazard. Mater.,* 2008, **157**, 220.

277. G.Z. Kyzas and K.A.Matis, *J. Mol. Liq.,* 2015, **203**, 159.

278. Yan Zhang, Ruixia Shi, Ping Yang, Xueling Song, Yuanna Zhu, Qian Ma, *Ceram. Inter*., **216**.

279. S. Kong, W. Zhang, S. Gao and D. Chen, *J. Exp. Nanosci.* 2019, **14**, 107.

280. N. C. Zheng, Z. Wang, J. Y. Long, L. J. Kong, D. Y. Chen and Z. Q. Liu, *J. Colloid Interface Sci.,* 2018, **525**, 225.

281. Z. Yang, J. Wei, H. Yang, L. Liu, H. Liang and Y. Yang, *Eur. J. Inorg. Chem*., 2010, **2010**, 3354.

282. J. Hu, W. Deng, and D. Chen, *ACS Sustainable Chem. Eng*., 2017, **5**, 3570.

283. J. Wu, J. Wang, Y. Du, H. Li and X. Jia, *J. Nanopart. Res.,* 2016, **18**, 191.

284. Q. Ling, J. Wei, L. Y. Chen, H. J. Zhao, Z. Lei, Z. G. Zhao, R. L. Xie, Q. P. Ke and P. Cui, J. Nanosci. Nanotechnol., 2020, **20**, 3225.

285. K. Skalska, J. S. Miller, S. Ledakowicz and K. Skalska, *Sci. Total Environ.,* 2010, **408**, 3976.

286. M. Piumetti, S. Bensaid, D. Fino and N. Russo, *Catalysis, Structure & Reactivity*, 2015, **1**, 155

287. Z. Zhang, Z. Jiang and W. Shangguan, *Catal. Today*, 2016, **264**, 270.

288. Y. Sun, E. Zwolinska and A. G. Chmielewski, *Crit. Rev. Environ. Sci. Technol.*, 2016, **46**, 119.

289. R. Prasad and P. Singh, *Catal. Rev. Sci. Eng.*, 2012, **54**, 224.

290. D. T. Thompson, Highlights of the International Conference on Catalytic Gold, Cape Town, South Africa, 2001.

291. R. J. H. Voorhoeve, D. W. Johnson, J. P. Jr. Remeika and P. K. Gallagher, Catal. Sci. Technol., 1977, **195**, 827.

292. U. Oran and D. Uner, *Appl. Catal. B,* 2004, **54**, 183.

293. M. Haruta, T. Kobayashi, H. Sano and N. Yamada, *Chem. Lett.,* 1987, **2**, 405.

294. S. Royer and D. Duprez, *Chem. Cat. Chem*., 2011, **3**, 24.

295. E. Aneggi, J. Llorca, M. Boaro and A. Trovarelli, *J. Catal.,* 2005, **234**, 88.

296. S. Royer and D. Duprez, *Chem. Cat. Chem,.* 2011, **3**, 24.

297. M. Piumetti, T. Andana, S. Bensaid, N. Russo, D. Fino and R. Pirone, *Nanoscale Res. Lett.,* 2016, **11**, 165.

298. D. Devaiah, L. H. Reddy, K. Kuntaiah and B. M. Reddy, *Indian J. Chem.*, 2012, **51**, 186.

299. M. Lohrenscheit and C. Hess, *Chem. Cat. Chem*., 2016, **8**, 523.

300. M. A. Centeno, C. Portales, I. Carrizosa and J. A. Odriozola, *Catal. Letters,* 2005, **102**, 289.

301. M. A. Centeno, T. R. Reina, S. Ivanova, O. H. Laguna and J. A. Odriozola, *Catalysts,* 2016, **6**, 158.

302. G. Avgouropoulos, M. Manzoli, F. Boccuzzi, T. Tabakova, J. Papavasiliou, T. Ioannides and V. Idakiev, *J. Catal.* 2008, **256**, 237.

303. N. K. Gamboa-Rosales, J. L. Ayastuy, M. P. González-Marcos and M. A. Gutiérrez-Ortiz, *Int. J. Hydrog. Energy,* 2012, **37**, 7005.

304. T. R. Reina, A. A. Moreno, S. Ivanova, J. A. Odriozola and M. A. Centeno, *Chem. Cat. Chem,.* 2012, **4**, 512.

305. T. R. Reina, S. Ivanova, M. I. Domínguez, M. A. Centeno and J. A. Odriozola, *Appl. Catal. A,* 2012, **420**, 58.

306. G. Avgouropoulos and T. Ioannides, *Appl. Catal. A,* 2003, **244**, 155.

307. O. H. Laguna, F. R. Sarria, M. A. Centeno and Odriozola, *J. Catal*., 2010, **276**, 360.

308. T. R. Reina, S. Ivanova, M. A. Centeno and J. A. Odriozola, *Int. J. hydrog. Energy,* 2015, **40**, 1782.

309. L. Ya. Margolis, *Adv. Catal.,* 1963, **14**, 429.

310. T. Seiyama, *Catal. Rev. Sci. Eng.,* 2006, **34**, 281.

311. Y.F. Yu Yao, *J. Catal*., 1984, **87**, 152.

312. F. Diehl, J. Barbier Jr., D. Duprez, I. Guibard and G. Mabilon, *Appl. Catal. B,* 2010, **95**, 217.

313. W. Liu and M. F. Stephanopoulos, J. Catal., 1995, **153**, 304.

314. C. Li, K. Domen, Maruya and T. Onishi, *J. Am. Chem. Soc*. 1989, **111**, 7683.

315. B. Harrison, A. F. Diwell and C. Hallet, *Platinum Metals Rev*., 1988, **32**, 73.

316. L. J. Kundakovic and M. F. Stephanopoulos, *J. Catal.,* 1998, **179**, 203.

317. Z. G. Yan and S. L. T. Anderson, *J. Catal.,* 1991, **131**, 350.

318. Q. Bkour, K. Zhaoa, L. Scudiero, D. J. Hanc, C. W. Yoon, O. G. Marin-Flores, M. G. Nortond, S. Ha, *Appl. Catal. B,* 2017, **212**, 97.

319. J. B. Zhong, D. Ma, X. Y. He, J. Z. Li and Y. Q. Chen, *Appl. Surf. Sci.* 2010, **256**, 2859.

320. Y. J. Wang, H. Dong, G. M. Lyu, H. Y. Zhang, J. Ke, L. Q. Kang, J. L. Teng, L. D. Sun, R. Si, J. Zhang, Y. J. Liu, Y. W. Zhang, Y. H. Huang and C. H. Yan, *Nanoscale,* 2015, **7**, 13981.

321. P. R. Solanki, A. Kaushik, V. V. Agrawal, B. D. Malhotra, *NPG Asia. Mater.,* 2011, **3**, 17.

322. A.W. Martinez, S.T. Phillips, M.J. Butte and G.M. Whitesides, *Angew. Chem. Int. Ed*., 2007, **46**, 1318.

323. M. Ornatska, E. Sharpe, D. Andreescu and S. Andreescu, *Anal. Chem.,* 2011, **83**, 4273.

324. A. Hayat, D. Andreescu, G. Bulbul and S. Andreescu, *J. Colloid Interface Sci*., 2014, **418**, 240.

325. E. Sharpe, T. Frasco, D. Andreescu and S. Andreescu, *Analys*t, 2013, **138**, 249.

326. X. Jiao, H. J. Song, H. H. Zhao, W. Bai, L. C. Zhang and Y. Lv, *Anal. Methods*, 2012, **4**, 3261.

327. R. Guo, Y. Wang, S. Yu, W. Zhu, F. Zheng, W. Liu, D. Zhang and J. Wang, *RSC Adv*. 2016, **6**, 59939.

328. Q. Liua, Y. Yang, X. Lv, Y. Ding, Y. Zhang, J. Jing and C. Xu, *Sens. Actuators B Chem.,* 2017, **240**, 726.

329. Q. Liu, Y. Ding, Y. Yang, L. Zhang, L. Sun, P. Chen and C. Gao, *Mater. Sci. Eng. C,* 2016, **59**, 445.

330. H. Cheng, S. Lin, F. Muhammad, Y. W. Lin and H. Wei, *ACS Sens.,* 2016, **1**, 1336.

331. J. Peng, J. Guan, H. Yao and X. Jin, *Anal. Biochem.,* 2016, **492**, 63.

332. L. Sun, Y. Ding, Y. Jiang, Q. Liu, *Sens. Actuators B Chem.,* 2017, **239**, 848.

333. N Shehata1, E Samir, S Gaballah, M.R.M. Rizk, B Mokhtar and M Azab, *Sensors and Smart Structures Technologies for Civil, Mechanical, and Aerospace Systems*, Proc. of SPIE, 10168, 2017.

334. N. Shehata, M. Azab, S. Kandas and K. Meehan, *Sensors,* 2015, **15**, 20193.

335. N. Shehata, K. Meehan and D. E. Leber, *J. Nanophotonics,* 2012, **6**, 063529.

336. N. Shehata, K. Meehan and D. Leber, *Nanoengineering: Fabrication, Properties, Optics, and Devices IX,* Proc. of SPIE, 8463, 2012.

337. N. Shehata, E. Samir and I. Kandas, *Appl. Sci.,* 2020, **10**, 1236.

338. E. Samir, N. Shehata and I. Kandas, *J. Nanophotonics,* 2018, **12**, 016007.

339. N. Shehata, E. Samir, S. Gaballah, A. Hamed and A. Elrasheedy, *Sensors,* 2016, **16**, 1371.

340. N. Shehata E. Samir and S. Gaballah, Sens. Actuators B Chem., 2016, **231**, 341.

341. N. Shehata, K. Meehan, I. Ashry, I. Kandas Y. Xu, *Sens. Actuators B* Chem., 2013, **183**, 179.

342. N. Shehata, E. Samir and I. Kandas, *Sensors,* 2018, **18**, 2818.

343. N. Shehata, I. Kandas and E. Samir, *Nanomaterials,* 2020, **10**, 314.

344. K. Negi, M. Kumar, G. Singh, S. Chauhan and M.S. Chauhan, *Ceram. Inter.,* 2018, **44**, 15281.

345. A. Krishnan, T. S. Sreeremya, and S. Ghosh*, J. Colloid Interface Sci*., 2013, **389**, 16.

346. J. Tian, W. Wei, J. Wang, S. Ji, G. Chen and J. Lu, *Anal. Chim. Acta,* 2017, **1000**, 265.

347. B. Liu, Z. Sun, P.J.J. Huang, J. Liu, *J. Am. Chem. Soc*., 2015, **137**, 1290.

348. A. Othman, A. Hayat and S. Andreescu, *ACS Appl. Nano. Mater*., 2018, **1**, 5722.

349. M. Ornatska, E. Sharpe, D. Andreescu and S. Andreescu, Anal. Chem., 2011, **83**, 4273.

350. A. Asati, C. Kaittanis, S. Santra and J. M. Perez, *Anal. Chem.,* 2011, **83**, 2547.

Chapter 2

Materials and Methods

2.1 Introduction

In this work, ceria/doped ceria nanoparticles were synthesized by different facile methods like precipitation, and sol-gel methods. This chapter mainly focuses on the various analytical techniques used to study the material properties and applications of the synthesized ceria nanoparticles. Different analytical techniques were used to study the structural, optical, thermal, and redox properties of the present CeO_2 based materials. X-ray diffraction (XRD), scanning electron microscopy (SEM), transmission electron microscopy (TEM), Fourier Transform infrared (FTIR) spectroscopy, X-ray photoelectron spectroscopy (XPS), Raman spectroscopy (RAMAN), etc. are used for the morphological and structural characterization of the developed materials. Optical properties are investigated by diffuse reflectance spectroscopy (DRS) and photoluminescence (PL) spectroscopy. Textural characteristics and surface area of the samples were analyzed by Brunauer–Emmett–Teller (BET) methods. Redox properties of the samples were studied by Temperature Programmed Reduction (TPR), and thermal properties were investigated using Thermogravimetric (TG) analysis. UV-vis and PL spectroscopy were used to investigate the sensing applications. UV visible spectroscopy is also used to monitor the photodegradation efficiency of CeO_2 nanoparticles. The present chapter lists the materials used in the preparation, characterization, and applications of CeO_2 based materials and also discusses the principle of various analytical techniques used in this study.

2.2 Materials Used

The details of the chemicals/materials used in the present investigation are given in Table 2.0.

Table 2.0 Materials used

Sl No.	Material	Manufacturer/Supplier
1	Cerium nitrate hexahydrate	Star Earth Minerals, Mumbai
2	Ammonia	NICE Chemicals Pvt. Ltd.
3	Cobalt nitrate	NICE Chemicals Pvt. Ltd.
4	Garlic	Local market
5	Fenugreek	Local market
6	Norfloxacin	Sigma Aldrich Pvt. Ltd. India
7	Congo red	NICE Chemicals Pvt. Ltd.
8	Hydrogen peroxide	NICE Chemicals Pvt. Ltd.
9	3,3′,5,5′-tetramethylbenzidine (TMB)	Sigma Aldrich Pvt. Ltd. India
10	Picric acid	NICE Chemicals Pvt. Ltd.
11	Phenol	NICE Chemicals Pvt. Ltd.
12	4-Chlorophenol	NICE Chemicals Pvt. Ltd.
13	Nitrobenzene	NICE Chemicals Pvt. Ltd.
14	4-Nitrophenol	NICE Chemicals Pvt. Ltd.

2.3 Material Designation

In the present work, four different sets of ceria systems are prepared and used for various applications such as photocatalytic degradation of dyes and antibiotics, adsorption of dye, photo Fenton

degradation, two-way catalysis for gaseous pollutants' treatment, H2O2 sensing, and fluorescent sensing of picric acid. One set of ceria catalysts were synthesized by precipitation method using varying concentrations of ammonia. Cobalt-doped ceria systems with different cobalt contents were prepared by wet impregnation of one of the above ceria system. The other two sets of ceria systems were prepared through sol-gel methods using garlic and fenugreek extracts. The designations of various synthesized ceria-based systems included in this thesis are given in table 2.2.

Sl. No.	Designation	Preparation method
1	CeO_2-1	Prepared by adding 25% ammonia solution to cerium nitrate solution followed by filteration, washing, drying and calcination
2	CeO_2-2	Prepared by adding 2 M ammonia solution to cerium nitrate solutionfollowed by filteration, washing, drying and calcination
3	CeO_2-3	Prepared by the addition of cerium nitrate solution to 2 M ammonia solutionfollowed by filteration, washing, drying and calcination.

4	CeO_2 g-10	Ceria sample prepared with garlic extract at a garlic concentration of 10 g/100 ml
5	CeO_2 g-20	Ceria sample prepared with garlic extract at a garlic concentration of 20 g/100 ml
6	CeO_2 g-30	Ceria sample prepared with garlic extract at a garlic concentration of 30 g/100 ml
7	CeO_2 g-40	Ceria sample prepared with garlic extract at a garlic concentration of 40 g/100 ml
8	CeO_2 FG-5	Ceria sample prepared with 5 ml fenugreek extract
9	CeO_2 FG-0	Without the addition of fenugreek in preparation
10	CeO_2 FG-10	Ceria sample prepared with 10 ml fenugreek extract
11	CeO_2 FG-30	Ceria sample prepared with 30 ml fenugreek extract
12	CeO_2	CeO_2 prepared by ammonia precipitation

13	1% Co/CeO_2	CeO_2 doped with 1 wt% cobalt by wet impregnation
14	2% Co/CeO_2	CeO_2 doped with 2 wt% cobalt by wet impregnation
15	3% Co/CeO_2	CeO_2 doped with 3 wt% cobalt by wet impregnation

2.4 Characterization Techniques

2.4.1 X-ray Diffraction (XRD)

X-ray diffraction is a non-destructive characterization technique commonly used for the analysis of crystalline substances. XRD gives information regarding the crystal structure, phase identification, crystal orientation, and other parameters such as average crystal size, crystal strain, and defects. X-ray diffractometer contains three basic components, an x-ray tube, a sample holder, and a detector, and its working is based on the constructive interferences of monochromatic X-rays produced by a cathode ray tube. Copper is the most common material used to produce X-rays with CuKα radiation of wavelength 1.5418Å. When these rays are directed towards the sample, the interaction between the rays and materials takes place to produce a diffracted ray if the condition satisfies the Braggs law,

$$n\lambda = 2d\sin\theta; \qquad \text{(eqn 2.1)}$$

where λ is the wavelength of electromagnetic radiation, θ is the diffraction angle and d is the lattice spacing in a crystalline sample. The diffracted X-rays are detected by a detector and process the signal to convert into the count rate. The obtained X-ray diffraction patterns are unique as the fingerprints of crystals and thus are the characteristic of the materials.

Each diffraction peak is attributed to the scattering from a specific set of parallel planes of atoms. Generally, the X-ray diffractogram is recorded at room temperature in open quartz sample holders in a 2θ range from 10° to 100° in the steps of 0.01°. Crystallites smaller than ~120 nm cause broadening of diffraction peaks, and thus the peak broadening can be used to estimate the average crystallite size of the crystals [1-3]. A Schematic diagram of X-ray diffraction is given in figure 2.1.

In the present study, the crystalline structure, and crystal phases of CeO_2 were identified from X-ray diffraction patterns by comparing them with the JCPDS database. X-ray diffraction measurements of the prepared samples were recorded by an advanced X-ray powder diffractometer (Bruker AXS D8) using CuKα radiation of 0.15406 nm wavelength. All the samples were analyzed in a 2θ range of 10° – 80° at room temperature.

The broadening of XRD peaks is controlled by the size and lattice strain, which is appropriately expressed by Williamson–Hall (W–H) equation, as given below,

$$\beta \cos\theta = \frac{K\lambda}{D} + 4\varepsilon \sin\theta \qquad \text{(eqn 2.2)}$$

where β is the full-width half maximum of the XRD peak, λ is the incident x-ray wavelength, θ is the diffraction angle, D is the crystallite size, and ε is the lattice strain [4].

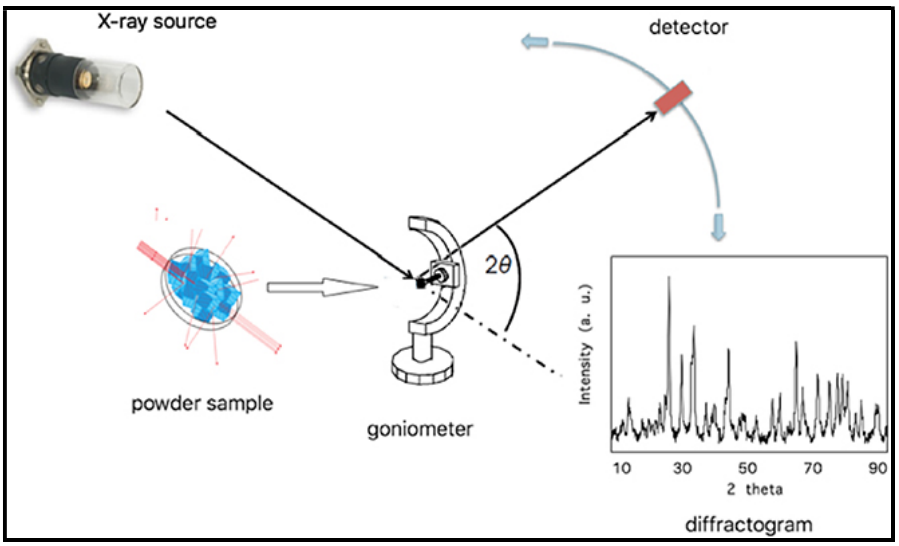

Fig. 2.1 Schematic diagram of X-ray diffraction [4].

Thus plotting 4sinθ along X-axis and β cosθ along Y-axis, a linear fit can be obtained, named Williamson-Hall (W-H) plot. The slope of the linear fit gives the lattice strain in nanocrystals. Lattice strain in the synthesized ceria crystals in this work has been calculated by using the W-H equation.

2.4.2 Scanning Electron Microscopy (SEM)

The scanning electron microscope (SEM) is one of the most resourceful advanced instruments used for analyzing the surface morphology of materials. Using SEM, it is possible to achieve a

detailed visual image of a particle with high-quality and spatial resolution up to 1 nm. Several qualitative information of materials such as morphology, topography, composition, and crystallographic ideas are revealed from SEM. In this technique, a focused beam of electrons is allowed to fall on a sample that provides energy to the electrons of the specimen leading to the emission of a variety of signals due to the Coulombic field interaction between the incoming electrons and the specimen electrons as well as the nucleus. The outcoming signals such as secondary electrons (SEs), backscattered electrons (BSEs), photons (X-rays used for elemental analysis), and visible light (cathodoluminescence – CL) are detected by a secondary electron detector, and different information of the sample could be obtained according to the detected signal. The sample morphology and topography are observed from secondary electrons. Since the electron beams are very narrow, SEM micrographs have a large depth of field, which gives a three-dimensional appearance and is very useful for the surface structure of the specimens. For SEM imaging, the sample surface should be electrically conductive, and so the sample is mounted on a double-sided carbon tape or aluminium or copper stub [5-8]. A Schematic diagram of the scanning electron microscope is shown in figure 2.2.

In this study, the surface morphology of the selected ceria-based systems was analyzed by Jeol JSM-6390LV/OXFORD XMX N scanning electron microscopy at an accelerating voltage of 0.5 to 30

kV. The microstructure of the samples was revealed from the SEM images.

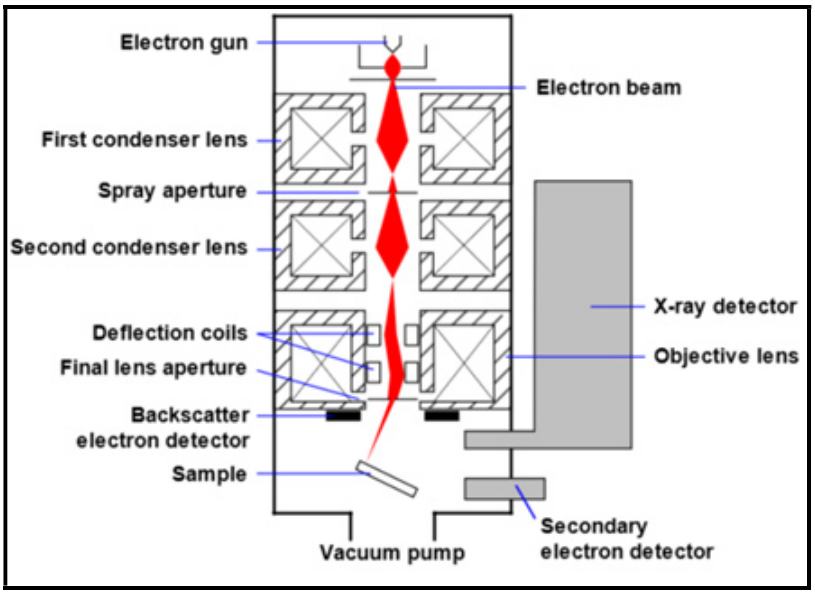

Fig. 2.2 Schematic diagram of a scanning electron microscope [8].

2.4.3 Transmission Electron Microscopy (TEM)

Transmission Electron Microscopy (TEM) is one of the common characterization techniques for nanomaterials in which a high-energy beam of electrons is transmitted through a thin specimen to provide chemical information, and images with a spatial resolution of atomic dimension level is obtained. The basic principles are the same as that of a light microscope and the difference is that the electron beam is used here instead of light, and electromagnetic lenses are provided instead of glass lenses. The interaction of electron beam and sample results in elastic and inelastic scattered electrons and the

corresponding images formed have significantly higher resolution than the light microscopes, due to the smaller de Broglie wavelength of electrons. The main components of TEM are a vacuum system in which the electrons travel, a source of electrons for the generation of the electron stream, and a series of electromagnetic lenses and electrostatic plates. For a conventional TEM, the specimens should be less than 100 nanometers thick.

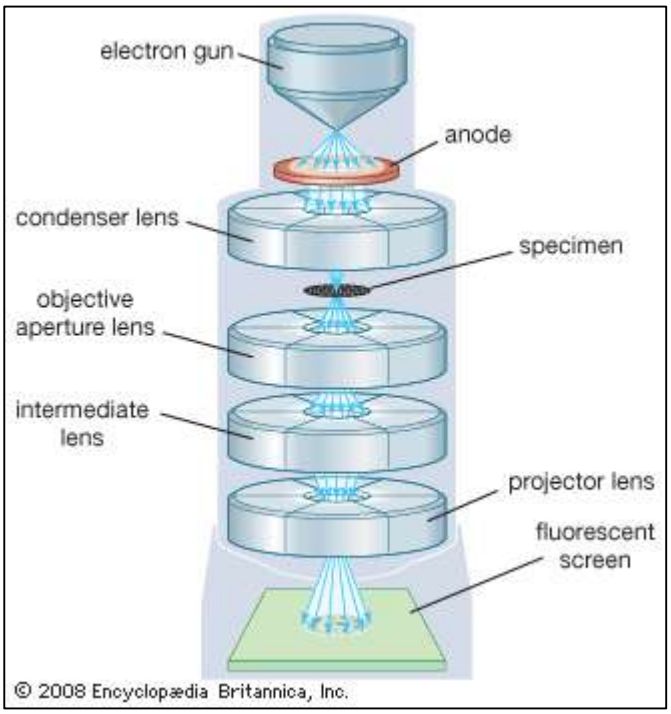

Fig. 2.3 Schematic diagram of transmission electron microscope [12].

TEM is primarily used for the determination of microstructure, chemical composition, morphology, size of the nanoparticles, and degree of aggregation. Using high-resolution transmission electron microscopy (HRTEM), imaging of the atomic structure of the sample

can be obtained that is used to study the properties of samples including semiconductors, metals, nanoparticles, graphene, carbon nanotubes, etc.

Elemental analysis and examination of chemical bonding in nano-objects can be obtained by incorporating spectroscopic methods (EDS and EELS), and crystallographic structure can be studied from selected area diffraction (SAED) patterns [9-12]. A Schematic diagram of the transmission electron microscope is given in figure 2.3.

The TEM images of the representative ceria samples synthesized in the present work were done by using Jeol/JEM 2100 high-resolution transmission electron microscope at an operating voltage of 200 kV. The SAED patterns of the systems were also analyzed by the same instrument. Information on the grain size, particle size, and size distribution of the particles is obtained from the TEM images.

2.4.4 Ultraviolet-Visible Spectroscopy

UV-vis spectroscopy is a technique used for the characterization and quantitative determination of substances based on their absorption of light. When a sample is illuminated with electromagnetic rays of various wavelengths in the visible, UV, or near IR region, depending upon the nature of the substance, light is partially absorbed. The transmitted light is recorded by a detector as a function of wavelength, giving the spectrum of the sample. A UV-vis spectrophotometer measures the intensity of light passing through a

sample solution in a cuvette and compares it to the intensity of the light before it passes through the sample. A UV-vis spectrophotometer consists of components such as a sample holder, a dispersive device to separate the different wavelengths of the light (e.g. a monochromator) and a suitable detector. Due to the absorption of some part of light by the sample, the fraction of light collected by the detector which is called the transmitted intensity will be less than the incident intensity (I0). The ratio I/I_0 is called transmittance (T), and the negative logarithm of the transmittance (-logT) is known as absorbance (A) or optical density. In general, a UV-vis spectrum is graphically represented as absorbance as a function of wavelength; the height of the absorption peaks is directly proportional to the concentration of the species. It is possible to determine the sample concentration from the measured absorbance value by using the Beer-Lambert law,

$$A = \varepsilon cd \qquad \text{(eqn 2.3)}$$

where c is the sample concentration, d is the path length of the cuvette, and ε is the extinction coefficient, describing how much the sample is absorbing at a given wavelength. The position and profile of the absorption peak can be used to identify the components present in the sample solution, and the sample concentration can be calculated from the absorbance value of the peak. Also, the peak position reveals information about the molecular structure of the sample and the microscopic environment of the sample molecules such as the presence of impurities or other solvents in the sample solution. It is commonly applied to organic molecules, inorganic ions or complexes in solutions,

and also to solid materials such as films or glass [13-16]. A schematic representation of the UV-vis spectrophotometer is shown in figure 2.4.

The solutions in the photocatalytic degradation of norfloxacin and photo Fenton degradation of Congo red were analyzed by using PerkinElmer UV WinLab Lambda 850 spectrophotometer.

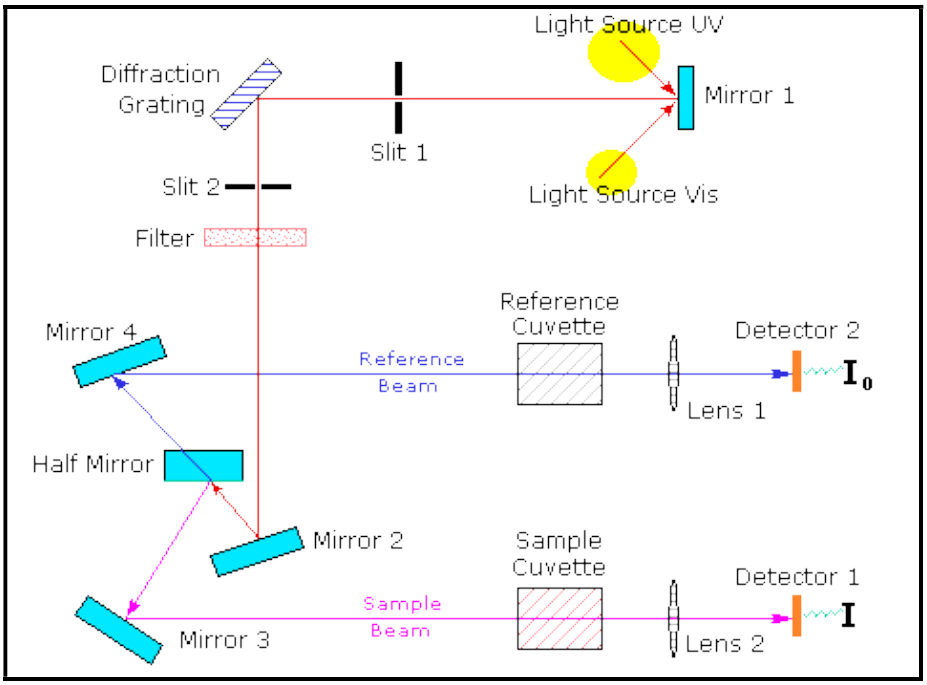

Fig. 2.4 Schematic representation of UV-visspectrophotometer [16].

The UV spectra of norfloxacin were measured in a wavelength range of 200 nm to 400 nm with an absorption maximum of wavelength 271 nm and that of Congo red solution in a wavelength range of 400 nm to 800 nm with an absorption maximum at 499 nm.

Optical sensing of H_2O_2 was monitored using PerkinElmer UV WinLab Lambda 850 spectrophotometer.

2.4.5 UV-visDiffuse Reflectance Spectroscopy (DRS)

Diffuse reflectance spectroscopy (DRS), also known as elastic scattering spectroscopy is commonly used in the optical characterization of materials in which the diffuse reflection of radiation is measured. When a sample is illuminated with a light source with a wavelength range from UV to near-infrared (NIR), some of them undergo reflection from the surface where the angle of incidence is equal to the angle of reflection called specular reflection. Some of them undergo diffuse reflection, which arises from the various interactions, reflection, refraction, diffraction, and absorption by particles oriented in all directions within the reaction volume of an element. The amount of diffuse light is measured and is used to characterize the optical properties of the samples. The intensity of the reflected light from the reaction layer of the sample and that of an ideal non-absorbing reference sample is measured as a function of the wavelength λ, and is expressed as percent reflectance (%R);

$$\% R = (I_s/I_r) R_r \qquad \text{(eqn 2.4.)}$$

where$I_s$is the reflected light from the sample, I_r is the reflected light from the standard reflector, and R_r is the percent reflectivity of the standard. Barium sulfate having an absolute reflectance of 0.973 to 0.988 is considered a suitable standard in DRS. Since these measurements have no linear relation with concentration, Kubelka–

Munk equation is used to linearize the relationship between %R and analyte concentration, which is given by,

$$C\alpha(K/S) = (1-R)^2/2R \qquad \text{(eqn 2.5.)}$$

where C is the concentration, K is the absorption coefficient, and S is the scattering coefficient [17-20]. A Schematic diagram of the diffuse reflectance spectrometer is presented in figure 2.5.

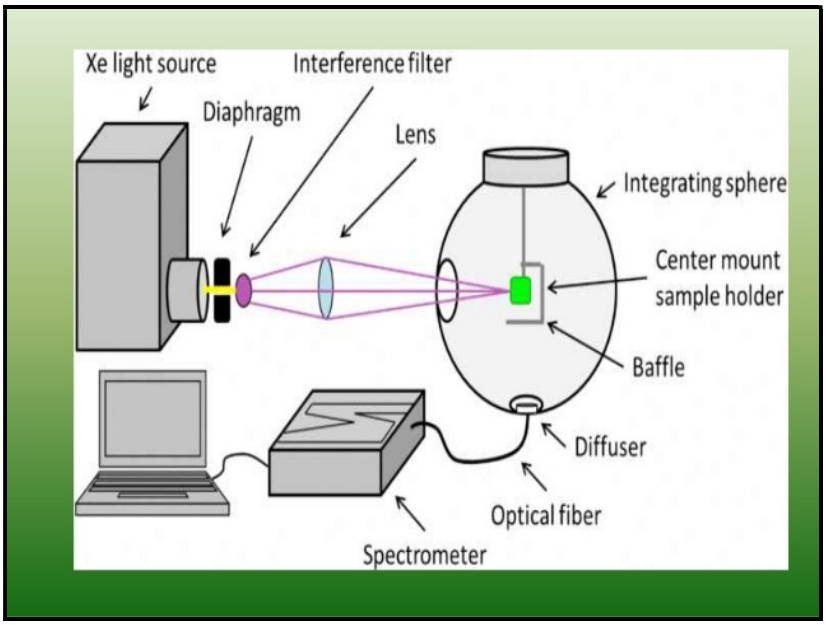

Fig. 2.5 Schematic diagram of diffuse reflectance spectrometer [20].

The optical properties of the CeO_2 samples prepared were analyzed by diffuse reflectance (DR) UV-vis spectra in the range of 200-800 nm by a Varian Cary 5000 model UV-vis NIR spectrophotometer. The reflectance data of the samples were used to

calculate the bandgap energy by applying the KubelkaMunk function to correlate with its photocatalytic performances.

2.4.6 Fourier Transform Infrared (FTIR) Spectroscopy

Infrared absorption spectroscopy is the study of the interaction of infrared radiation with the matter as a function of photon frequency and is used as a non-destructive technique for studying the chemical bonding in materials. Fourier Transform Infrared (FTIR) spectrometry was developed to overcome the limitations of the dispersive method by a mathematical technique called the Fourier transformation. The main drawback is the slow scanning rate. In FTIR, a very simple optical device called an interferometer produces a unique type of signal, which has all of the infrared frequencies "encoded" into it. The signal can be measured within one second or so, thus, reducing the analysis time to a few seconds rather than several minutes. The decoding of the individual frequencies was accomplished by a well-known mathematical technique called Fourier transformation performed by the computer, and a frequency spectrum is obtained for the desired spectral information for analysis. FTIR provides specific information about the vibration of the chemical bonds and molecular structures of both organic and inorganic materials. Since each molecule is a unique combination of atoms, an infrared (IR) spectrum can be considered as the fingerprint of molecules with the absorption peaks corresponding to the frequencies of vibrations of different bonds in the molecules. Most IR spectra are usually studied in the region 4000cm^{-1} to 400 cm^{-1} in which fundamental vibrations and rotations of the molecules are

observed. The region of 4000cm^{-1} – 1450 cm^{-1} is known as the functional group region in which the frequencies of functional groups present in the molecule are observed. The region below 1450 cm^{-1} is called a fingerprint region since it contains complicated absorption peaks corresponding to all bending vibrations of bonds. Besides, since the size of the peaks in the spectrum is a direct indication of the amount of material present, the FTIR spectrum can also be used for the quantitative estimation of materials in a mixture [21-24].

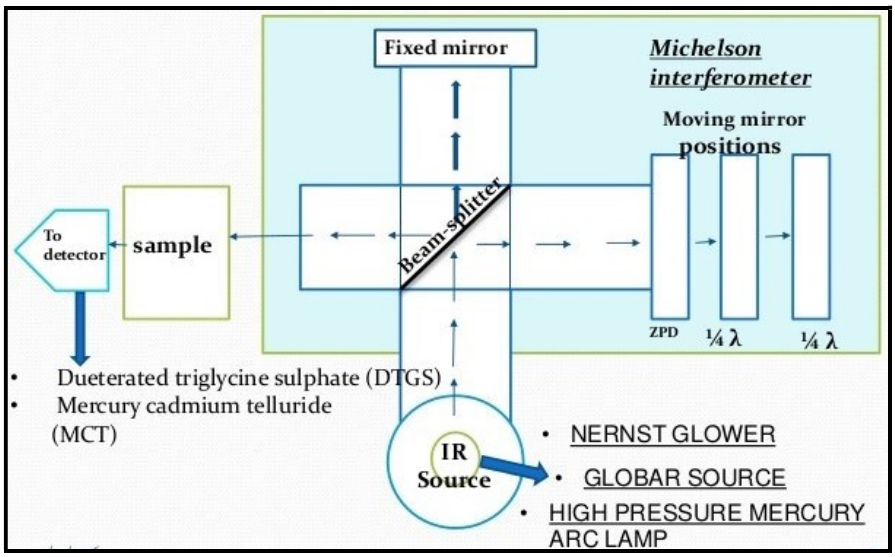

Fig. 2.6 Schematic representation of FTIR spectrometer [24].

A Schematic diagram of the FTIR spectrometer is shown in figure 2.6.

FTIR spectra of the samples used in Congo red degradation and picric acid-sensing were recorded with a Perkin Elmer spectrum two L1600300 FTIR spectrometer, whereas the spectra of catalysts used in

norfloxacin degradation and gaseous pollutant degradation (ceria and cobalt doped samples) were taken using Thermo Nicolet Avatar 370 FTIR spectrometer. All the samples were scanned in a range of 4000 cm^{-1} to 400 cm^{-1}.

2.4.7 X-ray Photoelectron Spectroscopy (XPS)

X-ray photoelectron spectroscopy (XPS) formerly known as ESCA (Electron Spectroscopy for Chemical Analysis), was developed in the mid-l960s by Kai Siegbahn and his research group at theUniversity of Uppsala, Sweden. XPS involves a single electron process based on the photoelectron effect described by Albert Einstein and gives information about the oxidation state and atomic composition of the analyzed compounds. The surface of the specimen is irradiated by X-ray with the energy of hν, and monoenergetic photons knock out the electrons from the surface atoms. Photons with higher energy penetrate deeper into the sample, and electrons are ejected from the inner atomic energy levels, which are bound to the nucleus with a binding energy E_b. The kinetic energy of the ejected electrons E_k, is determined by the following equation;

$$E_k = hv - E_b - \phi \qquad \text{(eqn 2.6.)}$$

where$\phi$is the work function, which is the minimum energy needed to remove an electron from a solid. The energies of the ejected electrons are detected, and a spectrum is obtained as a plot of the number of detected electrons per energy interval versus the kinetic energy. The chemical shift (variations in the elemental binding energy) in XPS,

which arises from differences in the chemical potential and the polarizability of compounds, can be used to identify the oxidation state and chemical composition of elements of the sample. Also, quantitative data can be obtained from the peak height or peak area [25-28]. Schematic representation of the X-ray Photoelectron spectrometer is given in figure 2.7.

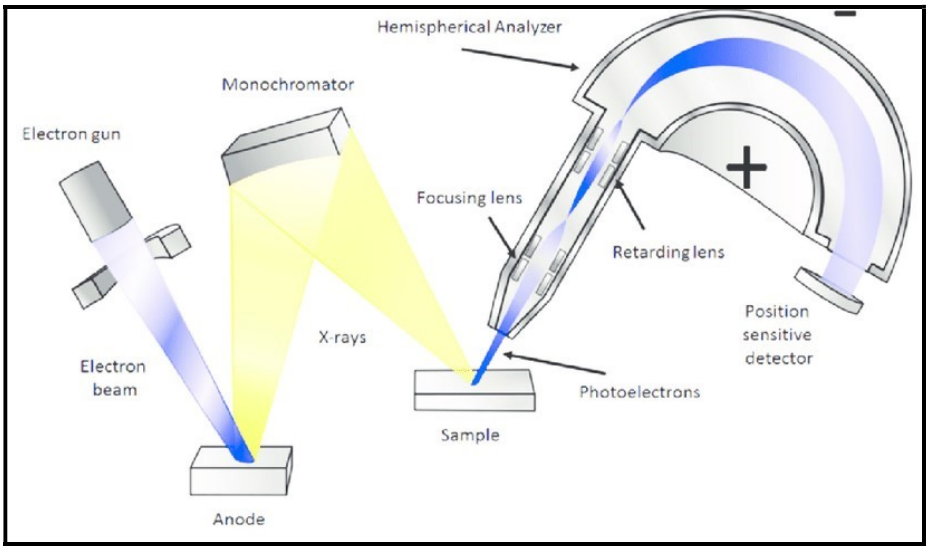

Fig. 2.7 Schematic representation of X-ray Photoelectron spectrometer [28].

X-ray photoelectron spectroscopy (XPS) analysis of the samples synthesized in this study was performed with an auger electron spectroscopy model PHI 5000 Versa Probe II, FEI. The oxidation state of the elements in the samples as well as their chemical compositions was analyzed from the spectra.

2.4.8 Photoluminescence (PL) Spectroscopy and Fluorescence Spectrophotometry

In Photoluminescence (PL) spectroscopy, the energy levels in a semiconductor are investigated using the phenomenon called photoluminescence, which is the emission of light when a substance is subjected to optical excitation. When a photon has energy greater than the bandgap energy of the semiconductor, the electrons are excited from the valence band up to the conduction band. These electrons eventually come back to the valence band, and it loses the excess energy in the form of luminescence emitted from the material, and the process is known as photoluminescence. The emitted luminescence is collected by a lens and passed through an optical spectrometer onto a photon detector. The obtained PL spectrum can be used to provide qualitative and quantitative information about chemical compositions, structural impurities, kinetic processes, energy transfer sensitivity, etc. Each excited state has a characteristic lifetime, and depending on the characteristic lifetime of emission, fast PL with a lifetime of sub-micro seconds is obtained, which is called fluorescence, whereas slower ones are referred to as phosphorescence. Fluorescence spectroscopy (also known as fluorimetry or spectrofluorometry) measures the fluorescence from a sample. Fluorescence spectrophotometry has been designed to measure fluorescence intensity, spectrum, lifetime, and polarization. Fluorescence intensity determines the presence of fluorophores and their concentrations. A typical fluorometer includes a light source, a specimen chamber with integrated optical components,

and high sensitivity detectors. Various light sources such as lasers, LEDlamps, xenon arcs, and mercury-vapor lamps may be used as excitation sources [29-32]. A Schematic diagram of the photoluminescence spectrometer is shown in figure 2.8.

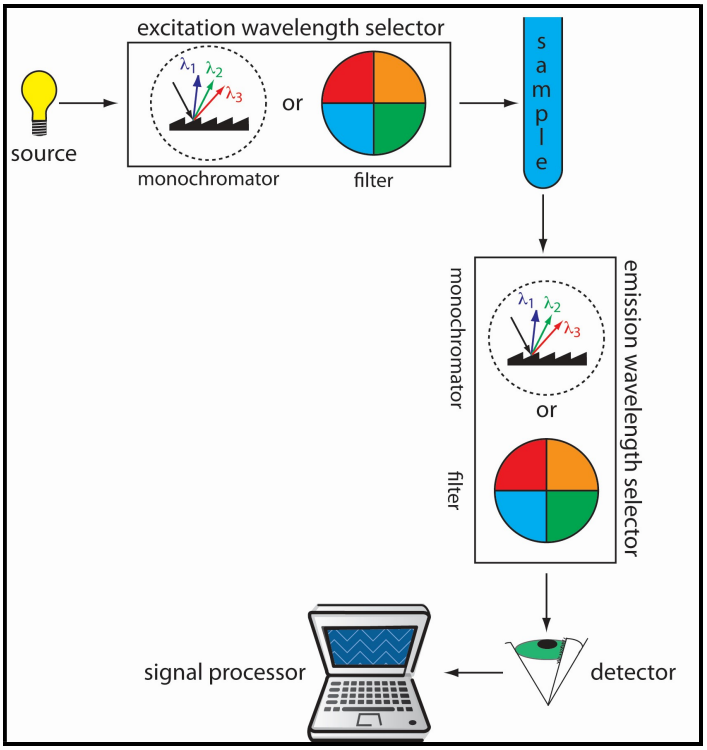

Fig. 2.8 Schematic diagram of photoluminescence spectrometer [32].

The fluorescence study of this work has been done by using PERKIN-ELMER FL 6500 spectrometer with a Xe lamp as the excitation source. All the experiments were carried out using aqueous dispersions of nanoparticles in the air as an emission filter and an emission slit of 5 nm.

2.4.9 Raman Spectroscopy

Raman spectroscopy is a technique used to determine the vibrational modes of a molecule and thus to obtain a structural fingerprint of the molecule. It is based on the inelastic scattering of light called Raman scattering. When a laser beam or a monochromatic light in the range of visible, near-infrared, or near-ultraviolet is allowed to interact with molecular vibrations or other excitations in the system, the scattered laser will be shifted in energy up or down. This energy shift is a characteristic of the vibrational modes of the molecules in the system and yields complementary information to IR spectroscopy. Modern spectrometers use a laser beam as the light source. Typically, when a sample is illuminated with a laser beam, the elastically scattered radiation is filtered out by a notch filter, and the remaining light is dispersed onto a detector. Raman scattered light is typically collected and either dispersed by a spectrograph or with an interferometer for detection by Fourier Transform (FT) methods. In solid-state physics, Raman spectroscopy is used to characterize materials, and to find the crystallographic orientation of a sample. If we know the point group of a crystal structure, the orientation of an anisotropic crystal can also be found from the polarization of Raman-scattered light to the crystal, and the polarization of the laser light [33-36]. A Schematic diagram of the Raman spectrometer is given in figure 2.9.

In the present study, the RAMAN scattering measurements of the synthesized samples were carried out using Confocal Raman

Microscope with AFM imaging (WiTec alpha 300, Germany). The cubic fluorite structures of ceria nanoparticles synthesized are confirmed from the Raman active mode of vibrational bands of ceria in the Raman spectrum, which supported the crystal phase identification from XRD analysis.

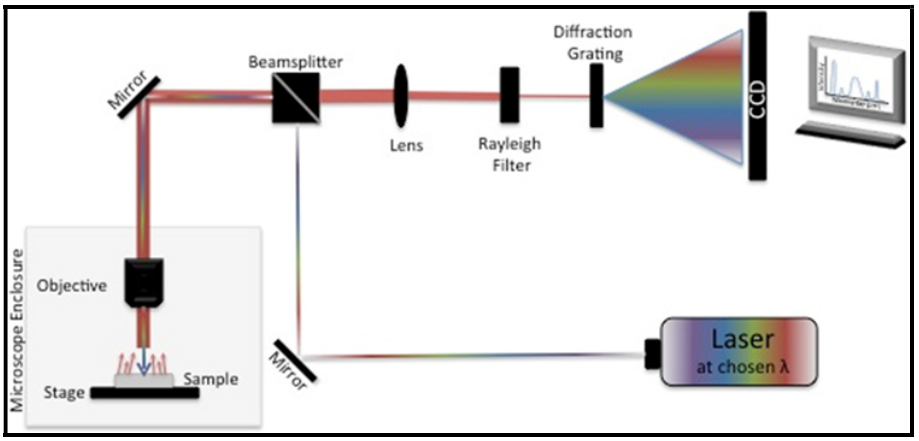

Fig. 2.9 Schematic diagram of Raman spectrometer [36].

2.4.10 Brunauer–Emmett–Teller (BET) Surface Area – Pore Volume Measurements

Brunauer–Emmett–Teller (BET) method is used in the area of nanotechnology for the determination of surface area, porosity, and thus the nature of materials. The specific surface area determines the contact area of the nanomaterial with other molecules or surfaces. BET method is the most standard method for surface area determination developed by Brunauer, Emmett, and Teller in 1938, and it is based on the multilayer physical adsorption of a non-corrosive gas such as argon, nitrogen, carbon dioxide, etc. on the solid material. Mainly

nitrogen is used because of its high purity and its strong physisorption to most solids. Before the analysis, the sample must be degassed to remove any contaminants. The sample is then is cooled down to 77K followed by nitrogen injection at various pressures. Surface area is determined from the amount of gas adsorbed corresponding to a monomolecular layer on the surface of the material by applying the BET equation,

$$\frac{P}{V(P-P_0)} = \frac{P}{P_0}\left[\frac{C-1}{VmC}\right] + \frac{1}{VmC} \qquad \text{(eqn 2.7)}$$

where P/P_0 is the relative pressure, P_0 is the gas saturation pressure, V is the volume of gas admitted into the sample chamber, C is the so-called BET constant, P is the partial saturation pressure of the adsorptive gas in equilibrium with the surface, and V_m is the volume of gas needed to create a monolayer on the sample.Barret-Joyner Halenda (BJH) analysis can also be utilized to determine pore area, specific pore volumes, and pore size distribution through adsorption and desorption techniques. The analysis data are obtained in the form of a BET isotherm, which plots the amount of gas adsorbed as a function of the relative pressure. Characteristic isotherm shapes are defined by the International Union of Pure and Applied Chemistry (IUPAC) and used to describe the classes of materials [37-40]. A Schematic diagram of the Brunauer–Emmett–Teller (BET) Surface Area analyzer is given in figure 2.10.

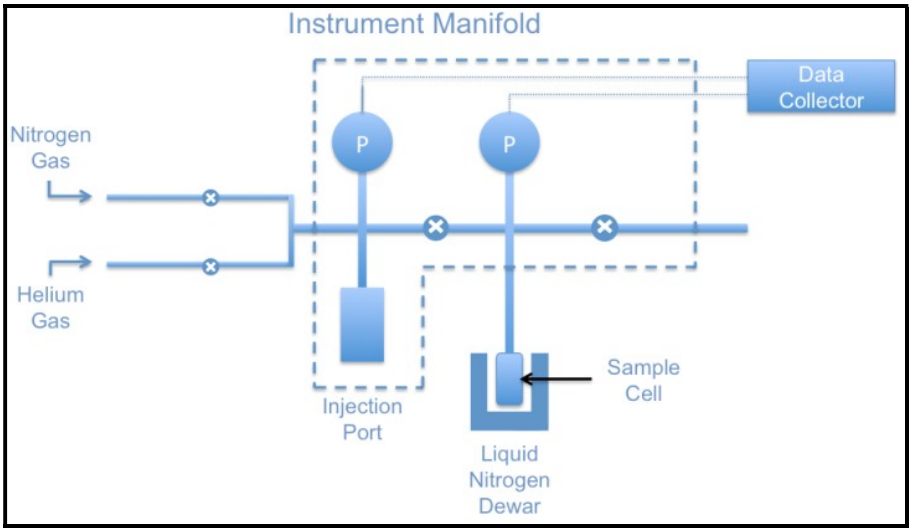

Fig. 2.10 Schematic diagram of Brunauer–Emmett–Teller (BET) Surface Area analyzer [40].

The specific surface area of the selected samples in the present work has been analyzed by the BET method and the pore size distribution was obtained by the BJH model from the nitrogen adsorption-desorption isotherm of the samples measured using Micromeritics ASAP 2010 analyzer at 77K. The surface areas of the ceria samples were correlated with their activity/response in different studies.

2.4.11 Temperature Programmed Reduction (TPR)

Temperature Programmed Reduction (TPR) is a widely used characterization technique to study the surface chemistry of metal oxides, mixed metal oxides, and metal oxides dispersed on a support. It provides quantitative information regarding the reducibility of the surface. It is most commonly used in the field of heterogeneous

catalysis to find the most competent reduction conditions. In this technique, a programmed temperature rise is applied on a solid oxide while passing a reducing gas (usually hydrogen diluted with an inert gas like N_2 or Ar) over it. This linear heating allows the reduction rate to be correlated with the temperature. A thermal conductivity detector (TCD) or mass spectrometer records the concentration of effluent gas, and the corresponding TPR profile is obtained. The peak maximum corresponds to the temperature where the rate of reduction is maximum, and the area under the peak in concentration vs. time (or temperature) gives the total gas consumed by the solid material for reduction. Qualitative information regarding the oxidation state of the reducible species, and the quantity of the available reducible sites can also be obtained from TPR profiles [41-44]. A Schematic diagram of Temperature programmed reduction measurement is shown in figure 2.11.

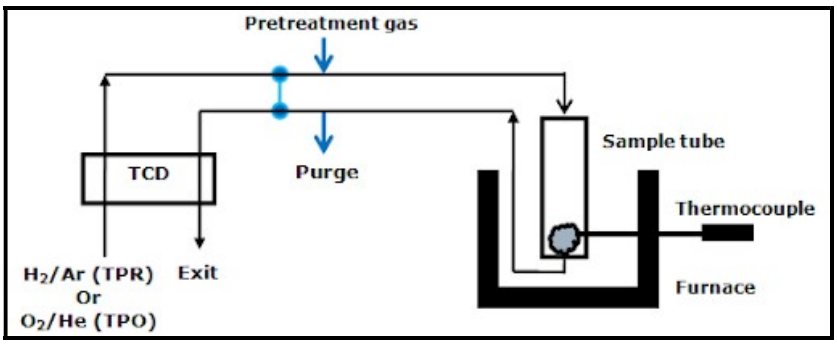

Fig. 2.11 Schematic diagram of temperature programmed reduction measurement [44].

Temperature programmed reduction was performed in a reaction device Micromeritics Instrument ChemiSoftTPx V1.02,

equipped with a TCD detector using 5% H_2 in Ar at a flow rate of 25 cm^3/min. TPR was recorded from room temperature to 900 °C at a heating rate of 10 °C/min. The reducibility of ceria and cobalt doped ceria catalysts used in the CO and HC oxidation study was analyzed using the H_2-TPR profile of the samples.

2.4.12 Thermogravimetric (TG) Analysis

Thermogravimetry (TG) or Differential Thermal Analysis (DTA) is a characterization method used to obtain information regarding the thermal stability, purity, and composition of a material. In this technique, the sample specimen is subjected to a specific temperature program in a controlled atmosphere, and the mass of the substance is monitored as a function of temperature or time. TG consists of a sample pan residing in a furnace that heats the sample and is supported by a precision balance. An inert or reactive gas flows over the sample and exits through the exhaust. The mass of the sample is monitored continuously while heating and the mass loss during the temperature change can be obtained in the form of a thermogram. The apparatus used for obtaining a thermogram curve (TG curve) is known as thermobalance and it consists of a continuously heated furnace, temperature programmer, and a recorder. The result of thermal analysis or thermogram is influenced by several factors such as the amount and particle size of the material, the speed of the recorder noting the change in weight, the shape of the sample container, the rate of heating the sample, and the ambient atmosphere during analysis.

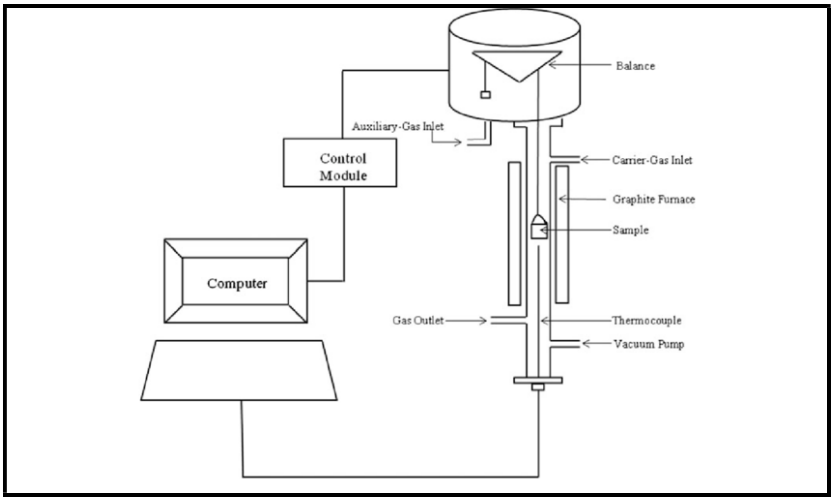

Fig. 2.12 Schematic diagram of Thermogravimetry (TG) or Differential Thermal Analysis [48].

A thermogram gives detailed information regarding the thermal stability of the sample at different temperatures and pressures of the environmental gases, the order of the degradation reaction, etc [45-48]. A Schematic diagram of Thermogravimetry (TG) analysis is shown in figure 2.12.Thermal analysis of the best ceria sample used in the Congo red degradation study was performed on a Perkin Elmer Diamond TG/DTA instrument in a temperature range from RT to 600 °C in the N_2 atmosphere.

References

1. Y. Waseda, M. Eiichiro, and K. Shinoda, *X-Ray Diffraction Crystallography*, Springer-Verlag Berlin Heidelberg, 2011.
2. K. U. Daniel and T. Z. Forbes, *Analytical Geomicrobiology: A Handbook of Instrumental Techniques*, Cambridge University Press, 2019.
3. G. Rene, *X-Ray Diffraction by Polycrystalline Materials*, ISTE Ltd, 2007.
4. N. K. Chandar and R. Jayavel, *Physica E,* 2014, **58**, 48.
5. L. Reimer, *ScanningScanning Electron Microscopy Physics of Image Formation and Microanalysis*, Springer-Verlag Berlin Heidelberg New York, 1998.
6. W. Zhou, R.Apkarian, Z. L. Wang and D. Joy, *Fundamentals of Scanning Electron Microscopy (SEM)*, Springer, New York, NY, 2006.
7. O. C. Wells, *Scanning Electron Microscopy*, McGraw-Hill, New York, 1974.
8. https://www.nanoscience.com/techniques/scanning-electron-microscopy/
9. D. B. Williams, C. B. Carter, *Transmission Electron Microscopy: A Textbook for Materials Science*, Springer Science + Business Media, LLC, 233 Spring Street, New York, 2009.

10. P. Buseck, J. Cowley and L.Eyring, *High-Resolution Transmission Electron Microscopy: and Associated Techniques,* Oxford University Press, Newyork, 1989.
11. J. Kuo, *Electron Microscopy: Methods and Protocols*, Humana Press Inc., Totowa, New Jersey, 2007.
12. https://www.britannica.com/technology/transmission-electron-microscope
13. H. C. Grinter and T. L. Threlfall, *UV-VIS Spectroscopy and its Applications*, Springer-Verlag Berlin, Heidelberg, 1992.
14. B. J. Clark, T. Frost, and M. A. Russel, *UV Spectroscopy Techniques, instrumentation, data handling,* Chapman & Hall, London, 1993.
15. T. Owen, *Fundamentals of Modern UV-visible Spectroscopy: A Primer,* Hewlett-Packard, Germany, 1996.
16. https://www2.chemistry.msu.edu/faculty/reusch/VirtTxtJml/Spectrpy/UV-Vis/uvspec.htm
17. J. E. Lohr, *Reflectance Spectroscopy: Principles, Methods, Applications,* Springer-VerlagNewYork, Inc. 1969.
18. M. Che and J. C. Vedrine, *Characterization of Solid Materials and Heterogeneous Catalysts*, Wiley VCH Verlag& Co KGaA, Boschstr, Germany, 2012.
19. S. D. Jackson and J. S. J. Hargreaves, *Metal Oxide Catalysis*, Wiley VCH Verlag& Co KGaA, Weinheim, 2009.
20. https://www.slideshare.net/oskp/uv-visible-reflectancespectroscopy-and-application

21. P. R. Griffiths and J. A. de Haseth, *Fourier Transform Infrared Spectrometry,* John Wiley & Sons Inc., Hoboken, New Jersey, 2007.
22. E. Moore, *Fourier Transform Infrared Spectroscopy (FTIR) Methods, Analysis, and Research Insights*, Nova Science Publishers, Incorporated, United States, 2016.
23. B. C. Smith, *Fundamentals of Fourier Transform Infrared Spectroscopy*, CRC Press, Taylor & Francis Group, Broken South Parkway, NW, 2011.
24. https://www.slideshare.net/ashwinisomayaji7/ftir-spectrophotometer
25. P. V. D. Heide, *X-Ray Photoelectron Spectroscopy: An Introduction to Principles and Practices,* John Wiley & Sons Inc., Hoboken, New Jersey, 2012.
26. J. W. Robinson, E. M. Skelly Frame and G. M. Frame, *Undergraduate Instrumental Analysis*, CRC Press, Broken South Parkway, NW, 2004.
27. J. F. Moulder and J. Chastain, *Handbook of X-ray Photoelectron Spectroscopy*, Physical Electronics, United States, 1995.
28. C. Cushman, S. Chatterjee, G. H. Major and N. J. Smith, *Vacuum Technology & Coating*, 2016.
29. J. R. Lakowicz, *Principles of Fluorescence Spectroscopy,* Springer Science + Business Media, LLC, New York, 1999.

30. J. Thirumalai, *Luminescence-An Outlook on the Phenomena and Their Applications*, JanezaTrdine Rijeka, Croatia, 2016.
31. J. R. Albani, *Principles and Applications of Fluorescence Spectroscopy,* Blackwell Publishing Professional, State Avenue USA, 2007.
32. https://chem.libretexts.org/Under_Construction/Purgatory/Book%3A_Analytical_Chemistry_2.0_(Harvey)/10_Spectroscopic_Methods/10.6%3A_Photoluminescence_Spectroscopy.
33. U. Agarwal and R. H. Atalla, *Surface Analysis of Paper*, CRC Press, 1995.
34. P. R. Carey, *Biochemical Applications of Raman and Resonance Raman Spectroscopies*, Academic Press, California, 1982.
35. J. R. Ferraro, K. Nakamoto, and C. W. Brown, *Introductory Raman Spectroscopy*, Elsevier Science, USA, 2003.
36. M. J. Baker, C. S. Hughes, and K. A. Hollywood, *Biophotonics: Vibrational Spectroscopic Diagnostics*, Morgan & Claypool Publishers, 2016.
37. F. Ambroz, T. J. Macdonald, V. Martis, and I. P. Parkin, *Small Methods,* 2018, **2**, 1800173.
38. P Sinha, A. Datar, C. Jeong, X. Deng, Y. G. Chung and L. C. Lin, *J. Phys. Chem. C* 2019, **123**, 20195.
39. J. B. Condon, *Surface Area and Porosity Determinations by Physisorption: Measurements and Theory*, Elsevier, Amsterdam, The Netherlands, 2006.

40. https://chem.libretexts.org/Bookshelves/Analytical_Chemistry/Book%3A_Physical_Methods_in_Chemistry_and_Nano_Science_(Barron)/02%3A_Physical_and_Thermal_Analysis/2.03%3A_BET_Surface_Area_Analysis_of_Nanoparticles
41. J.A. Moulijn, P.W.N.M. van Leeuwen and R.A. van Santen, *Stud Surf SciCatal.,* 1993, **79**, 401.
42. A. Jones, *Temperature-Programmed Reduction for Solid Materials Characterization*, Marcel Decker Inc., New York, 1986.
43. Gervasini andAntonella, *Calorimetry and Thermal Methods in Catalysis, Springer Series in Materials Science*, Springer-Verlag Berlin Heidelberg, 2013.
44. http://eacharya.inflibnet.ac.in/data-server/eacharya-documents/55daa452e41301c73a2cb5ac_INFIEP_208/344/ET/1.html
45. D. I. Donato, G. Lazzara and S. Milioto, *J. Therm. Anal. Calorim.*, 2010, **101**, 1085.
46. P. Gabbott, *Principles and Applications of Thermal Analysis,*BlackWell Publishing Ltd., Oxford, UK, 2008.
47. P. J. Haines, *Thermogravimetry. In: Thermal Methods of Analysis*. Springer, Dordrecht, 1995.
48. https://www.researchgate.net/figure/A-schematic-diagram-of-the-TGA-setup-SETARAM-TGA-92_fig1_257708944.

Chapter 3

Photocatalytic Degradation of Norfloxacin Under UV, Visible and Solar light using Ceria Nanoparticles

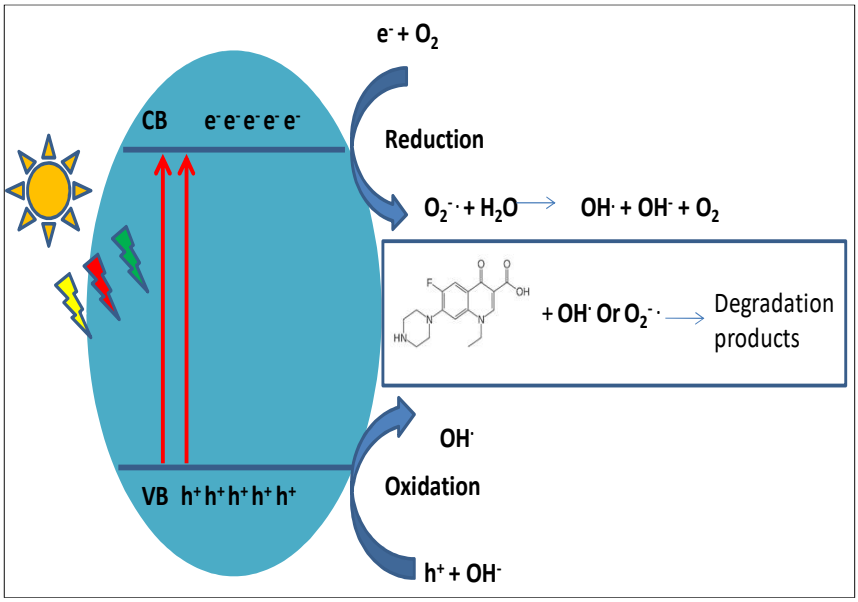

Cerium oxide nanoparticles were synthesized by ammonia precipitation method and have been effectively used for the photocatalytic degradation of norfloxacin antibiotics.

3.1 Introduction

The environmental pollution due to the occurrence of pharmaceuticals, especially antibiotic residuals, in water bodies is of great concern for the past few decades [1]. Norfloxacin (NOF) is a class of drugs belonging to fluoroquinolone antibiotics that are used to treat so many diseases in both humans and animals [2]. But a major part of it is excreted into the environment because of its lower metabolism and poor biodegradability. Even a trace amount of NOF in water may interfere with bacterial DNA replication that leads to the growth and spread of antibiotic-resistant bacteria. NOF is also known to be somewhat toxic to aquatic organisms and humans. So it is very crucial to remove these antibiotic residuals from water effectively [3]. Some of the techniques used to remove antibiotics from water bodies involve adsorption, biodegradation, air stripping, reverse osmosis, ultrasonic techniques, and advanced oxidation processes (AOPs) [4-6]. Heterogeneous photocatalysis using metal oxide semiconductors is one of the most suited methods for pollutant removal due to its high degradation and mineralization capacity. Metal oxides can function by high energy utilization of either solar or any other light sources as mentioned in chapter 1, section 1.3. [7-9]. Catalytic recycling makes the environmentally benign photocatalytic approach less expensive.

Many synthetic strategies are reported to reduce the rate of recombination of electron-hole pairs and also to increase the visible light absorption capacity of ceria. Wen and coworkers have synthesized a

ternary Ag/AgCl-CeO_2 photocatalyst by in-situ deposition followed by the photoreduction process for NOF degradation [2]. They have also reported a ternary Ag_2CO_3/CeO_2/AgBr photocatalyst for degrading levofloxacin under visible light irradiation [10]. A novel Ag_2O/CeO_2 heterojunction photocatalyst was reported for the degradation of an antibiotic, enrofloxacin, under visible light [1]. Most CeO_2 photocatalysts with heterojunctions contain noble metals, and their synthetic methods are time-consuming multistep processes.

Among the several methods of preparation of ceria, chemical precipitation is an attractive methodology as it is easily scalable, low cost, and is simple to operate. In this work, we synthesized pure ceria in ultrasmall dimensions by simple precipitation method using ammonia as the precipitating agent and cerium nitrate as the precursor. Three different ceria catalysts were prepared; (1) by adding 25% NH_3 to the precursor solution, (2) by adding 2M NH_3 to the precursor solution, and (3) by adding the precursor solution to 2M NH_3 solution. The sizes of the nanoparticles synthesized were correlated with the synthesis method. The prepared catalysts were characterized by several analytical techniques and their photocatalytic activity in NOF degradation was studied under UV, solar, and visible light irradiation.

3.2 Experimental

3.2.1 Catalyst Preparation

Different cerium oxide catalysts were prepared by the ammonia precipitation method. In the first method, 25% NH_3 solution was added

dropwise to a solution of 0.05 M cerium nitrate while stirring at room temperature till the pH of the solution became 10. The obtained cerium hydroxide suspension was stirred continuously to oxidize Ce^{3+} to Ce^{4+} state. The resultant yellow colored suspension was filtered and the precipitate was washed several times with water till the washings are free from nitrate ions.

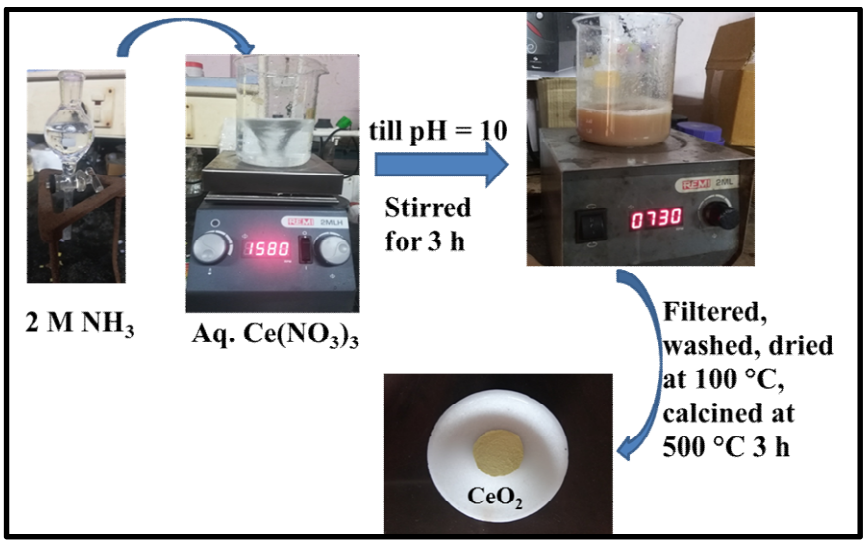

Fig. 3.1 Synthesis of ceria nanoparticles by ammonia precipitation.

The precipitate was dried overnight at 100 ℃ in an oven and calcined at 500 °C for 5 h. The prepared system was designated as CeO_2-1. The second catalyst was prepared by adding 2 M ammonia solution as the precipitating agent following the previous preparation method. The sample prepared was designated as CeO_2-2. The third sample (CeO_2-3) was prepared by the addition of cerium nitrate solution to 2 M ammonia solution. Further steps are the same as before. The preparation method is depicted in figure 3.1.

3.2.2 Photocatalytic Degradation of NOF

Photocatalytic activities of the three prepared systems were examined in NOF antibiotic degradation. In a typical procedure, 50 mg of the prepared photocatalyst was added to a 50 ml solution of NOF of concentration 10 mg/L and stirred in a photoreactor illuminated with an 8x8 W UV lamp at room temperature. After fixed time intervals, the reaction mixture was taken from the reactor and centrifuged to remove the catalyst particles. The concentration of the antibiotic was measured with a UV-vis spectrophotometer at an absorption wavelength maximum of 277 nm. The photocatalytic degradation was investigated by varying the reaction time, catalyst weight, solution volume, and solution concentration to find out the best conditions of the reaction for effective photocatalysis.

3.2.3 Catalyst Reusability Studies

The reusability of the catalyst in repeated runs was also investigated in the degradation of 50 ml of 10 mg/L NOF solution over 0.05 g catalyst under visible light irradiation. The catalyst (CeO_2-2) was collected by filtration after the photocatalytic reaction, washed several times with distilled water and acetone, dried, and activated at 500 ℃ for 1 h before further use. The reaction was then carried out again under the same conditions as above and the percentage of degradation was calculated. The process was repeated for four cycles to study the reusability of the catalyst. FTIR spectrum of the spent catalyst after the

fourth cycle was then measured to investigate the changes that occurred to the catalyst in repeated runs.

3.3 Results and Discussion

Crystal structure and phase identification of the prepared systems are done from X-ray diffraction analysis.

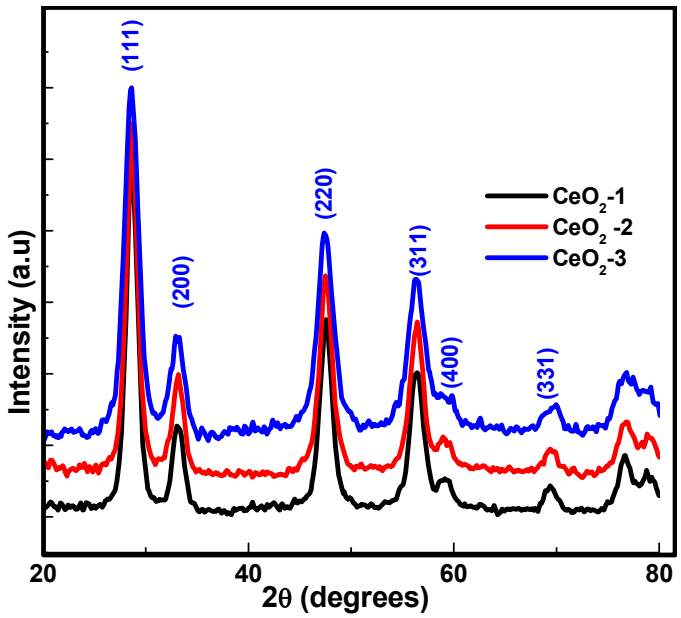

Fig. 3.2 XRD patterns of ceria samples prepared by precipitation method.

All the peaks observed in the diffraction pattern (figure.3.2) can be indexed to the cubic fluorite structure of ceria with space group Fm3m (JCPDS 34-0394) [11-13]. The broadened peaks are due to the small crystallite size of the particles. The crystallite size of the nanoparticles was calculated by using Scherrer formula, from the main intense peak

that is of the (111) plane of CeO_2 [14]. The lattice parameter was also calculated from the XRD pattern.

The crystallite size and lattice parameter calculated for the samples are below 8 nm (table 3.1). The slight increase in the lattice parameter compared to that of bulk ceria (0.5411 nm) indicates more Ce^{3+} ions in the crystal lattice [14]. Structural defects in crystals cause lattice strain, which is a quantitative measure of dislocations and crystal defects. Oxygen vacancies or defects in the ceria lattice results in the lattice strain, which can reduce by lattice expansion [15]. The lattice strain involved in the prepared nanocrystals is calculated from the Williamson-Hall plot as presented in figure 3.3, and the values are in table 3.1. The characteristic strain in the ceria crystals is due to the small crystallite size of the particles.

Table 3.1 Crystal parameters analyzed from XRD patterns.

Sample	The crystallite size (nm)	Lattice Parameter(nm)	Lattice strain
CeO_2-1	7.1	0.5424	0.0022
CeO_2-2	5.5	0.5441	0.0068
CeO_2-3	6.9	0.5421	0.00469

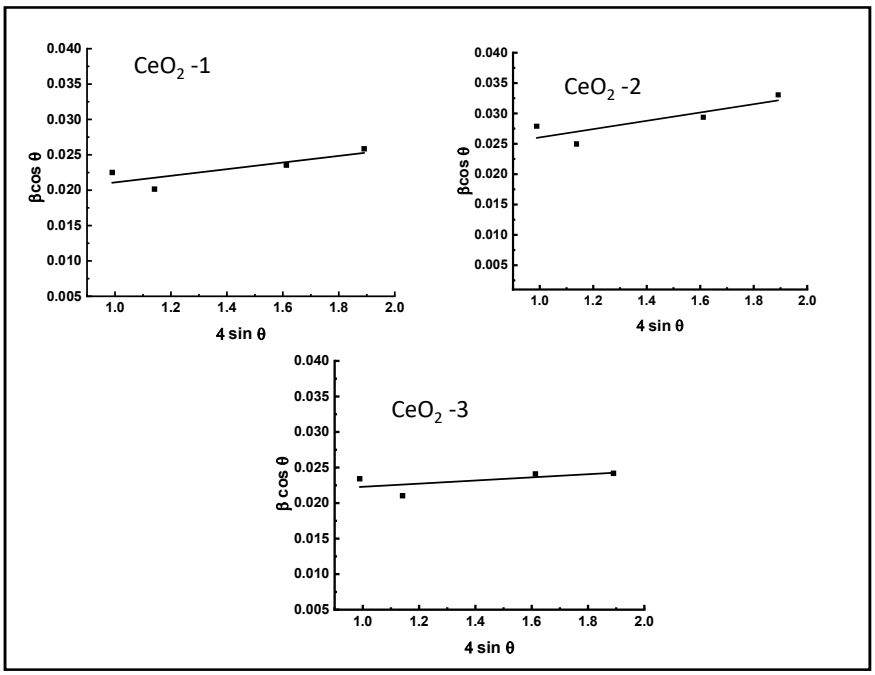

Fig. 3.3 Williamson-Hall plot of ceria crystals.

The FTIR spectra of the three ceria samples are presented in figure 3.4. Characteristic absorption peaks are observed at 500 cm^{-1}, 729 cm^{-1}, 870 cm^{-1}, 2340 cm^{-1} and 3450 cm^{-1} which are attributed to the formation of pure CeO_2 phase [16]. The band around 500 cm^{-1} is due to the symmetric stretching vibration of the Ce-O bond, whereas the peaks centered at 729 cm^{-1} and 870 cm^{-1} are assigned to the Ce-O-Ce vibrations. The peak at 1320 corresponds to the O-H bending vibration of the Ce-OH bond [14]. The broad absorption bands at 3450 cm^{-1} and 1610 cm^{-1} are the stretching and bending vibrations O-H bond of water molecules physically adsorbed on the surface of ceria particles. Surface hydroxyl groups also contribute to the band centered at 3450 cm^{-1}.

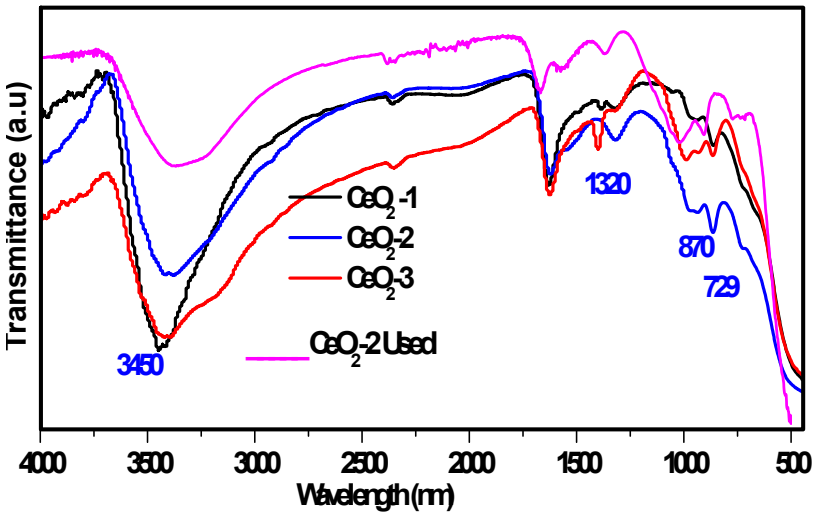

Fig. 3.4 FTIR spectra of ceria samples.

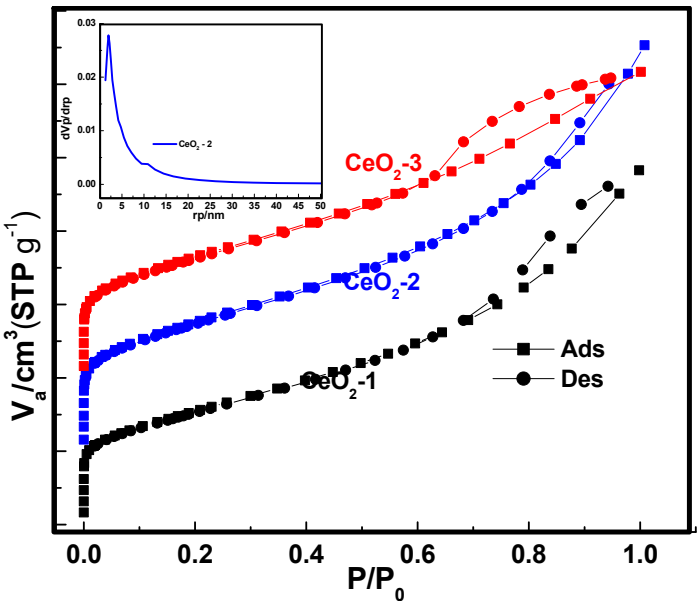

Fig. 3.5 Adsorption-desorption isotherm of ceria samples and pore size distribution of the sample CeO_2-2 is shown inset.

The specific surface area and pore size distribution of the prepared systems were obtained by measuring the adsorption-desorption isotherm (given in figure 3.5.) and by BJH methods. The isotherms are of Type IV indicating the presence of mesoporous nature of the catalysts [17]. The specific surface area, pore size distribution, and particle size calculated from TEM images of the ceria sample are given in Table 3.2.

In the diffuse reflectance spectra of the ceria catalysts (figure. 3.6), a strong absorption band is observed between 350 and 400 nm. Kubelka–Munk plot is used for estimating the bandgap of ceria and the plot of CeO_2-2 is shown in figure 3.7 [16]. The energy gap values lower the reported value of bulk ceria (3.19 eV), which may be due to the quantum confinement of the synthesized ceria nanoparticles [18-19].

Table 3.2 Characteristic parameters of ceria samples.

Sample	BET S.A. (m^2/g)	Pore volume (cm^3/g)	Bandgap (eV)	Particle size (nm)
CeO_2-1	108.3	0.147	3.07	8.0
CeO_2-2	123.2	0.164	3.01	6.5
CeO_2-3	116.6	0.127	3.10	7.1

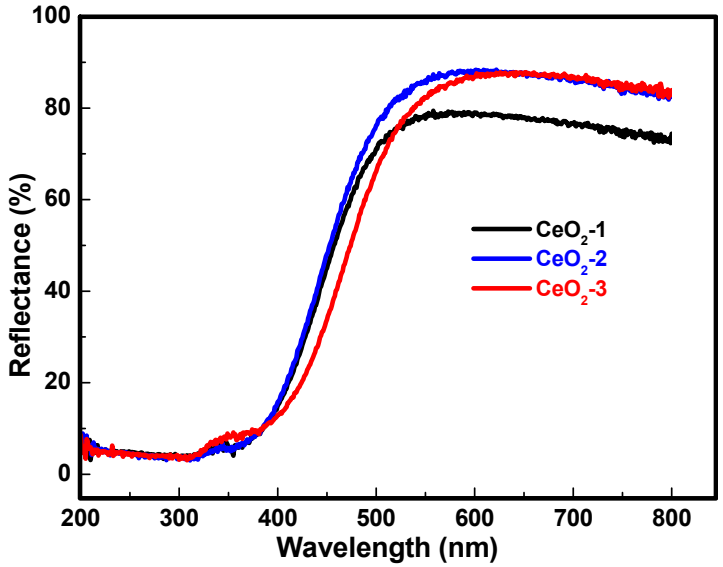

Fig. 3.6 Diffuse reflectance spectra of the ceria samples.

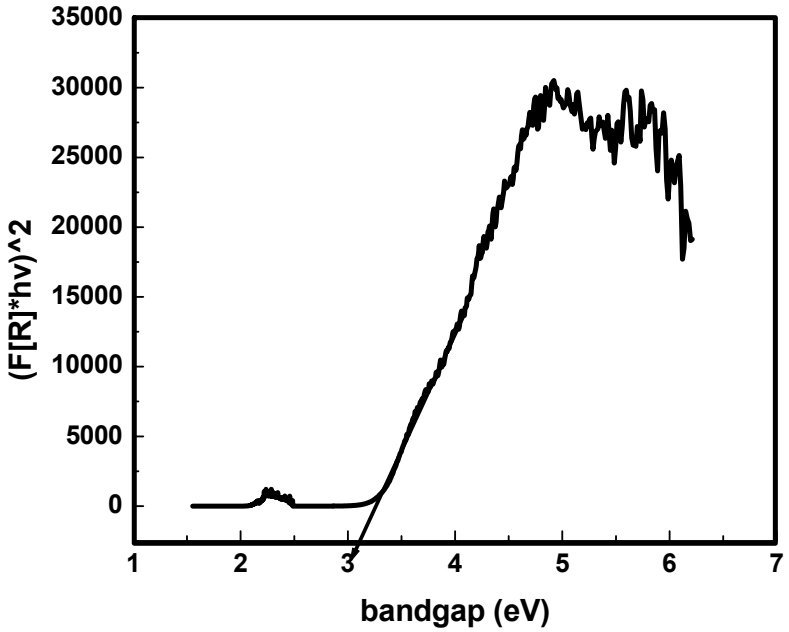

Fig. 3.7 Kubelka – Munk plot of CeO_2-2 for calculating the bandgap.

The microstructure and morphology of the catalysts are examined by TEM and SEM analyses (figure 3.8.) All three catalysts are spherical and the well-distributed spherical particles in the size range of 5–8 nm are visible in the TEM images. The average particle size is given in Table 3.2, the trend of which agrees with the crystallite size obtained from XRD analysis and this justifies the quantum confinement effect as suggested from the low bandgap values obtained from DR UV-vis spectral analysis.

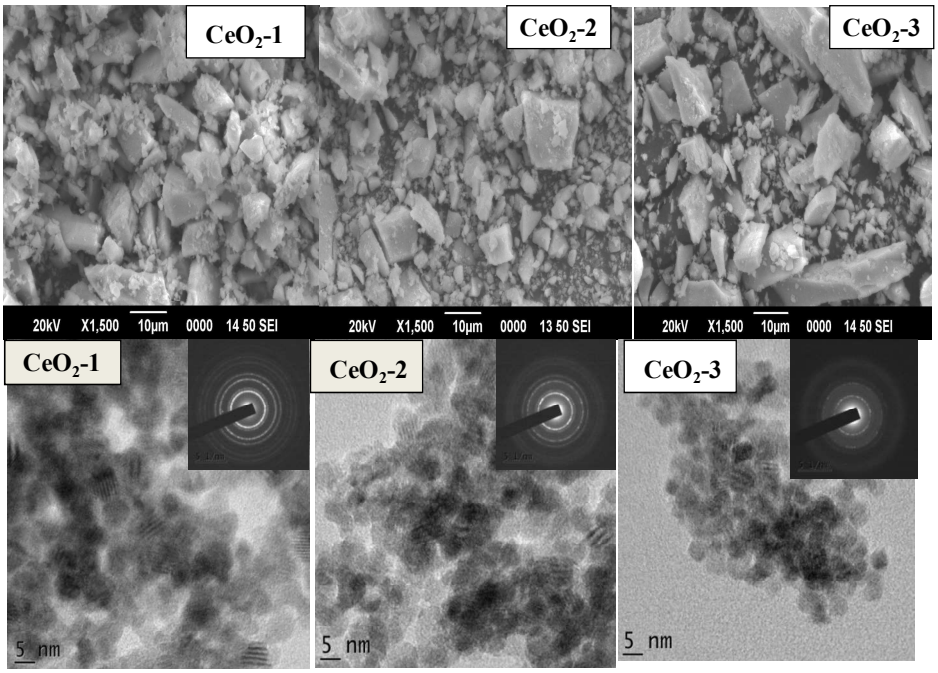

Fig. 3.8 SEM and TEM images of ceria samples. The SAED patterns of the corresponding samples are shown inset.

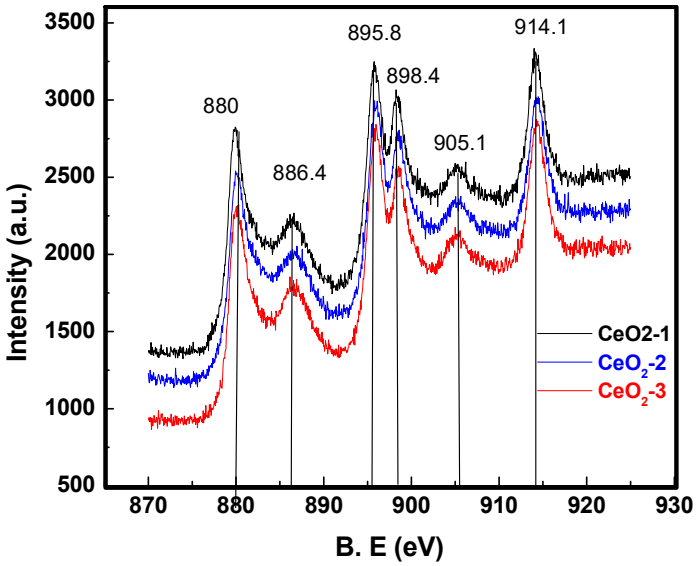

Fig. 3.9 XPS spectra of Ce 3d region of ceria samples.

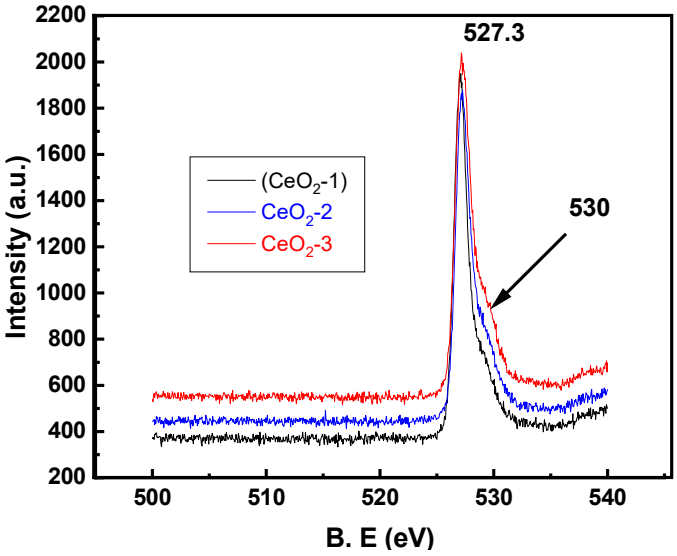

Fig. 3.10 XPS spectra of O1s region.

All the three ceria samples were investigated by XPS analysis and the Ce 3d region and O1s region of the spectra are shown in Figures 3.9 and 3.10 respectively. In Ce 3d XPS spectra, the peaks at 882 eV, 886 eV, 895 eV, 898 eV, 905 eV and 914 eV corresponds to Ce^{4+} state and the peak at 880 eV is due to the presence of Ce^{3+} oxidation state of cerium [14, 10]. The O1s spectra of ceria contain two peaks. The peak at 527.3 eV is assigned to the lattice O^{2-} ions, whereas the less intense shoulder peak at 530 eV is assigned to the surface hydroxyl groups [19].

The photocatalytic performance of the synthesized catalysts on NOF degradation is compared under UV light using a 10 mg/L solution of NOF. The reactions were carried out at different time intervals. A maximum of 98.9% degradation was obtained using CeO_2-2 under UV light within 1 h. The effect of catalyst weight, solution volume, and antibiotic concentration were studied using the CeO_2-1 catalyst and the results are presented in figures 3.11 to 3.14. 50 ml NOF solution of concentration 10 mg/L was used to study the effect of catalyst weight and the reaction was carried out for 10 min. The percentage of degradation increased with an increase in the catalyst weight since the availability of photoactive sites increases with the catalyst dosage. The effect of the volume of NOF solution was studied using a 0.05 g catalyst for a 10 min reaction. The percentage of degradation decreased with an increase in the solution volume. When the concentration of NOF solution was increased from 10 mg/L to 25 mg/L, the percentage of degradation decreased from 95.7% to 73.5%. The decrease in the percentage degradation with the amount/concentration of dye molecules is due to the

availability of the same number of active sites for more NOF molecules since the catalyst amount is kept constant. Among the three catalysts, CeO_2-2 synthesized by adding 2 M NH_3 to the precursor solution showed the highest activity compared to others. This may be due to its smaller particle size and higher surface area, as evidenced by TEM and BET SA-pore volume analyses.

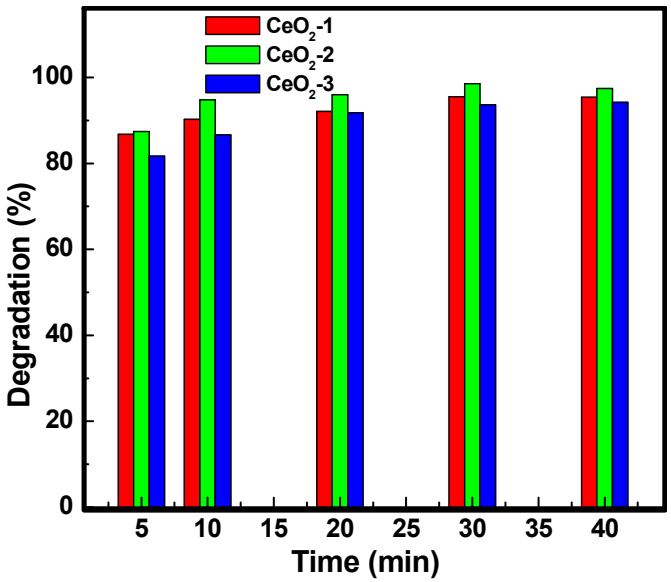

Fig. 3.11 Photocatalytic activity of ceria samples on NOF degradation in different time intervals at the reaction conditions of 50 ml NOF solution with 10 mg/L concentration and 50 mg catalyst.

The photocatalytic activity of the catalyst CeO_2-2 on NOF degradation is compared with the degradation of commercially available NOF tablet solution of the same concentration, and the result is presented in figure 3.15. The catalyst is almost equally active in the degradation of both samples.

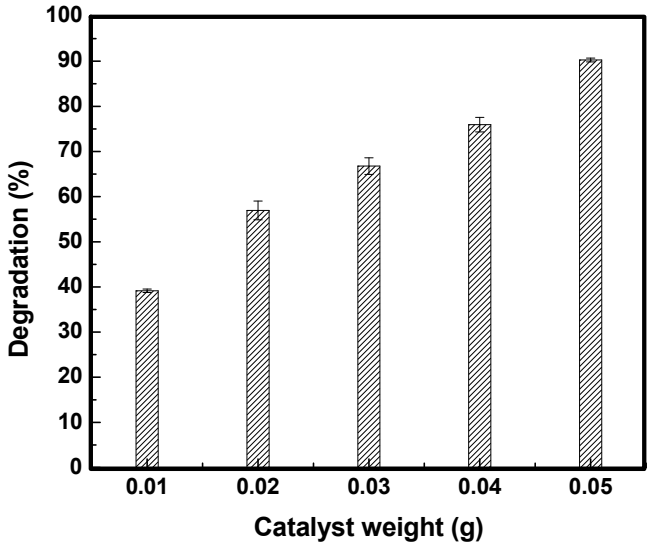

Fig. 3.12 Effect of catalyst weight in the degradation of 50 ml NOF solution with 10 mg/L concentration for 10 min reaction.

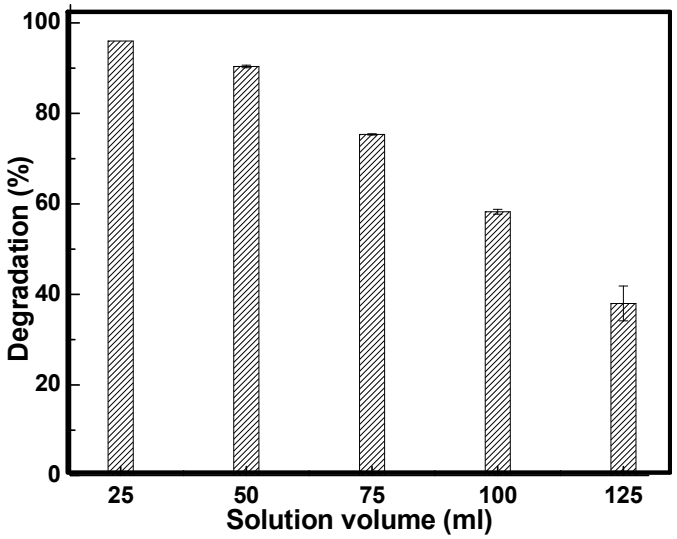

Fig. 3.13 Effect of solution volume on NOF degradation over 0.05 g CeO_2-2 catalyst with 10 mg/L NOF concentration for 10 min reaction.

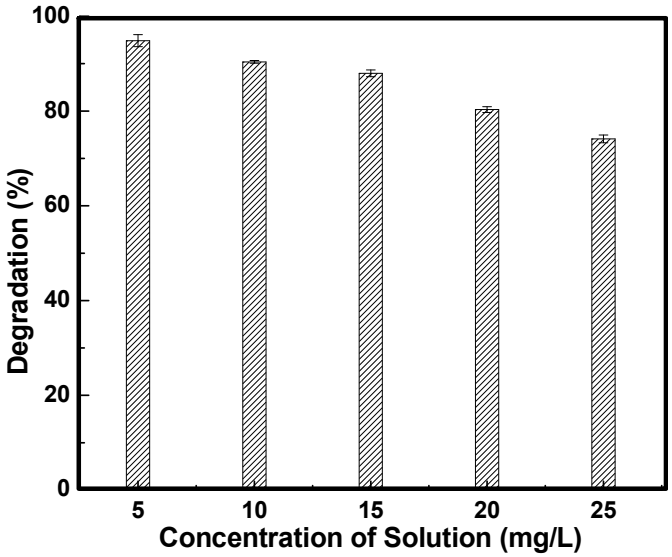

Fig. 3.14 Effect of NOF concentration over 0.05 g catalyst CeO_2-2 in the degradation of 50 ml NOF solution for 10 min reaction.

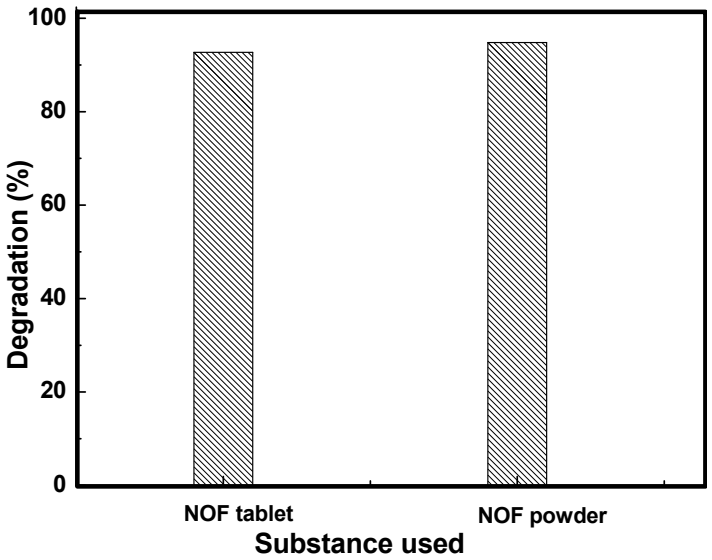

Fig. 3.15 Comparison of photocatalytic degradation activity of CeO_2 -2 on NOF chemical (dry powder) and tablet.

The reusability of the best catalyst, CeO_2-2, is checked for four consecutive cycles (figure. 3.16), and the stability of the catalyst after the fourth run was investigated using FTIR spectroscopic analysis of the spent catalyst. The catalyst retained 97% of its initial activity even after four cycles and the functionalities of the catalyst remained unaffected even after repeated uses, as evident from the FTIR spectra of the initial and spent catalysts (figure. 3.4).

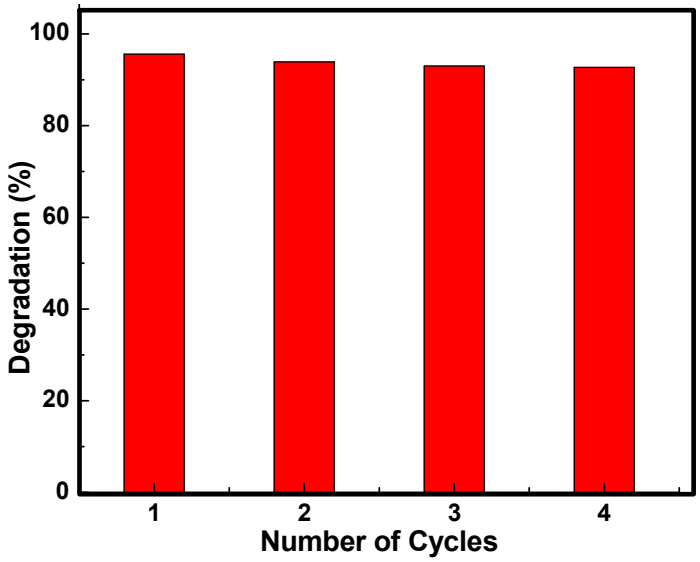

Fig. 3.16 Reusability study of the best catalyst CeO_2-2. 50 ml NOF solution of 10 mg/L concentration and 0.05 g catalyst used for 30 min reaction.

The photocatalytic activities of all the three catalysts were also investigated under the sun and visible light, and the results are given in Table 3.3. All the prepared catalysts are active in visible and solar irradiation. This may be attributed to the lower bandgap of nanoceria as calculated from the UV data.

Table 3.3. Comparison of photocatalytic degradation under different light sources*.

	% Degradation		
Catalyst	UV light	Visible light	Solar light
CeO_2-1	90.2	91.4	89.1
CeO_2-2	94.8	92.1	90.4
CeO_2-3	85.5	77.2	81.7

* 50 ml NOF solution of 10 mg/L concentration and 0.05 g catalyst was used for 10 min irradiation.

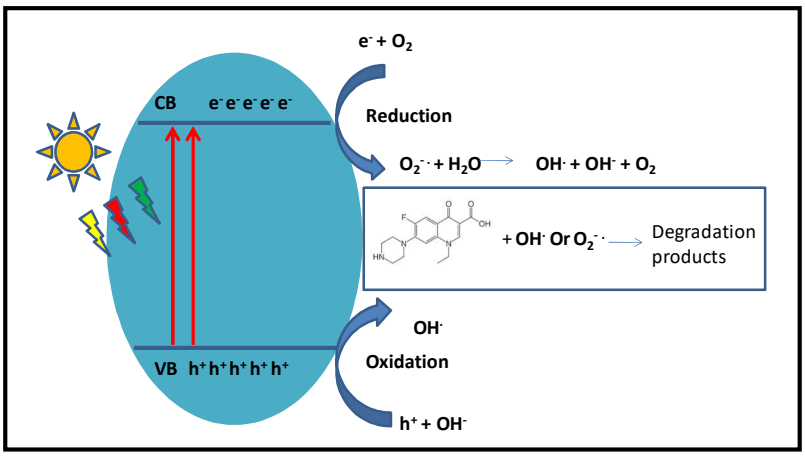

Fig. 3.17. A plausible mechanism of photocatalytic degradation of norfloxacin by ceria nanoparticles.

A plausible mechanism of photocatalytic degradation of NOF in the presence of ceria nanoparticles is represented in figure 3.17. When the catalyst was photo-irradiated, the electrons get excited from the

valence bond (VB) of CeO_2 to the conduction band (CB) and holes (h^+) are created in the VB. The electrons in the CB combined with O_2 to produce superoxide radical anion ($O_2^{\cdot-}$), which then reacts with a water molecule to form hydroxyl radicals and ions ($OH^{\cdot}$ and OH^-). Holes (h^+) in the VB react with OH^- ions or water to form hydroxyl radicals. The highly oxidizing species such as $OH^{\cdot}$ or $O_2^{\cdot-}$etc. react with NOF to decompose it into intermediate radicals and finally to complete demineralization products such as H_2O, CO_2, etc.

3.4 Conclusions

Here, pure ceria nanoparticles were synthesized in the ultra-small dimension by a simple precipitation method using NH_3 as the precipitating agent. Material characterization by XRD, FTIR spectroscopy, XPS, DR UV–vis spectroscopy, SEM, and TEM revealed the structure and morphology of different ceria photocatalysts. The photocatalytic performance of the catalysts on NOF degradation was studied under UV, visible, and solar light irradiation. The effect of irradiation time, catalyst weight, solution volume, and antibiotic concentration on photocatalytic activity were studied under UV light. The use of 2 M NH_3 as the precipitating agent leads to the formation of CeO_2 nanoparticles showing maximum degradation of 98.9% of 50 ml 10 mg/L NOF solution for 30 min UV light irradiation over 0.05 g catalyst. The present study reported an efficient catalyst in the photodegradation of norfloxacin that showed good reusability in its consecutive cycles.

References

1. X. J. Wen, C. G. Niu, L.Zhang, C. Liang and G. M. Zeng, *Appl. Catal., B*, 2018, **221**, 701.

2. X. J. Wen, C. G. Niu, D. W. Huang, L.Zhang, C. Liang and G. M. Zeng, *J. Catal*2017, **355**, 73.

3. A. M. A. Wahab, A. S. A. Shirbini, O. Mohamed, and O. Nasr, *J. Photochem. Photobiol.*, 2017, **347**, 186.

4. M. Brigante and P. C. Schulz, *Micropor. Mesopor. Mat.*, 2012, **156**, 138.

5. A. Khataee, P. Gholamia, D. Kalderisc, E. Pachatouridoud and M. Konsolakise, *UltrasonSonochem* 2018, **41**, 503.

6. M. Idrissi, Y. Miyah, Y. Benjelloun and M. Chaouch, J. *Mater. Environ. Sci*. 2016, **7,** 50.

7. T. Divya and N. K. Renuka, *J. Mol. Catal. A: Chem.*, 2015, **408**, 41.

8. A. Touati, L. Jlaiel, W. Najjar and S. Sayadi, *Euro-Mediterranean Journal for Environmental Integration*, 2019, **4**, 2365.

9. G. A. Apostolescu, C. Cernatescu, C. Cobzaru, R. E. T. Farmus and N. Apostolescu, *J. Environ. Chem.* 2015, **2**, 415.

10. G. B. Vieira, H. J. Jose, M. Peterson, V. Z. Baldissarelli, P. Alvarez and R. F. P. M. Moreira, *J. Photochem. Photobiol.* 2018, **353**,325.

11. M. Darroudi, S. J. Hoseini, R. K. Oskuee, H. A. Hoseini, L. Gholami and S. Gerayli, *Ceram Inter.*, 2014, **40,** 7425.

12. L. J. Xu and J. L. Wang, *Appl. Catal. B*, 2013, **142**, 396.

13. M. Zahoor, A. Arshad, Y. Khan, M. Iqbal, S. Z. Bajwa, R. A. Soomro, I. Ahmad, F. K. Butt. M. Z. Iqbal, A. Wu and W. S. Khan, *Appl.,* 2018, **8**, 1091.

14. S. Tsunekawa, K. Ishikawa, Z. Q. Li, Y. Kawazoe and A. Kasuya, Phys. Rev. Lett., 2000, **85**, 3440.

15. M. Kurian and C. Kunjachan, Int. Nano Lett., 2014, **4**, 73.

16. B. S. Rohini, H. Nagabhushana, G. P. Darshan, R. B. Basavaraj, S. C. Sharma and R. Sudarmani, *Appl. Nanosci.,* 2017, **7**, 15.

17. N. S. Arul, D. Mangalaraj, P. C. Chen, N. Ponpandian, P. Meena and Y. Masuda, *J Sol-Gel Sci. Technol.,* 2012, **64**, 15.

18. B. Choudhury, P. Chetri and A. Choudhury, *J. Exp. Nanosci.*, 2015, **10**, 103.

19. G. K. Pradhan and K. M. Parida, *J. Eng. Sci. Technol.*, 2010, **2**, 53.

Chapter 4

Adsorption and Photo Fenton Degradation of Congo red Dye by Ceria Nanoparticles Synthesized using *Allium Sativum* Extract

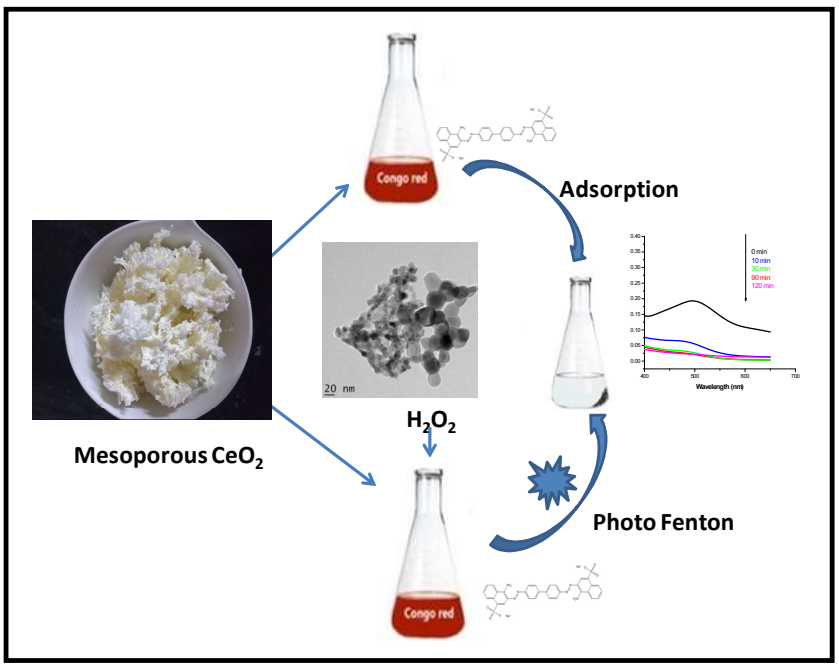

Nanostructured mesoporous ceria materials are synthesized by sol-gel method using aqueous *Allium sativum (*garlic) extract and have been used both as adsorbents and as photo Fenton catalysts for the removal of Congo red dye.

4.1 Introduction

Azo dyes with azo bonds(-N=N-) are used in various industries like textiles, paper, leather, cosmetics, and plastic [1]. Contamination of water bodies by the release of azo dyes is of great concern in this period as most of them are toxic, mutagenic, carcinogenic, and non-biodegradable [2]. Since these dyes are stable, continuous release of them into water bodies creates tribulations like eutrophication, turbidity, and poses long-term health hazards to both humans and aquatic organisms [3]. Congo red [1naphthalene sulfonic acid, 3,30-(4,40-biphenylenebis(azo))bis(4amino-)disodium salt] (CR) is an anionic water-soluble diazo dye used especially as an indicator and biological stain. Most of the traditional treatment processes such as adsorption, ion exchange, chlorination, chemical oxidation, coagulation, flocculation, and biological degradation are less effective since many of them result in secondary pollutants during dye removal [4]. Among these traditional methods, adsorption is of great significance in dye removal due to the low cost, simple operation, and high efficiency of the process [5-9]. So it is highly advantageous to produce better-quality adsorbents by some economic and facile approaches.

Among advanced oxidation processes (AOPs) of pollutant removal, Fenton processes are attractive methods due to their simplicity, low toxicity, cost-effectiveness, and high performance [10-11]. The oxidation efficiency of classical Fenton reactions can modify by the Photo Fenton reaction in the presence of light [12,13]. Among the rare earth elements, CeO_2 possesses distinctive advantages like

high adsorption ability for H_2O_2, superior chemical stability, abundant oxygen vacancies, and very low metal ion leaching compared to other Fenton-like systems.

Bare ceria exhibits either adsorption or photocatalytic degradation of dyes, and the composites of ceria have efficient Fenton-like degradation activity. Wu et al. synthesized porous CeO_2 nanotubes via a nanowire-directed templating method and studied its adsorption behavior for the typical azo dye CR [14]. Hu et al. presented ceria hollow spheres derived from the sol-gel reaction of cerium nitrate on polymeric templates showing efficient adsorption towards the acid dye acid black 210 [15].

Xu et al. synthesized a superparamagnetic nanoscaled Fe_3O_4/CeO_2 composite by the impregnation method for the Fenton-like degradation of 4-chlorophenol [16]. Ouyang et al. presented new composite material, $Fe_2O_3@CeO_2$-ZrO_2/Palygorskite heterogeneous catalyst with high degradation efficiency toward CR dye [5]. Wei et al. synthesized nanotubes and nanocubes via the hydrothermal method for the adsorption-degradation of methylene blue (MB) and CR in the nanoceria-H_2O_2 system under alkaline conditions [17]. Li et al. prepared a magnetic-ordered mesoporous Fe_3O_4/CeO_2 composite that played a dual-function role as both adsorbent and Fenton-like catalyst with low metal leaching [18]. Gan et al. has synthesized a magnetic nanocomposite Fe_3O_4/CeO_2 using three different preparation methods for the Fenton-like degradation of Orange G [1].

Physical and chemical methods usually adopted for the synthesis of metal oxide nanoparticles require reactive reducing agents or precipitating agents, which impart destructive effects on the environment. Also, most of these methods involve tedious procedures and rigorous experimental conditions and have to eliminate the non-eco-friendly byproducts to get the nanoparticles in the pure form [19]. Therefore several research works are focused on developing alternate green chemistry methods for the synthesis of nanoparticles. Several biological sources, such as plant-based extracts, algae, fungi, agricultural and food products, etc., have been used for synthesizing nanoparticles [20]. The extract components act as capping agents that prevent aggregation, leading to stable and homogeneous nanoparticles. The phyto-mediated sol-gel method is a relatively simple method for the large-scale production of nanoparticles and is also cost-effective [21].

Garlic has been used as an ingredient in food for more than a thousand years and contains carbohydrates and organo-sulfur compounds, i.e., allyl sulfide groups, alliin, ajoene, allyl cysteine, and allicin, as well as other compounds such as vitamins, phospholipids, flavonoids, amino acids, and fatty acids that impart its medicinal properties [22]. The various components in garlic extract can act as reducing and stabilizing agents in the synthesis of nanoparticles. Several research works have been reported for synthesizing metal and metal oxide nanoparticles using garlic extractfor their various applications. Phyto-synthesis of silver nanoparticles is reported with an

average particle size of 8 nm, showing remarkable antioxidant activity using garlic extract by Selvan et al. [23]. White et al. reported the synthesis of garlic extract mediated stable, monodisperse silver nanoparticles and indicated from spectroscopic studies that allicin and carbohydrates in the garlic extract are the primary nanoparticles stabilizing moieties [24]. Synthesis of copper nanoparticles of 100 nm particle size and gold nanoparticles of 15 nm, both having spherical shape have also been reported using aqueous *Allium sativum* extract [25-26]. ZnO nanoparticles prepared in the presence of garlic extract showed a narrowing in its bandgap and higher efficiency for the photodegradation of methylene blue dye compared to ZnO nanoparticles prepared in the absence of plant extract [27]. Garlic extract has also been used for the synthesis of stable nanoparticles of NiO and nanocomposites such as Ag@CeO_2, magnetic and photocatalytic Fe_3O_4–Ag by some other research groups [22,28-31].

In this work, we report a novel and green approach for the sol-gel synthesis of ceria by using *Allium sativum* (garlic) extract.The morphology and physicochemical properties of the synthesized ceria samples were characterized using different methods. The obtained ceria played a dual function role as adsorbent and heterogeneous photo Fenton catalyst for the removal of CR dye from an aqueous solution.

4.2 Experimental

4.2.1 Preparation of Garlic Extract

20 g *Allium sativum* (garlic) was chopped into slices and taken in a beaker. 100 ml water was added to this and stirred at 80 °C or 30

min. The resulting solution was filtered to get a turbid garlic extract. The extracts were prepared just before the experiments on the preparation of ceria. Extracts having different plant extract concentrations were used by varying the initial amount of garlic to 10 g, 20 g, 30 g, and 40 g in 100 ml water.

4.2.2 Preparation of Ceria Using Garlic Extract

To 50 ml of the freshly prepared garlic extract, 5 g cerium nitrate was added at room temperature. An off-white sol was formed with stirring, and it was again continuously stirred at 80 ℃ till it becomes a thick gel. The gel was dried at 95 ℃ for 16 h, and the resulting black-colored mass was calcined at 400 ℃ for 2 h to obtain CeO_2 g-20 catalyst. It was ground to a powder and used for the adsorption and photo Fenton degradation of CR dye under different experimental conditions.

Four different samples were synthesized using garlic extract having four different concentrations. The other samples prepared were labeled as CeO_2 g-10, CeO_2 g-30, and CeO_2 g-40, wherethe numbers indicate the amount of garlic (in g) added to 100 ml water to prepare the extract. For activity comparison, a sample without the addition of garlic is also prepared, following the above procedure. A pictorial representation of the synthesis method is shown in figure 4.1.

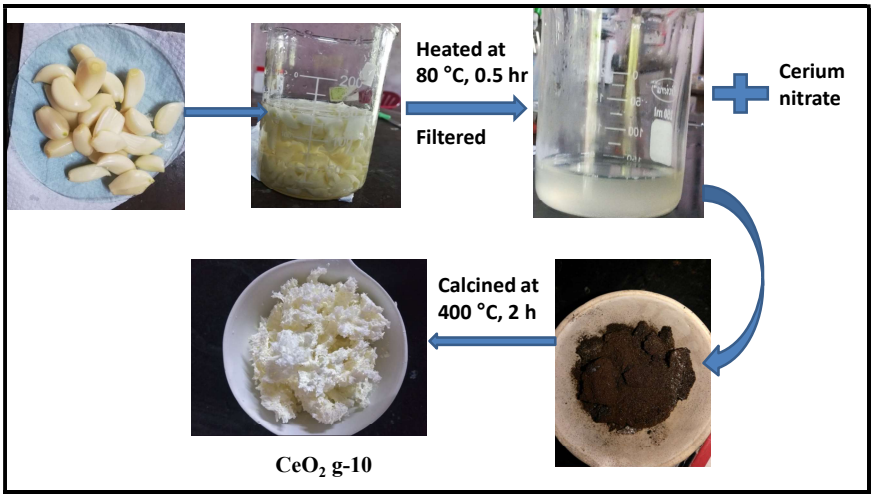

Fig. 4.1 Pictorial representation of the preparation of ceria by sol-gel method using *Allium sativum* (garlic) extract.

4.2.3 Efficiency of Congo Red Dye Removal

4.2.3.1 Adsorption Procedure

50 mg of the synthesized ceria adsorbent was added to a 50 ml solution of CR dye of 20 mg/L concentration and stirred at room temperature in the dark. The reaction mixture was taken out after a definite time interval and centrifuged to remove the adsorbent particles. The decrease in the CR concentration was monitored by recording the absorbance at 490 nm using a colorimeter. The percentage of dye removal was calculated by measuring the absorbance before and afterthe adsorption experiments.

The adsorption capacity of CR onto CeO_2 at time 't' was calculated by the following equation;

$$q_t = (C_0-C_t)V/m \qquad \text{eqn (4.1)}$$

where q_t (mg/g) is the amount of CR adsorbed at time t, C_0 and C_t (mg/L) are the concentrations of CR at the initial time, and at time t respectively, V is the volume of the solution in L and m (g) is the mass of the adsorbent.

4.2.3.2 Photo Fenton Degradation of CR by CeO_2

In a typical procedure, 50 mg of CeO_2 g-20 was added to a 50 ml solution of CR dye at a concentration of 20 mg/L. 2 ml of H_2O_2 (30 wt%) was added into the suspension, and the reaction mixture was stirred at room temperature in a photoreactor illuminated with 8x8W visible lamps. The reaction mixture was taken out after a fixed time interval and centrifuged to remove the catalyst particles. The CR concentration in the resultant solution was calculated as before. The percentagedegradation of dye was calculated using the equation;

$$\% \text{ Degradation} = (A_0-A_t)\ x100/A_0 \qquad \text{eqn (4.2.)}$$

where A_0 is the initial absorbance of CR solution and A_t represents the absorbance after the reaction.

For the investigation of the effect of time of Photo Fenton degradation on dye removal, the absorbance at a particular wavelength of 499 nm. Absorbance measurements were done using a PerkinElmer UV WinLab Lambda 850 spectrophotometer.

4.3 Results and Discussion

In the present investigation, garlic extract is used for the preparation of CeO_2 nanoparticles for the first time. A plausible mechanism for the formation of ceria using garlic extract is represented in figure 4.2.

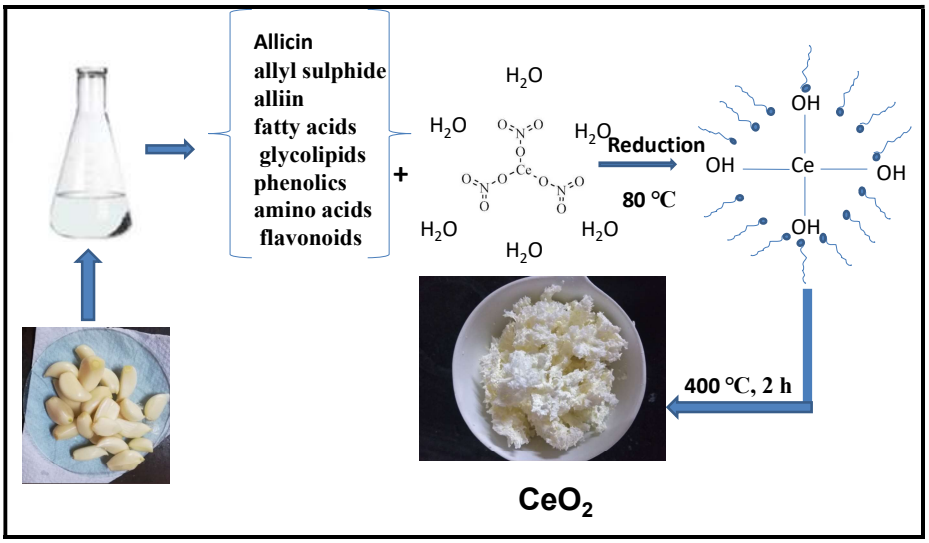

Fig. 4.2 Formation of ceria using garlic extract.

Various phytochemicals of garlic aqueous extracts (allicin, allylsulphide, alliin, fatty acids, glycolipids, phenolics, amino acids, and flavonoids) can act as capping and chelating agents that control the crystal growth of ceria nanoparticles.The carbohydrates present in the extract can assist the gelation of the sol. In the presence of the extract, nanoparticles with smaller crystallite sizes and reduced agglomeration can be produced. Ceria nanoparticles obtained after calcination at 400 ℃ is porous in structure due to the elimination of various

phytochemical components in the mixture through combustion. The material characterization studies revealed the properties and morphology of the prepared CeO_2 nanoparticles.

X-ray diffraction patterns of ceria nanoparticles synthesized by the sol-gel method using garlic extract are shown in figure 4.3; it revealed the crystal structure and phase of the samples. The sharp peaks observed at 2θ values of 28.5°, 32.9°, 47.5°, 56.3°, 59.0°, 69.3°, 76.7°, and 78.8° corresponds to the diffraction from the respective (111), (200), (220), (311), (222), (400), (331) and (420) crystal planes of cubic fluorite CeO_2 (JCPDC: 89-8436) [32-33].

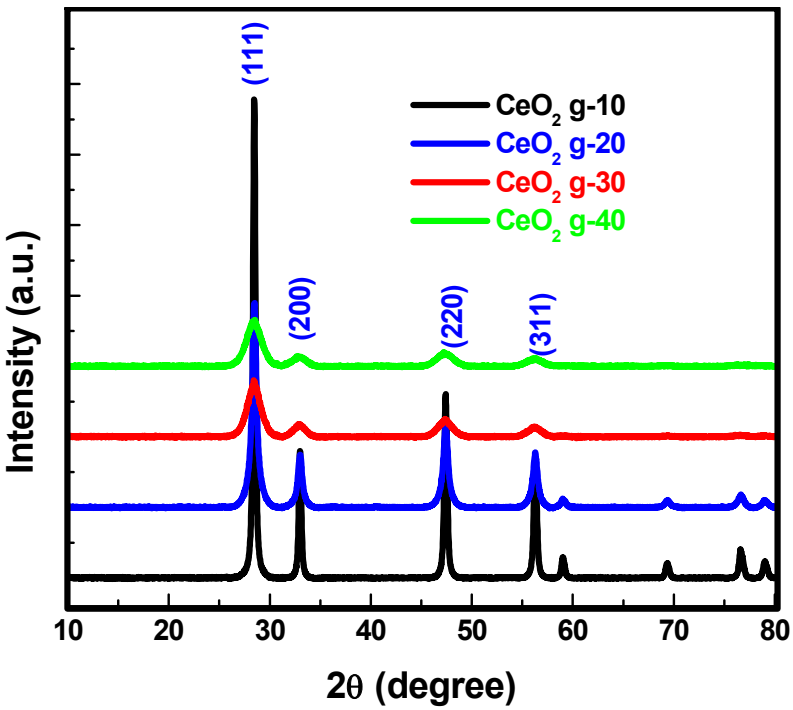

Fig. 4.3 XRD patterns of ceria nanoparticles synthesized using garlic extract of different concentrations.

As no additional peaks are observed in the XRD patterns, it is deduced that the ceria samples prepared using garlic extracts are having a pure cubic fluorite structure. The diffraction peaks of CeO_2 g-30 and CeO_2 g-40 are broader compared to the other two ceria systems due to their smaller crystallite sizes. The average crystallite size was calculated from the full width at half maximum of the most intense diffraction peak at 28.5° using the Scherrer equation; the lattice parameter is given in table 4.1 [34].As expected, an increase in garlic weight in the preparation leads to a decrease in crystallite size.

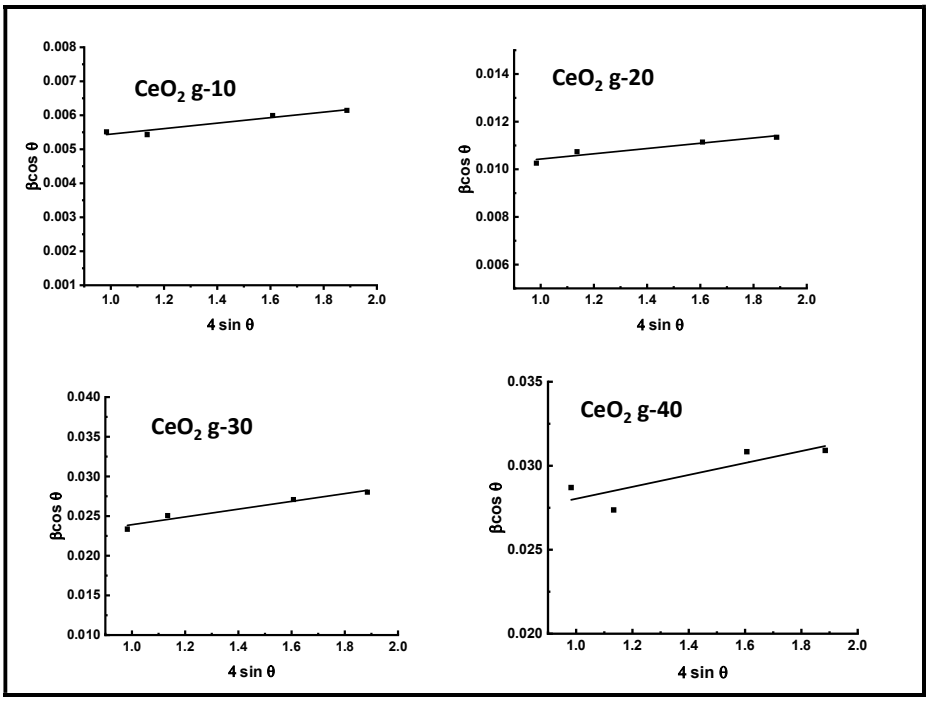

Fig. 4.4. Williamson Hall plot of synthesized ceria systems.

The lattice strain in the prepared nanocrystals was also calculated from W-H plot analysis as shown in figure 4.4, and the values are given in

table 4.2. The lattice strain in the crystals indicates oxygen vacancies and is slightly higher in samples CeO_2 g-30 and CeO_2 g-40 compared to others as expected from their lower crystallite size values.

FTIR spectra of the synthesized samples are given in figure 4.5. The broad absorption bands at 3450 cm^{-1} and 1610 cm^{-1} are the stretching and bending vibrations of water molecules physisorbed on the surface of ceria particles [35]. The band around 500 cm^{-1} is due to the symmetric stretching vibration of the Ce-O bond and the peaks at 718 cm^{-1} may be attributed to the Ce-O-Ce vibration, characteristic of CeO_2. [36-37]. In all the spectra of CeO_2 samples, even that prepared without the addition of extract, the peak observed at 1516 cm^{-1} corresponds to the stretching vibrations of nitrate groups which may be present in trace amount as impurity [38]. The band at 1315 cm^{-1}indicates Ce-OH bending vibration [35]. The additional bands observed in CeO_2 samples synthesized with garlic extract are due to the functional groups related to the incomplete decomposition of organic residuals. In the sample CeO_2 g-40, with the maximum amount of the extract, those peaks are more pronounced as expected.

The peak at 1118 cm^{-1} can be attributed to the S=O bond of the sulfur compounds, and the peak at 1749 cm^{-1} corresponds to the stretching vibrations of C=O group contaminants present in the CeO_2 systems [39]. These observations further confirm the stabilization of CeO_2 by the active bio components of garlic extract that can act as capping agents, reducing the particle agglomeration.

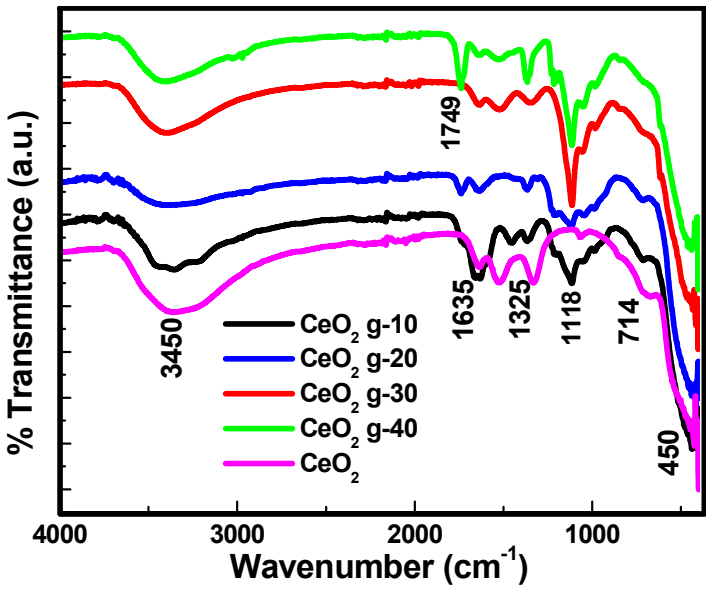

Fig. 4.5 FTIR spectra of ceria nanoparticles.

Thermogravimetric analysis of the gel obtained by heating the sol and further drying at 250 ℃ is represented in figure 4.6. In the TG curve, the weight loss up to 110 ℃ is due to the removal of loosely bound water molecules. After 110 ℃, the weight loss corresponds to the decomposition of the remaining components of garlic extract together with the conversion of ceria precursor species to ceria.

The weight loss of around 250 ℃ is due to the decomposition of S-allylcysteine (SAC),which is one of the active sulfur compounds in garlic extract [40]. No weight loss is observed after 400 °C, which indicates the formation of stable CeO_2.

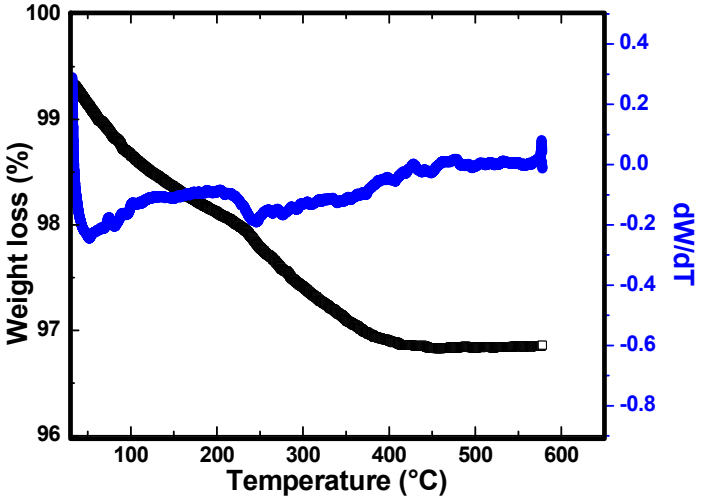

Fig. 4.6 TG and DTG curves of the ceria gel dried at 250 °C.

The morphology and structure of the CeO_2 g-20 were investigated by SEM (shown in figure 4.7) and TEM analysis. TEM images of the samples CeO_2 g-10 and CeO_2 g-20 are given in figure 4.8. CeO_2 g-20 showed the topography of foams with high porosity, as evident from the SEM images.

The particles are arranged as flake-like, having a spherical shape with particle size in the range of 10 nm - 40 nm. The particle size is lower in CeO_2 g-10 (5-15 nm) in comparison, but the particles are thickly agglomerated there, which can result in decreased photoactivity due to the limited exposure of active sites towards CR. The brighter spots with the ring-like pattern obtained in the selected area diffraction pattern confirmed that the material is polycrystalline in nature and nano-dimensional.

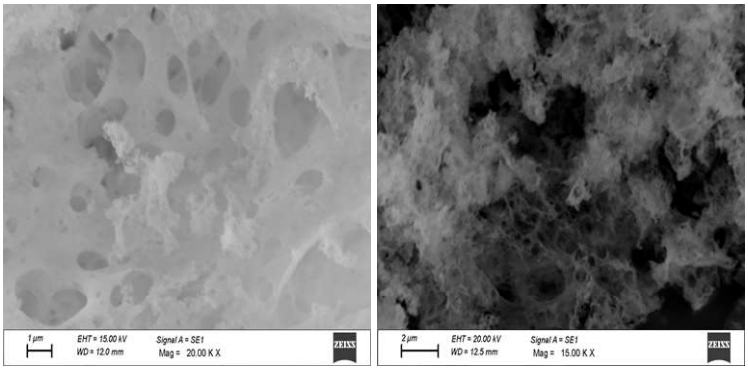

Fig. 4.7 SEM images of CeO_2 g-20.

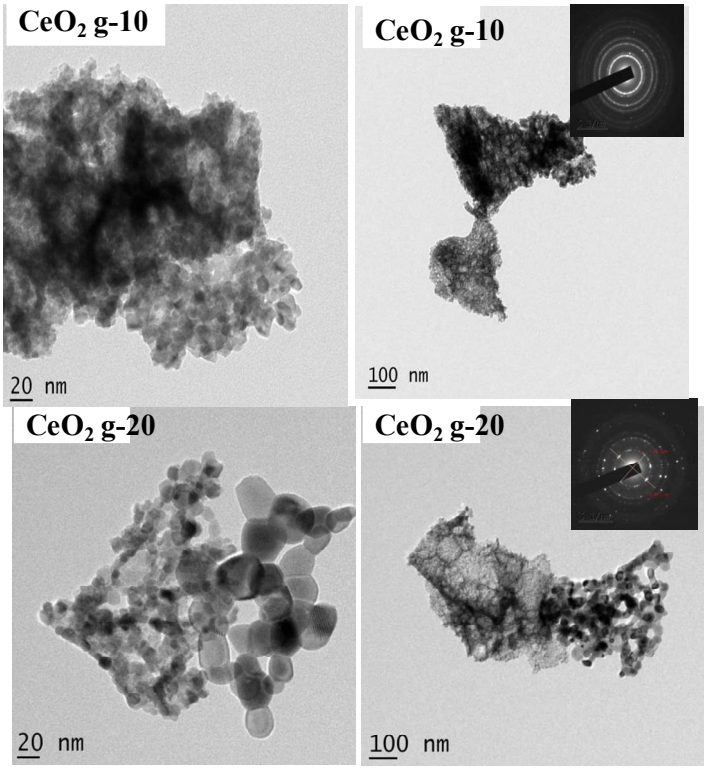

Fig. 4.8 TEM images of (a) CeO_2 g-10 and (b) CeO_2 g-20; SAED patterns are shown inset.

Table 4.1 Physical characteristics of ceria nanoparticles.

Catalyst	Crystallite size (nm)	Lattice parameter (nm)	Lattice strain	Bandgap E_g (eV)
CeO_2 g-10	28.2	0.5419	0.00081	3.09
CeO_2 g-20	15.8	0.5420	0.0011	3.08
CeO_2 g-30	5.4	0.5427	0.0048	3.01
CeO_2 g-40	4.7	0.5428	0.0036	3.00

Table 4.2 Surface properties of ceria systems obtained from BET SA and pore volume measurements.

Catalyst	Sp. S.A. (m^2/g)	Pore volume (cm^3/g)	Pore diameter (nm)
CeO_2 g-10	16.23	0.019	4.9
CeO_2 g-20	39.51	0.042	4.3
CeO_2 g-30	37.77	0.034	3.6
CeO_2 g-40	45.39	0.038	3.4

Diffuse reflectance spectroscopy was used to study the optical properties and bandgap of the synthesized ceria samples. A broad absorption peak was observed in the UV region, extending to the visible range as seen from the spectra shown in figure 4.9. This absorption shows that all the synthesized ceria catalysts have a strong UV light absorption capacity [32]. This peak corresponds to the charge

transfer between the full 2p (O) orbital and the empty 4f (Ce) orbital. The bandgap is calculated from the Tauc plot and the plot of CeO_2 g-20 is shown in figure 4.10. The band gap values of the samples are given in table 4.1 and this bandgap confirms visible region absorption.

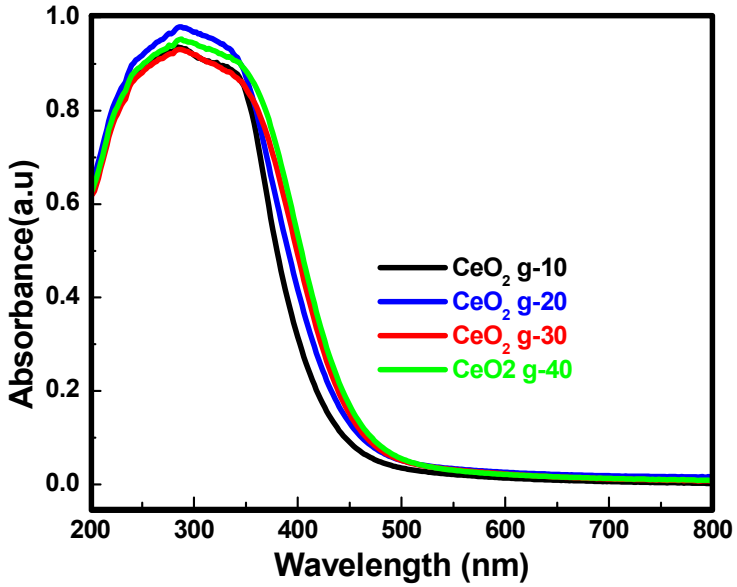

Fig. 4.9 UV- vis diffuse reflectance absorption spectra of ceria catalysts prepared using garlic extract.

It is reported that the bandgap of ceria usually increases with decreasing particle size due to the quantum confinement effect [41]. Particle size obtained from the TEM images of CeO_2 g-10 and CeO_2 g-20 supports the above observation. Thus it is assumed that the major role of the garlic extract in improving the properties of CeO_2 lies in its power to control the nanoparticle agglomeration. Also, the presence of a considerable amount of Ce^{3+} ions in the ceria lattice that aroused as a result of the reducing agents present in the garlic extract, can generate

oxygen vacancies and defects, which has a high influence on the bandgap.

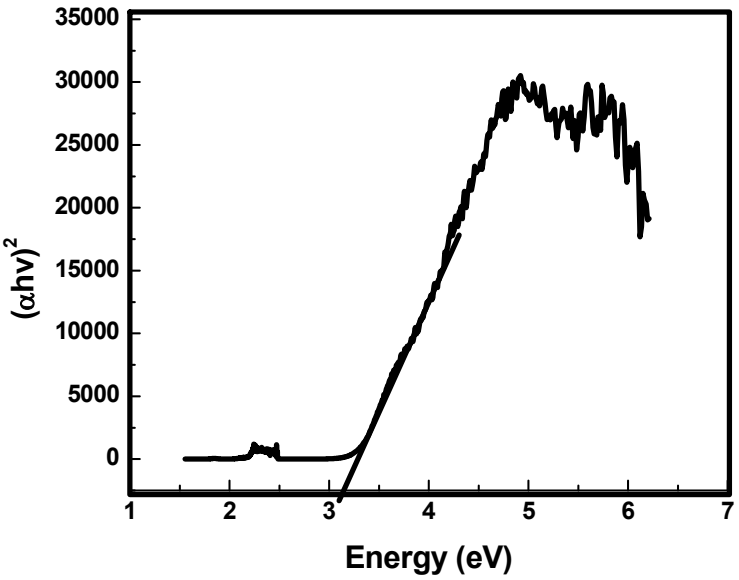

Fig. 4.10 Tauc plot of CeO_2 g-20 for calculating bandgap energy.

To determine the surface area, and pore size distribution, nitrogen adsorption-desorption isotherms at 77 K were recorded. The adsorption-desorption isotherms and the corresponding pore size distribution curves for different samples are shown in figures 4.11 and 4.12 respectively. and the BET surface area and pore size values are given in table 4.2. The isotherms of all the samples can be categorized as type IV with an H4 hysteresis loop according to IUPAC classification, which indicates that the synthesized materials are mesoporous with narrow slit pores [42]. The pore size distributions were calculated by the BJH model from the desorption branch of isotherms thatshows an average pore size between 3 nm to 5 nm.

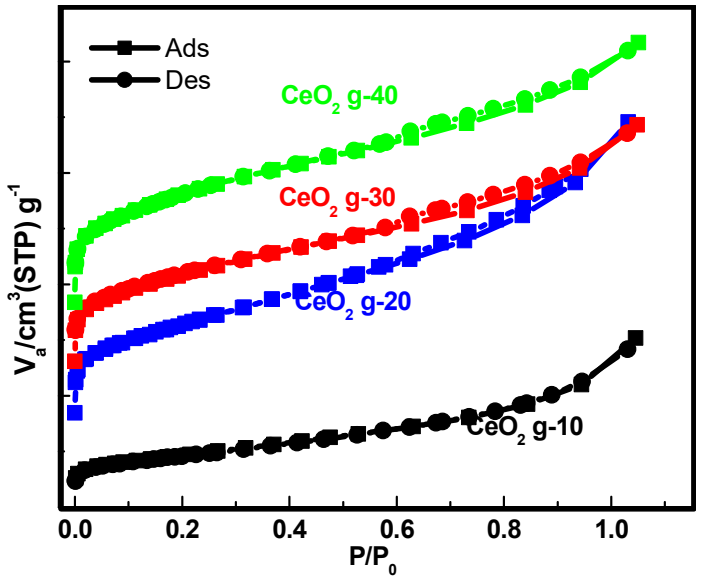

Fig. 4.11 N_2 adsorption-desorption isotherms of ceria catalysts.

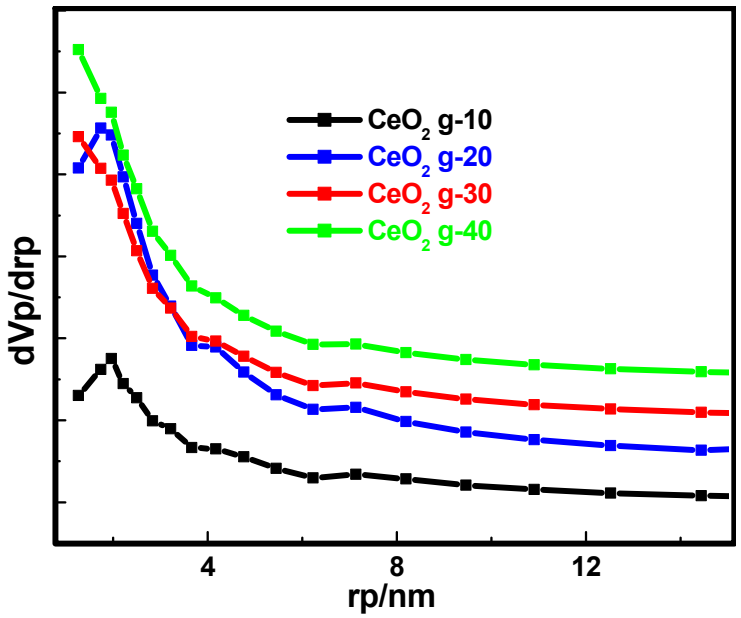

Fig. 4.12 Pore size distribution cures of ceria catalysts.

Raman spectroscopic analysis was carried out to study the surface defects and crystal structure of the samples. The spectraare shown in figure 4.13. A sharp Raman active triply degenerated mode F_{2g} is observed in the case of CeO_2 g-10 around 458 cm^{-1}, which can be attributed to thesymmetrical stretching vibration of the Ce-8O vibrational unit [35].This band is a characteristic of the cubic fluorite structure of ceria as confirmed from the XRD patterns. This F2g band is sensitive to any type of disorder in the crystal lattice created due to the small grain size. The broadening of this peak with an increase in the amount of garlic extract in the preparation is an additional indication of the decreasing of ceria nanoparticles [36].

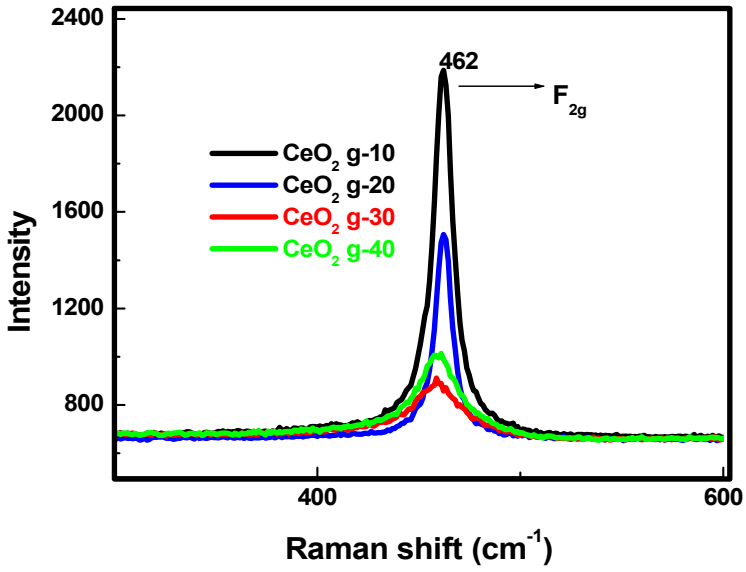

Fig. 4.13 Raman spectra of different ceria catalysts.

XPS analysis was performed to study the surface purity, binding states, and elemental composition of the synthesized samples.

The survey scan, wide scan spectra corresponding to Ce3d and O1s of CeO_2 g-20 are shown in figures 4.14, 4.15, and 4.16.

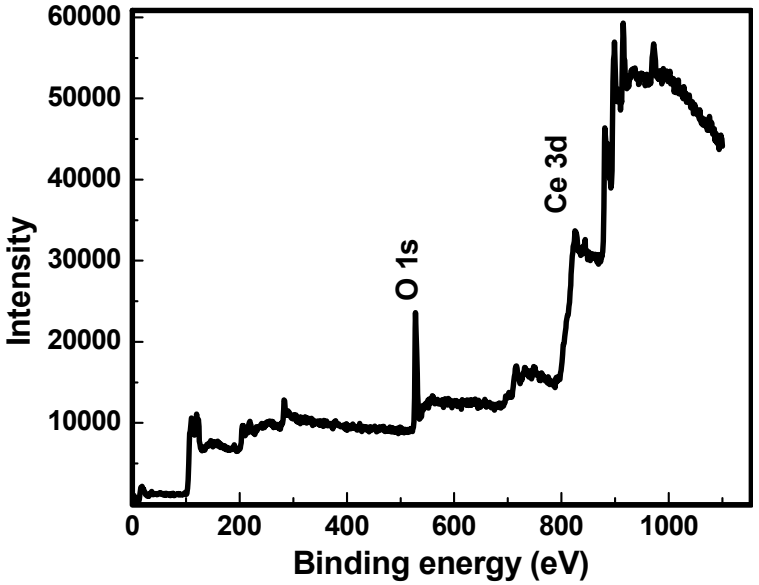

Fig. 4.14 Wide scan XPS spectra of CeO_2 g-20.

The presence of Ce and O elements are confirmed from the survey scan. The peaks observed in the Ce3d core level spectrum indicate that Ce exists in both Ce^{4+} and Ce^{3+} oxidation states in the sample. The peaks at BE values 882.7 eV, 898.8 eV and at 914.7 eV correspond to Ce^{4+} and peaks at 880.5 eV, 887.1 eV, 896.3 eV and at 905.4 eV are characteristic of Ce^{3+}oxidation states in ceria. In the O1s spectrum, the peak at 527.1 eV is due to the Ce-O bond, and that at 529.7 eV corresponds to oxygen vacancies of ceria lattice. A small shoulder peak at 531.5 eV belongs to the chemisorbed oxygen in the surfacehydroxyl groups (HO-) [18, 4, 43- 44].

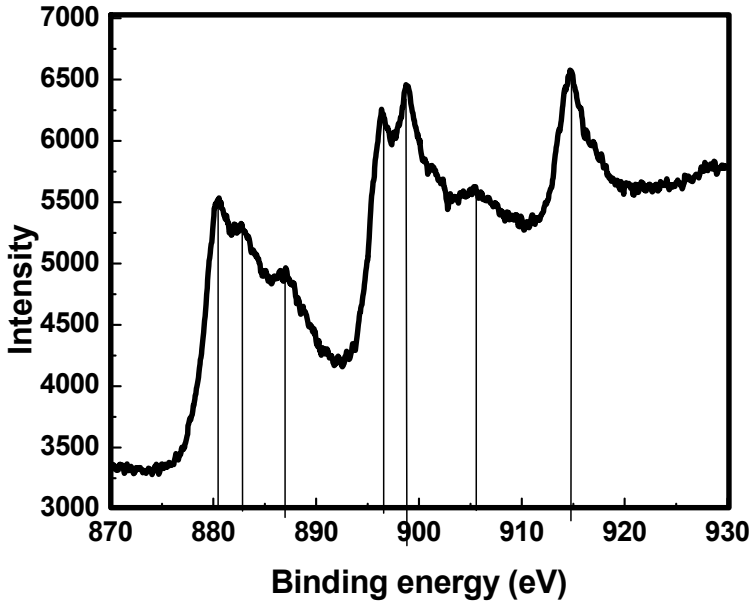

Fig. 4.15 XPS high-resolution spectrum of cerium Ce3d of CeO_2 g-20.

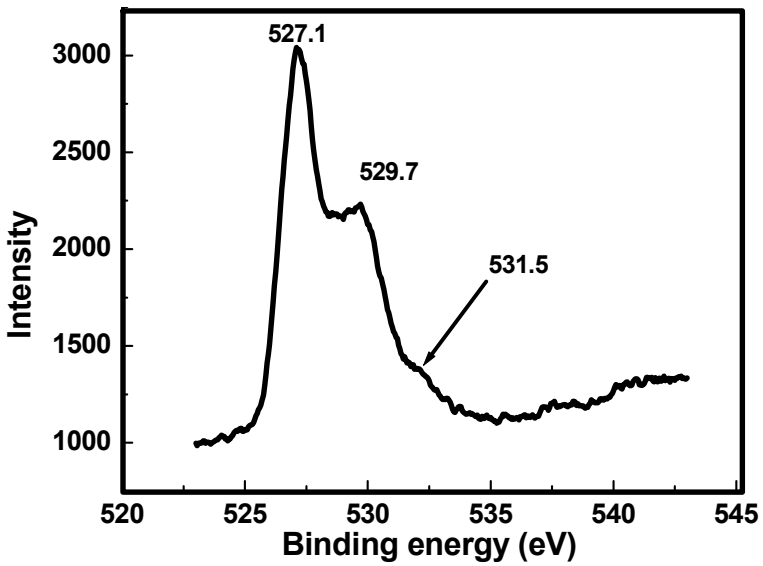

Fig. 4.16 XPS high-resolution spectrum of O1s of CeO_2 g-20.

The ceria samples synthesized in this study have a dual capacity, both as adsorbents and photo Fenton catalysts. CR was used as a model organic pollutant to study the adsorption, and photo Fenton catalytic activity of the synthesized ceria samples. The effects of time on the adsorption of CR on different ceria samples were studied, and the results are represented graphically in figure 4.17. Even though the catalyst CeO_2 g-40 shows the highest adsorption in 10 min itself, CeO_2 g-20 attained the same activity after stirring 60 min. Based on the system prepared using a low amount of garlic extract for efficient performance, CeO_2 g-20 was selected for further adsorption studies. It is observed that the adsorption of CR is well correlated with the surface area of different CeO_2 samples since it is a surface phenomenon.

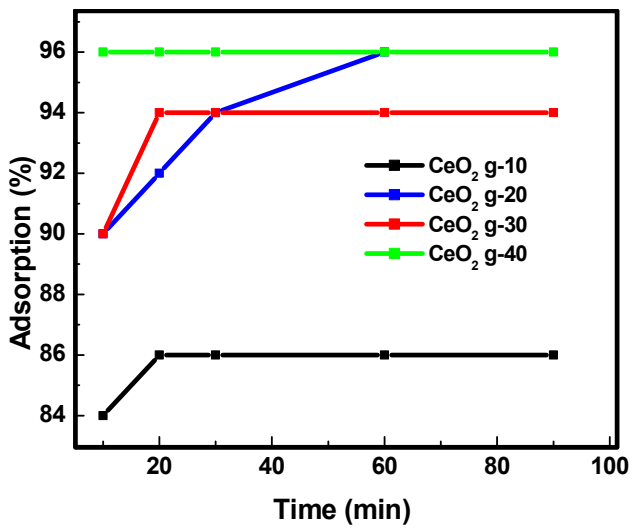

Fig. 4.17 Percentage CR dye adsorption by different ceria samplesat different time intervals. 50 ml CR solution of 20 mg/L concentration with 0.05 g adsorbent was used.

To obtain the best adsorbent dosage, adsorption experiments were carried out by varying the amount of ceria powder added to 50 ml CR solution of 20 mg/L concentration at a stirring time of 30 min (figure 4.18). The percentage of dye removal increased sharply with an increase in the adsorbent weight from 0.01 g to 0.04 g, and then the rate of dye removal is only slightly increased. When the adsorbent dosage reached 0.08 g, the removal percentage attained saturation and remained constant, which indicates that the best adsorbent dosage is 0.08 g.

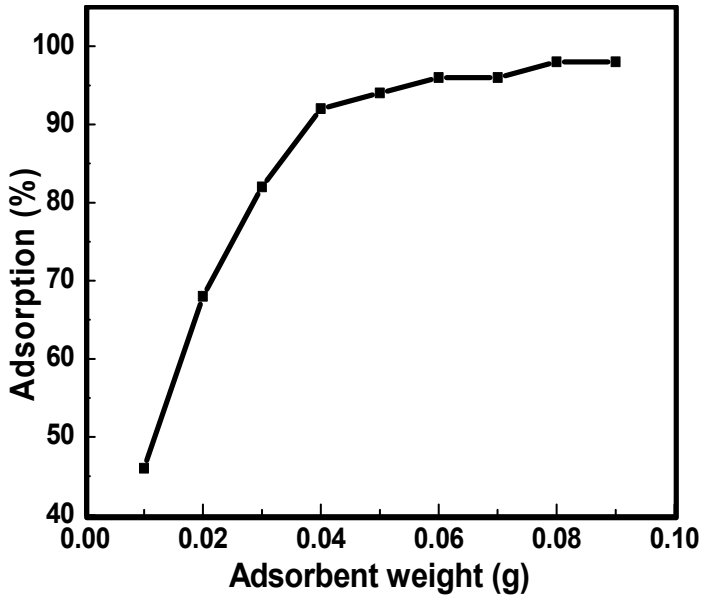

Fig. 4.18 Effect of adsorbent dosage using 50 ml dye solution of 20 mg/L concentration in 30 min stirring.

The effect of dye solution volume was studied by varying the volume of CR of 20 mg/L concentration using 0.08 g adsorbent at a stirring time of 30 min. The percentage removal decreased from 100%

to 80% when the amount of CR solution was increased from 25 ml to 125 ml as given in figure 4.19.

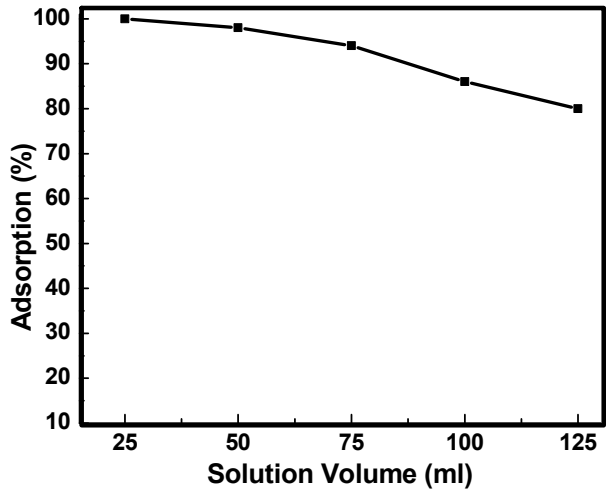

Fig. 4.19 Effect of solution volume using 0.08 g adsorbent in CR solution of 20 mg/L concentration for 30 min adsorption.

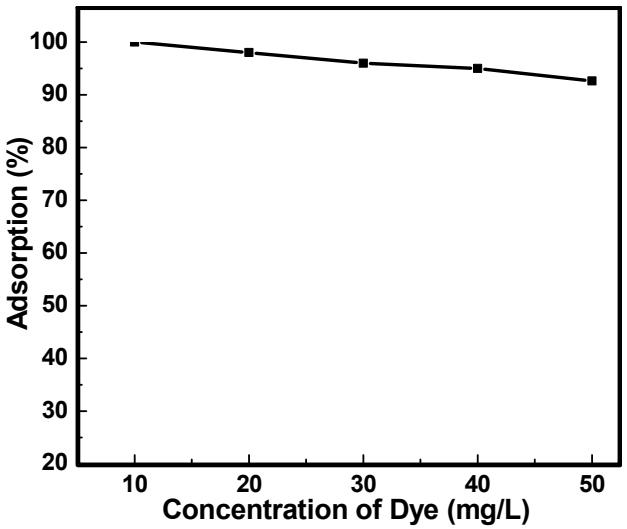

Fig. 4.20Effect of CR solution concentration using 0.08 g catalyst and 50 ml solution for 30 min adsorption.

The effect of dye concentration was also studied by varying the concentration from 10 mg/L to 50 mg/L, using a 50 ml dye solution and 0.08 g CeO_2 g-20 and the results are presented in figure 4.20. The percentage removal decreased only slightly (from 100% to 92.6%) on an increase in the concentration from 10 mg/L to 50 mg/L.

Table 4.3 Maximum adsorption capacities of ceria adsorbents to different dyes.

Adsorbent	Dye	q_e(mg/g)	Reference
Ceria hollow sphere	Acid orange 7	22	45
Ceria multiple layers	Acid orange 7	25	45
Ceria nanoparticles	Congo red	18	18
Ceria nanoparticles	Acid black 210	35.29	15
Powdered activated carbons	Acid black 210	12.95	15
Ceria hollow sphere	Acid black 210	175	15
CeO_2 g-20	**Congo red**	**46**	**This work**

The equilibrium adsorption capacity, q_e, was calculated according to equation 4.1 and is given in table 4.3, and the values are compared with the values obtained from the literature review.

PhotoFenton degradation was also carried out on CR dye solution using different CeO_2 samples in visible light. Time of

degradation reaction of 50 ml, 20 mg/L CR solution using 0.07 g CeO_2 g-20 was varied, and the CR absorption band got reduced in its intensity at the absorption maxima with an increase in the time of adsorption (figure 4.21. and 4.22).

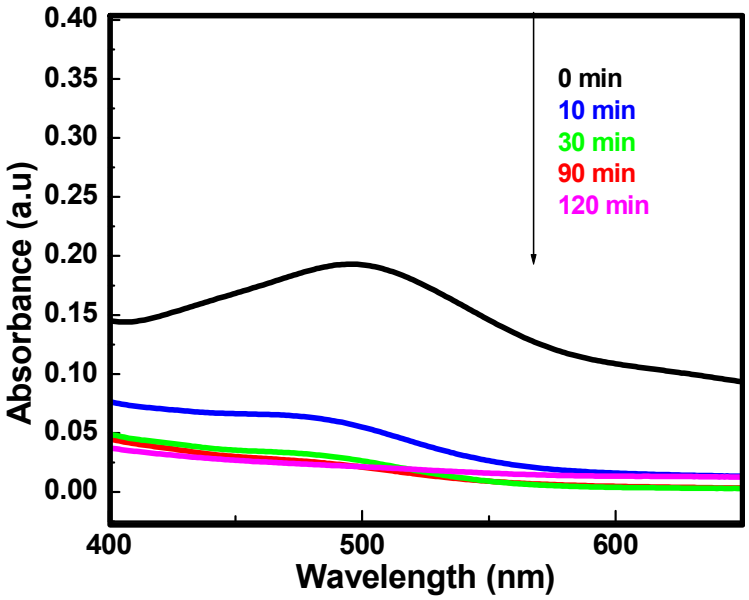

Fig. 4.21UV-vis spectra taken at different time intervals during photo-Fenton degradation of 50 ml CR solution of concentration 20 mg/L using 0.07 g CeO_2 g-20 catalyst and 1 ml 30% H_2O_2.

In figure 4.22, the bands observed at 499 nm and 345 nm in the solution of CR have been assigned to the azo bonds of CR and the naphthalene ring structure of the dye molecule. Since both the absorption bands are decreased in intensity after 120 min of photo Fenton reaction, the result indicates the complete degradation of the dye molecules.

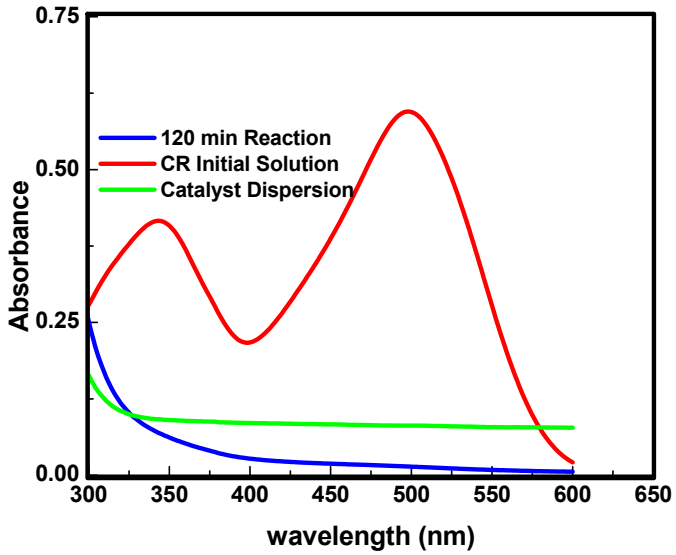

Fig. 4.22 UV-vis absorption spectrum of Congo red solution of 20 mg/L concentration before and after 120 min degradation reaction. 50 ml solution, 0.07 g CeO_2g-20 catalyst, and 1 ml 30% H_2O_2were used.

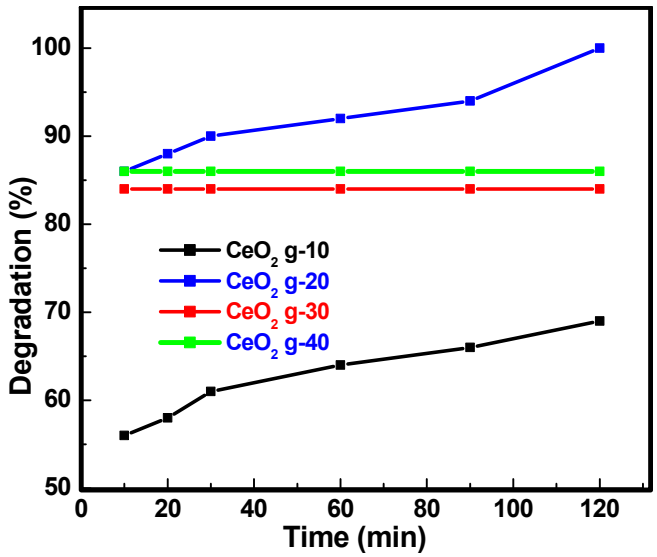

Fig. 4.23 Results on CR dye degradation by different ceria catalysts at different time intervals. 50 ml CR solution of 20 mg/L concentration with 0.05 g catalyst was used.

The degradation reaction results over different CeO_2 systems using a 50 ml CR solution of 20 mg/L concentration at various time intervals are shown in figure 4.23. 1 ml 30% H_2O_2 solution was added in the entire photo Fenton experiments. 100% degradation was obtained in 120 min reaction using 0.07 g CeO_2 g-20 catalyst. Then here also,the CeO_2 g-20 sample was selected for further studies.

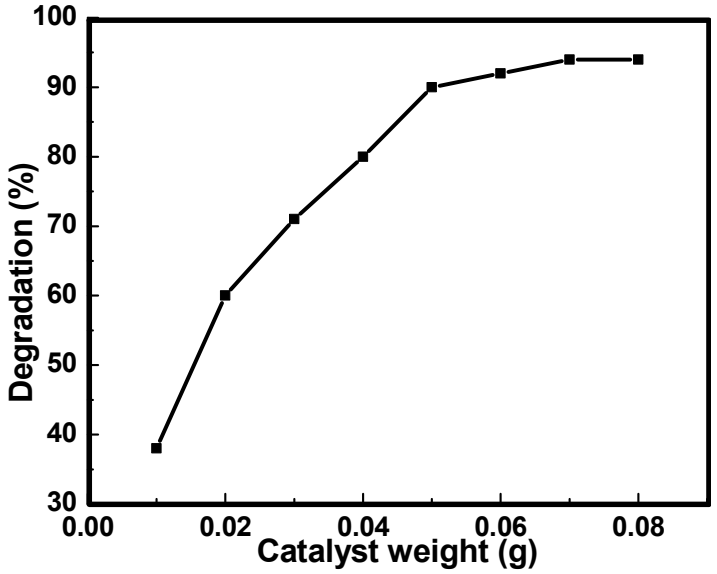

Fig. 4.24 Effect of catalyst weight in the photodegradation of 50 ml dye solution of 20 mg/L concentration in 30 min reaction.

Effect of catalyst weight was studied in 30 min reaction using 50 ml of CR solution having 20 mg/L concentration, and the best catalyst weight leading to 100 % dye degradation was 0.07 g (figure 4.24). Thereafter the activity remained unaffected with catalyst amount indicating active site saturation.

The effect of solution volume was studied by varying the volume of dye solution from 25 ml to 125 ml, and the percentage degradation decreased from 100% to 70% (figure 4.25).

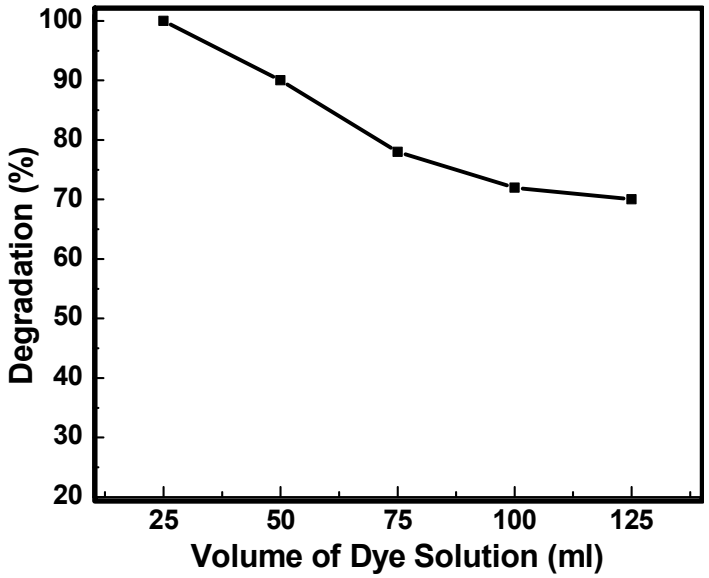

Fig. 4.25 Effect of solution volume on degradation using 0.07 g catalyst, 50 ml CR solution of 20 mg/L concentration for 30 min reaction.

We also studied the degradation activity of the catalyst at different dye concentrations, varying from 10 mg/L to 50 mg/L, where the dye degradation efficiency decreased from 100% to 81% (figure 4.26). The catalyst is thus effective even for the degradation of CR in highly concentrated solutions. The slight decrease in the activity with an increase in both the dye solution volume and concentration is due to the availability of the same number of active sites even with an increase in the number of dye molecules.

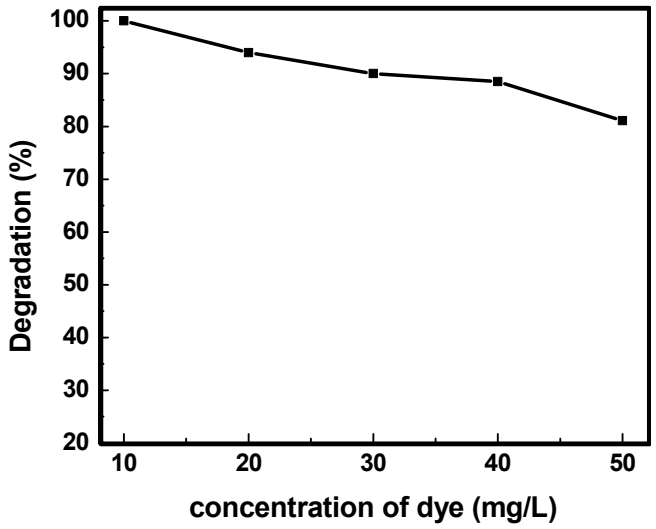

Fig. 4.26 Effect of CR solution concentration in the degradation reaction using 0.08 g catalyst and 50 ml solution for 30 min.

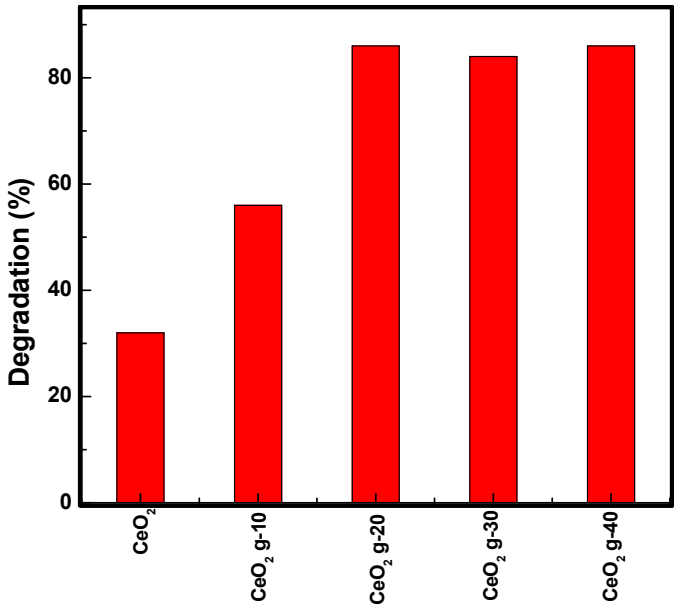

Fig. 4.27 Comparison of photo Fenton activity of catalysts synthesized using garlic extract with that of conventional catalyst for a reaction of 10 min.

A graphical representation of the photo Fenton activity of all the catalystsprepared using garlic extract and its comparison with the catalyst prepared without garlic extract via solution combustion method is given in figure 4.27. All the garlic-derived catalysts showed higher performance in photo Fenton degradation of CR.

The CeO_2 g-20 catalyst after 120 min Fenton reaction was collected, dried, and conducted the FTIR spectral analysis. The FTIR spectra of CeO_2 g-20 before and after the photo Fenton reaction are given in figure 4.28.

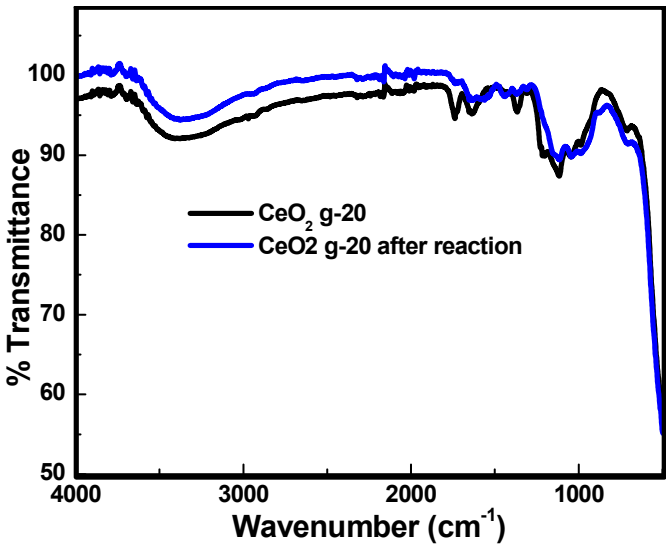

Fig. 4.28 The FTIR spectra of CeO_2 g-20 before and after photo Fenton reaction.

No additional peaks are observed in the FTIR spectrum of CeO_2 g-20 after photo Fenton reaction than that of pure CeO_2 g-20, which points out that all the dye molecules present on the surface of the catalyst are completely degraded, and there are no adsorbed CR molecules remaining on the catalyst surface. Also, the result indicates

that the catalyst structure also remained unaffected after the photoreaction.

4.4 Conclusions

In summary, we have reported a green synthesis of ceria nanoparticles having a particle size in the range of 5 nm to 40 nm by the sol-gel method using various concentrations of aqueous garlic extract. The concentration of garlic extract played an important role in the surface area, crystallite size, and thus on the activity of the nanoparticles. All the synthesized samples could act both as adsorbents and as photo Fenton catalysts in the removal of Congo red dye. The high adsorption properties of the samples are mainly due to the mesoporous nature of the nanoparticles, which was confirmed from the N_2 adsorption-desorption studies. Out of the four, CeO_2 g-20 synthesized using50 ml extract (prepared using 20 g garlic in 100 ml water and 5 g cerium nitrate) provided better results in the removal of Congo red dye in both studies. At the best reaction conditions, 96% Congo red (20 mg/L, 50 ml solution) was removed by adsorption using 0.08 g CeO_2 g-20 within 60 min, and 100% dye is removed by Photo Fenton degradation using 0.07 g CeO_2 g-20 within 120 min reaction.

References

1. G. Gan, J. Liu, Z. Zhu, Z. Yang, C. Zhang and X. Hou,*Chemosphere*, 2017, **168**, 254.
2. A. Asghar, A. A. Abdul Raman and. M. A. W. Daud, *J. Clean. Prod*., 2014, **87**, 826.
3. H. Wang, Y. Zhong, H. Yu, P. Aprea and S. Hao, *J. Alloys. Compd*., 2018,**776**, 96.
4. T. V. M. Sreekanth, P. C. Nagajyothi, G. R. Reddy, J. Shim andK. Yoo, *Sci. Rep*., 2019, **9**, 14477.
5. J. Ouyang, Z. Zhao, S. L. Suib, H. Yang, *J. Colloid. Interf. Sci.*, 2018, **539**, 135.
6. C. L. Hsueh, Y. H. Huang, C. C. Wang andC. Y. Chen, *Chemosphere*, 2005, **58**, 1409.
7. V. Kavitha and K. Palanivelu, *Chemosphere*, 2004, **55**, 1235.
8. A. Khenifi, Z. Bouberka, H. Hamani, H. Illikti, M. Kameche and Z. Derriche, *Environ. Sci. Technol*., 2012, **33**, 1081.
9. H. Lachheb, E. Puzenat, A. Houas, M. Ksibi, E. Elaloui,C. Guillard and J. M. Herrmann, *Appl. Catal. B Environ*., 2002, **39**, 75.
10. A. D. Bokare and W. Choi, *J. Hazard. Mater*. 2014, **275**, 121.
11. H. Li, Q. Gao, G. Wang, B. Han, K. Xia and C. Zhou, *Appl. Surf. Sci.*, 2020, **502**, 144295.
12. I. Zucker, N. Dizge, C. Fausey, E. Shaulsky, M. Sun and M. Elimelech, *RSC Adv*., 2019, **9**, 19408.

13. Y. Li, D. Chen, S. Fan and T. Yang, *J. Taiwan. Inst. Chem. E*, 2018, **96**, 185.
14. J. Wu, J. Wang, Y. Du, H. Li and X. Jia, *J. Nanopart. Res.,* 2016, **18**, 191.
15. J. Hu, W. Deng and D. Chen, *ACS Sustainable Chem. Eng.,* 2017, **5,** 3570.
16. L. Xu and J. Wang, *Environ. Sci. Technol*., 2012,**46,** 10145.
17. X. Wei, Y. Wang, Y. Feng, X. Xie, X. Li and S. Yang, *Sci. Rep.,* 2019, **9**, 4964.
18. K. Li, Y. Zhao, C. Song and X. Guo, *Appl. Surf. Sci.,* 2017, **425**, 526.
19. S. H. Gebre and M. G. Sendeku,*SN Applied Sciences*, 2019, **1**, 928.
20. B. Kumar, K. Smita, L. Cumbal, A. Debut and Y. Angulo, *J. Saudi. Chem. Soc*., 2017, **21**, S475.
21. N. A. Samata and R. M. Nor, *Ceram. Inter*., 2013, **39**, S545.
22. S. Khaghani and D. Ghanbari, *J. Mater. Sci: Mater. Electron*., 2017, **28**, 2877.
23. D. A. Selvan, D. Mahendiran, R. S. Kumar and A. K. Rahiman, *J. Photoch. Photobio. B*, 2018, **180**, 243.
24. G. V. White, P. Kerscher, R. M. Brown, J. D. Morella, W. McAllister, D. Dean, and C. L. Kitchens, *J. Nanomater.,* 2012, **2012**, 730746.
25. A. T. Joseph, P. Prakash and S. S. Narvi, *IJSET.,* 2016, **4**, 2395.
26. Y. Yulizar, H. A. Ariyanta and L. Abdurrachman, *BCREC*, 2017, **12**, 212.

27. M. Stan, A. Popa, D. Toloman, A. Dehelean, I. Lung and G. Katona, *Mater. Sci. Semicond. Process.,* 2015, **39**, 23.
28. M. Stan, A. Popa, D. Toloman, T. D. Silipas and D. C. Vodnar, *Acta. Metall. Sin. Engl. Lett*., 2016, **29**, 228.
29. D. K. Slman, R. D. A. Jalill and A. N. Abd, *J. Pharm. Sci. & Res.,* 2018, **10**, 1590.
30. A. Haider, M. Ijaz, S. Ali, J. Haider, M. Imran, H. Majeed, I. Shahzadi, M. M. Ali, J. A. Khan and M. Ikram, *Nanoscale. Res. Lett*., 2020, **15**, 50.
31. D. Ayodhya and G. Veerabhadram, *J. Mol. Struct.,* 2020, **1205**, 127611.
32. R. R. Muthuchudarkodi and A. Ashli, *Int. J. Chemical Concepts,* 2017, **3,** 293.
33. J. K. Sharma, P. Srivastava, S. Ameen, M. S. Akhtar, S. K. Sengupta and G. Singh, *J. Mater. Res. Bull*., 2017, **91**, 98.
34. N. M. Tomi, Z. D. D. Mitrovi, N. M. Paunovi and D. Z. Mijin, *Langmuir*, 2014, **39**, 11582.
35. M. Darroudi, S. J. Hoseini, R. K. Oskuee, H. A. Hosseini, L. Gholami and S. Gerayli,*Ceram. Int.,* 2014, **40**, 7425.
36. B. S. Rohini, H. Nagabhushana, G. P. Darshan, R. B. Basavaraj, S. C. Sharma and R. Sudarmani, *Appl. Nanosci.,* 2017, **7**, 815.
37. K. Negi, M. Kumar, G. Singh, S. Chauhan and M. S. Chauhan, *Ceram. Inter*., 2018, **44**, 14953.
38. Y. Kodera, A. Suzuki, O. Imada, S. Kasuga, I. Sumioka, A. Kanezawa, N. Taru, M. Fujikawa, S. Nagae, K. Masamoto, K. Maeshige and K. Ono, *J. Agric. Food Chem*., 2002, **50**, 622.

39. S. Gao, W. Zhang, Z. An, S. Kong and D. Chen, *Adsorpt. Sci. Technol.* 2019, **37**, 185.
40. S. R. Ali, R. Kumar, S. K. Kadabinakatti and M. C. Arya, *Mater. Res. Express.*, 2018, **6**, 025513.
41. N. Phonthammachai, M. Rumruangwong, E. Gulari, A. M. Jamieson, S. Jitkarnka and S. Wongkasemjit, *Colloid. Surf. Physicochem. Eng. Asp*., 2004, **247**, 61.
42. S. Gnanam and V. Rajendran, *J. Alloys. Compd*., 2018, **735**, 1854.
43. G. K. Pradhan and K. M. Parida, *Int. J. Eng. Sci. Technol.,* 2010, **2**, 53.
44. L. J. Xu and J. L. Wang, *Appl. Catal. B*, 2013, **142**, 396.
45. L. He, J. Li, Z. Feng, D. Sun, T. Wang, R. Li and Y. Xu, *Appl. Sur. Sci.*, 2014, **322**, 147.

Chapter 5

Fluorescence Sensing of Picric Acid by Ceria Nanostructures Derived from Fenugreek Extract

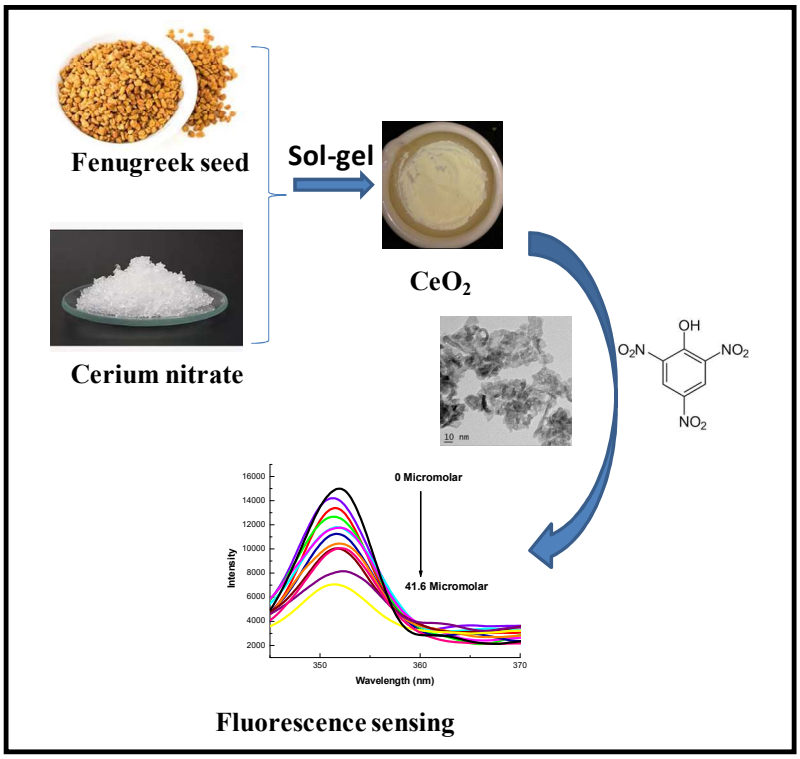

Cerium oxide nanoparticles were synthesized by the sol-gel method using fenugreek extract and have been used for the selective fluorescence sensing of picric acid.

5.1 Introduction

The development of suitable analytical techniques for the selective and sensitive detection of polynitroaromatic compounds (PNACs) is an interesting field of research. 2,4,6-trinitrophenol (TNP is known as picric acid (PA)), 2,4,6-trinitrotoluene (TNT), 2,4-dinitrophenol (2,4-DNP), etc. are the commonly used PNAC ingredients in explosives used in the military [1]. Among these, PA is a strong acid (pK_a = 0.38), which is more explosive in the dehydrated state than TNT. PA is also widely used in different fields such as dye industries, pharmaceuticals, drug analysis, pesticides, rocket fuels, chemical fibers, fireworks, and chemical laboratories [2,3]. Since PA is highly soluble in water, it will even contaminate soil when it is released into the environment from various industries and military installations.

According to The National Institute for Occupational Safety and Health (NIOSH USA) the immediate dangerous to life and health (IDLH) and the Permissible Exposure Limit (PEL) are acute oral toxicity of 75 mg/m3 and in air 0.1 mg/m3 respectively [4]. With the consumption of 3 liters of water per day, the doses corresponding to the PEL and IDLH will be achieved at 1 nM and 1 μM picric acid concentrations in water. American Conference of Governmental Industrial Hygienists (ACGIH) reports that ingestion of 1 -2 g picric acid (approximately 14−28 mg/kg) can cause severe poisoning in humans resulting in headache, vertigo, nausea, vomiting, abdominal

cramps, diarrhea, yellow coloration of the skin, conjunctiva, myalgia, hematuria, albuminuria etc. At higher doses, PA destroys erythrocytes, gastroenteritis, hemorrhagic nephritis, acute hepatitis, stupor, convulsions, and even death. So the development of efficient technologies for sensing PA in the environment in micromolar and nanomolar concentrations is crucial.

Several analytical methods such as surface-enhanced Raman spectroscopy/IR, gas chromatography-mass spectroscopy (GC-MS), ion-mobility spectroscopy (IMS), X-ray diffraction (XRD), nuclear quadrupole resonance, neutron activation analysis, etc., are generally used for the detection of PA [5]. Most methods are limited in their application due to sensitivity issues to interfering analytes, low selectivity, complicated procedures, high cost, long duration of analysis, and expensive instruments. So it is of great significance to find easy and fast responding techniques to overcome these disadvantages. In this context, luminescent-based methods are of high potential due to their high sensitivity, specificity, simplicity, and real-time feasibility [6].

Triethylbenzene derived organic composites, 2,6-divinylpyridine appended anthracene derivatives, Zn(II) - metal-organic framework (MOF), Pentacenequinone nanoaggregates, Rhodamine derivatives, anthracene-functionalized fluorescent tris-imidazolium salts, etc., have been used for the photoluminescent-based detection of PA [1, 6, 7-10]. Huang et al. fabricated reduced graphene

oxide modified with 1-pyrenebutyl–amino-β-cyclodextrin (PyCD) with good sensitivity to PA [11]. Li et al. synthesized carbon nanodots by hydrothermal method using grape skin as a starting material and used it for sensing PA by quenching of fluorescence [12]. Khan et al. synthesized nitrogen and sulphur co-doped water soluble carbon quantum dots (NS-CQDs) through hydrothermal treatment of L-Lysine and thiourea as a fluorescent probe for the selective and sensitive detection of PA in aqueous solution with a detection limit 0.24 μM [13]. Kaja et al. report a gold nanoparticle (AuNP)-based sensor for detection of PA in aqueous condition, based on metal-enhanced fluorescence (MEF) of poly(allylamine) hydrochloride (PAH) showing excellent selectivity for PA with a detection limit of 79 nM [14]. Sadhanala et al. used boron, and nitrogen co-doped carbon nanoparticles (BN-CNPs) synthesized via the hydrothermal method for the selective and sensitive detection of PA [15]. Negi et al. have synthesized α-Fe_2O_3 nanoparticles which have photocatalytic and PA sensing applications [16].

The coexistence of two oxidation states Ce^{3+} and Ce^{4+} on the surface and the ability to interchange between the redox conditions is the basis of sensing applications of ceria [17-19]. The presence of the Ce^{3+} state on the ceria surface forms charge deficiencies compensated by oxygen vacancies and leads to defects. The percentage of Ce3+ oxidation state in ceria is directly related to its fluorescence efficiency [20]. The oxygen vacancies can act as adsorption centers for some quenchers and can quench the intensity of fluorescence of ceria

nanoparticles by which sensing of quencher is possible. Fluorescence properties of cerium oxide nanoparticles have been used in the sensing of peroxide, dissolved oxygen, and tiny metal particles but not much explored in the sensing of PA. Negi et al. have reported nanostructured CeO_2 synthesized using a solution combustion approach for both the photocatalytic and PA sensing applications [21]. A linear range of 0.33 μM – 7.60 μM is observed in their study.

Green synthesis of metal and metal oxide nanoparticles using biological media has been developed to avoid the toxicological attributes of the conventional synthesis routes. Plant extracts, fungus, algae, yeasts, and bacteria can be used as biological media in nanoparticle synthesis [22]. The surface modification of the nanoparticles can be achieved by these methods which may strongly influence the physical, chemical, electrical, and optical properties of the nanoparticles [23]. It is also advantageous in cost-effectiveness, large-scale commercial production, and pharmaceutical applications. Plant extracts are the source of a large number of bioactive compounds used for the synthesis of nanoparticles. Different parts of plants, leaves, stem, bark, seeds, flowers, and root can be used for preparing extracts. The various secondary metabolites in the extract act as a weak base sources, capping agents, chelating, and effective oxidizing agents in the synthesis without requiring any other compounds to produce the nanoparticles [24].

Several research groups have been reported the synthesis of CeO_2 nanoparticles by using plant extracts including *Oleaeuropaea*, G. superb, *Prosopisjuliflora*, *Aloe vera, Acalyphaindica, Daturametel, Origanummajorana L., Sidaacuta, Azadirachtaindica*, *Pisoniaalba,* etc. [23, 25-33]. Elahi et al. have used bio media of *Salvia macrosiphon Boiss* seed extract and Thovhogi et al. used *Hibiscus Sabdariffa* flower extract for the green synthesis of CeO_2 nanoparticles [22,34].

Fenugreek (*Trigonellafoenum-graecum*) is an important spice and aromatic crop that belongs to the family Leguminosae and usually found in Pakistan, India, Egypt, and Middle Eastern countries [35]. Its dried seeds have wide applications as a galactagogue (milk producing agent) in food, flavoring agent, beverages, and medicine. Phytochemical studies revealed that fenugreek seeds contain lysine and L-tryptophan-rich proteins, mucilaginous fiber, and other rare chemical constituents such as saponins, coumarin, fenugreekine, nicotinic acid, sapogenins, phytic acid, scopoletin, and trigonelline [36].

In this work, we report a green method of ceria preparation using the extract of fenugreek for the first time. Material characterization studies revealed the presence of Ce^{3+} sites in the oxide. Qualitative and quantitative sensing of PA at the micro-level was studied by quenching of fluorescence of ceria nanoparticles by the addition of PA having different concentrations.

5.2 Experimental

5.2.1 Catalyst Preparation Using *Trigonellafoenum-graecum* (Fenugreek) Seed extract.

Dried fenugreek seeds were ground to a fine powder. 5 gm of this powder was extracted into 100 ml distilled water by heating at 80 ℃ for 30 min. The mixture was filtered and centrifuged to get the fenugreek extract. In a typical synthesis of CeO_2, 5 g cerium nitrate was dissolved in 50 ml water, and 10 ml of the extract was added to this solution with stirring at room temperature. The yellow-colored suspension was heated at 70 ℃, and stirred continuously until it becomes a gel, which was dried overnight at 90 ℃.

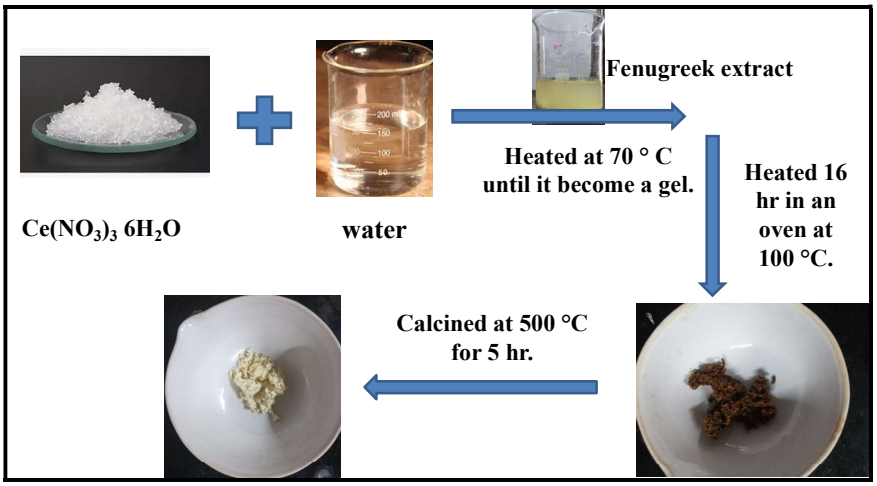

Fig. 5.1 Synthesis of ceria nanoparticles by sol-gel method using fenugreek extract.

The yellow-colored mass obtained was calcined at 500 ℃ for 3 h to get ceria nanoparticles. The sample was designated as CeO_2 FG-10. Three different ceria catalysts were also synthesized by varying the

amount of fenugreek extract as 0 ml, 5 ml, and 30 ml to prepare the samples, CeO_2 FG-0, CeO_2 FG-5, and CeO_2 FG-30 respectively. A pictorial representation of the synthesis procedure is shown in figure 5.1.

5.2.2 Detection of Picric Acid using Fluorescence Spectroscopy

Fluorescence properties of the synthesized samples were studied by measuring the fluorescence spectra using PERKIN-ELMER FL 6500 spectrometer with 150 W Xe lamp as the excitation source. For the detection of picric acid, ceria nanoparticles of concentration 3 mg/50 ml water were used. To 3 ml of this dispersion, PA at different concentrations were added, and the fluorescence spectrum was recorded at an excitation wavelength of 315 nm. Fluorescence quenching was also studied in tap water, well water, and river water (from Bharathapuzha, Velliyamkallu, Pattambi) to evaluate the applicability of the method in sensing picric acid in real water samples.

5.2.3 Selectivity Evaluation

Selectivity of the system towards picric acid is analyzed by studying the fluorescence quenching in the presence of nitro compounds and phenolic compounds. In a typical procedure, to 3 ml of ceria dispersion (3 mg/50 ml), whose fluorescence intensity is quenched by adding 2 mM picric acid, other compounds of the same concentration were added to measure the effect of fluorescence quenching.

5.3 Results and Discussion

In the sol-gel process, the metal ions have to distribute uniformly throughout the sol and have to maintain in the transformation to gel also. Here, an eco-friendly method is used for CeO2 formation in the presence of fenugreek extract. The phytochemicals present in the fenugreek seed extract including capping and a stabilizing agent such as antioxidants, saponins, flavonoids, polyphenols, carbohydrates, mucilages (mostly galactomannans), and proteins operate as size controlling agents, and averts nucleation and coalescence of nanoparticles; as a result, regulates the aggregation or agglomeration of nanoparticles. Phenolic compounds present in the extract can facilitate the complexation of cerium cations (Ce^{+3}) to create an initial molecular matrix by coating and stabilizing the cerium species, resulting in the formation of CeO_2-NPs.

The X-ray diffraction patterns of the ceria samples synthesized using fenugreek extract are given in figure 5.2. The diffraction peaks at 28.4°, 32.9°, 47.3°, 56.2°, 69.2°, and 76.6° are the diffraction from the planes (111), (200), (220), (311), (400) and (311) respectively of face-centered cubic fluorite (fcc) structure (JCPDS 65-5923) of ceria lattice with space group Fm3m [37,38]. The relatively broad diffraction peaks indicate that the synthesized samples wih fenugreek extract have small crystallites. The lattice parameter of the cubic fluorite CeO_2 obtained from the (111) plane of the ceria (given in table 1) is slightly higher than the reported value of its bulk counterpart (a = 0.54113 nm) in the

standard data JCPDS 34-0394 [39,40]. This slight increase in the lattice parameter in nanocrystals is attributed to the increased amount of oxygen vacancies [40]. The lattice parameters increase slightly with the amount of extract used in preparation. The presence of oxygen vacancies also contributes to lattice strain in crystals, which can be obtained from the Williamson Hall plot (figure 5.3) and the calculated lattice strain is presented in table 5.1.

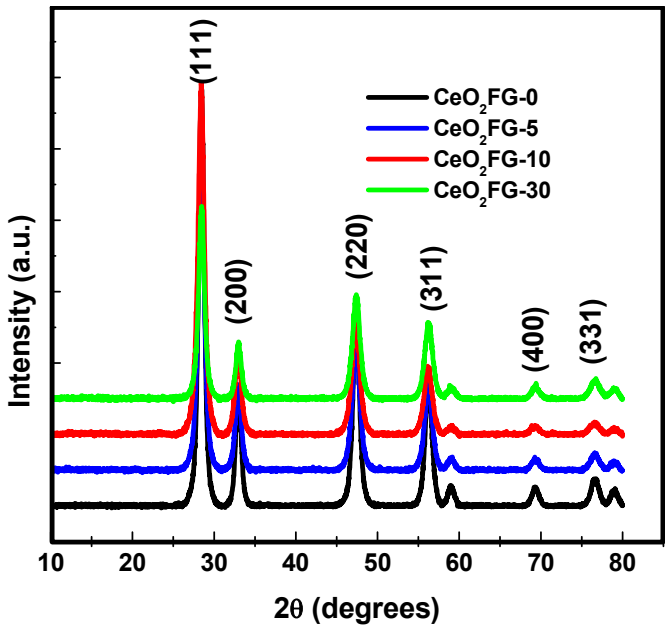

Fig. 5.2 XRD patterns of ceria samples synthesized using different concentrations of fenugreek extract.

FTIR spectra of the synthesized CeO_2 NPs are analyzed to confirm the role of saponins, proteins, carboxylic acids, and other phytochemicals in the capping and stabilization of NPs (figure 5.4).

Table 5.1 Physical characteristics of ceria nanoparticles

Sample	Crystallite Size (nm)	Lattice parameter (nm)	Lattice strain	Bandgap energy (eV)
CeO_2 FG 0	9.96	0.5421	0.0033	3.08
CeO_2 FG 5	9.94	0.5423	0.0030	3.03
CeO_2 FG 10	8.89	0.5424	0.0045	3.01
CeO_2 FG 30	9.67	0.5426	0.0038	3.02

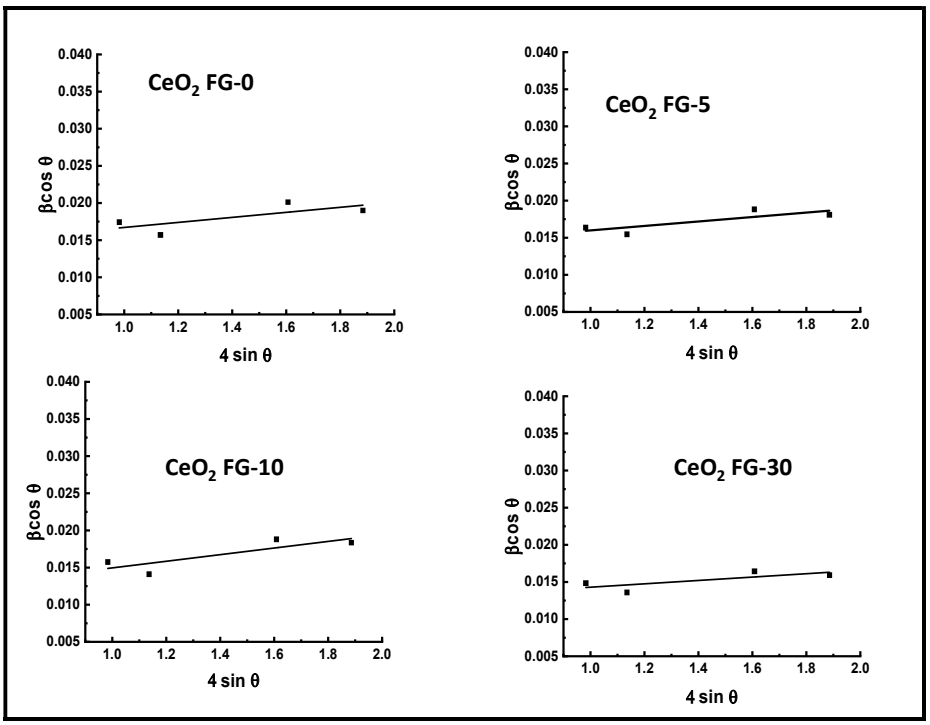

Fig. 5.3 Williamson Hall plot of ceria systems prepared with and without using fenugreek extract.

The FTIR spectra of the CeO_2-NPs shows absorption peaks at 3403 cm^{-1}, 1636 cm^{-1}, 1531 cm^{-1}, 1306 cm^{-1}, 1047 cm^{-1}, 680 cm^{-1} and 450 cm^{-1}. The broad absorption bands at 3403 cm^{-1} are due to the stretching vibration of water molecules physically adsorbed on the surface of ceria particles and also from surface hydroxyl or N-H groups on CeO_2.

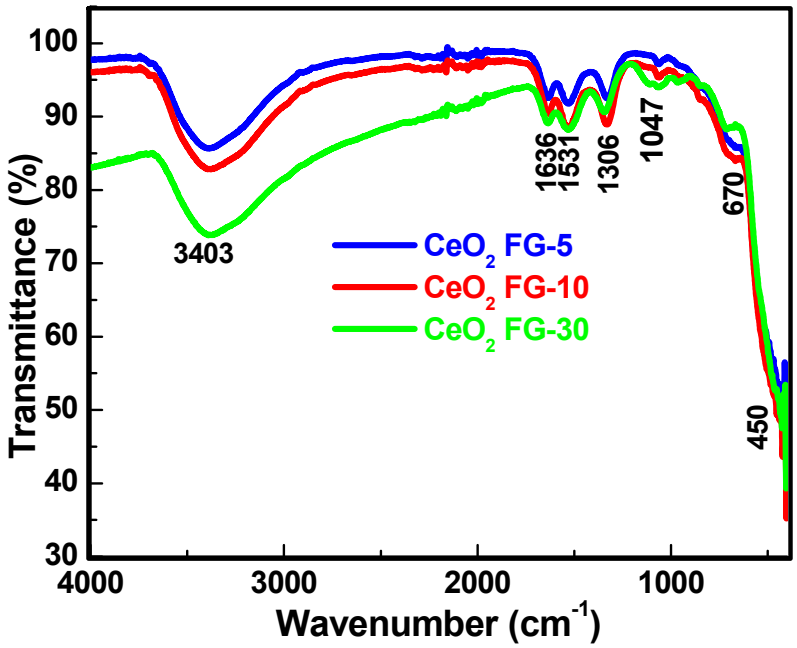

Fig. 5.4 FTIR spectra of ceria nanoparticles.

The band at 1624 cm^{-1} is due to the bending O-H vibrations of adsorbed water. Bands observed at 1531 cm^{-1}, and 1047 cm^{-1} in the samples synthesized using fenugreek extract (amide II band and C–O/C-N stretching respectively) indicate the involvement of proteins, phytochemicals, etc., in the formation of ceria nanoparticles as capping

and stabilizing agents. The peaks observed at 450 and 680 cm^{-1} are attributed to the symmetric stretching of Ce-O and Ce-O-Ce vibrations respectively. Ce-OH bending is observed at 1306 cm^{-1} [50]. The FTIR analysis of biosynthesized CeO_2-NPs thus shows the prominent role of the above-mentioned phytochemicals/plant components in the formation and stabilization of CeO_2-NPs and suggested the capping of these phytochemicals on the surface of the CeO_2-NPs.

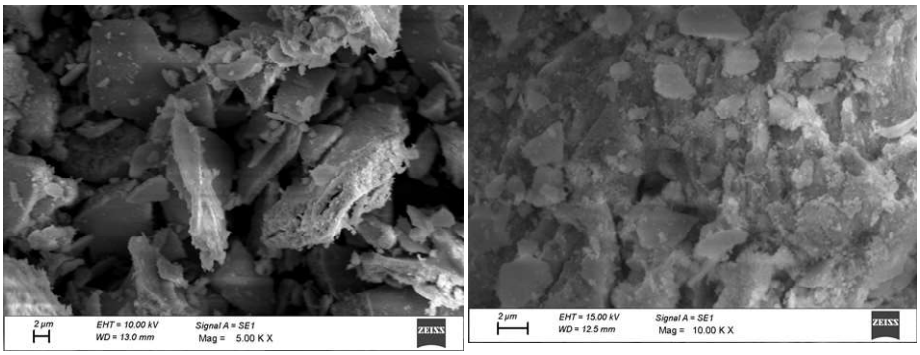

Fig. 5.5 SEM images of sample CeO_2 FG-10.

The morphology of the catalyst, CeO_2 FG-10, was obtained from SEM images (figure 5.5.). Agglomerated nanocrystals in flake-like nature are observed in the SEM. Additional information about the nanostructure of CeO_2 FG-10 was obtained from TEM images given in figure 5.6 and is compared with that of the CeO_2 FG-0 sample prepared without the addition of fenugreek extract. The nanostructures show a random morphology of spheres and rods.

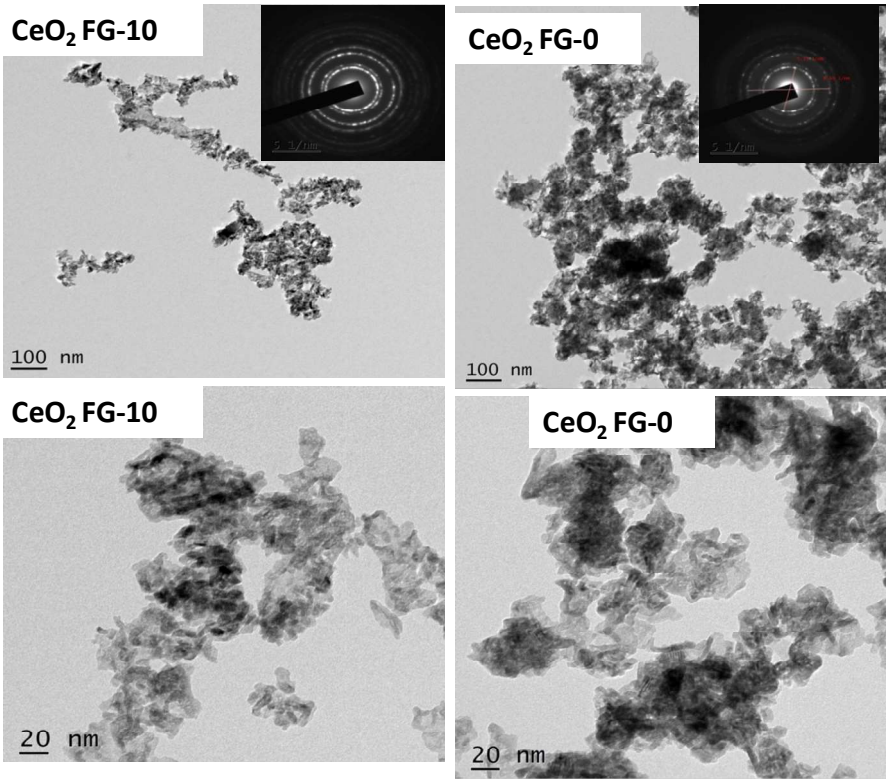

Fig. 5.6 TEM images of sample CeO_2 FG-10 and CeO_2FG-0 samples. SAED patterns are shown inset.

It is clear from the images that the particles are more agglomerated in CeO_2 FG-0 compared to CeO_2 FG-10. Selected area diffraction patterns are also shown in the figures, and the bright circular rings in the SAED pattern indicate the polycrystalline nature of the nanoparticles. The particles were bigger in the CeO_2 sample prepared in the absence of extract. Particle size lies in the range of 5-20 nm in CeO_2 FG-10 and 10-30 nm in CeO_2 FG-0. The result reveals the effect of fenugreek on the preparation of smaller nanoparticles of CeO_2 with uniform size distribution.

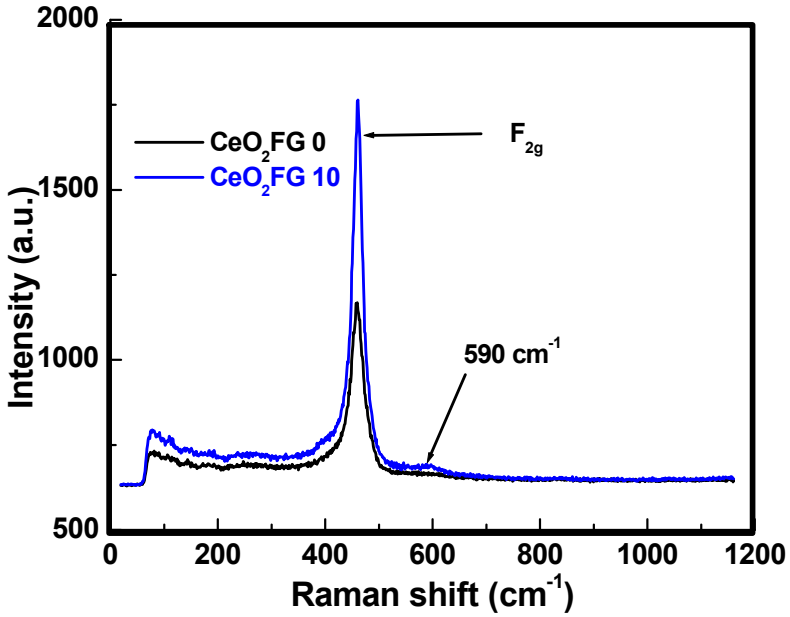

Fig. 5.7 Raman spectra of samples CeO_2 FG-0 and CeO_2 FG-10.

The defects and oxygen vacancies in the synthesized ceria crystals were characterized by Raman spectral analysis (figure 5.7.). The intense peak at 462 cm^{-1} is the Raman active vibrational mode of (F_{2g}), characteristic of the pure cubic phase of ceria [42]. This F2g mode is ascribed to the symmetrical stretching mode of oxygen atoms around cerium ions in the FCC ceria [39]. The higher intensity, and a slight shift towards a higher wavenumber of this band can be attributed to the high crystallinity of the nanoparticles. The less intense band at around 590 cm^{-1}observed in the sample prepared with fenugreek extract is due to the presence of oxygen vacancies generated by the charge compensation due to the presence of Ce^{3+} state [43,44].

DR UV-vis absorption spectra of the samples are presented in figure 5.8. According to literature, the two absorption bands observed in this spectra at 282 nm and 344 nm are attributed to the charge transfer transitions $Ce^{3+} \rightarrow O^{2-}$ and $Ce^{4+} \rightarrow O^{2-}$ respectively [45]. The presence of a band at 282 nm is an additional indication of the presence of Ce^{3+} ions in the prepared systems.

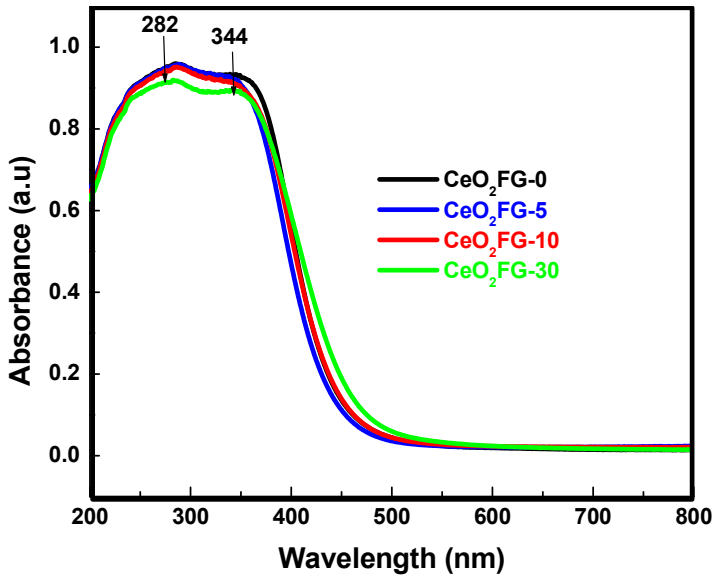

Fig. 5.8 DR/UV-vis absorption spectra of the prepared ceria samples.

The bandgap energy was calculated by using the Tauc plot [46]. The Tauc plot of all the samples is presented in figure 5.9 and the bandgaps calculated are given in table 5.1. We observe a decrease in the bandgap with the amount of fenugreek extract used in the preparation, which may be due to the increase in the Ce^{3+} concentration, and the corresponding formation of a higher number of defects in the crystals [47]. A defect-related band is thus observed

within the bandgap of the material that resulted in a decrease of bandgap as evident from the bandgap values obtained from the Tauc plot.

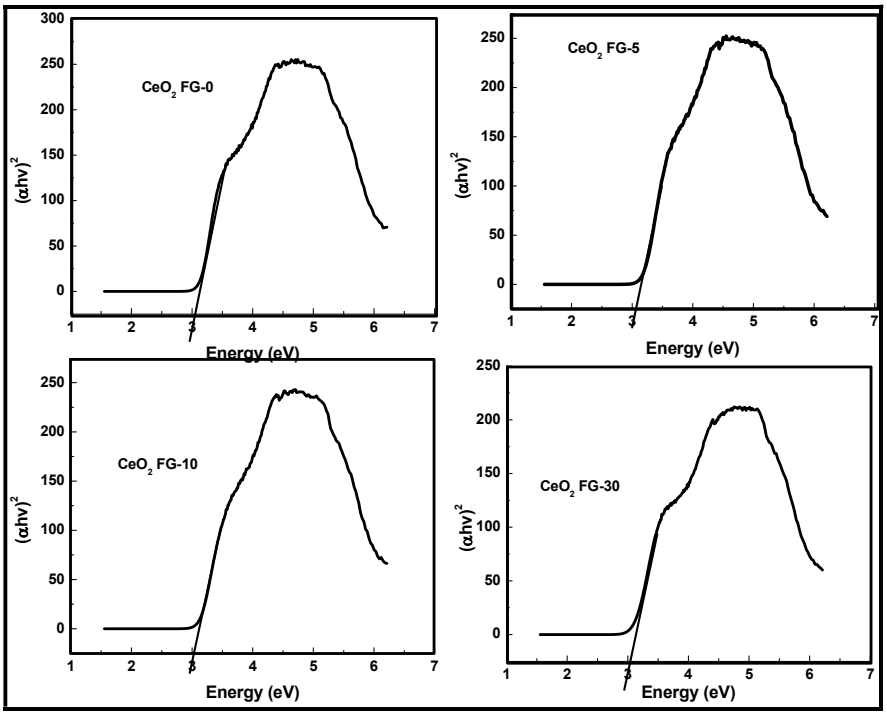

Fig. 5.9 Tauc plot of ceria samples.

Nitrogen adsorption-desorption isotherms were recorded at 77 K to determine the surface area and pore size distribution. The adsorption-desorption isotherms and the corresponding pore distribution cures for different samples are shown in figures 5.10 and 5.11 respectively and the BET surface area and pore size parameters are given in table 5.2. The isotherms of all the samples are type IV with H3 hysteresis loop according to IUPAC classification, which indicates that the synthesized materials are mesoporous in nature and

aggregates of plate-like particles forming slit-like pores [48]. The pore size distributions were calculated by the BJH model from the desorption branch of isotherms and show an average pore size between 10 nm to 20 nm. All the ceria samples synthesized with the extract showed a slight increase in the surface area compared to the one prepared without using the extract. Maximum surface area and pore volume are shown by the sample CeO_2 FG-10, which indicates more availability and exposure of active sites of that sample.

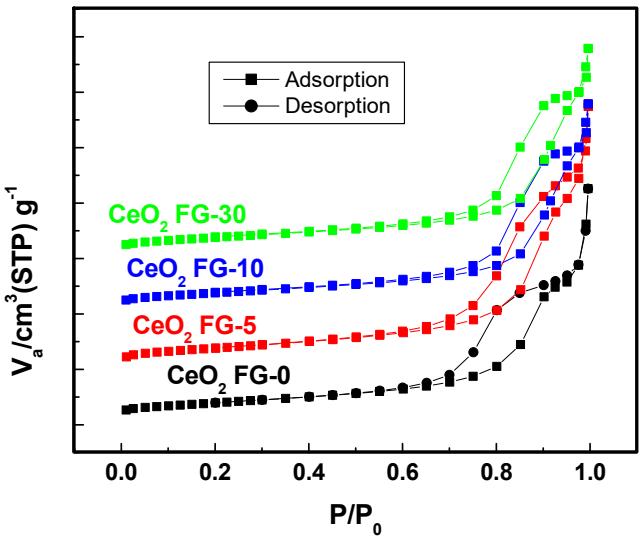

Fig. 5.10 N_2 adsorption-desorption isotherms of ceria systems.

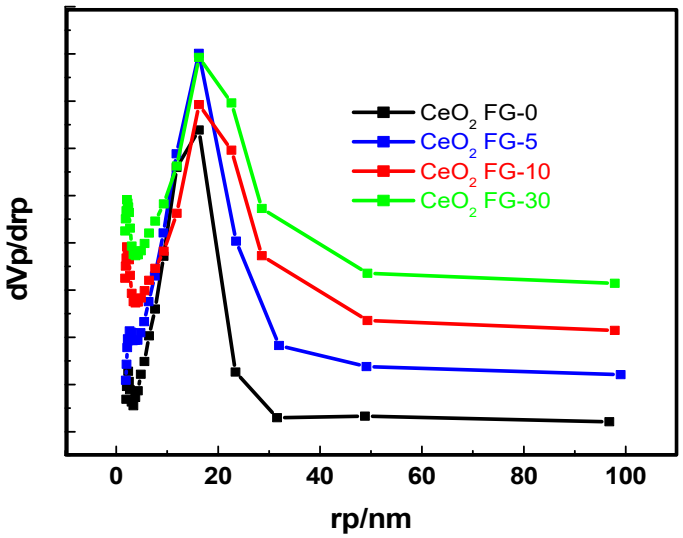

Fig. 5.11 Pore size distribution cures of ceria systems.

Table 5.2 The surface area and pore structure parameters of the samples

Sample	BET SA ($m^2 g^{-1}$)	Pore size (nm)	Porevolume ($cm^3 g^{-1}$)	LOD (μM)
CeO_2 FG-0	60.55	16.7	0.2761	2.66
CeO_2 FG-5	68.33	17.8	0. 2626	0.33
CeO_2 FG-10	69.96	17.8	0. 3193	0.33
CeO_2 FG-30	66.96	21.1	0.2105	0.66

The valence states of cerium were further investigated by XPS analysis and are reported in figure 5.12. The Ce3d level spectrum (figure 5.13) was analyzed in detail to study the oxidation state of Ce in the sample. The peaks show two spin-orbit components (Ce $3d_{3/2}$ and Ce $3d_{5/2}$) and each of these components shows further subcomponents due to the final state effect [49]. Ce 3d peaks are observed in the range of 880 eV to 920 eV. The peaks observed at 880.2 eV, 883.1 eV, 887.5 eV, 896.0 eV, and 898.4 eV belongs to the Ce $3d_{5/2}$ multiplets and the other peaks centered at 901.3eV, 904.3eV, 907.9 eV, 914.5eV and 921.2 eV correspond to the multiplet of Ce $3d_{3/2}$ [26,50]. The presence of peaks at 880.2, 901.3, 904.3 eV, and 883 eV in the Ce 3d spectrum indicates the existence of cerium ions as Ce^{3+} in the crystal lattice, and this support the information obtained from UV-DRS analysis [51].

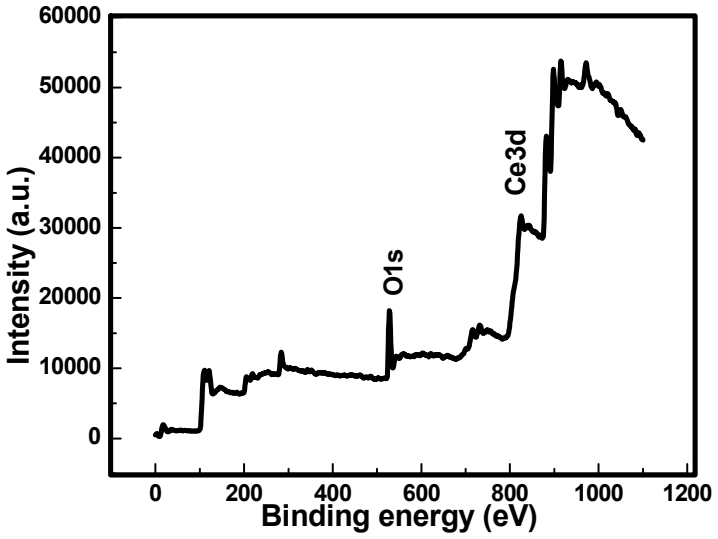

Fig. 5.12 XPS wide scan spectra of sample CeO_2 FG-10.

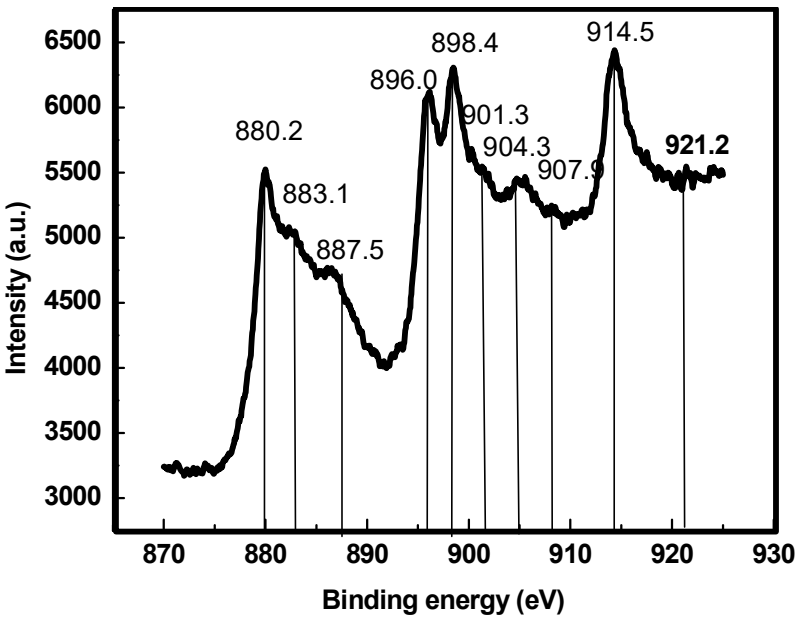

Fig. 5.13 Ce3d core level spectra of sample CeO_2 FG-10.

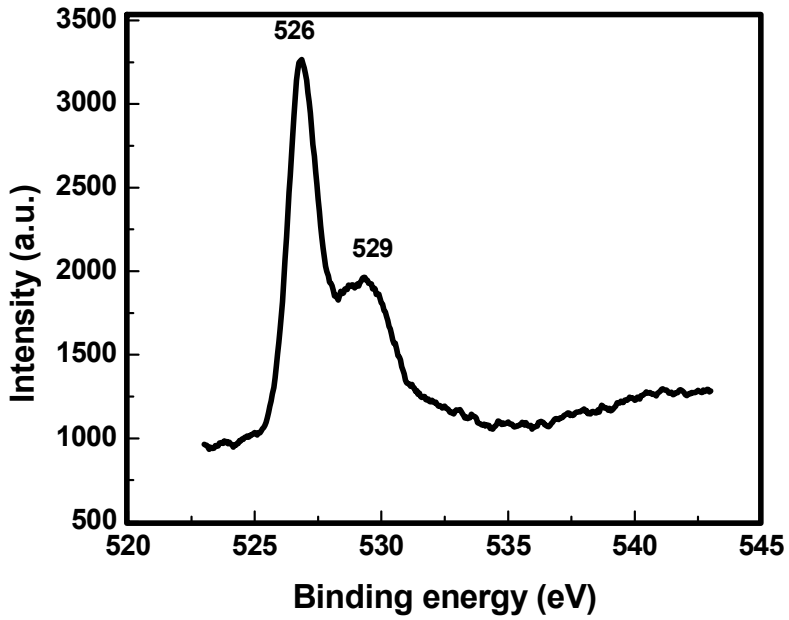

Fig. 5.14 O1s spectra of CeO_2 FG-10 sample.

The peaks corresponding to Ce^{4+} are of comparatively higher intensity, indicating the higher Ce^{4+}/Ce^{3+} ratio in the sample [49, 52]. In the O 1s core-level XPS spectrum (figure 5.14), the peak at 530 eV is originated from the lattice oxygen atoms, and the peak at 526 eV is due to chemisorbed oxygen atoms of hydroxyl groups on the surface of CeO_2 [43].

The photoluminescence properties of ceria nanostructures were studied for the sensing of picric acid using fluorescence spectroscopy. The sensing of 4 μM PA with CeO_2 FG-10 nanoparticle dispersion is shown in the figure. 5.15.

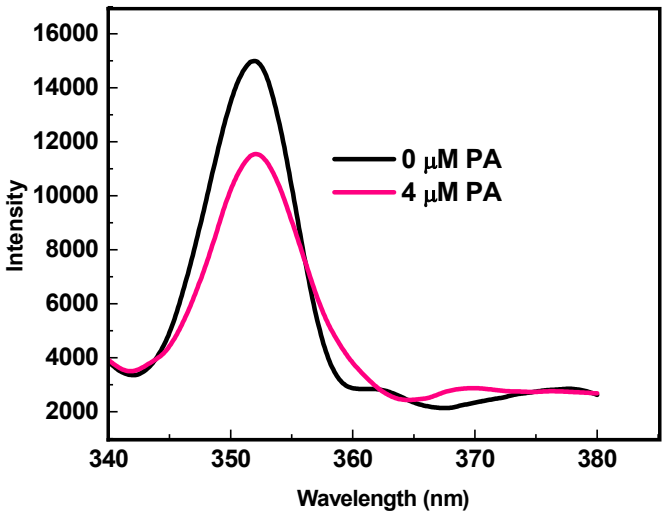

Fig. 5.15 Quenching of fluorescence intensity of CeO_2 FG-10 on the addition of 4μM PA.

The fluorescence band of ceria observed in the UV region is related to the bandgap associated with ceria nanoparticles. In this

spectrum, the emission band of ceria centered at around 351 nm corresponds to the bandgap of ceria. It originated from the recombination of electrons from the localized Ce-4f state to holes in the O-2p valence band. The bandgap of ceria is also related to the size of nanoparticles, which in turn to the concentration of Ce^{3+} on the surface [47]. Upon addition of PA, quenching of fluorescence occurred and the PL emission got reduced in its intensity.

The fluorescence intensity of all the ceria samples synthesized in the presence of fenugreek has higher intensity compared to the system synthesized by the conventional method in the absence of the extract (figure 5.16). Also from the fluorescence intensity comparison, it is observed that the intensity of CeO_2 FG-10 was found to be highest among all the CeO_2 samples.

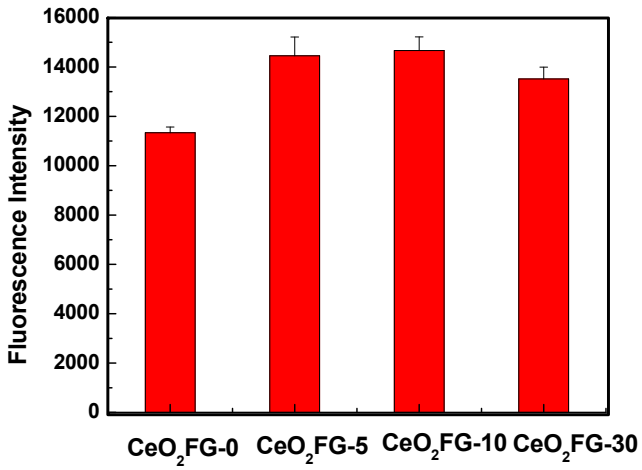

Fig. 5.16 Comparison of fluorescence emission intensity of all the prepared samples.

The violet emission band observed at 430 nm (spectra are given in figure 5.17.) is related to the oxygen defect states (F-centers) that exist between the Ce 4f band and O 2p band; and also corresponds to Ce^{3+} sites in the ceria nanostructures [38]. The intensity of this band is directly linked to the concentration of Ce^{3+} ions in the structure. The emission intensity of this band also is highest for the CeO_2 FG-10 sample, which indicates more number of defects and Ce^{3+} concentration in that sample, and this particular ceria system is thus used for the further sensing of picric acid.

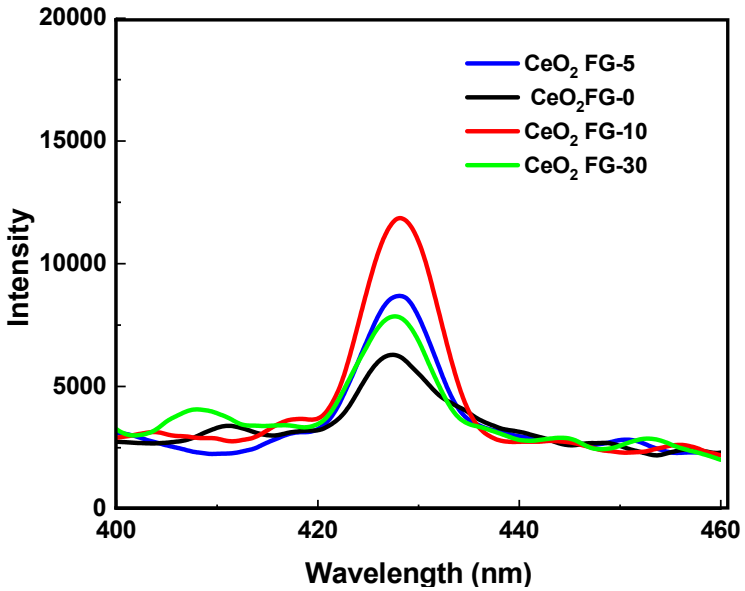

Fig. 5.17 The violet emission band of the prepared ceria systems under excitation of 330 nm.

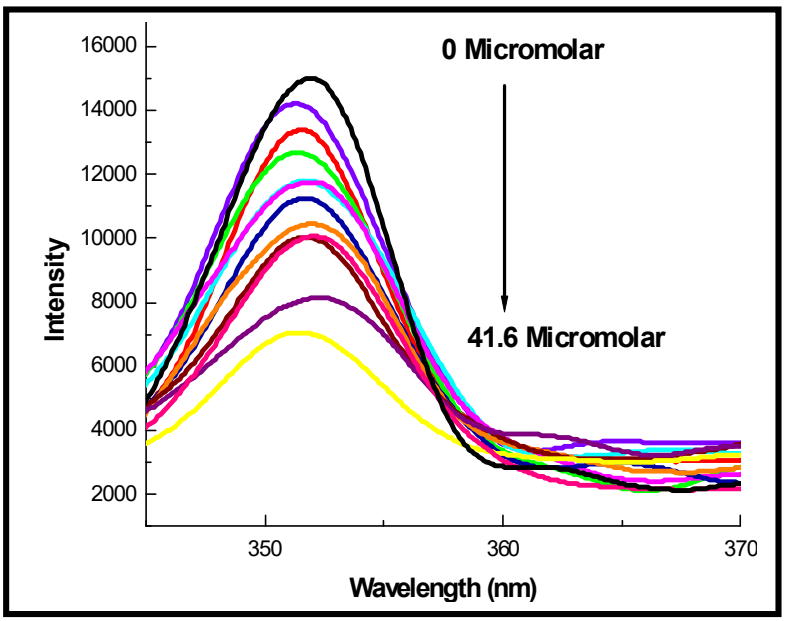

Fig. 5.18 Fluorescence emission spectra of CeO_2 FG-10 with different concentrations of picric acid from 0 to 41.6 μM.

Fluorescence sensing of picric acid was also carried out by adding different concentrations of picric acid to the aqueous dispersion of the CeO_2 FG-10, and the change in intensity of fluorescence was recorded at the excitation wavelength of 315 nm wavelength. It is observed that on increasing the concentration of picric acid, the fluorescence intensity at 351 nm got decreased with PA concentration, indicating PL quenching as represented in figure 5.18. The relationship between quenching in PL intensity and the quencher concentration is represented in figure 5.19 and the linear part of it (figure 5.20) can be described by Stern –Volmer equation (equation 5.1),

$$\mathbf{I_0/I = 1 + K_{SV}[Q]} \qquad \text{eqn (5.1.)}$$

where I_0 and I are the fluorescence intensities without and with the addition of quencher, PA, [Q] is the concentration of PA and $K_{SV}$is the Stern – Volmer quenching constant which indicates the sensitivity of the nanoparticles to sense the quencher [2].

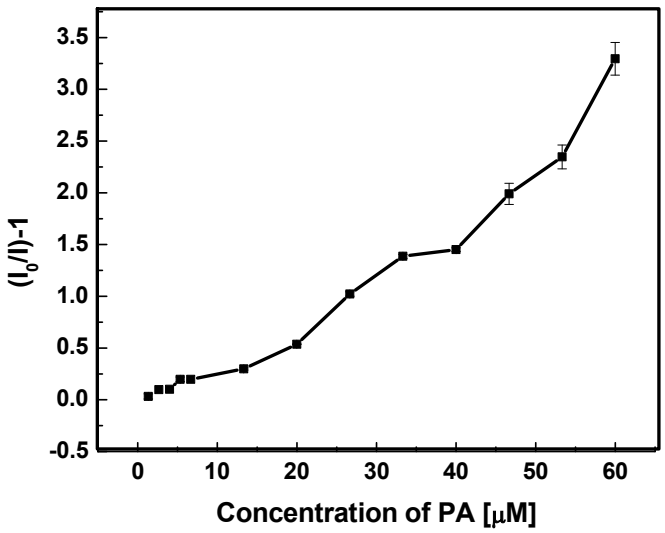

Fig. 5.19 Variation of relative fluorescence intensity with picric acid concentration.

The value of K_{SV}, obtained from the slope of the linear fit (figure 5.19) up to 41.6 μM concentration of PA, was found to be 5.754 x 10^5 M^{-1} and the linear regression coefficient (R^2) is observed to be 0.9890. The high value of K_{SV} in this study indicates a strong interaction between PA and ceria nanostructure.

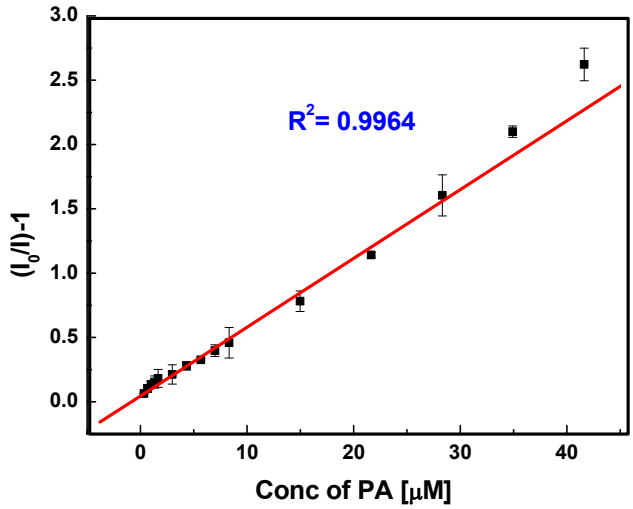

Fig. 5.20 Linear plot of $(I_0/I)-1$ versus picric acid concentration in the range 0.33 – 41.6 μM.

The LOD values of all the other CeO_2 samples in PA sensingwere also determined and the results are given in table 5.2. All the ceria nanosystems synthesized using fenugreek extract showed better LOD values compared to CeO_2 prepared without the addition of extract, which is due to the combined effect of the smaller particle size, less agglomeration of particles and higher surface area of fenugreek assisted CeO_2 samples. Since the level of picric acid exceeding 1 μM will badly affect the health, LOD should be less than this value. LOD of bare ceria is 8 times higher (2.66 μM) than that of the best sample, CeO_2 FG-10 (0.33 μM), which confirms the necessity of fenugreek in present CeO_2 preparation for its use in the effective sensing of PA.

A linear curve in the S-V plot indicates the participation of a single mechanism, whereas a non-linear portion in the curve of the S–

V plot indicates a mixture of mechanisms governing the quenching [53]. In the present study, the quenching mechanism at a lower concentration of picric acid is static, which can be due to the formation of the ground-state complex (GSC) that is confirmed by a shift in the absorption maxima of the ceria nanoparticles after the addition of the picric acid along with the shift in the bandgap of ceria (figure 5.21 and 5.22).

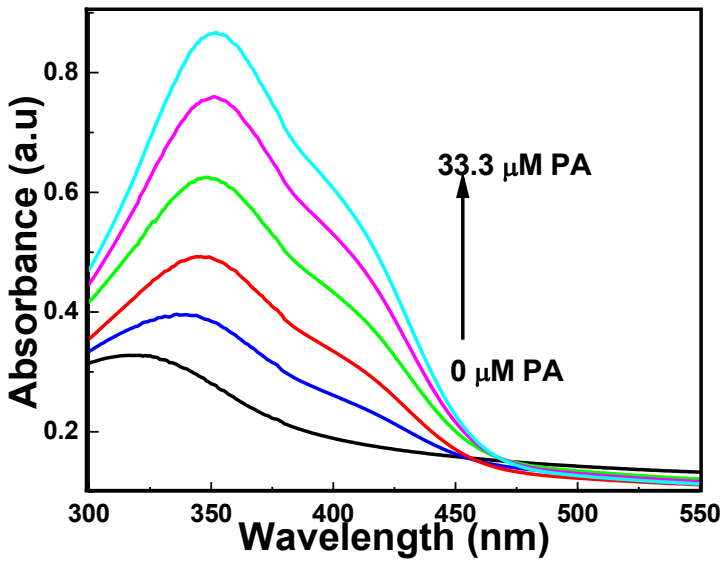

Fig. 5.21 UV/Vis spectra of ceria nanoparticle dispersion on continuous addition of picric acid.

In dynamic quenching, the quenchers are reducing the fluorescence intensity without being part of the sensing material and corresponds to no change in absorbance and bandgap.

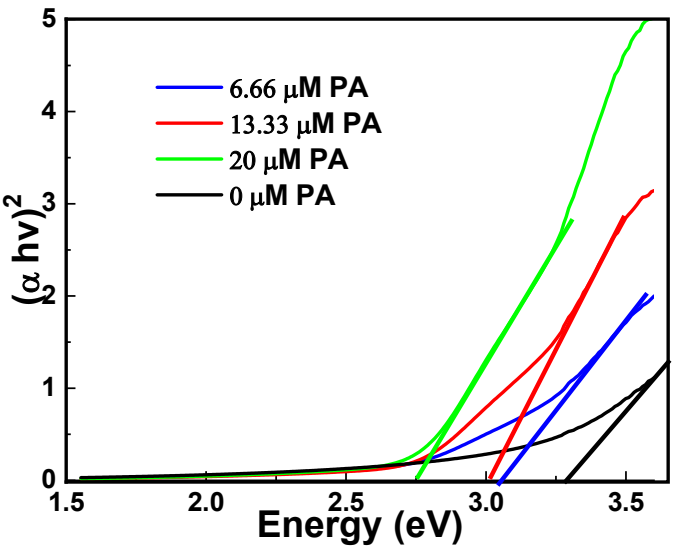

Fig. 5.22 Change in the bandgap of ceria nanoparticle on continuous addition of picric acid

Thus a non-fluorescent charge transfer complex exhibiting a distinct absorption spectrum (absorption band at around 410 nm) could be formed due to the interaction between PA and ceria particles in the ground state before its excitation and can undergo non-radiative decay. With an increase in the concentration of PA beyond 41.6 μM, the plot becomes less linear, which can be due to the occurrence of both static and dynamic quenching simultaneously [25]. A schematic representation of the fluorescence quenching mechanism is presented in figure 5.23.

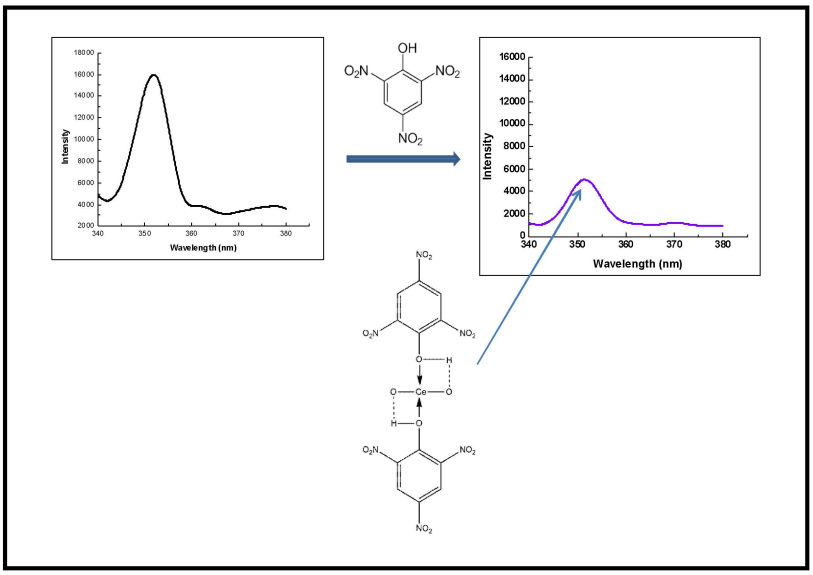

Fig. 5.23 Schematic representation of fluorescence quenching mechanism in PA sensing.

Fluorescence sensing of picric acid was also carried out in aqueous solution from various sources such as tap water, well water as well as river water (Bharathapuzha, Velliyamkallu, Pattambi) to evaluate the efficiency of the present method in the presence of different interfering matrices. The synthesized CeO_2 nanoparticles are effective in all the above water sources with slightly higher LOD values compared to that obtained in deionized water, indicating the suitability of present CeO_2 in sensing PA in natural water sources. The linear plots for tap water, well water and river water are given in figures 5.24, 5.25 and 5.26 respectively.

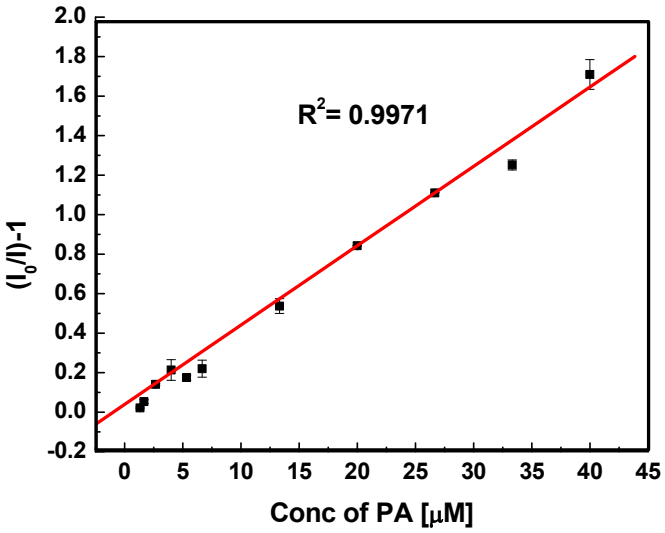

Fig. 5.24 Linear plot between fluorescence intensity variation and concentration of PA studied in tap water solution.

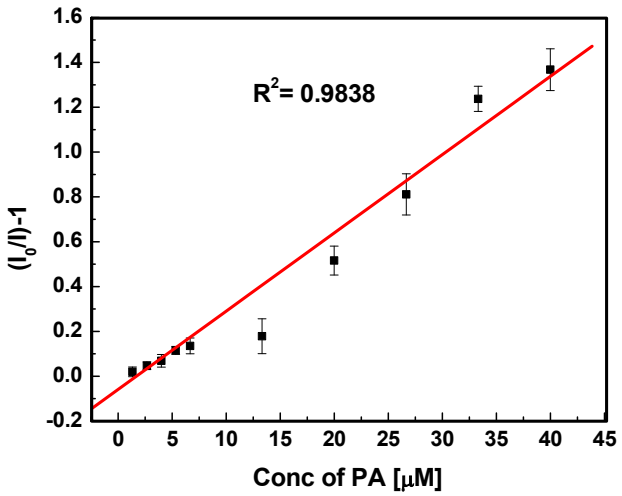

Fig. 5.25 Linear plot between fluorescence intensity variation and concentration of PA studied in well water.

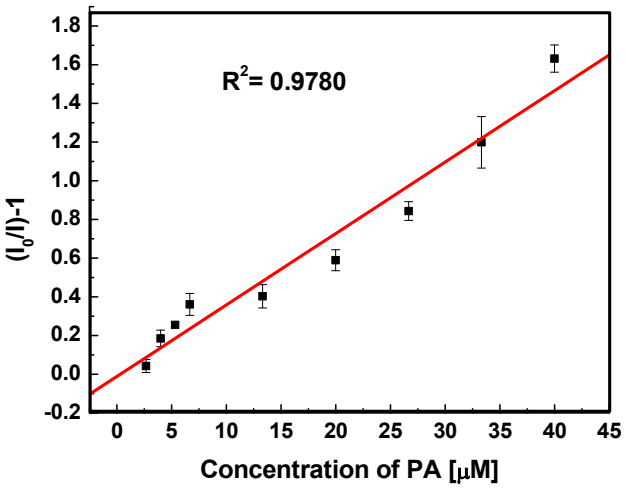

Fig. 5.26 Linear plot between fluorescence intensity variation and concentration of PA studied in river water.

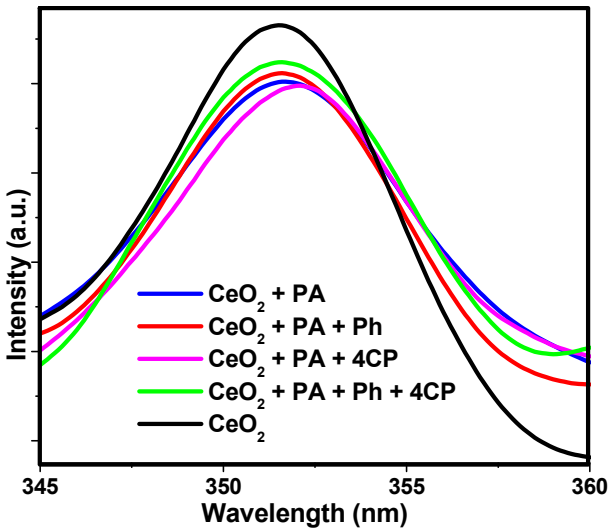

Fig. 5.27 Selectivity study of CeO_2 FG-10 nanoparticle dispersion to the presence of phenolic compounds.

The experimental limit of detection was 0.66 μM in tap water and well water and is 1.33 μM in river water, slightly higher than that obtained from deionized water (0.33 μM).

We spiked with a known concentration of PA (4 μM) to each of the water samples and tested for the recovery using the respective linear plots obtained. The detection lies in the range of 97-115%, as shown in table 5.3. The results further indicate the suitability of the present method in analyzing PA in real situations.

Table 5.3. Detection of PA in 4 μM spiked water samples

Sample	Added (μM)	Found (μM)	Recovery (%)
DI water	4	4.00	100
Tap water	4	4.16	104
Well water	4	3.88	97
River water	4	4.61	115

Selectivity is an important criterion of an effective sensor, and thus the selectivity of the CeO_2 FG-10 in PA sensing was investigated by observing the change in fluorescence intensity of the ceria nanoparticles in presence of other phenolic compounds. The results are presented in figure 5.27. The addition of phenolic compounds, such as phenol and 4-chlorophenol, didn't change the PL intensity of PA quenched CeO_2 dispersion. By examining the selectivity with other nitroaromatic compounds, an obvious change in fluorescence spectrum

is observed, which indicates that the CeO_2 FG-10 nanoparticles are not suitable for sensing other nitroaromatic molecules or in the sensing of PA in the presence of other nitro compounds.

Because of the presence of three electron withdrawing $–NO_2$ groups in picric acid, the high positively charged H atoms of O-H bond can forms strong hydrogen bonds with oxygen atoms of ceria resulting in the formation of a ground state complex responsible for the fluorescence quenching of ceria nanoparticles. Other phenolic compounds such as phenol and 4 chlorophenol cannot form this type of interaction and so the PA sensing is selective in presence of these compounds. Wheras when we do sensing in presence of other nitrocompounds such as 4-nitrophenol it will also interact with oxygen atoms of ceria and reduce the sensitivity towards the detection of PA.

The sensing parameters such as linear range and limit of detection of the CeO_2 FG-10 have been compared with that obtained from the fluorescence quenching of other systems in literature and are presented in table 5.4. CeO_2 FG-10 is showing a good linear range, LOD, and an appreciably high Stern-Volmer constant in PA sensing.

Table 5.4 Comparison of various sensing parameters by different systems using PL quenching.

Material	Linear range (μM)	LOD (μM)	K_{SV} M^{-1}	Reference
α – Fe_2O_3 nanoparticles	1.66 – 5	3.33	3.094×10^5	[13]

Carbon nanodots	0.06 – 79.4	0.01		[11]
CeO_2 NPs	0.33 - 7.60	0.52	2.33×10^5	[18]
Fe-doped ZnOnanoellipsoids	5 – 60	2.9	0.126×10^5	[2]
Fluorescent nano aggregates of Pentacenequinone derivative	0 – 150	1	4.3×10^3	[8]
Nitrogen and Sulphur co-doped carbon quantum dots (NS-CQDs)	1 – 10 µM	0.24 µM		13
Poly(allylamine) hydrochloride (PAH) incubated with Au@SiO2 nanoparticles	0.01 – 0.70 µM	79 nM	1.2 x 10^6 M^{-1}	14
CeO_2 FG-10	**0.33 – 41.62**	**0.33**	**5.754 x 10^5**	**This work**

5.4 Conclusions

In this report, sol-gel ceria nanostructures were synthesized using fenugreek extract. The formation of cubic fluorite structured ceria was identified from XRD analysis and Raman spectra. The

surface morphology of the CeO_2 was identified from SEM analysis. TEM images displayed less particle agglomeration in ceria nanoparticles prepared in the presence of fenugreek extract. The presence of Ce^{3+} ions in the ceria lattice was confirmed from the XPS, Raman spectroscopy and UV-vis DRS spectral analyses. The fluorescence properties of the samples were studied to apply the nanoparticles as a sensor for aquatic pollutant picric acid. The nanoparticle dispersion showed a quenching in fluorescence intensity on the increasing addition of picric acid. The best among the prepared CeO_2 sensor showed a linear concentration range of 0.33 – 41.6 μM with a LOD of 0.33 μM picric acid. The high Stern-Volmer constant in this study indicated a strong interaction between ceria nanoparticles and picric acid. The nanoparticles used in this study are also proved to be selective towards the sensing of PA in the presence of other phenolic compounds. The best ceria sample of the present study is highly effective in the sensing of nature water samples such as well water, and river water and is also found to be effective in the sensing of PA in tap water.

References

1. Y. Hu, M. Ding, X.Q. Liu, L.B. Sun and H.L. Jiang, *Chem. Commun*., 2016, **52**, 5734.
2. R. Kumar, A. Umar, D.S. Rana, P. Sharma, M.S. Chauhan and S. Chauhan, *Mater. Res. Bull*.,2018, **102**, 282.
3. G. Venkatesan, R. Vijayaraghavan, S.N. Chakravarthula, G. Sathiyan, *FRT*, 2019, **2**, 2002.
4. Q. J. Zhao, Provisional peer-reviewed toxicity values for picric acid (CASRN 88-89-1) and ammonium picrate (CASRN 131-74-8), EPA/690/R-20/008F | September 2020 | FINAL
5. G. Sivaraman, B. Vidya and D. Chellappa, *RSC Adv*. 2014, **4**, 30828.
6. S. Sanda, S. Parshamoni, S. Biswas and S. Konar, Chem. *Commun*.,2015, **51**, 6576.
7. R. Kumar, S. Sandhu, P. Singh, G. Hundal, M.S. Hundal and S. Kumar, *Asian J. Org. Chem*. 2014, **3**, 805.
8. D.C. Santra, M.K. Bera, P.K. Sukul and S. Malik, *Chem. Eur. J.*2016, **22**, 2012 .
9. V. Bhalla, A. Gupta and M. Kumar, *Org. Lett.,* 2012, **14**, 3112.
10. B. Roy, A.K. Bar, B. Gole and P.S. Mukherjee, *J. Org. Chem*.,2013, **78**, 1306.
11. J. Huang, L. Wang, C. Shi, Y. Dai, C. Gua, J. Liu, *Sens. Actuators B Chem.,* 2014, **196**, 567.
12. J. Li, L. Zhang, P. Li, Y. Zhang and C. Dong, *Sens. Actuators B Chem.*,2018, **258**, 580.

13. Z. M. S. H. Khan, S. Saifi, Shumaila, Z. Aslam, S. A. Khan and M. Zulfequar, *J. Photochem. Photobiol A*, 2020, **388**, 112201.
14. S. Kaja, D. P. Damera and A. Nag, *Anal. Chim. Acta*. 2020, **1129**, 12.
15. H.K. Sadhanala and K.K. Nanda, *J. Phys. Chem. C*,2015, **119**, 13138.
16. K. Negi, D.S. Rana, M. Kumar, P. Sharma, R. Kumar, A. Umar, S. Chauhan and M. S. Chauhan, J. *Nanosci. Nanotechnol.*,2019, **19**, 2695.
17. N.A.M. Fadzil, M.H.AB. Rahim and G.P. Maniam, *Mater. Res. Express.*,2018, **5**, 085019.
18. M. Darroudi, S.J. Hoseini, R.K. Oskuee, H.A. Hosseini, L. Gholami and S. Gerayli, *Ceram. Int.,*2014, **40**, 7425.
19. R. Schmitt, A. Nenning, O. Kraynis, R. Korobko, A.I. Frenkel, I. Lubomirsky, S.M. Hailef and J.L.M. Rupp, *Chem. Soc. Rev*. 2020, **49**, 554.
20. N. Shehata, K. Meehan, M. Hudait and N. Jain, *J. Nanopart. Res*.,2012, **14**, 1173.
21. K. Negi, M. Kumar, G. Singh, S. Chauhan and M.S. Chauhan, *Ceram. Int.,*2018, **44**, 15281.
22. B. Elahi, M. Mirzaee, , M. Darroudi, R.K. Oskuee, K. Sadrib and M.S. Amiri, *Ceram. Int.,*2019, **45**, 4790.
23. T. Arunachalam, M. Karpagasundaram and N. Rajarathinam, *Mater. Sci. Poland*, 2017, **35**, 791.

24. Y. Yulizar, E. Kusrini, D.O.B. Apriandanu and N. Nurdini, *Surf. Interfaces.,* 2020, **19**, 100437.
25. Q. Maqbool, M. Nazar, S. Naz, T. Hussain, N. Jabeen, R. Kausar, S. Anwaar, F. Abbas and T. Jan, *Int. J. Nanomedicine.,* 2016, **11**, 5015.
26. A. Arumugam, C. Karthikeyan, A.S.H. Hameed, K. Gopinath, S. Gowri and V. Karthika, *Mater. Sci. Eng. C.*2015, **49**, 408.
27. D. Dutta, R. Mukherjee, M. Patra, M. Banik, R. Dasgupta, M. Mukherjee and T. Basu, *Colloid. Surface. B*,2016, **147**, 45.
28. G.S. Priya, , A. Kanneganti, , K.A. Kumar, , K.V. Rao and S. Bykkam, *Int. J. Sci. Res.,*2014, **4**, 2250.
29. S.K. Kannan and M. Sundrarajan, *Int. J. Nanosci.,*2014, **13**, 1450018.
30. S. A. Nezhad, A. Es-haghi and M. H. Tabrizi, *Appl. Organometal. Chem*.,2020, **34**, 5314.
31. R.P. Senthilkumar, V. Bhuvaneshwari, R. Ranjithkumar, S. Sathiyavimal, V. Malayaman and B. Chandarshekar, *Int. J. Biol. Macromol.*,2017, **104**, 1746.
32. J.K. Sharma, P. Srivastava, S. Ameen, M.S. Akhtar, S.K. Sengupta and G. Singh, *Mater. Res. Bull.,*2017, **91**, 98.
33. G. Sharmila,C. Muthukumaran, H. Saraswathi, E. Sangeetha, S. Soundarya and N.M. Kumar, *Ceram. Inter.,*2019, **45**, 12382.
34. N. Thovhogi, A. Diallo, A. Gurib-Fakim and M. Maaz, *J. Alloys Compd.*,2015, **647**, 392.

35. S.B. Bukhari, M.I. Bhanger and S. Memon, *Pak. J. Anal. Environ. Chem.*, 2008, **40**, 78.
36. I.M.A.AL. Mashkor, *Int. J. Pharmacogn.,* 2014, **6**, 841.
37. L. J. Xu and J. L. Wang, *Appl. Catal.,* 12013, **142**, 396.
38. V. Ramasamy and G. Vijayalakshmi, *J. Mater. Sci: Mater. Electron.*, 2016, **27**, 4723.
39. S. Maensiri, C. Masingboon, P. Laokul, W. Jareonboon, V. Promarak, P.L. Anderson and S. Seraphin, *Cryst. Growth Des.,* 2007, **7**, 950.
40. N.S. Arul, D. Mangalaraj, P.C. Chen, N. Ponpandian, P. Meena and Y. Masuda, *J. Sol-Gel Sci. Technol.,*2012, **64**, 515.
41. T.V. Surendra and S.M. Roopa, *J. Photochem. Photobiol. B.*2016, **161**, 122.
42. M.J. Muñoz-Batista, M. de los M. Ballari, A. Kubacka, A.E. Cassano, O.M. Alfano and M. Fernández-García, *Chem. Eng. J.,*2014, **255**, 297.
43. M.A.M. Khan, W. Khan, M. Ahamed and A.N. Alhaza, *Sci. Rep*.,2017, **7**, 12560.
44. A. Aranda, E. Aylon, B. Solsona, R. Murillo, A.M. Mastral, D.R. Sellick, S. Agouram, T. Garcıa and S.H. Taylor, *Chem. Commun,.*2012, **48**, 4704.
45. A. Aboukaïs, M. Skaf, S. Hany, R. Cousin, S. Aouad, M. Labak and, E.A. Aad, *Mater. Chem. Phys.,*2016, **177** , 570.
46. R.R. Muthuchudarkodi and A. Ashli, Int. *J. Chemical Concepts*,2017, **3**, 293.

47. R. Udayabhaskar,S.F. Sahlevania, T. Prabhakaran, T. Pandiyarajan, B. Karthikeyan, D. Contreras and R.V. Mangalaraja, *Sol. Energy Mater Sol.,*2019, **195**, 106.
48. F. Sotomayor, K. A. Cychosz and M. Thommes, *Acc. Mater. Surf. Res.*, 2018, **3**, 34.
49. A.T. Miah, B. Malakar and P. Saikia, *Catal. Letters,*2016, **146**, 291.
50. G. Grzybek, P. Stelmachowski, S. Gudyka, P. Indyka, Z. Sojka, N.G. Hurtado, V.R. Perez, A.B. Lope and, A. Kotarba, *Appl. Catal. B*. 2016, **180**, 622.
51. Y. Zhu, Z. Yang, L. Song, M. Chi, M. Li, C. Wang and X. Lu, *Part. Syst. Charact.,*2018, **35,** 1800049.
52. P.K. Sane, S. Tambat, S. Sontakke and P. Nemade, *J. Environ. Chem. Eng.*, 2018, **6,** 4476.
53. A. S. Tanwar, N. Meher, L. R. Adil and P. K. Iyer, *Analyst*. 2020, **145**, 4753.

Chapter 6

Cobalt Doped Ceria Catalysts for the Removal of Gaseous Pollutants and Colorimetric Detection of H_2O_2

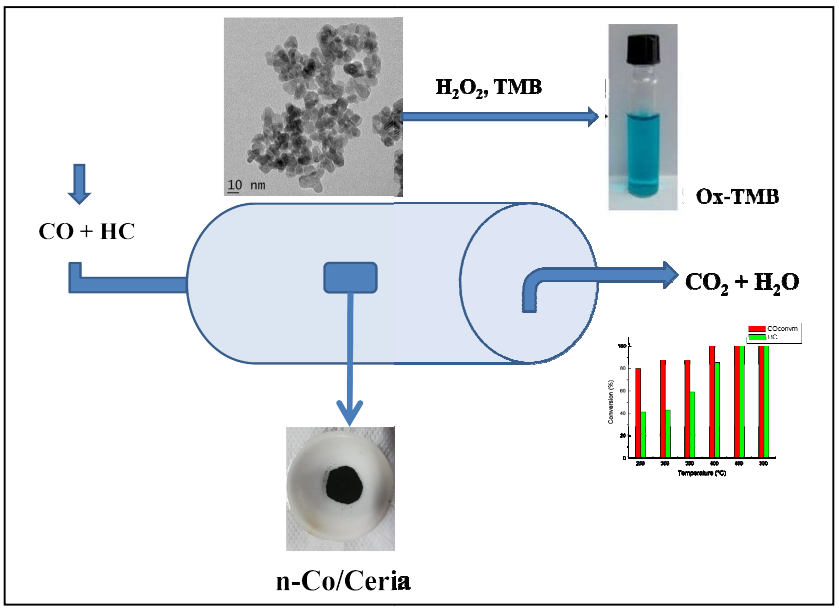

Cobalt doped cerium oxide nanoparticles were synthesized by ammonia precipitation followed by wet impregnation and have been used for the simultaneous oxidation of carbon monoxide and hydrocarbon; and also for the colorimetric detection of H_2O_2.

6.1 Introduction

The increased use of automobiles universally from the last century onwards has become a serious concern to the research groups due to the continuous release of carbon monoxide (CO) and unburnt hydrocarbons (HC). Combustion of fossil fuels in power plants and other incineration processes are also responsible for the emission of CO and HC into the environment [1]. Abundant CO and HC are generated from automobiles having cold start technology due to the incomplete combustion of fuels [2]. HC and CO are two major air pollutants that can impose hazards to human health and the environment [3]. Propane is an HC emitted by diesel and gasoline engines that can be effectively converted to carbon dioxide and water by catalytic oxidation [4]. Noble metal catalysts involving Pt, Rh, Au, Ir, Ru, Pd, etc., showing good catalytic performance and stability, are often used in the removal of CO and HC [5]. But due to their high cost and low availability, alternative, cost-effective catalysts having similar catalytic activity need to be developed.

Ceria is an important rare earth oxide, which is the readily available and stable catalyst that has been investigated in many studies as a substitute for noble metal-based catalyst materials. The oxygen storage/release capacity (OSC) of ceria is responsible for its various catalytic properties, including catalytic oxidation of gaseous pollutants like CO and HC, and different biological applications. Doping with other metals can improve the OSC, and thermal stability of ceria to enhance the catalytic ability [6]. Much research is focused on doping

with several transition metal ions like Mn, Fe, Cu, Ni, Co, etc., because of their low cost, good stability, and higher activity [7]. Among these, cobalt-doped ceria catalysts have proven to be good candidates for the low-temperature oxidation of CO. It is reported that cobalt/ceria catalysts have also achieved good results in HC combustion [8]. Thus it is viable to synthesize cobalt ceria mixed catalysts for the simultaneous oxidation of CO and HC. Zhang et al. synthesized cobalt-cerium spinel oxide catalysts by a citric acid complex method showing superior propane oxidation activity at low temperatures [9]. Song et al. prepared porous ceria nanorods modified with Fe and Co in which Co-doped ceria showed the highest activity in propane oxidation [4]. Several research groups such as Tian et al., Luo et al., Jampaiah et al., Guo et al., etc., have reported cobalt doped ceria nanostructures for the low-temperature oxidation of CO [6,8,10,11]. Cobalt based ceria catalysts with different morphologies have been used for the last few years for other applications such as preferential oxidation (PROX) of CO, soot combustion, water-gas shift reaction, methane reforming, NO oxidation, etc.

Ceria can act both as an oxidizing and reducing catalyst depending on the reaction conditions. It is reported that in an acidic environment, ceria nanoparticles have an intrinsic oxidase-like activity that can make use for the biochemical sensing of hydrogen peroxide [12]. H_2O_2 is a reactive oxygen species (ROS) formed as a byproduct of metabolic reactions in human beings. Excessive production of H_2O_2 in our body leads to several diseases like diabetes, cancer,

cardiovascular problems, etc. [13]. Thus it is significant to have facile and rapid methods for the detection of H_2O_2. Several analytical methods such as HPLC detection, optical sensing, electrochemical analysis, colorimetric method, chemiluminescence, fluorescence, etc., are used for the sensing of H_2O_2 [14]. Recently ceria-based nanomaterials have been developed for the colorimetric estimation of H_2O_2 via a color reaction of a substrate based on their peroxidase-like enzymatic activity. Several researchers including Guo et al., Ornatska et al., Ozdemir Olgun et al., Jiao et al., etc., have reported ceria nanoparticle-based colorimetric sensing of H_2O_2 [15,16,17,18,]. Zhang et al. used $Ce(OH)CO_3$ powder for this purpose by adding H_2O_2 and a peroxidase substrate 3,3′,5,5′tetramethylbenzidine (TMB) [14]. Wang synthesized 3-dimensional C/CeO_2 hollow nanostructure frameworks that catalyze the oxidation of TMB in the presence of H_2O_2 to produce a blue product [19]. Liu et al. has prepared an Au/Co_3O_4-CeOx nanocomposite possessing excellent peroxidase-like activity as an ultrasensitive colorimetric sensor for H_2O_2 [13]

In this work, we have synthesized nanosized ceria particles modified with cobalt having two versatile applications. Ceria powder was prepared by the precipitation method using ammonia as the precipitating agent, which is a simple and widely used method. The synthesized ceria was doped with different percentages of cobalt by the wet impregnation method. The synthesized catalysts were used for the simultaneous catalytic oxidation of CO and propane, the remarkable

hydrocarbon pollutant, and also for the peroxidase-like enzymatic activity for the colorimetric detection of H_2O_2.

6.2 Experimental

6.2.1 Catalyst Preparation

1:1 ammonia was added dropwise to an aqueous solution of cerium nitrate of 0.05 M concentration at room temperature while stirring. The purple-colored suspension containing $Ce(OH)_3$ was continuously stirred until it becomes yellow-colored $Ce(OH)_4$. The precipitate was filtered, washed several times with water, and dried at 100 ℃ for 12 h followed by calcination at 500 ℃ for 5 h to get ceria.

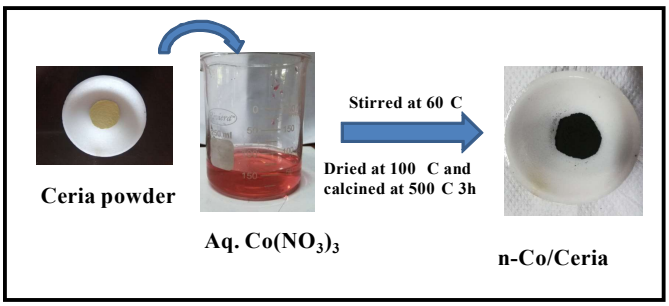

Fig. 6.1 Synthetic steps of cobalt-doped ceria by wet impregnation method.

Ceria was then powdered and used for the preparation of cobalt-doped ceria catalysts by the wet impregnation method. For this, powdered ceria was added to cobalt nitrate solution of definite concentration and stirred at 60 ℃ until the excess solvent was evaporated, drying was then performed at 100 ℃. The dark-colored substance was calcined at 500 ℃ for 3 h to get the Co/CeO_2 catalyst. A

pictorial depiction of the impregnation of cobalt into ceria is shown in figure 6.1. The percentage of cobalt doping was varied as 1 wt%, 2 wt %, and 3 wt % to obtain different catalysts. The systems were designated as n-Co/CeO_2, where n indicates the weight percentage of Co used in the preparation.

6.2.2 Catalytic Oxidation of CO and Propane

The catalytic activity of the synthesized samples on simultaneous oxidation of CO and propane (model hydrocarbon pollutant) was conducted in a fixed bed reactor of 13 mm internal diameter using a standard cylinder having a mixture of 7000 ppm CO, 1300 ppm propane, and 10000 ppm oxygen. The inlet gas flow rate was varied using a mass flow controller (MFC AABORG, USA) before entering the reactor. The catalyst bed was fixed inside the reactor, which is programmed at a definite temperature. The composition of the effluent gas after the catalytic reaction was monitored using a gas analyzer (AVL DiGas 444, India). The catalytic reaction was performed at different temperatures from 250 °C to 500 °C to find out the temperature of the maximum conversion of CO and propane. The effect of reaction parameters such as inlet gas flow rate, catalyst weight, and percentage of cobalt loading in the catalyst was also studied to identify the best conditions of the reaction. Blank reactions were also conducted at different conditions. The percentage conversion was calculated according to the equation;

$$\% \text{ conversion of CO/propane} = [(\text{CO/propane}_{\text{blank}} - \text{CO/propane}_{\text{cat}})/\text{CO/propane}_{\text{blank}}] \times 100$$

where $CO/propane_{blank}$ and $CO/propane_{cat}$ are the percentage volume of CO/propane in the blank and catalyzed reactions respectively. The picture of the experimental setup for the catalytic oxidation is shown in figure 6.2.

Fig. 6.2 Experimental setup for the catalytic oxidation of CO and HC.

6.2.3 Peroxidase-Like Activity of Co/CeO_2

The peroxidase-like activity of the cobalt doped catalysts was investigated in the oxidation reaction of a chromogenic substrate TMB to form oxidized TMB with a blue color. Oxidation of TMB was catalyzed by Co/CeO_2, as a peroxidase-like material, in the presence of H_2O_2 in a 0.2 M acetate buffer. In a typical reaction, 0.4 ml TMB (0.3 mg/ml in DMSO) and 0.4 ml H_2O_2 (0.25 M) and 0.4 ml Co/CeO_2 (0.3 mg/ml) are mixed in 0.2 M acetate buffer so as to make total volume of

4 ml. The reaction mixture was kept at room temperature for 20 min, the absorbance of the obtained blue-colored solution at a wavelength of 650 nm was measured using a spectrophotometer.

6.2.4 Colorimetric Sensing of the Linear Range of H_2O_2

The detection of H_2O_2 was performed as follows: 50 µL TMB (3 mg/ml) and 50 µL Co/CeO_2 nanoparticle suspension (3 mg/ml) were mixed with 3 ml acetate buffer. H_2O_2 solution of different concentrations was added, and the absorbance of the mixture was monitored after 10 minutes reaction. The relation between absorbance and H_2O_2 concentration was investigated by varying the concentration of H_2O_2 from 3.33 µM to 5000 µM keeping the other reaction conditions unchanged.

6.3 Results and Discussions

Figure 6.3 shows the X-ray diffraction patterns of ceria and cobalt-doped ceria samples. The presence of diffraction lines of (111), (200), (220), (311), (222), (400), (331), and (420) planes are indexed to the cubic fluorite structure of ceria with Fm3m space group [20]. The intense and broad peaks observed in the XRD show the well crystalline nature of the small crystallites. No additional peaks are observed in 1 wt% and 2 wt% cobalt doped samples, which indicate the proper incorporation of cobalt into the ceria lattice. The homogeneous Co-Ce-O solid solution formation is thus evident in these two samples. The low intense peak at 36.7° observed in the 3% Co/CeO_2 sample corresponds to the cobalt oxide phase (Co_3O_4) [21].

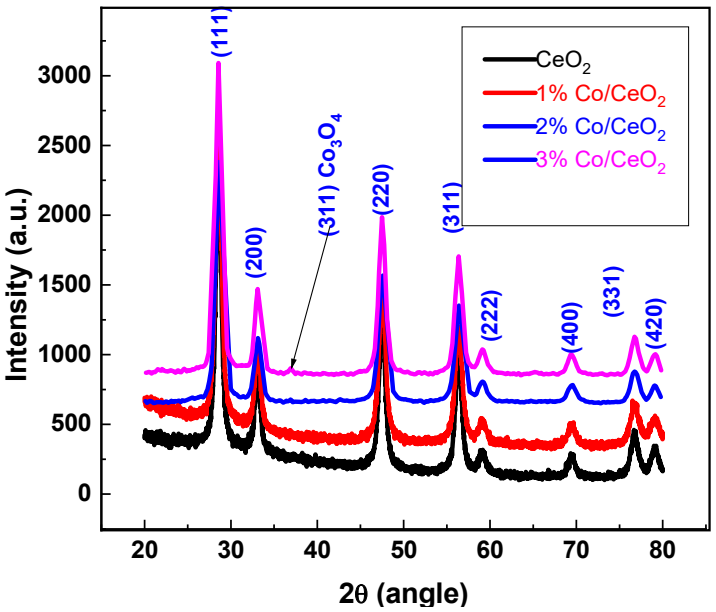

Fig. 6.3 X-ray diffraction patterns of CeO_2 and cobalt doped catalysts.

The average crystallite size and lattice parameter of CeO_2 samples are calculated from the diffraction peak from the (111) plane and are given in table 6.1 [22]. The lattice parameter of the doped samples is slightly less than the bulk counterparts (5.4113 Å). This lattice contraction is due to the substitution of small divalent or trivalent cobalt ion [$r(Co^{2+})$ = 0.90 Å and $r(Co^{3+})$ = 0.61Å] for Ce^{4+} ions [$r(Ce^{4+})$ = 0.97 Å] in the ceria lattice [22].

The lattice strain involved in the nanocrystals is calculated from the Williamson-Hall plot (figure 6.4) analysis, and the values are presented in table 6.1.

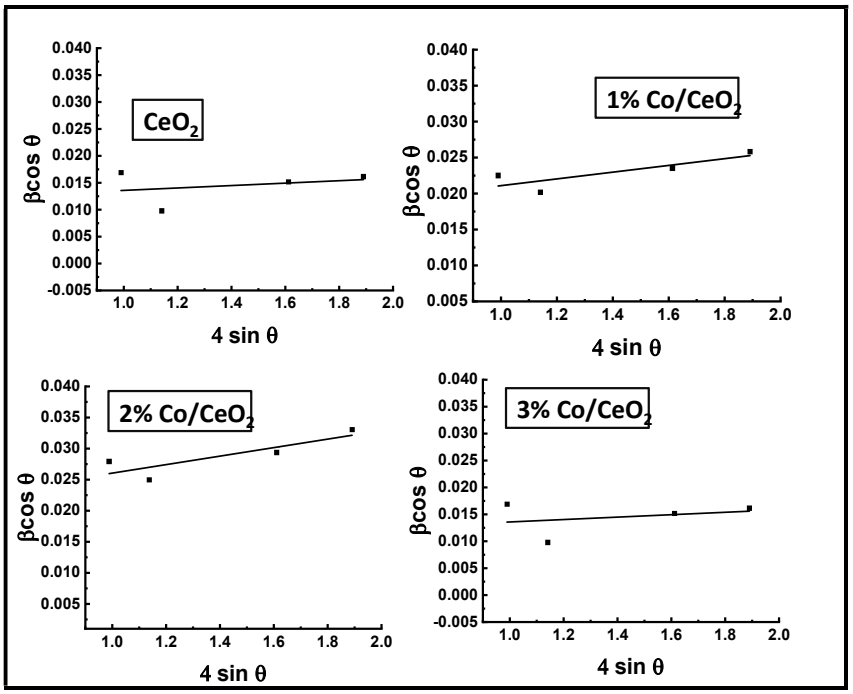

Fig. 6.4 Williamson-Hall plot of ceria and cobalt doped crystals.

It is observed that the slight increase in the lattice strain of cobalt doped ceria samples is due to the slight increase in the number of oxygen vacancies. The increase in lattice strain is beneficial for the catalytic reactions because it can enhance the reducibility of the catalyst by decreasing the strength of the metal-oxygen bond.

The FTIR spectra of the synthesized samples are shown in figure 6.5. The characteristic absorption band at 500 cm^{-1} is due to the symmetric stretching vibration of the Ce-O bond, and the peak at 1320 cm^{-1}corresponds to the O-H bending vibration of the Ce-OH bond [23].

Table 6.1 Physical characteristics of samples.

Sample	Crystallite size (nm)	Lattice Parameter (nm)	Lattice strain	Particle Size (nm)	BET S. A (m^2/g)	Mean pore dia (nm)	Pore volume (cm^3/g)
CeO_2	7.2	0.5418	0.0023	8.8	57.9	6.7	0.106
1% Co/CeO_2	6.4	0.5417	0.0047	9.4	59.9	6.9	0.099
2% Co/CeO_2	3.4	0.5414	0.0069	7.8	63.1	7.8	0.117
3% Co/CeO_2	3.9	0.5413	0.0051		55.9	7.5	0.105

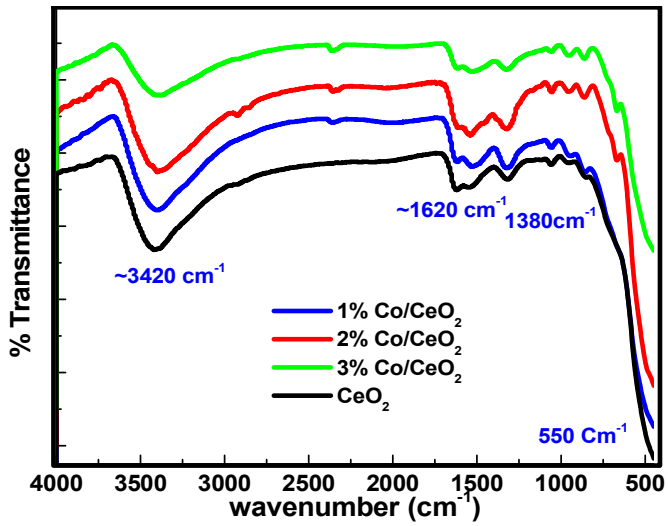

Fig. 6.5 FTIR spectra of CeO_2 and cobalt doped ceria catalysts.

The stretching and bending vibrations O-H bond of water molecules; that are adsorbed on the surface of ceria particles are observed as broad absorption bands at 3450 $cm^{-1}$and 1610 cm^{-1} respectively.

The scanning electron microscopic images of CeO_2 and 2% Co/CeO_2 samples are shown in figure 6.6. The morphology of the bare ceria catalyst was not affected much by cobalt doping.

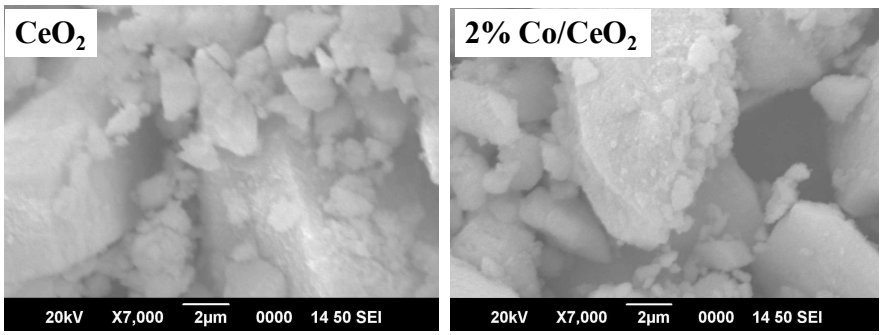

Fig. 6.6 SEM images of CeO_2 and 2% cobalt doped ceria catalysts.

The particle size of the nanoparticles was investigated by Transmission electron microscopy. The TEM images (figure 6.7) of the representative samples show spherical homogeneous particles within the size range of 8 nm to 14 nm. It is found that the particle size decreased on cobalt doping which agrees with the crystallite size calculated from XRD analysis using the Debye Scherrer formula.

Thermogravimetric analysis results of 2% Co/CeO_2 are shown in figures 6.8 and 6.9). The weight loss up to 100 ℃ is due to the removal of physically adsorbed water on the sample.

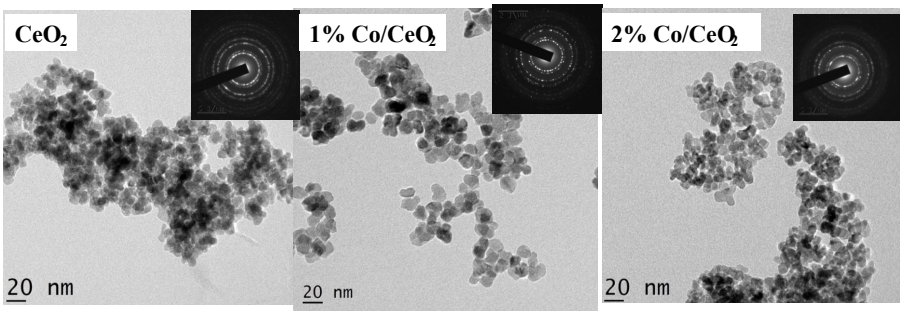

Fig. 6.7 TEM images of CeO_2 and cobalt-doped ceria catalysts.

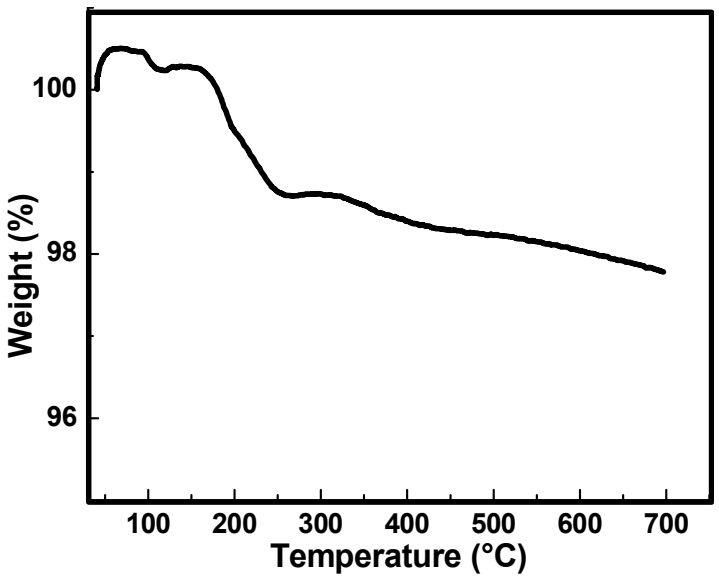

Fig. 6.8 TG curves of 2% Co/CeO_2.

Weight loss from 100 ℃ to 200 ℃ corresponds to the decomposition of nitrates on the surface of the material, and the weight loss around 300 ℃ is due to the complete decomposition of bulk cobalt nitrate, which was the precursor of cobalt species in the sample.

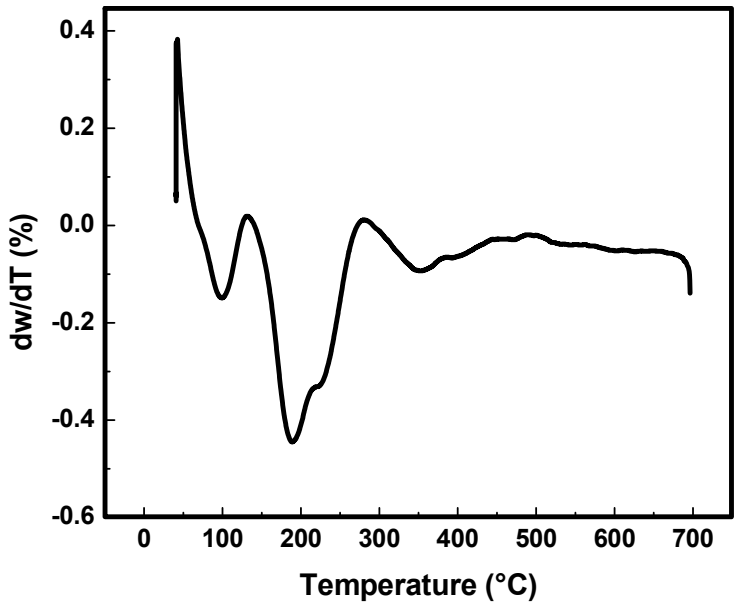

Fig. 6.9 DTG curve of 2% Co/CeO_2.

The elemental composition and the oxidation states of elements in the CeO_2, 1% Co/CeO_2, and 2% Co/CeO_2 were analyzed by XPS. The wide scan spectra, Ce3d, O1s, and Co2p regions are presented in figures 6.10, 6.11, 6.12, and 6.13 respectively. In Ce3d spectra, the peaks at 880 eV, 886 eV, and 895 eV correspond to the Ce $3d_{5/2}$. Peaks corresponding to Ce $3d_{3/2}$ are observed at 898 eV, 905 eV, and 914 eV. These three pairs of peaks arise from the different Ce 4f electronic configurations in the final state of Ce^{4+} [24].

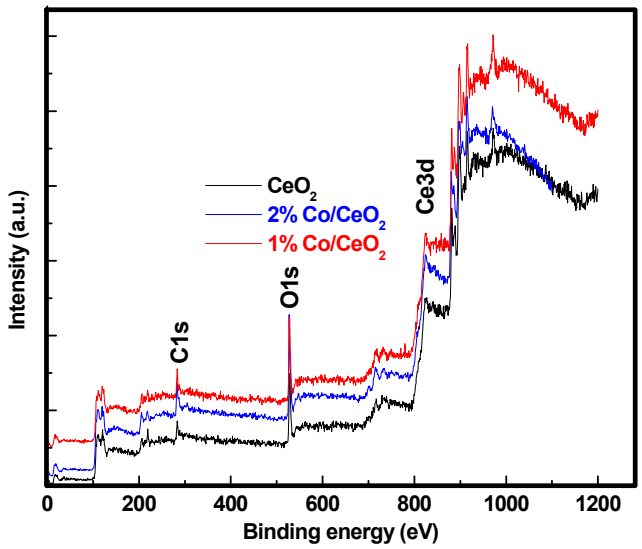

Fig. 6.10 XPS wide scan spectra of ceria and cobalt doped ceria.

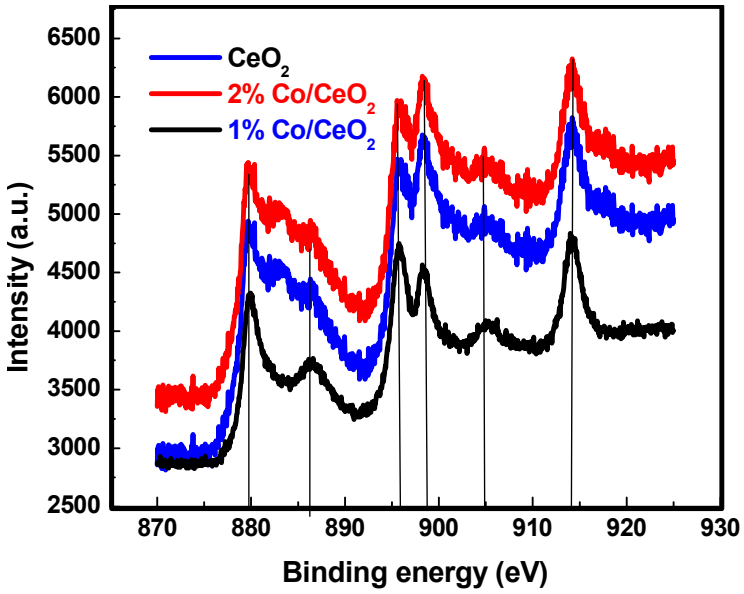

Fig. 6.11 XPS Ce3d core spectra of ceria and cobalt doped ceria.

Two peaks are observed in O1s spectra (figure 6.12). One at 528 eV can be assigned to the lattice oxygen and the other at 530 eV is due to surface adsorbed oxygen in ceria.

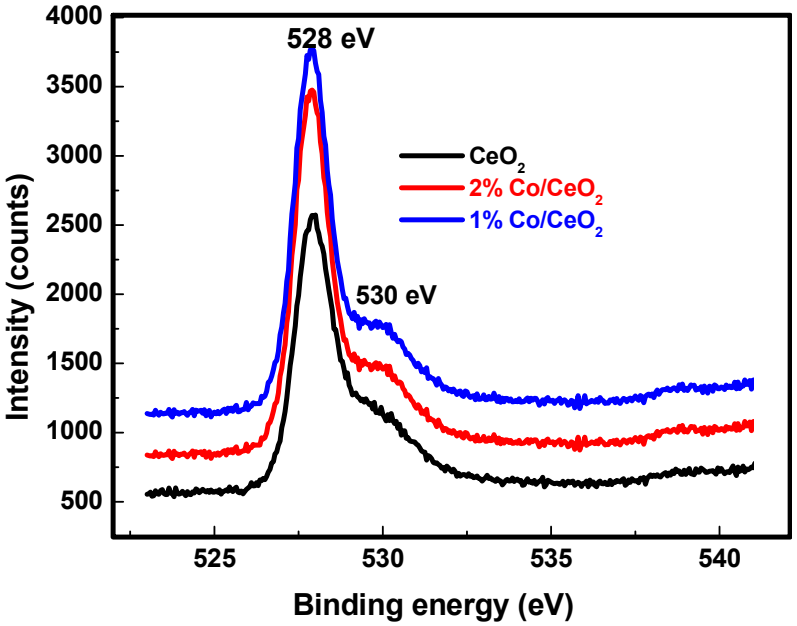

Fig. 6.12 XPS O1s spectra of ceria and cobalt doped ceria.

In the Co 2p XPS (figure 6.13) the two peaks observed at 780 eV and 795 eV are due to the Co $2p_{3/2}$ and Co $2p_{3/2}$ spin-orbital peaks respectively [25]. The peak at 779 eV suggests surface Co^{3+} species while the other at 781.2 eV is assigned to surface Co^{2+} species [4]. For the 1% and 2% cobalt doped CeO_2 samples the wt% of cobalt obtained from the XPS analysis is 8.78%. XPS mainly gives the concentration of the surface and immediate bulk. Thus the incorporated Co mainly exists on the surface of the nanomaterial.

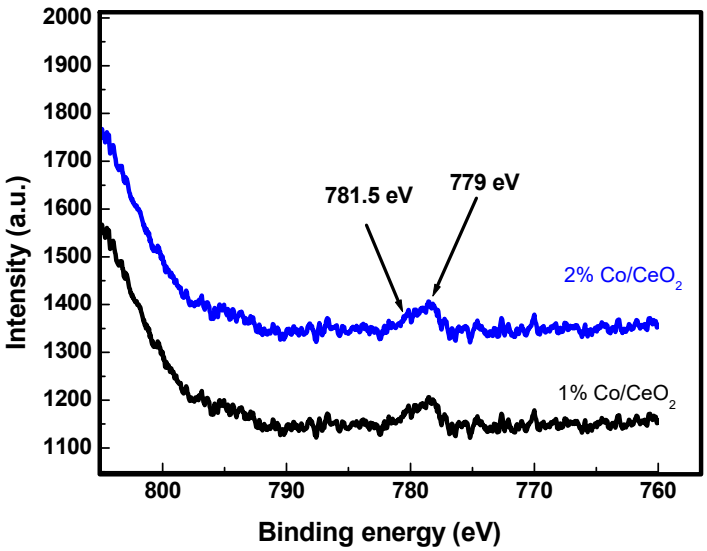

Fig. 6.13 XPS Co2p spectra of ceria and cobalt doped ceria.

Oxygen storage capacity and reducibility of CeO_2 and 2% Co/CeO_2 samples were characterized by temperature-programmed reduction (TPR) with H_2. Two notable reduction peaks are observed in the H_2-TPR of CeO_2 (figure 6.14). One centered at 501 ℃ is due to the reduction of surface lattice oxygen, and the second one at 802 ℃ is ascribed to the reduction of bulk lattice oxygen [9]. This difference in the reduction temperatures is due to the distinct binding energy between the Ce^{4+} and oxygen in the crystal. In the cobalt doped sample, the reduction peaks of ceria have decreased to 773 ℃ and 400 ℃ respectively, as shown in figure 6.15. Thus the introduction of cobalt ions into the ceria lattice increases the reducibility of ceria as it weakens the Ce-O bond in the solid solution [7].

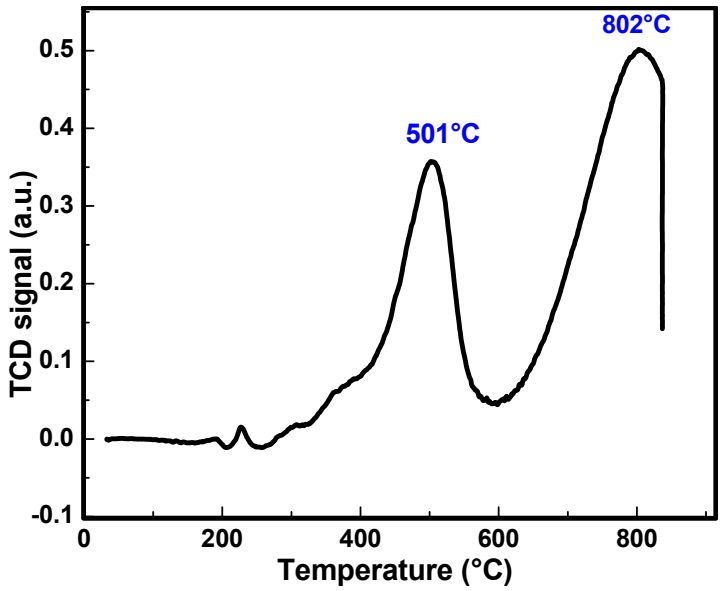

Fig. 6.14 H_2 TPR profile of CeO_2.

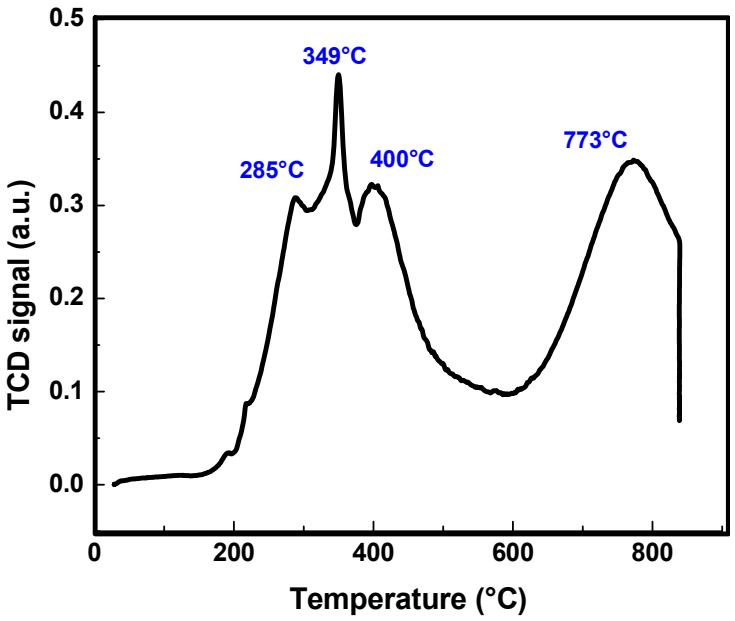

Fig. 6.15 H_2 TPR curve of 2% Co/CeO_2.

Previous reports show that the reduction of Co_3O_4 occurs below 400 °C in two steps: $Co^{3+} \rightarrow Co^{2+}$ and $Co^{2+} \rightarrow Co^0$ [3]. The peak at 285 °C, designated as β, is due to the reduction of Co^{3+} to Co^{2+} ions. The γ peak at 349 °C can be ascribed to the reduction of Co^{2+} to Co^0 [21]. The reduction properties of cobalt are influenced by the metal-support interaction in the catalyst, and the Co^{2+} to Co0 reduction is thus enhanced here [26].

Quantitative H_2 consumption obtained from TPR profiles is shown in Table 6.2. The results confirmed that the Co-doped samples possess enhanced redox properties, and thus a greater concentration of active oxygen is present there than the pure CeO_2. The total hydrogen consumption of the Co-doped system is considerably higher than pure CeO_2, indicating the movement of more reducible oxygen atoms to the surface driven by the smaller cobalt species in the lattice.

Table 6.2. H_2 consumption data of CeO_2 and 2% Co/CeO_2 as calculated from TPR profiles.

Sample	H_2 consumption (mmol/g)		
	Surface oxygen	Bulk oxygen	Total
CeO_2	1.695	2.829	4.524
2% Co/CeO_2	5.327	3.682	9.009

Raman spectra are used to study the oxygen vacancies in the solid solution. Raman spectra are given in figure 6.16. The band centered at 464 cm^{-1} shown in the pure CeO_2 sample is characteristic of the triply degenerate Raman active mode of cubic fluorite structure of ceria.

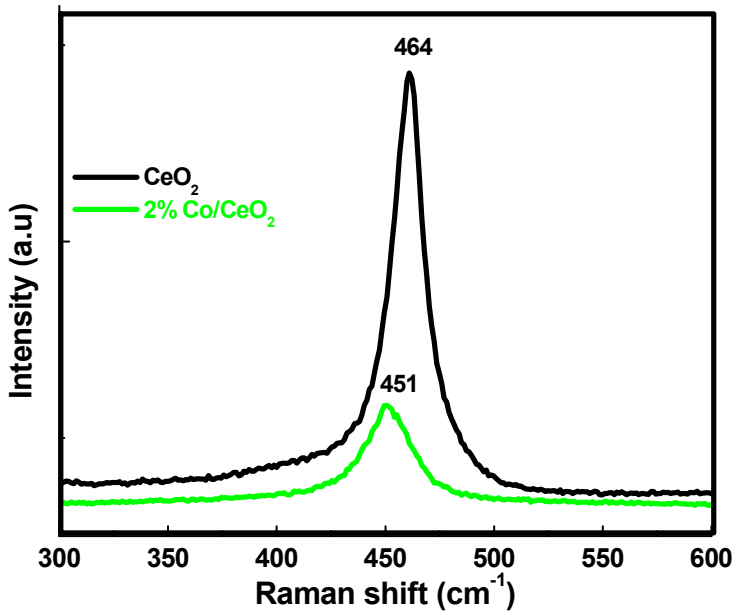

Fig. 6.16 Raman spectra of ceria and cobalt doped ceria catalyst.

This Raman peak of ceria is shifted to lower wavenumber for 2% Co/CeO_2 sample. The redshift of the peak may be attributed to the lattice contraction as a result of the doping with smaller cobalt ions in the crystal lattice of ceria. XRD results supported this observation [3].

The BET surface area and pore size measurements were carried out for all the samples.

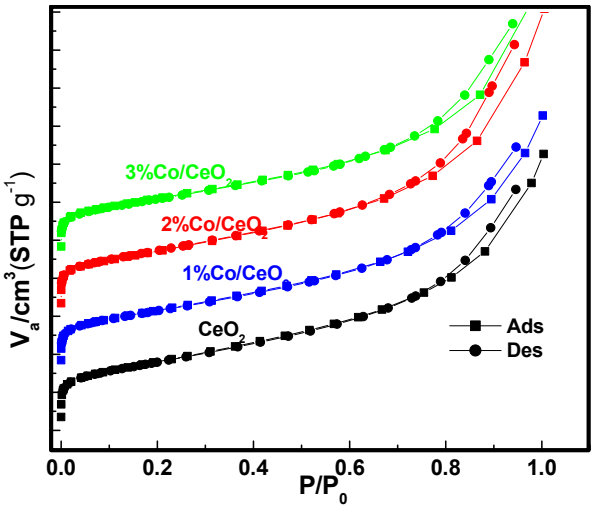

Fig. 6.17 Nitrogen adsorption-desorption isotherms of ceria and cobalt doped ceria catalyst.

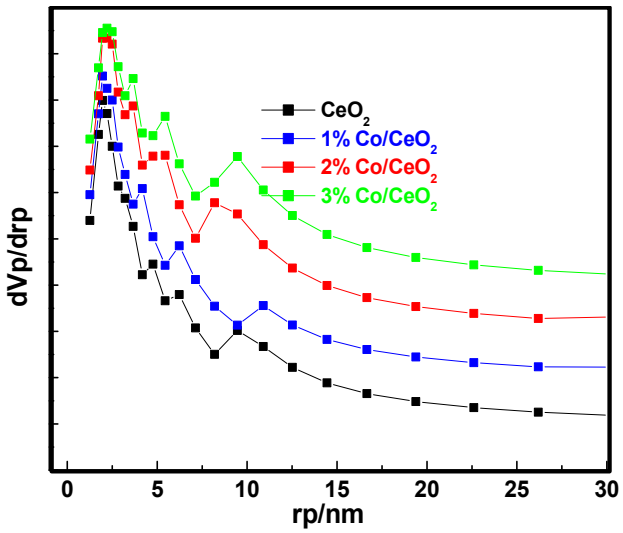

Fig.6.18 BJH pore size distribution of ceria and cobalt doped ceria catalyst.

The adsorption-desorption isotherms and the BJH pore size distribution of the samples are presented in figures 6.17 and 6.18 respectively. It can be observed from figure 6.17 that all the samples can be categorized as Type IV with an H3 hysteresis loop indicating the mesoporous nature of the catalysts with narrow slit-shaped pores. The specific surface areas of the cobalt-doped systems are slightly higher, compared to the bare ceria as given in table 6.1.

The catalytic activity in the oxidation of CO and propane was investigated using the bare ceria and cobalt doped catalysts as described in the experimental section. The effect of different reaction parameters such as reaction temperature, inlet gas flow rate, catalyst weight in the reactor, and percentage of cobalt loading in ceria catalysts was studied. Initially, the oxidation reaction was carried out using 0.75 g 2% Co/CeO_2 catalyst at different temperatures varying from 250 ℃ to 500 ℃ at an interval of 50 ℃. It is evident from figure 6.19 that the cobalt-doped catalysts have achieved 80% CO oxidation at 250 °C itself so that the catalyst can be effectively used for low-temperature CO oxidation reaction.

The conversion of CO and propane increased with increasing reaction temperature, and 100% CO oxidation and 85% propane oxidation are obtained at 400 ℃. Even though the catalysts are less active in HC oxidation at low temperatures, 100% CO and HC oxidation are observed on further increase in the reaction temperature to 450 ℃. Conversion remained 100% at 500 ℃ too.

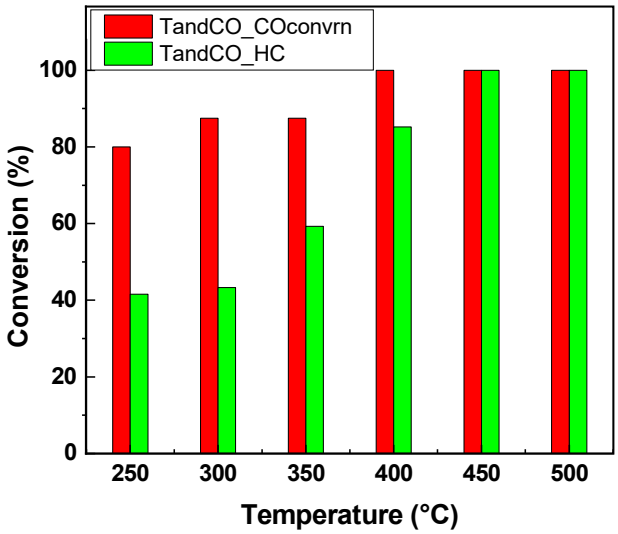

Fig. 6.19 Effect of reaction temperature on % conversion of CO and HC using 0.75 g 2% Co/CeO_2 catalyst.

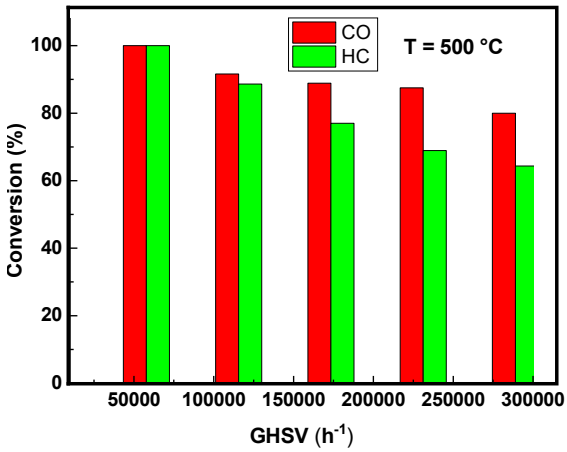

Fig. 6.20 Effect of gas hourly space velocity (GHSV) on the conversion of CO and HC. 0.75 g, 2% Co/CeO_2 catalyst was used at a reaction temperature of 500 °C.

The effect of the gas hourly space velocity (GHSV) of CO and HC in conversion was studied with 0.75 g 2% Co/CeO_2 catalyst at 500 ℃, and the result obtained is presented in figure 6.20. The GHSV was varied from 57800 h^{-1} to 289000 h^{-1} by controlling the inlet gas flow using the mass flow controller shown in the experimental setup. 100% conversion of CO and HC was obtained at gas flow rates of 100 ml/min and less, but both the oxidation rate decreased on further increasing the gas flow rate as expected. This decrease in activity is because more gas molecules are entered into the same number of active sites of the catalyst during the residence time with an increase in the flow rate.

The effect of catalyst weight on the percentage conversion was investigated at 400 ℃ using 2% Co/CeO_2 catalyst by varying the amount of catalyst, and the results are given in figure 6.21. On increasing the catalyst weight from 0.25 g to 1.00 g, both the oxidation activity of CO and HC occurs in an inverted parabolic manner. The optimum catalyst weight is 0.75 g. On further increase in the amount of catalyst inside the catalyst bed, the conversion is decreased, which can be due to the slow diffusion of gaseous reactant/product molecules into/from the active sites of the catalyst.

The effect of the amount of cobalt on ceria was also studied in the reaction conducted with different percentages of cobalt incorporated ceria at 400 ℃ using 0.75 g of all the catalysts prepared.

Best results are obtained in CO and HC conversion using the 2 wt% cobalt loaded catalyst as shown in figure 6.22.

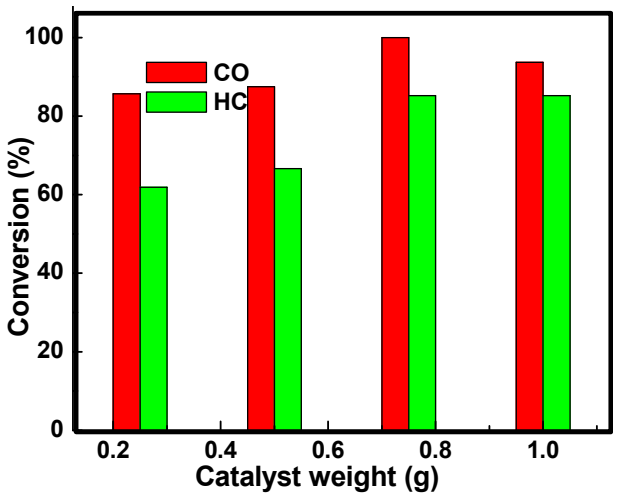

Fig. 6.21 Effect of catalyst weight on % conversion of CO and HC at 400 °C using 2% Co/CeO_2.

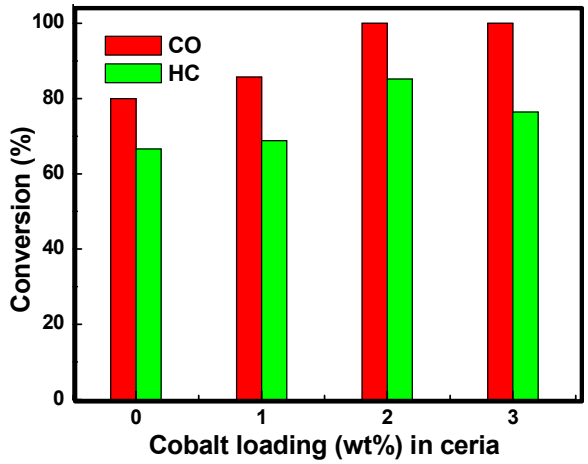

Fig. 6.22 Effect of percentage cobalt loading in ceria on the catalytic activity of CO and HC oxidation at 400 °C using 0.75 g catalyst.

The highest activity of 2% Co/CeO_2 is due to the combined effect of smallest particle size, and highest surface area – pore volume as revealed from TEM and BET surface area analyses; and also by the improvement in the formation of oxygen vacancies through cobalt incorporation into the ceria lattice. 3% Co/CeO_2 catalyst have slightly lesser catalytic activity than 2% Co/CeO_2 and the decreased activity is due to the lesser incorporation of Co into the ceria lattice as evidenced from the indication of the formation of Co_3O_4 from the XRD patterns. The catalytic activity of the pure Co_3O_4 is found to be lower than cobalt-doped ceria for the simultaneous oxidation of CO and HC. The maximum HC conversion is obtained as 80%, where the Co/CeO_2 gave 100% oxidation of both CO and HC.

From the results obtained in the simultaneous oxidation of Co and HC, it can be seen that the activity of the Co doped systems was enhanced relative to CeO_2 by the synergistic interactions between the Co species and CeO_2. Also, the replacement of Ce by smaller-sized Co enhances the oxygen storage-release capacity of the ceria lattice. The H_2-TPR results confirmed that the Co doped sample got reduced at lower temperatures compared to pure ceria. The specific reaction rates expressed in mol Kg $catalyst^{-1}$ s^{-1} calculated for all the samples are given in Table 6.3. The reaction rate studies also suggested the higher activity of cobalt-doped ceria catalysts compared to bare ceria. The highest value in both CO and propane oxidation for 2% Co doped catalyst is also evident from the data.

Table 6.3 specific reaction rates calculated for cobalt doped ceria catalysts in CO and propane oxidation reaction.

Catalyst	Specific reaction rate (mol Kg catalyst^{-1} s^{-1})	
	CO	Propane
CeO_2	0.0317	0.4026 x 10^{-3}
1% Co/ CeO_2	0.0340	1.1786 x 10^{-3}
2% Co/ CeO_2	0.0397	1.4600 x 10^{-3}
3% Co/ CeO_2	0.0397	1.3080 x 10^{-3}

The plausible catalytic mechanisms of CO and propane oxidation are shown in figures 6.23 and 6.24, which are initiated by the adsorption of the reactant molecules on the active $Ce_{1-x}Co_xO_2$ (where x is ~0.0878) species.

CO molecules can easily adsorb on the surface of $Ce_{1-x}Co_xO_2$, which then forms bidentate carbonate species that are the intermediates in CO oxidation (as per the Mars-Van krevelen (MvK) mechanism) [2,27]. The adsorbed CO extracts the surface oxygen atom to form a CO_2 molecule. The CO_2 molecule then converts on the surface as bicarbonate species using the second oxygen in the vacant sites. This oxygen is then exchanged with the neighboring adsorbed CO molecule forming CO_2 again. Desorption of these two CO_2 molecules recovers the oxygen vacant sites for the adsorption of gaseous O_2. Thus the catalytic efficiency mainly depends on the mobility of lattice oxygen

exposed on the surface. As already mentioned, cobalt incorporation and the resultant lattice expansion is the reason for the improvement in the catalytic performance upon doping. [27].

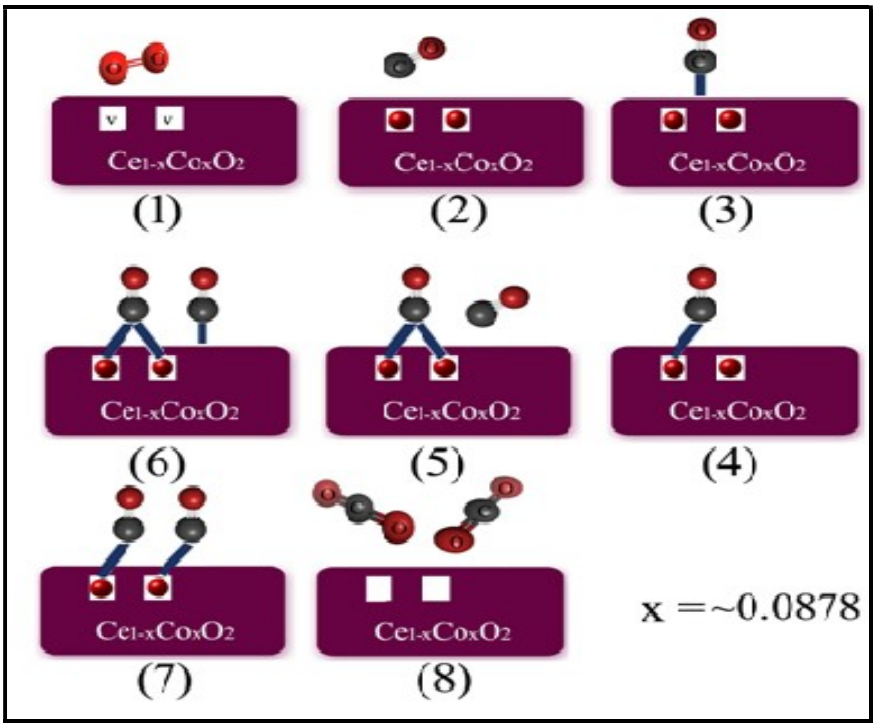

Fig. 6.23 CO oxidation mechanism over cobalt doped ceria.

Generally, the C-H bond breaking is a crucial step during the combustion of hydrocarbons over both noble metal and metal oxide catalysts. The activation of propane over metal oxides occurs by the abstraction of hydrogen atoms from the weakest C-H bond, with a simultaneous reduction of the surface sites and the successive formation of the surface hydroxide ions. Therefore, propene, the dehydrogenation intermediate, has been detected during the total

oxidation of propane [2]. It is then converted to different intermediates as shown in Figure 10, and is finally converted to and desorbed as H_2O and CO_2 [2]. Surface oxygen plays a crucial role here also, and the presence of Co enhances the exchange of lattice oxygen in CeO_2.

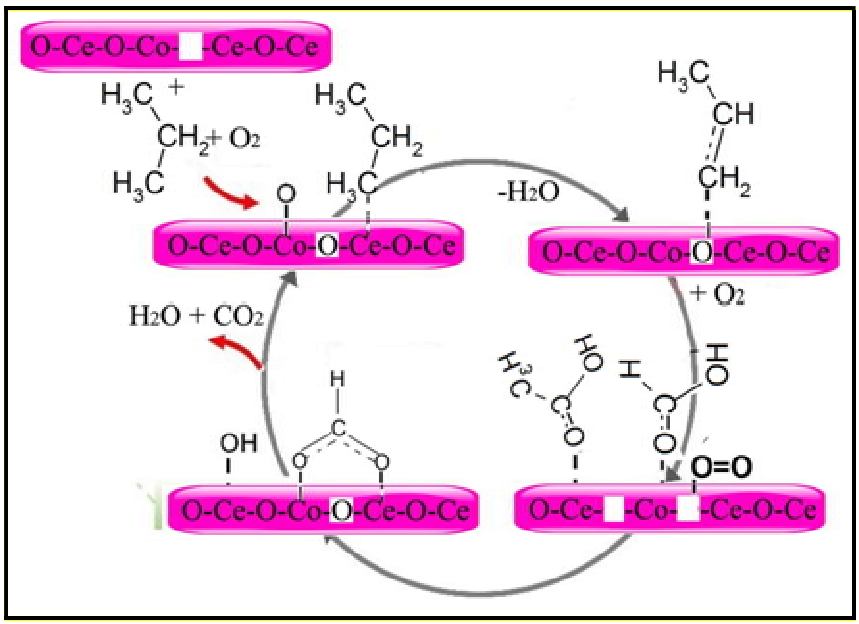

Fig. 6.24 Plausible mechanism for the oxidation of propane over cobalt doped ceria.

A comparison of the catalytic activity of the best catalyst sample, i.e., 2% Co/CeO_2 is performed with the other reported cobalt incorporated ceria samples in the literature, and the results are shown in Table 6.4. Present results are promising since the reactions were possible even at reasonably low temperatures, and simultaneous oxidation of both CO and HC are also achieved. The simplicity in the preparation procedure and the absence of the use of any template

material is the additional advantage of the present investigation. Significant oxidation activities are obtained in both CO and propane oxidation using the present cobalt doped CeO_2 catalyst prepared by simple precipitation method and further wet impregnation of Co. Usually, catalysts were subjected to deactivation during continuous run owing to the formation of coke on the catalysts' surface. Since CeO_2 can also act as a soot combustion catalyst, the coke formation that can lead to catalyst deactivation may be limited over ceria, especially at high temperatures. It is also observed that the present 2% Co/CeO2 catalyst retained 100% of its initial activity even after 5 hours of continuous run.

Table 6. 4. Comparison of the performance of 2% Co/CeO_2 in CO and propane oxidation with the reported cobalt incorporated CeO_2 samples.

Catalyst	Preparation method	Catalytic reaction	T_{50} (°C)	Specific reaction rate (mol $Kg_{catalyst}^{-1}$ s^{-1})	Reference
Cobalt-cerium spinel oxide	Citric acid complex method	Propane oxidation	220	0.22 x 10^{-3}	9
Co	Hydrothermal	Propane	328	-	4

modified CeO_2 nanorods		oxidation			
$(Co_3O_4)x/ CeO_2$	Hydrothermal, deposition precipitation	CO oxidation	84	-	6
Co_3O_4-CeO_2	Surfactant template	CO and Propane oxidation	94 (CO) 223 (propane)	-	2
Co-CeO_2 nanorods	Hydrothermal	CO oxidation	145	-	1
Co-CeO_2 nanodisk	Hydrothermal	CO oxidation	176		11
Co30Ce urea	Precipitation	Methane oxidation	343	0.373 x 10^{-3}	28

		n			
Co30Ce	Coprecipitation	Propene oxidation	-	0.055 x 10^{-3}	29
2% Co/CeO_2	**Precipitation and wet impregnation**	**CO and Propane oxidation**	**150 (CO) 325 (propane)**	**0.0397 (CO) 1.4600 x 10^{-3} (propane)**	**This work**

The cobalt-doped catalysts have also been used for the colorimetric determination of H_2O_2 due to its peroxidase-like performance. To demonstrate the peroxidase-like mimics a colorimetric method is used in the oxidation of a chromogenic substrate TMB to a blue-colored Ox-TMB (3,3′,5,5′-tetramethylbenzidine diimine) with the assistance of H_2O_2 as shown in the equation below.

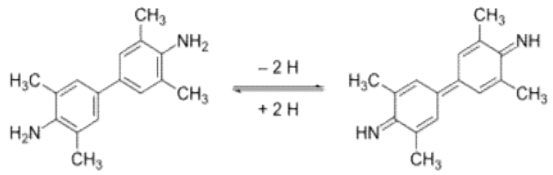

TMB **Ox-TMB**

The absorbance spectra, of the blue-colored solution, centered at 650 nm were monitored and used to compare the catalytic activity of the synthesized catalysts. The absorption spectrum of TMB oxidized by different systems in acetate buffer is shown in figure 6.25 and it is clear that an intense absorption band at 650 nm is observed only in presence of catalysts, i.e.; ceria or cobalt doped ceria, indicating that presence of ceria is an essential requirement for the oxidation of TMB with H_2O_2. A comparison of the absorbance values of ox-TMB by different catalyst systems is shown in figure 6.26. Also, it is evident from the figure that Co/CeO_2 exhibited more catalytic activity in TMB oxidation compared to undoped CeO_2.

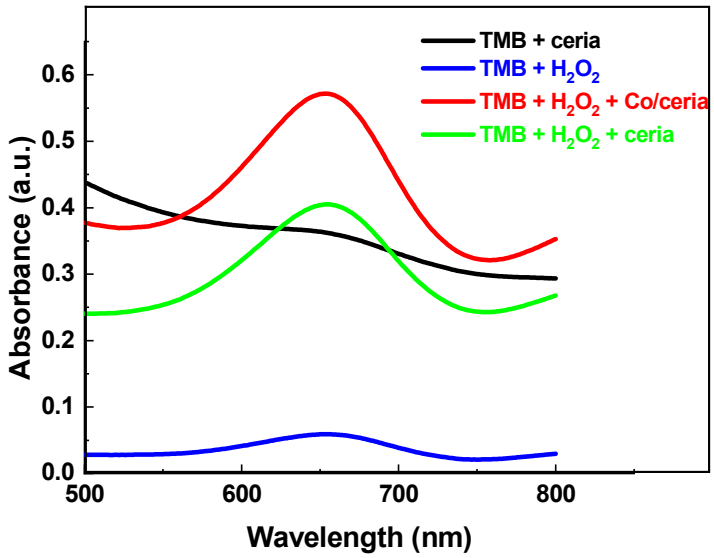

Fig. 6.25 UV-vis absorption spectrum of TMB oxidized at different conditions in acetate buffer.

The oxidation of TMB has been reported to proceed via a Fenton-like mechanism in which OH radicals are responsible for the formation of blue-colored Ox-TMB [30]. The oxidation reaction occurs by an electron transfer from a nonbonding orbital (NBO) of TMB to the lowest unoccupied molecular orbital of H_2O_2 [31]. The presence of a cobalt-doped catalyst can effectively facilitate the electron transfer from TMB to H_2O_2 resulting in enhanced peroxidase-like activity.

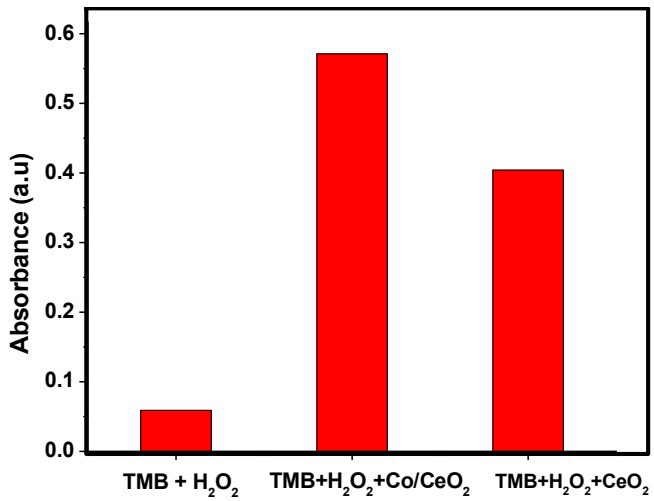

Fig. 6.26 Comparison of absorbance of ox-TMB obtained by oxidation in the presence of CeO_2 and 2% Co/CeO_2 by in acetate buffer.

The catalytic activity of the cobalt doped samples monitored by absorbance measured in time course at 650 nm is presented in figure 6.27. In all the cases, the absorbance increased with time, indicating that the cobalt-doped ceria catalysts effectively catalyze the oxidation of TMB in presence of H_2O_2. It can be observed from the figure that the rate of oxidation is different in the three cases. After 10 min

reaction time, an increase in oxidation rate is observed in 3% Co/CeO_2 compared to 1% Co/CeO_2. On comparing the absorbance values of the systems at 10 min there is only a slight difference in the activities of 1 wt% and 3 wt% cobalt doped systems.

By choosing the catalyst synthesized using a minimum amount of cobalt doping in ceria, 1% Co/CeO_2 has been selected for further studies on the colorimetric determination of H_2O_2.

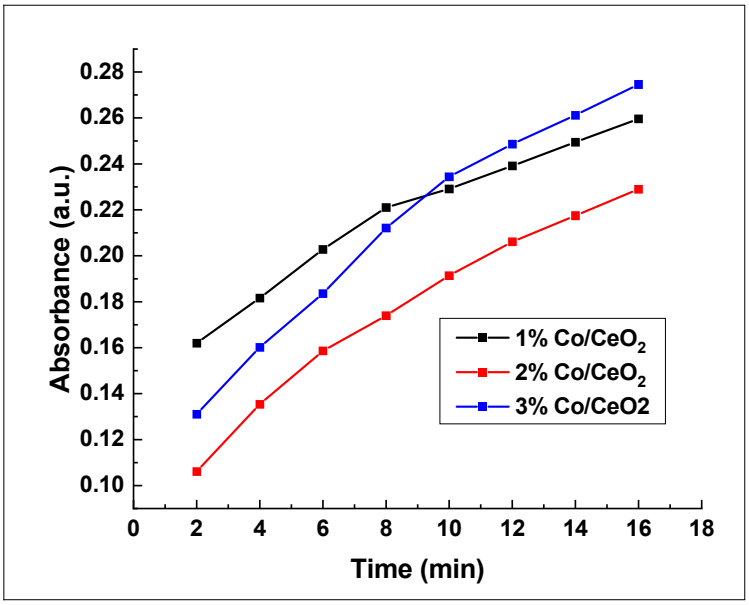

Fig. 6.27 Time-dependent absorption changes at 650 nm using cobalt-doped ceria catalysts.

Absorbance values of Ox-TMB were measured continuously on adding H_2O_2 in different concentrations to 1% Co/CeO_2 catalyst-TMB mixture as specified in the experimental section and the concentration-response curve is plotted in figure 6.28.

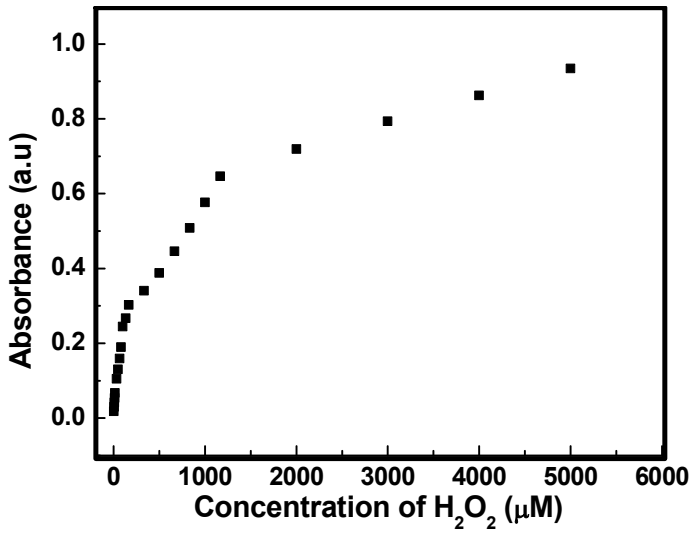

Fig. 6.28 Concentration-dependent curve of Ox-TMB with the addition of H_2O_2 of different concentrations.

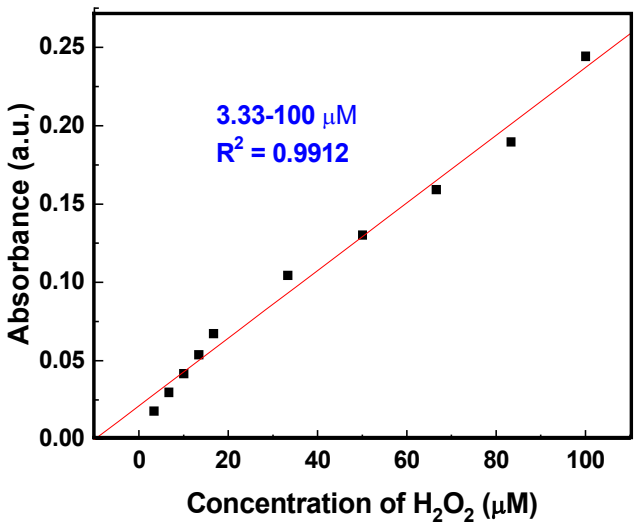

Fig. 6.29 Linear calibration plot for H_2O_2 in the concentration range of 3.33 μM-100 μM.

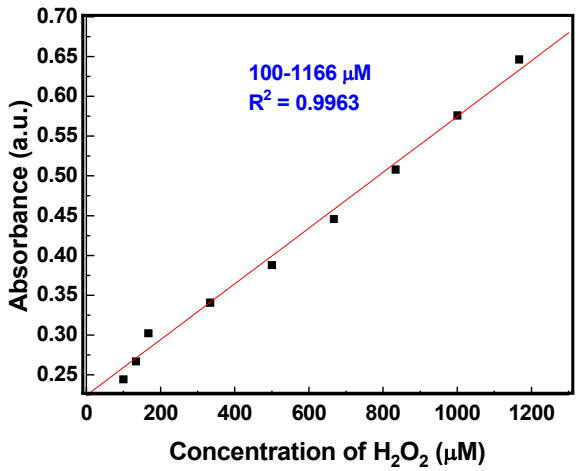

Fig. 6.30 Linear calibration plot for H_2O_2 in the concentration range of 0.1 mM-1.16 mM.

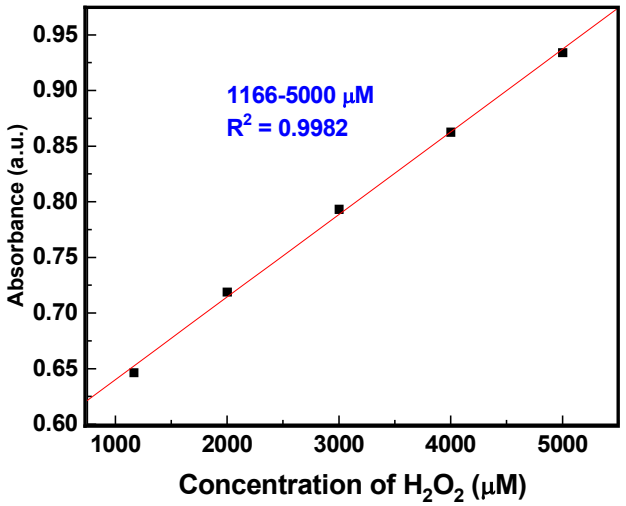

Fig. 6.31 Linear calibration plot for H_2O_2 in the concentration range of 1.16 mM-5 mM.

The absorbance increases with the concentration of H_2O_2 and three linear ranges are observed in the curve. The lowest detection limit is 3.33 μM, and the three linear ranges observed are 3.33 μM-100 μM (R^2 = 0.9912), 100 μM-1166 μM (R^2 = 0.9963) and 1166 μM-5000 μM (R^2 = 0.9982) as given separately in figures 6.29, 6.30 and 6.31 respectively.

Table 6.5 Linear range and LOD in peroxidase-like H_2O_2 sensing using reported CeO_2 catalysts.

Catalyst	Linear range (μM)	LOD (μM)	Ref
CeO_2/C nanowires	0.5 - 100	0.42	32
porphyrin functionalized CeO_2	10 - 100	1.8	13
CeO_2 NPs	0.6 - 1.5	0.5	18
CeO_2 NPs	4 - 40	2.5	15
porphyrin functionalized CeO_2 nanorods	10 – 100	6.1	33
Co_3O_4 nanoparticles inside CeO_2 nanotubes	2-80	1.2	34
Co/CeO_2	**3.33-100, 100-1166, 1166-5000**	**3.33**	**This work**

The linear range and limit of detection of H_2O_2 in the colorimetric determination using the Co/ceria catalyst synthesized in this work has been compared with the values from literature studies and is presented in table 6.5. Compared to the corresponding values in

the reports, a wide linear range (3.33-100 μM, 100-1166 μM, and 1166-5000 μM) is obtained using the catalyst synthesized in this work.

6.4 Conclusions

In this work, cobalt-doped ceria catalysts were synthesized by precipitation followed by a wet impregnation method using cerium nitrate and cobalt nitrate as the precursors and ammonia as the precipitating agent. The samples were well characterized by different techniques. The prepared systems were examined on the catalytic oxidation of pollutants, carbon monoxide, and propane (a model hydrocarbon pollutant). The effect of polluted gas flow rate, reaction temperature, catalyst weight, and the effect of cobalt loading in ceria, on CO and HC oxidation, were studied in detail. All the cobalt-doped ceria systems were more active in both CO and propane oxidation than bare ceria. 100% CO and propane conversion were obtained at 450° C using 0.75 g 2 wt% cobalt doped ceria catalyst. The cobalt doped systems were also applied in the colorimetric determination of H_2O_2 due to their peroxidase-like performance. Three linear ranges; viz 3.33-100 μM, 100-1166 μM, and 1166-5000 μM were observed in the H_2O_2 sensing with a good LOD value using a 1% Co/CeO_2 sample.

References

1. D. Jampaiah, P. Venkataswamy, V. E. Coyle, B. M. Reddy and S. K. Bhargava, *RSC Adv.,* 2016, **6**, 80541.
2. J. Y. Luo, M. Meng, Y. Q. Zha and L. H. Guo, *J. Phys. Chem. C*, 2008, **112**, 8694.
3. Y. Gao, S. Teng, Z. Wang, B. Wang, W. Liu, W. Liu and L. Wang, J. Mater. Sci.,2020, 55, 283.
4. Q. Song, R. Ran, J. Ding, X. Wu, Z. Si and D. Weng, *Mol. Catal.,* 2020, **480**, 110663.
5. Y. Chen, D. Liu, L. Yang, M. Meng, J. Zhang, L. Zheng and S. Chu, *Chem. Eng. J.*,2013, **234**, 88.
6. J. Tian, W. Na, H. Wang and W. Gao, *Adv. Mat. Res.,*2013, **643**, 76.
7. J. Wang, M. Shen, J. Wang, J. Gao, J. Ma, S. Liu, *J. Rare Earths,*2012, **30**, 878.
8. W. Liu, M. F. Stephanopoulos, *J. Catal.,* 1995, **153**, 304.
9. S. Zhang, S. Liu, X. Zhu, Y. Yang, W. Hu, H. Zhao, R. Qu, C. Zhen and X. Gao,*Appl. Surf. Sci*.,2019, **479**, 1132.
10. D. Jampaiah, S. J. Ippolito, Y. M. Sabri, B. M. Reddy and S.K. Bhargava, *Catal. Sci. Technol*., 2015, **5**, 2913.
11. X. H. Guo, C. C. Mao, J. Zhang, J. Huang, W. N. Wang, Y. H. Deng, Y. Y. Wang, Y. Cao, W. X. Huang and S. H. Yu, *Small,* 2012, **8**, 1515.
12. H. Wang, L. Zhang, M. Li, Y. Liu and X. Bai, *J. Rare Earths,*2013, **31**, 565.

13. H. Liu, Y. Ding, B. Yang, Z. Liu, Q. Liu and X. Zhang, *Sens. Actuators B Chem*., 2018, **271**, 336.
14. Z. Zhang, Z. Jiang and W. Shangguan, *Catal. Today*, 2016, **264**, 270.
15. J. Guo, Y. Wang and M. Zhao, *Talanta,* 2018, **182**, 230.
16. M. Ornatska, E. Sharpe, D. Andreescu, and S. Andreescu, *Anal. Chem.,* 2011, **83**, 4273.
17. F. A. O. Olgun, A. Üzer, B.D. Ozturk and R. Apak, *Talanta*, 2018, **182**, 55.
18. X. Jiao, H. Song, H. Zhao, W. Bai, L. Zhang and Y. Lv, *Anal. Methods*, 2012, **4**, 3261.
19. Q. Wang, K. L. Yeung, M. A. Banares, *Catal. Today*, 2019.
20. H. Wang, B. Yuan, R. Hao, Y. Zhao and X. Wang, *Chem. Eng. J.*2019, **378**, 122155.
21. P. Gawade, B. Bayram, A. M. C. Alexander and U. S. Ozkan, *Appl. Catal. B: Environ.,*2012, **128**, 21.
22. A. A. Ansari, J. Labis, M. Alam, S. M. Ramay, N. Ahmad and A. Mahmood, *Phase Transit.,* 2016, **89**, 261.
23. B. Elahi, M. Mirzaee, M. Darroudi, R. K. Oskuee, K. Sadri, M. S. Amiri, *Ceram. Inter.,*2019, **45**, 4790.
24. L. Xu, C. Zhang, H. He and Y. Teraoka, *Catal. Today*,2007, **126**, 449.
25. H. Wu, G. Pantaleo, G. D. Carlo, S. Guo, G. Marcì, P. Concepción, A. M. Venezia and L. F. Liotta, *Catal. Sci. Technol.,* 2015,**5**, 1888.

26. Z. Zhao, X. Lin, R. Jin, Y. Dai, G. Wang, *Catal. Sci. Technol.,* 2012, **2**, 554.
27. J. Y. Luo, M. Meng, X. Li, X. G. Li, Y. Q. Zha, T. D. Hu, Y. N. Xie and J. Zhang, J. catal., 2008, 254, 310.
28. H. Wu, G. Pantaleo, G. Di. Carlo, S. Guo, G. Marci, P. Concepcion, A. M. Venezia and L. F. Liotta, Catal. Sci. Technol., 2015, 5, 1888.
29. L.F. Liotta, M. Ousmane, G. Di Carlo, G. Pantaleo, G. Deganello , G. Marcı, L. Retailleau and A. Giroir-Fendler, Appl. Catal. A: Gen., 2008, 347, 81.
30. Z. M. Tian, J. Li, Z. Y. Zhang, W. Gao, X. M. Zhou and Y. Q. Qu, Biomaterials 2015, **59**, 116.
31. F. Yuan, H. M. Zhao, H. M. Zang, F. Ye and X. Quan, *ACS. Appl. Mater. Interfaces,* 2016, **8**, 9855.
32. W. Dong and Y. Huang, *Microchim. Acta.,* 2020, **187**, 11.
33. Q. Liu, Y. Ding, Y. Yang, L. Zhang, L. Sun, P. Chen and C. Gao, *Mater. Sci. Eng. C*, 2016, **59,** 445.
34. Y. Zhu, Z. Yang, L. Song, M. Chi, M. Li, C. Wang and X. Lu, Part. Part. Syst. Charact.2018, **35**, 1800049.

Chapter 7

Summary and Conclusions

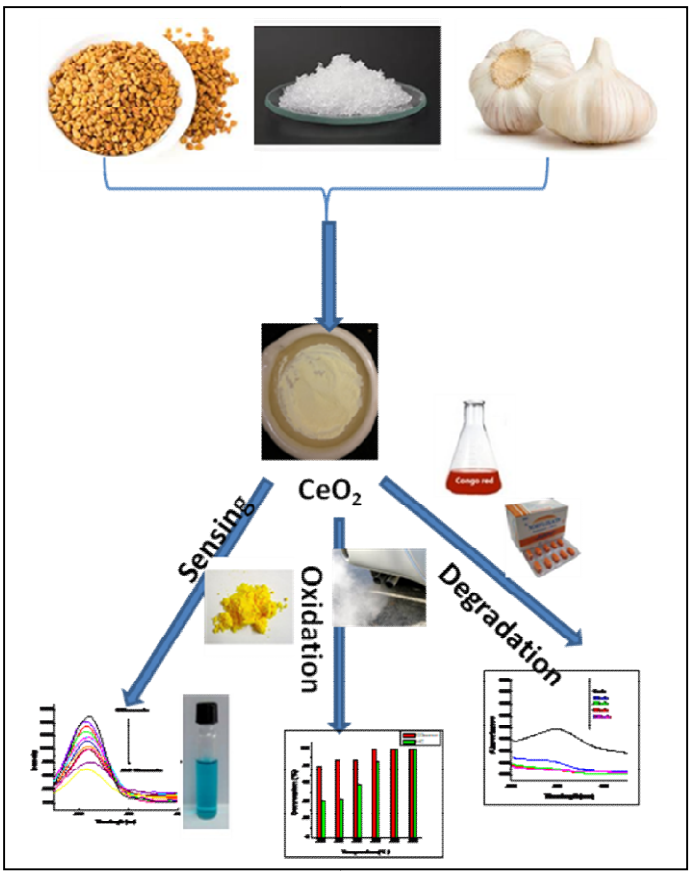

7.1 Introduction

Cerium oxide is a relevant rare earth metal oxide exhibiting unique properties such as oxygen storage capacity (OSC). The simplistic oscillations of cerium between +3 and +4 in ceria crystal with the corresponding formation of oxygen vacancies are responsible for the OSC of cerium oxide [1]. This peculiar redox property of cerium makes ceria a suitable material applicable as a catalyst in many redox reactions such as three-way catalysis, water gas shift reactions, oxidation of volatile organic compounds, photocatalysis, etc [2]. The fluorescence emission properties of ceria nanoparticles can use for the sensing of biologically and environmentally relevant molecules. In addition to the several physical and chemical synthesis methods for the preparation of ceria nanoparticles, green methods involving active bio components in plant extracts as chelating and stabilizing agents are of high significance [3].

7.2 Summary

In summary, the present work deals with the synthesis of ceria nanoparticles via green approaches and the characterization of the prepared materials by various techniques. The synthesized materials have been used for multipurpose applications such as photocatalytic antibiotic and dye degradation, adsorption, gaseous pollutant degradation, and fluorescence sensing. The synthesis methods adopted here are simple and relatively greener. The thesis is structured into 7 chapters together with a summary and conclusions chapter. The

summary of each chapter and the conclusions arrived at are discussed in brief in the following sessions.

7.2.1 Chapter 1: Ceria: Brief Introduction and Literature Review

The first chapter introduces ceria and describes its unique properties such as redox properties, OSC, optical properties, and electronic properties. The OSC and oxygen vacancies of ceria, which arise in the material as s result of facile conversion between the two oxidation states of cerium as Ce^{3+} and Ce^{4+} are the key factors involved as the basis of various properties of ceria [4]. The different solid-state reactions explaining how this property arises in ceria and how the nanosize of the particles affect these properties are additionally mentioned here. Some methods to improve the inherent properties of ceria, such as the incorporation of metal ions, formation of mixed oxides, morphological modifications through synthesis adopted by various research groups, etc., are briefly discussed. Several synthesis methodologies commonly used for ceria including newly developed green strategies are also detailed in this chapter. Ceria, being a semiconductor metal oxide, has applications in different fields, and the various applications of ceria involving three-way catalysis, pollutant degradation, adsorption, colorimetric, and fluorescence sensing of significant molecules such as H_2O_2, dissolved oxygen, glucose, etc. are explained in the chapter. The major objectives of the present study, including the green synthesis methods and the

applications of prepared CeO_2 nanoparticles are mentioned in the last part of the chapter.

7.2.2 Chapter 2: Materials and Methods

The 2nd chapter deals with the experimental methods and the materials used throughout this work. The various characterization techniques used and their working principles are briefly explained here. The technical details of the various instruments used for the characterization of the materials synthesized, and also for their applications are given.

7.2.3 Chapter 3: Photocatalytic Degradation of Norfloxacin under UV, Visible and Solar Light using Ceria Nanoparticles

Chapter 3 discussed the synthesis of ceria nanoparticles in the ultra-small dimension by simple precipitation method starting from cerium nitrate and its application in the removal of norfloxacin (NOF), a widely used antibiotic. Three different ceria catalysts were prepared there, by varying the concentration of the precipitating agent, NH_3, the synthesis procedures are also discussed. The samples were well characterized by different techniques and confirmed the formation of mesoporous ceria nanoparticles having a particle size in the range of 5-8 nm. The obtained catalysts showed absorption in the visible light also, as evidenced by their bandgap values calculated from UV-vis analysis. Photocatalytic degradation of NOF was studied under UV, visible and solar light irradiation. The effect of irradiation time, catalyst weight, solution volume, and antibiotic concentration on

photocatalytic activity were studied under UV light. Maximum degradation of 98.9% NOF was obtained with ceria synthesized by the addition of 2M NH_3 to the precursor solution and the catalyst is also found to have good reusability. The efficiency of the catalyst in the photocatalytic degradation of NOF under visible and solar irradiation is also examined and proved. A plausible mechanism of photocatalytic degradation of NOF using ceria is narrated here. Since ceria-based nanocomposites involving noble metals or those containing two or three heterojunctions are usually reported for the effective degradation of antibiotics, here, the use of bare cerium oxide nanoparticles synthesized by simple precipitation method having excellent catalytic properties is truly advantageous, which highlights the importance of the present work.

7.2.4 Chapter 4: Adsorption and Photo Fenton Degradation of Congo Red Dye by Ceria Nanoparticles Synthesized using *Allium Sativum* Extract

This chapter narrates the preparation of nanostructured mesoporous ceria from cerium nitrate by the sol-gel method using aqueous *Allium sativum (*garlic) extract. The structural, optical, and electronic properties of the ceria samples prepared using different amounts of garlic extract were characterized by various methods. The results showed that the synthesized cubic fluorite ceria nanoparticles are spherical, with particle sizes between 10 nm to 40 nm. N_2 adsorption-desorption studies revealed the mesoporous nature of the

ceria samples having narrow slit-like pores. Here we used the various phytochemicals present in garlic extract as the chelating and stabilizing agents for the preparation of CeO_2 nanoparticles having reduced particle agglomeration. The synthesized materials are having both adsorption and photo-Fenton activity in the removal of a model pollutant Congo red. The porous nature of the material, which could be attained through the decomposition of the organic compounds in the extract during heat treatment is beneficial for the adsorption of dye molecules. The effect of different reaction parameters, such as time, ceria dosage, the volume of dye solution, and dye concentration on the percentage removal was studied in both cases. A maximum of 96% Congo red was removed by adsorption and 100% dye was degraded by photo-Fenton degradation using the best CeO_2 sample prepared in this study.

7.2.5 Chapter 5: Fluorescence Sensing of Picric Acid by Ceria Nanostructures Prepared using Fenugreek Extract

Chapter 5 is focused on the fluorescence detection of picric acid in water using ceria nanoparticles synthesized in the presence of fenugreek (*Trigonella foenum-graecum*) extract by the sol-gel method. Easy and fast detection of aquatic pollutants is highly demanded to avoid water contamination. The nanostructure and material morphology of the obtained cubic phase fluorite ceria is investigated using different techniques. The use of fenugreek extract in the synthesis of ceria nanoparticles helped to reduce particle agglomeration and lead to the formation of smaller particles, which in

turn is advantageous in exhibiting excellent fluorescence properties. Optical studies confirmed its strong absorbance and intense photoluminescence emission. Sensing of picric acid is indicated by fluorescence quenching of the nanoparticle dispersion. Ceria nanoparticle dispersion synthesized in this study showed a linear concentration range of 0.33 μM – 41.6 μM with a lower detection limit of 0.33 μM picric acid. The strong interaction between nanoceria and picric acid is indicated from the high Stern-Volmer constant. The CeO_2 nanoparticles are also found to be selective to picric acid in presence of other phenolic compounds.

7.2.6 Chapter 6:Cobalt Doped Ceria Catalysts for the Removal of Gaseous Pollutants and Colorimetric Detection of H_2O_2

Chapter 6 describes the synthesis of cobalt-doped ceria catalysts by precipitation followed by the wet impregnation method using cerium nitrate and cobalt nitrate as precursors and ammonia as the precipitating agent. The samples were thoroughly characterized by different techniques and identified the formation of CeO_2 nanoparticles in the size range of 8-14 nm. The activity of the prepared systems was examined in the simultaneous oxidation of carbon monoxide and hydrocarbons (HC). The effect of pollutant gas flow rate, reaction temperature, catalyst weight, and cobalt loading in ceria on CO and HC oxidation was also studied. All the cobalt-doped ceria systems were more active compared to undoped ceria in pollutant gas treatment. 100% CO and HC conversion were obtained at 450 °C using

0.75 g 2 wt% Co doped ceria catalyst. The reducibility of ceria nanoparticles could be increased by cobalt doing. The peroxidase-like performance of cobalt doped systems was also studied and applied in the colorimetric determination of H_2O_2, which is an important intermediate formed in several metabolic reactions in our body. Three linear ranges, viz 3.33-100μM, 100-1166 μM, and 1166-500 μM were observed in the analysis, with a good LOD value using 1 wt% Co doped CeO_2 sample.

7.2.7 Chapter 7: Summary and Conclusions

The 7th chapter summarizes the results of the present work on the synthesis of ultra-small ceria nanoparticles by simple modifications of the reaction conditions in the existing methods and by novel green methods; and their applications in pollutant treatment, fluorescence sensing, and H_2O_2 optical sensing.

7.3 Conclusions

In the present study, we have synthesized ceria nanoparticles by three different green methods, and cobalt-doped ceria catalyst systems are also prepared by the wet impregnation method. We have used garlic extract and fenugreek extract in the sol-gel preparation, the components of which can act as gelating and chelating agents during preparation. The various phytochemicals make a key role in the formation of small particles of ceria with less agglomeration. The prepared ultrasmall ceria particles by ammonia precipitation have been proved to be excellent photocatalysts in norfloxacin degradation with

good reusability. The mesoporous ceria synthesized by the sol-gel method in presence of garlic extract has been utilized for the removal of Congo red dye both by adsorption and Photo Fenton reaction in visible light. Cobalt doped ceria systems were found to have better performance in the simultaneous oxidation of CO and HC. Co/CeO_2also showed peroxidase-like performance, which has been utilized in the colorimetric determination of H_2O_2. Ceria nanostructures synthesized by the sol-gel method in presence of fenugreek extract is utilized for the selective sensing of picric acid in real water through the fluorescence quenching method. Ceria showed a wide linear range in sensing, and a low limit of detection is observed.

7.4 Future Outlook

The present work has the potential for extension in various dimensions. Nowadays, the synthesis of metal oxide nanoparticles using bio-components has been widely studied, and in this work, we have synthesized cerium oxide nanoparticles by using garlic and fenugreek extracts via sol-gel method. The formation of nanoparticles having different morphologies can be tried by varying some synthesis parameters. These synthesis methodologies can be extended by making use of other bio-components present in different parts of plants, which are easily available in our nature. The ceria synthesized by the ammonia precipitation method, which is proved to be an excellent photocatalyst in norfloxacin degradation, can also be examined in the degradation of various other antibiotics and also dyes. Similarly, the

photo Fenton catalyst synthesized by garlic extract that has been applied in the removal of azo dye Congo red may also be used in the removal of other classes of dyes. The three-way catalytic properties of cobalt doped systems can also be studied or it can be utilized in some other applications such as in solid oxide fuel cells. The colorimetric method of determination of H_2O_2 by cobalt-doped ceria samples can be applied for glucose sensing. Fluorescence sensing of other relevant molecules such as dissolved oxygen, tiny metal particles such as Fe, Pb, Hg, etc., may be examined using the ceria nanoparticles synthesized using fenugreek extract which has been used here for fluorescence sensing of picric acid.

References

1. J. Kašpar, P. Fornasiero, M. Graziani, Catal. Today, 1999, **50**, 285.
2. M. Darroudi, S.J. Hoseini, R.K. Oskuee, H.A. Hosseini, L. Gholami and S. Gerayli, Ceram. Int., 2014, **40**, 7425.
3. B. Kumar, K. Smita, L. Cumbal, A. Debut and Y. Angulo, J. Saudi. Chem. Soc., 2017, **21**, S475.
4. X. Wang and R. J. Gorte, Catal. Lett., 2001, **73**, 15.

LIST OF PUBLICATIONS

1. Remani K.C, Binitha N.N, “Cobalt doped ceria catalysts for the oxidative abatement of gaseous pollutants and colorimetric detection of H_2O_2”, Materials Research Bulletin, 2021, 139, 111253.
2. Remani K.C, Binitha N.N, “Fluorescence sensing of picric acid by ceria nanostructures prepared using fenugreek extract”, Journal of the Iranian Chemical Society, Article in Press.
3. Remani K.C, Binitha N.N, “Photocatalytic degradation of norfloxacin under UV, visible and solar light using ceria nanoparticles”, Materials Today: Proceedings, 2020, 25, 246–251.

LIST OF PAPERS PRESENTED

1. Participated and presented a paper entitled “Photocatalytic Degradation of Norfloxacin under UV, Visible and Solar light using Homogeneously Precipitated Cerium oxide Nanoparticles” in the International Conference on Science and Technology of Advanced materials (STAM 20) on 14, 15 and 16 th January 2020 organized by Mar Athaasius College, Kothamangalam.

2. Presented a paper entitled “Cobalt Doped Ceria Catalysts for the Simultaneous Removal of Carbon monoxide and Hydrocarbons” in the National seminar on Recent Trends in Material Science and Technology during 27-28 Novermber 2018 organized by SNGS College Pattambi.
3. Presented a paper entitled “Manganese Doped Ceria-Zirconia and its Catalytic Activity Study on Soot Combustion” in the National seminar on EMERGING TRENDS IN NANOMATERIALS SCIENCE AND TECHNOLOGY (ETNST – 2017) organized by Post Graduate Department of Chemistry, Sree Neelakanta Govt. Sanskrit College Pattambi during 19-20 December 2017.
4. Presented a paper entitled “Synthesis of Molybdenum Doped Ceria-Zirconia and its Catalytic Activity on Hydrocarbon Oxidation” in the UGC sponsored National conference on RECENT ADVANCES IN CHEMISTRY organized by Post

Graduate Department of Chemistry, Vimala College (Autonomous) Thrissur on 9th January 2017.

5. Presented a paper entitled “Ceria-Zirconia Solid Solution: Synthesis and its Catalytic Activity Study on Benzyl Alcohol Oxidation” in UGC sponsored National seminar on RECENT ADVANCES IN NANOTECHNOLOGY (RAN – 2015) organized by Post Graduate Department of Chemistry, Sree Neelakanta Govt. Sanskrit College Pattambi during 29-30 January 2015.